APPENDICES

Appendix A	CHAPTER SUPPLEMENTS
Appendix B	CASE STUDY
Appendix C	FINLAB
Appendix D	DESIGN OF THE STEEL SHAFT

Title main report:
“Hydrodynamic loading on the shaft of a gravity based offshore wind turbine”

Final report Master Thesis
Delft, 26 May 2014
Written by Henno Smaling

TABLE OF CONTENTS - APPENDICES

Appendix A CHAPTER SUPPLEMENTS

A.1. CHAPTER 2: TARGETS AND ECONOMICS

A.1.1. Targets

The whole concept of wind energy is mainly based on the next two motives:

- A decrease of available fossil fuels, the search for alternative energy sources
- Targets to diminish the amount of CO2 pollution, the search for sustainable energy

Offshore wind energy has grown over the past years. Half of the installed offshore wind capacity is installed in the United Kingdom. Most of it in relatively shallow water (<20 m) and not too far out of the coast (<20 km).
Installation of small farms started around the mid 90's. In 2001 the wind farm Middelgrunden in Denmark was taken in operation. With a total capacity of 40 MW this was the first rather large wind farm.

Figure A.1 shows that at the end of 2012 about 283 GW of wind power was installed globally. The offshore wind capacity at the end of 2012 was about 5.4 GW (Figure A.2).

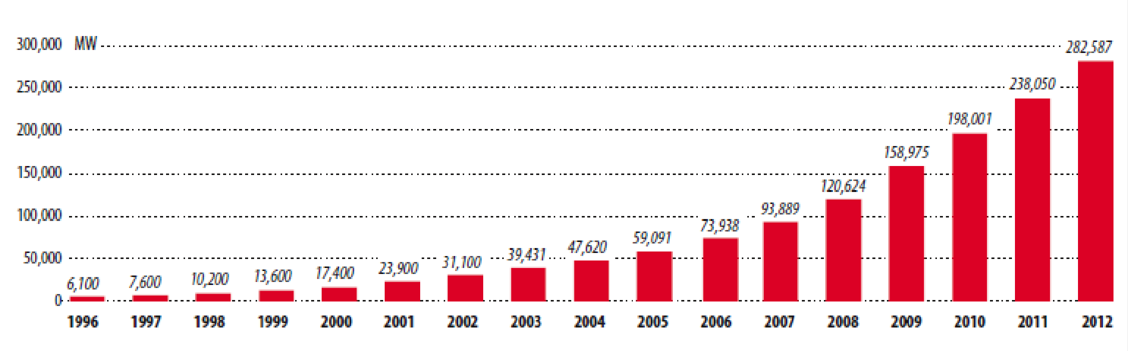

Figure A.1 - Global Cumulative Installed Wind Capacity 1996-2012 [1]

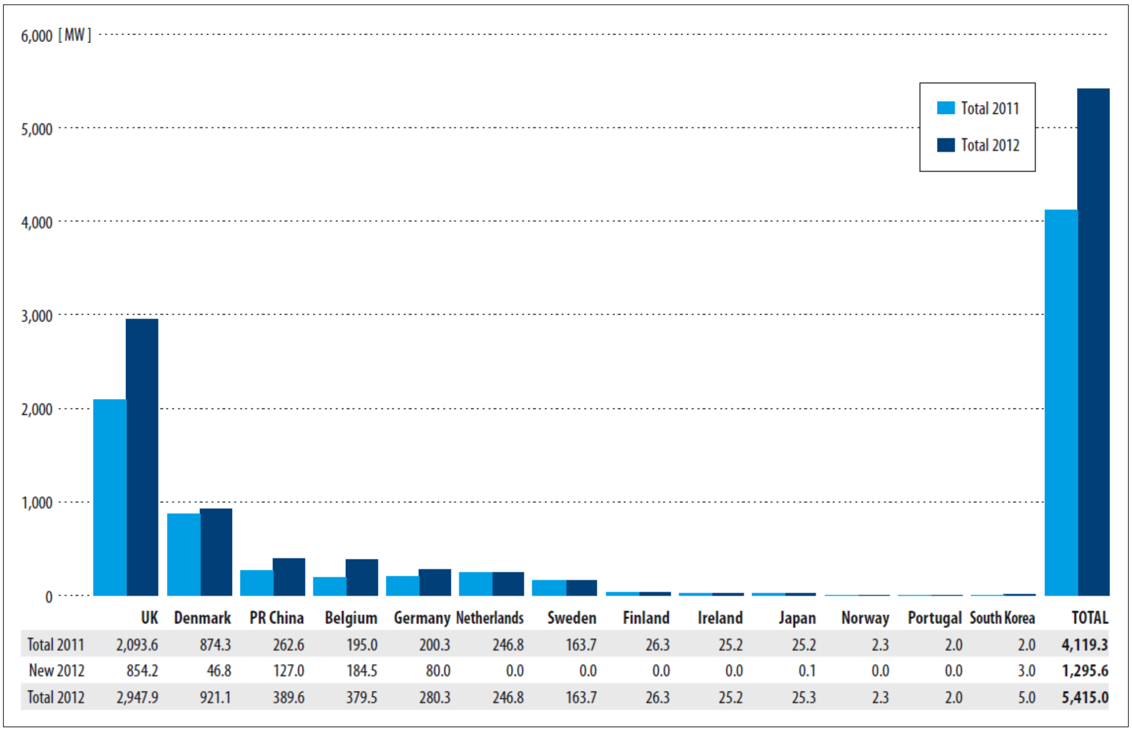

	UK	Denmark	PR China	Belgium	Germany	Netherlands	Sweden	Finland	Ireland	Japan	Norway	Portugal	South Korea	TOTAL
Total 2011	2,093.6	874.3	262.6	195.0	200.3	246.8	163.7	26.3	25.2	25.2	2.3	2.0	2.0	**4,119.3**
New 2012	854.2	46.8	127.0	184.5	80.0	0.0	0.0	0.0	0.0	0.1	0.0	0.0	3.0	**1,295.6**
Total 2012	2,947.9	921.1	389.6	379.5	280.3	246.8	163.7	26.3	25.2	25.3	2.3	2.0	5.0	**5,415.0**

Figure A.2 - Global Cumulative Offshore Installed Capacity in 2012 [1]

The market for offshore wind is expected to increase. In [2] a prediction is given for the global offshore wind power development (Table A.1). Several countries have targets for the total amount of offshore wind power. The European Wind Energy Association has identified a target for the EU members of 40 GW offshore wind power to be installed by 2020 [3]. By 2030 the target is 150 GW. In addition the target for the United States is between 54 and 89 GW by 2030. These targets correspond with the numbers of Table A.1. According to Table A.1 around 2050 the total wind energy production is expected to be about 36% of the world energy consumption, of which 6% from offshore energy.

The predictions of 2007 (Table A.1) are based on an annual growth rate of 34% in the period till 2015. According to the numbers at the end of 2012 the annual growth rate is 36% in the period of 2006 – 2012 (Table A.1 for the 2012 values).

Year	Offshore wind [GW]	Offshore of total wind power [%]	Production from offshore wind [TWh/y]	Expected global energy consumption [TWh/y]	Penetration of offshore wind [%]
2006	0.9	1.2	3	15500	0.0
2015	12.8	2.6	42	21300	0.2
2020	42.4	4.0	140	23800	0.6
2030	251.1	9.5	829	29750	2.8
2050	773.8	18.4	2559	40100	6.4

Table A.1 - Scenario for global offshore wind power development [2]

A.1.2. Economical aspects

Costs are determined by:

- Construction costs
    - Costs of design
    - Material costs
    - Fabrication costs
    - Installation
- O&M
- Balancing of power production
- Demolition

Comparison of different energy generating concepts is often done by determination of the Levelized Costs Of Energy (LCOE). This term calculates all the costs over the lifetime for a certain quantity of energy (often 1 kWh).
In [3] a quantative comparison for the for a tri-floater (a floating offshore wind turbine) has been made, see Table A.2.

	2012 price [€/kWh]	Target 2020 [€/kWh]	Target 2030 [€/kWh]
Onshore	0.08	-	-
Offshore	0.17	0.10	0.06

Table A.2 - LCOE comparison for onshore and offshore wind turbines (tri-floater), exchange rate 2012: 1 USD = 0.78 EUR [3]

The German institute ISE Fraunhofer has calculated the LCOE for on- and offshore wind farms [5]. An important parameter is the operation time. For an onshore wind turbine the operation time is between 1300 and 2700 full load hours per year, depending on the location. For an offshore wind turbine in the North Sea the range is 2800 – 4000 full-load hours per year.

For onshore wind farms with average conditions the LCOE is between 0.06 and 0.08 €/kWh (Figure A.3). For offshore wind farms with average conditions this is between 0.11 and 0.16 €/kWh. Despite the higher amount of full-loaded hours, the LCOE is about 2x as much. This is because of the higher investment and O&M costs.

For the future (till 2030) a prediction for the LCOE is made, based on learning curves (Figure A.4). The LCOE for onshore wind power will on average stay the same with about 0.07 €/kWh. For offshore wind power the LCOE is expected to decrease to an average of 0.12 €/kWh.

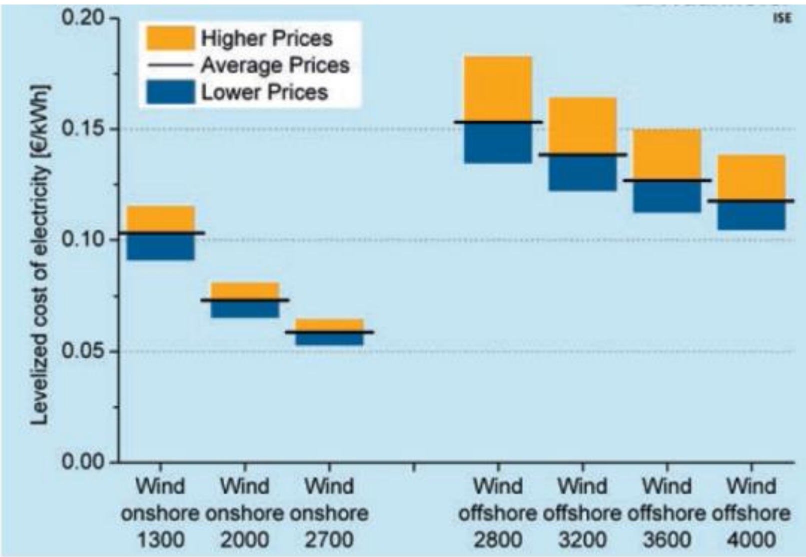

Figure A.3 - LCOE for wind farms (2012 prices) [5]. Numbers underneath the axis are full-load hours per year.

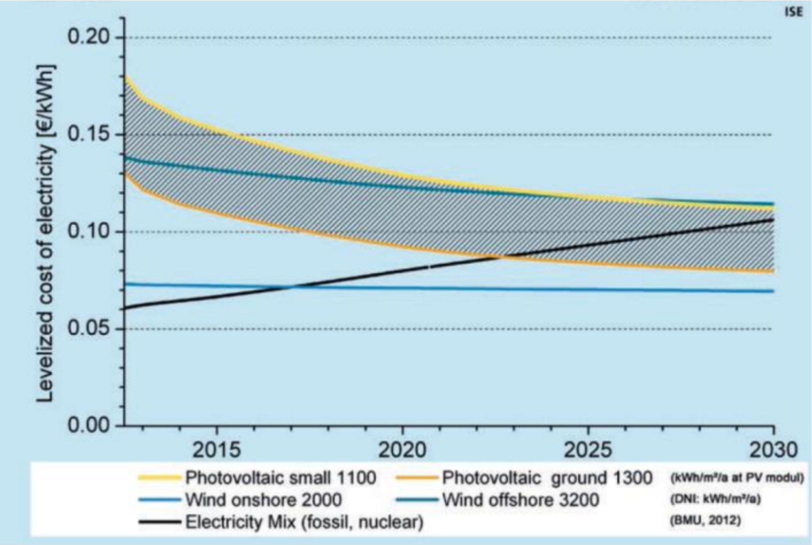

Figure A.4 - LCOE forecast of renewable energies in Germany to 2030, based on learning curves [5]. Numbers in the legend are full-load hours per year.

These numbers seem to correspond with other investigations. The Institute for Energy Research (IER), located in the USA, has made a prediction for 2018 [39]. The LCOE for onshore wind is expected to be 0.07 €/kWh in 2018 which corresponds quite well with Figure A.4. The LCOE for offshore wind in 2018 is predicted to be 225 USD/MWh, being equal to €0.16/kWh (1 USD = 0.73 EUR, 2011 prices) which is slightly higher than the numbers of Figure A.4.

The LCOE of renewable sources are being compared with the current energy price, the Electricity Mix in Figure A.4, consisting of fossils and nuclear power in Germany. These prices are expected to increase from €0.06 in 2012 till €0.11 in 2030, so a doubling of the prices in about 20 years. This is most probably an extrapolation of the energy price of the last 20 years. From Figure A.4 it can be concluded that there is still a long way to go for offshore wind to become competitive with other technologies. For onshore wind the case seems more beneficial, as this technology is expected to become competitive in an economic sense from 2017 if the price of the electricity mix keeps rising.

A.1.3. Cost distribution

In the long term offshore wind energy is expected to be about 1.5 x more expensive than onshore wind. The cost distribution of the construction costs, see section A.1.2, for an offshore wind turbine is given in Figure A.5. The distribution is based on a hypothetical 500 MW offshore wind farm with 5 MW turbines on monopiles in a water depth of 20 – 30 m. The costs of the support structure are according to the definitions of Figure 2.4. Some remarks:

- Material costs of the total steel shaft of the support structure are 3% of the total costs. The other part of the support structure cost exist mainly on assembly of the substructure. Compared to a similar wind turbine size onshore the costs of the support structure are about 2.5 times as much [2], mainly due to the high costs of assembly of the support structure.
- The cost distribution is to a large extent influenced by the location. The costs of the turbine are relative insensitive for the location at sea. For the support structure the situation is different: when water depths increase the contribution of the cost of the support structure is expected to become bigger and bigger. Especially the costs of the steel shaft are expected to increase. The contribution of the electrical infrastructure may increase when the wind farm is located further offshore.

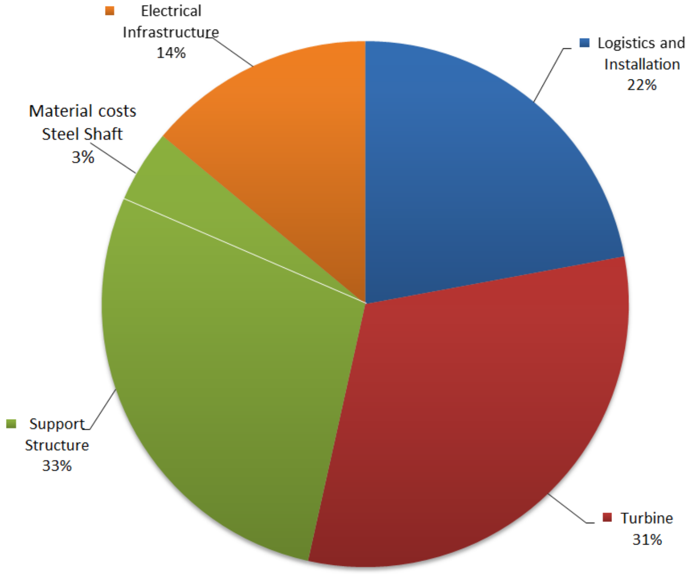

Figure A.5 - Cost distribution of construction costs for a hypothetical 5MW offshore wind turbine in a water depth of 20-30 m; partly based on [6]

For the offshore wind farm the main areas for development today are amongst other things [2]:

- More efficient methods to determine wind resources
- Developments of more efficient methods to determine the external design conditions
- More efficient methods to design and construct the offshore wind turbine
- Innovations in the wind turbine production, transportation and installation methods

A.2. CHAPTER 2: SUPPORT STRUCTURES

A.2.1. Support structure concepts

A.2.1.1. Monopile

In the past in about 80% of the cases the monopile (Figure A.6) was applied as substructure [16]. The vertical loads can easily be transferred to the soil through wall friction and tip resistance. The lateral loads, in comparison much larger, are conveyed to the foundation through bending. The loads are subsequently transferred laterally to the soil [7].

Due to stiffness requirements large diameters are required when the water depth increases. Fabrication and installation limits result in a maximum water depth of about 25 m [2].

The biggest advantage of monopiles is the easy fabrication. On the other hand expensive pile driving equipment is required to install the monopile, which also leads to environmental impact like noise and vibrations due to pile drilling.

Figure A.6 – The monopile and GBS [40]

A.2.1.2. GBS

The Gravity Base Structure (GBS) is based on the philosophy of applying a large dead load over a relatively large base to stabilize the structure (Figure A.6) [2]. At the transition with the bottom, skirts can be applied to reduce scour and to improve stability. In the past most GBS have been applied in water depths smaller than 10 m. The GBS is fabricated onshore and transported to site by barge. There it is lifted into its final position and filled with ballasting material. Before the seabed has to be prepared to provide a flat and stable base. The applicable water depth is about 30 m, mainly because of the limits in lifting capacity.

A.2.1.3. Suction bucket

Suction buckets (Figure A.7) are cylindrical in shape and have diameters up to 10 to 15 m. Installation takes place by sinking into the seabed and then pumping the water out of the bucket. The hydrostatic pressure thus developed pushes the anchor to the design depth. Installing suction buckets is relatively time consuming. However, the bucket is self-installing, what means that only tug boats are required to transport and install the unit [41]. Suction buckets resist tension loads by relying on the weight of the soil encased by the steel bucket along with side friction on the walls and hydrostatic pressure. Suction buckets are expected to be particularly suitable for foundations in soft cohesive sediments. These foundations cannot be used in rock, in gravel or in dense sand [42]. Under high loads suction buckets behave less stiff with respect to monopiles. Suction piles might be applicable rather for moderate (10-20 m) water depths [43].

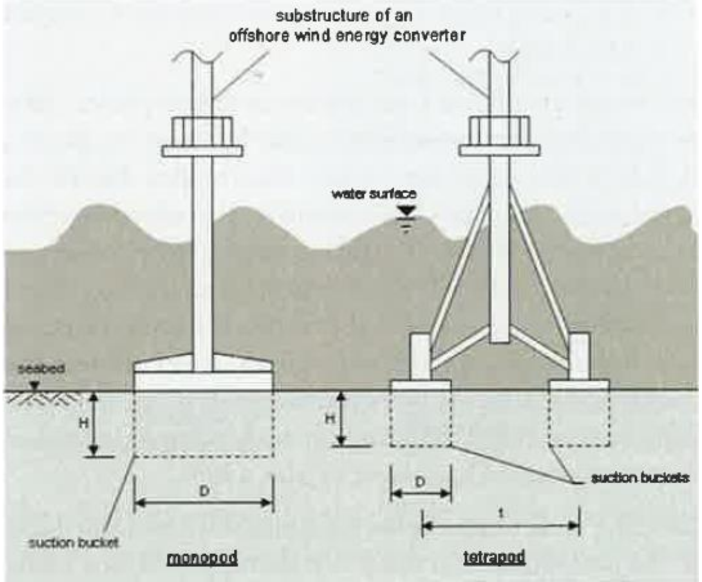

Figure A.7 - The suction bucket [41]

A.2.1.4. Tripod

The tripod is a monopile connected to a framework (Figure A.8). The tripod is built onshore and transported to its final location. There it is lifted in position. Next the piles at the bottom of the framework are hammered. The tripod has a large resistance against overturning due to its wide base. With respect to monopiles the tripod has the disadvantage of difficult transport. The applicable water depth is about 30 m, due to the relative large weight [2].

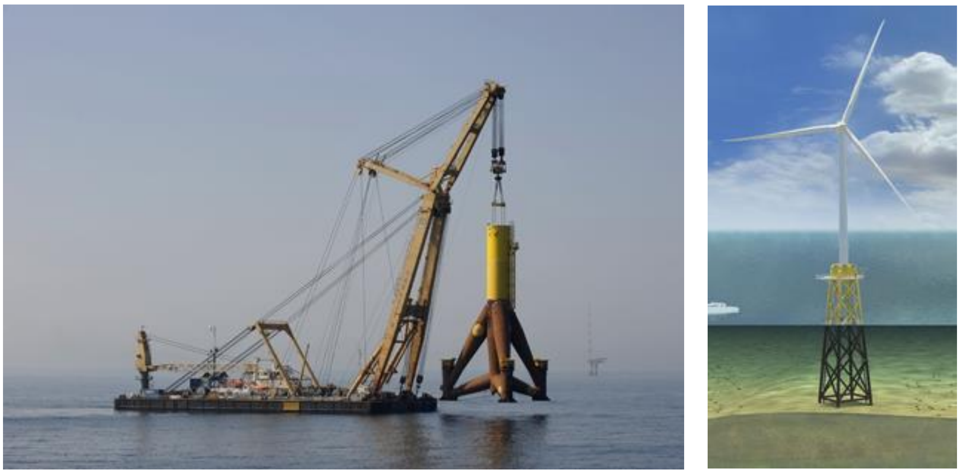

Figure A.8 - Installation of a tripod and a jacket [40]

A.2.1.5. Jacket

The load bearing concept of a jacket is the same as for a tripod. The jacket consists of three or four legs connected by slender braces (Figure A.8). Piles are hammered into the soil to transfer the loads. The jacket structure is relative light. Welding of the joints requires however a lot of man-hours. Transportation is also an issue, due to the relative large dimension. For the offshore wind industry the applicable water depth is about 40 m [2].

A.2.1.6. Floating

Floating concepts become interesting for water depths > 50 m because of the relative high cost of the mooring system. In the offshore industry a lot of floating structures have been installed. In the offshore wind industry this isn't the case yet. The most promising concepts are [2]:

- The deep-spar buoy: a slender cylinder is floating with a large part of its length below the water surface, creating a pendulum effect (Figure A.9). The cylinder is moored to the bottom with catenary mooring lines. The HyWind project is an example of this. As a test this concept was applied in 2009 for a 2.3 MW turbine at a location with a water depth of 100 m [44].
- The mini TLP: a three-legged body is floating below the water line and connected to the bottom with tensioned mooring lines (Figure A.9).

Except from pilot project no floating wind turbines are installed yet [45].

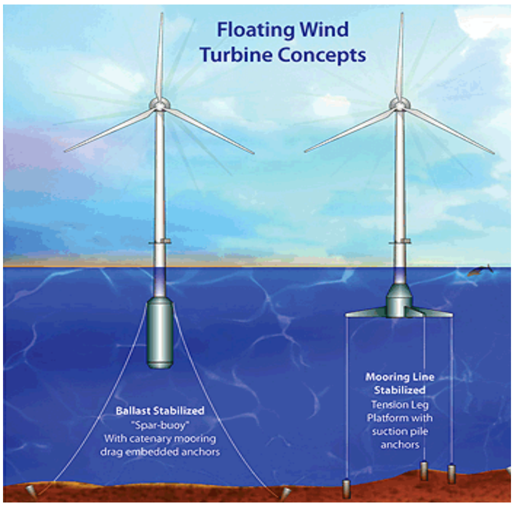

Figure A.9 - The deep-spar buoy and the mini TLP [46]

A.2.2. Transition piece

The connection between support structure and turbine tower is a so called transition piece. An important task of the transition piece is to correct for a misalignment of the support structure. In general one can distinguish two types of transition pieces:

1. Grouted
2. Bolted

The type of support structure has a strong influence on the choice. This has to do with prefabrication of additional elements

The next additional elements have to be added to an offshore wind turbine:

- Boat landing: fenders and a steel ladder
- Platform: platform to carry people and give access to the wind turbine
- J-tube: tube for the connection of the power cable to the wind turbine

For a monopile often a grouted connection is chosen, see Figure A.10a. Due to pile driving nothing can be fitted to the driven foundation pile. Therefore a prefabricated transition piece is installed between the foundation pile and the wind turbine. Boat landing, platform and J-tube (at the outside) are connected to it. The transition piece is grouted to the foundation pile and turbine tower.

For a GBS with a steel shaft also a bolted connection is an option. Due to the absence of pile driving, the additional elements can be prefabricated at the GBS, see Figure A.10b. The J-tube is at the inside of the GBS. On top of the steel shaft a ring is connected. This ring is bolted to an identical ring at the turbine tower.

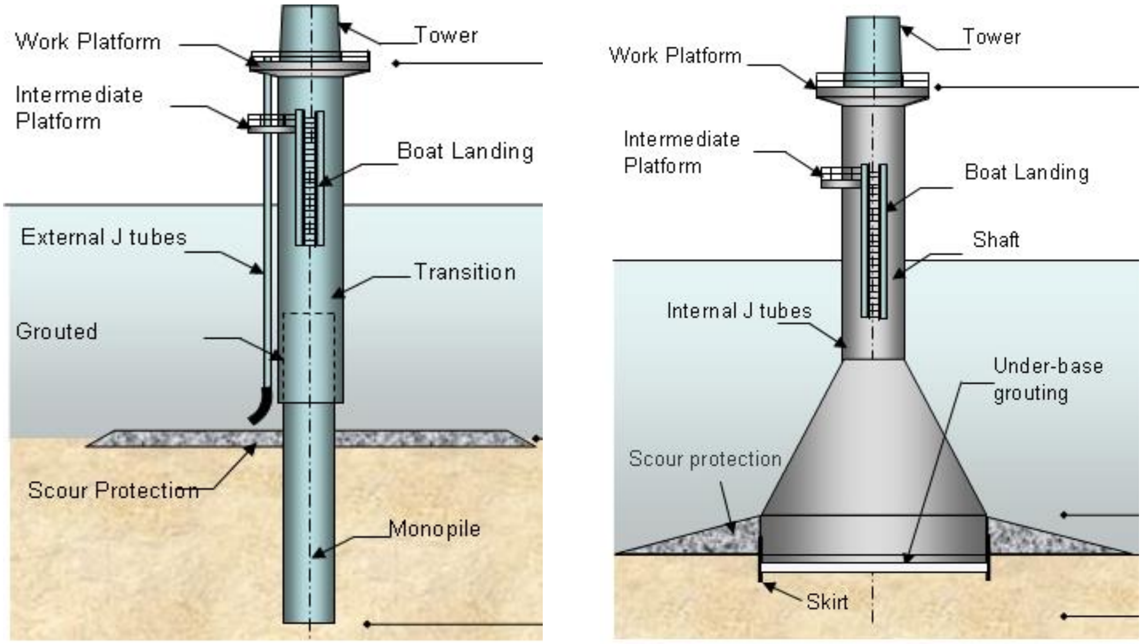

Figure A.10 - Transition pieces for a) monopile b) GBS

A.2.3. Development of the GBS

A.2.3.1. History

The first offshore wind farm with a GBS was the Vindeby project in Norway in 1991. Eleven wind turbines, with a total capacity of 5 MW, were installed in a water depth of about 5 m. Since that moment several other offshore wind farms with a GBS have been constructed, most of them in the relative shallow Baltic Sea around Denmark, see Figure A.11. The reason is that a GBS is suited for locations with ice loads and subsoils with rocks.

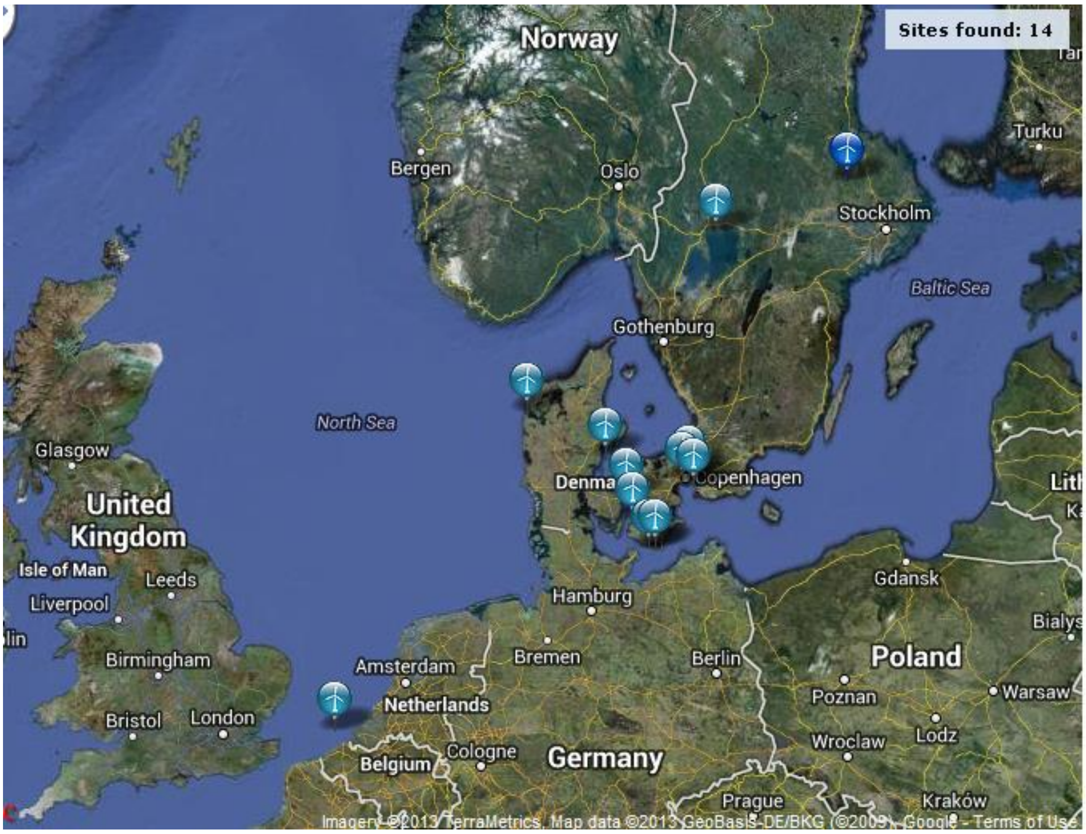

Figure A.11 - Offshore wind farms with a GBS in NW-Europe [45]

Project name	Year	Total capacity [MW]	Water depth [m]	Diameter [m]
Vindeby (DK)	1991	5	2-6	no data
Tunø Knob (DK)	1995	5	3-6	no data
Middelgrunden (DK)	2001	40	3-5	17
Rødsand/Nystedt (DK)	2003	166	6-10	11
Lillgrund (SWE)	2007	110	4-10	19
Thornton Bank (B)	2008	30	12-28	24

Table A.3 - Well known GBS projects [41] [45]

Some well-known projects are listed in Table A.3. As follows from the table most GBS are applied in areas up to 10 m water depth. The project of the Thornton bank is an exception, as the maximum water depth is 28 m.
As this thesis focuses on a concept of a GBS in relative deep water (35 – 60 m), the Thornton Bank project is investigated in more detail below as a reference project.

A.2.3.2. Thornton Bank

This project consists of the installation of about 60 offshore wind turbines on the Thornton Bank near the coast of Belgium with a capacity of 5MW. The project is executed in 3 phases. The first phase of 6 wind turbines on a GBS was executed in 2008. Reasons to choose for a GBS were [47]:

- The harsh North-Sea environment and complex soil situation led to a basic monopile design with excessive diameters and wall thicknesses

- An increase of the steel price
- Concerns around the feasibility of pile driving as there was a very dense fine sand layer at +/-28 m below the seabed

Figure A.12 shows a design lay-out. Parameters with respect to the GBS and the groundwork can be found in Table A.4 and Table A.5.

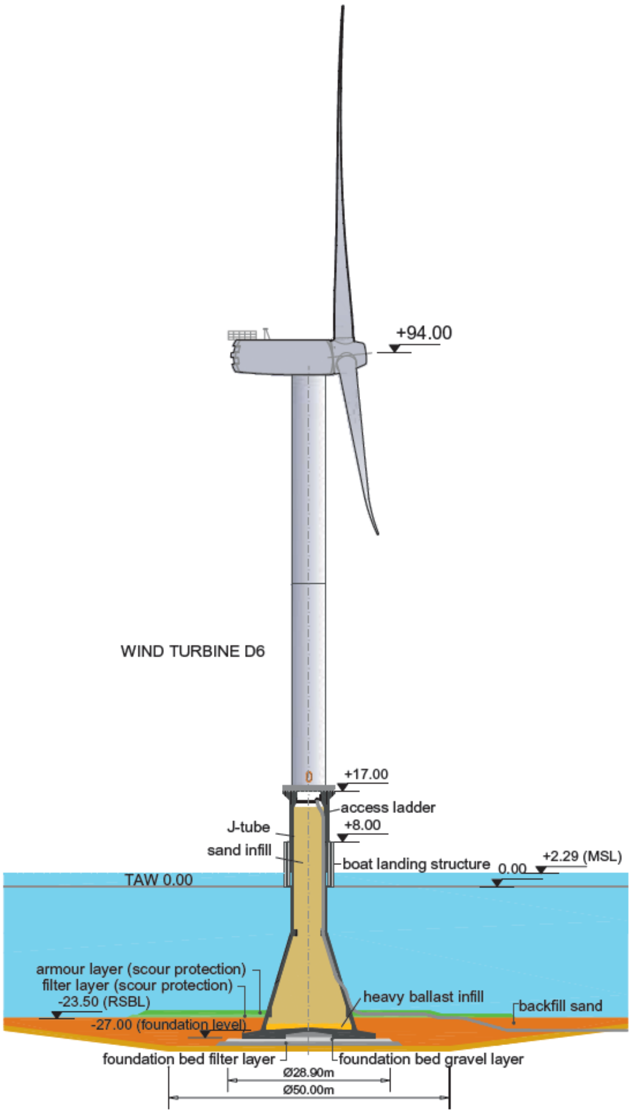

Figure A.12 - Design lay-out of the GBS applied at Thornton Bank [47]

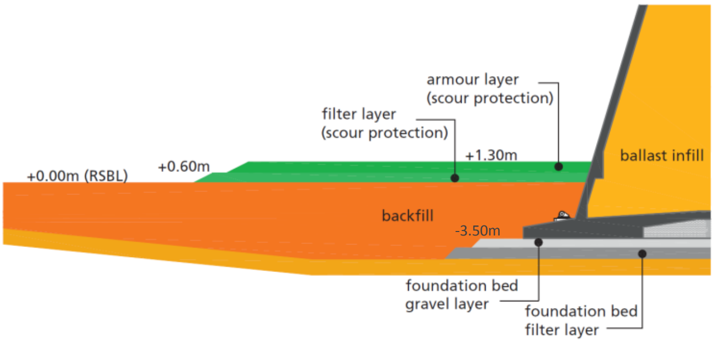

Figure A.13 - Detail of the foundation [47]

The 'Erlenmeyer' shaped GBS were constructed on a quay onshore. Before placing the GBS the seabed was dredged until the bottom of the foundation bed layer (Figure A.13). Afterwards the foundation bed layer was installed. The top of the foundation bed layer was located 3.5 m below reference seabed level (RSBL). The main function of the bed is to lower the excess pore pressure and uplift forces due to extreme waves, to achieve a more accurate bed flatness and to minimize scour problems during the installation phase. The RSBL at a given foundation location is defined as the minimum level or design seabed level (SBL) that can be guaranteed during the lifetime (30 years) of the foundation, considering the mobility of sand waves and natural erosion and accretion

Parameter	Value	Unit
Outer diameter base slab	23.50	m
Outer diameter conical part	6.50	m
Height conical part	17	m
Height cylindrical part	23	m
Wall thickness	0.50	m
Total weight	2800-3000	t
Ballast material (1500 kg/m^3)	3000	t

Table A.4 - GBS parameters (levels from -23.5 till + 17.0 m TAW) [47]

Parameter	Value	Unit
Dredged material	90.000	m^3
Foundation bed layer	>0.80	m
Amount of rock foundation bed	3700	t
Backfill material	60.000	m^3
Scour protection	1.30	m
Amount of rock scour protection	unknown	t

Table A.5 - Groundwork related parameters [47]

Figure A.14 - Transport of a GBS with a heavy lift vessel [48]

After construction the GBS were transported to the Thornton Bank with a heavy lift vessel, where the lowest part of about 10 m was below the water surface during transport (Figure A.14). After the installation on the foundation bed, the dredged area was backfilled with sand till RSBL. To prevent scour a scour protection was placed on top of it. Mainly for horizontal stability the GBS was filled with ballast material (about 2000 m^3 of sand).

Some lessons learned of this project, as described in [49], are the man power-intensive works in the harbour because of weather conditions. It took about 6 months to construct one GBS.
Also it was a logistically complex project and the many marine preparation and finishing works made the construction subject to weather risks.

For the second (a batch of 30 turbines) and third phase (a batch of 18 turbines) the GBS concept was exchanged for a jacket with pre-piling. Arguments were a decrease in steel price compared to the first phase, less time required, simpler logistics, less weather sensitiveness, less harbour space needed, less marine preparation works and less design issues.

A.3. CHAPTER 3: BASICS OF WIND TURBINES

A.3.1. Concept of wind energy generation

This section describes the process of transforming wind energy to electric power. The description is based on [14]. A wind turbine produces electricity by slowing down the flow of air through its rotor plane. The air flow is transformed to kinetic energy in the rotating blades driving the generator, which in turn converts the kinetic energy to electric power. All the components for this conversion are housed in the nacelle, see Figure A.15. In the future possibly the gearbox is replaced by a hydraulic pump [50]. With this system the electric power is not generated at the nacelle any more, but at a central hydro power station in a wind farm. This will lead to a reduction of the weight of the nacelle.

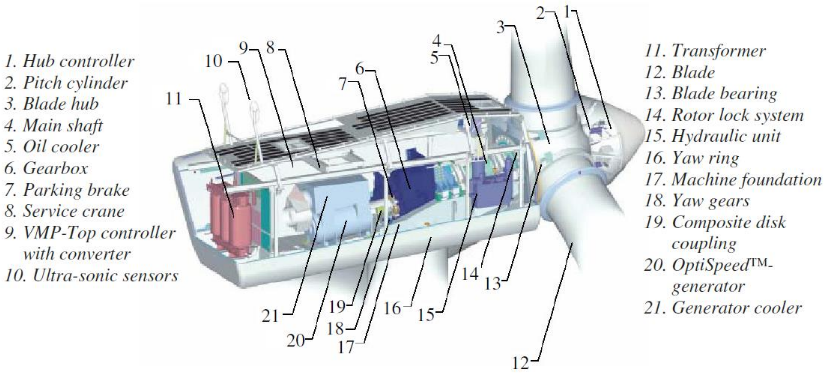

Figure A.15 - Nacelle of a Vestas V80 turbine [14]

In order to maximize the power output the rotor has to face the wind. This is achieved by rotating the nacelle with respect to the tower. This is the so called ‘yaw’ direction (see Figure A.16). Also, by rotating the blades around their axis in longitudinal direction the amount of power output is influenced. This process is the so called ‘pitch’.

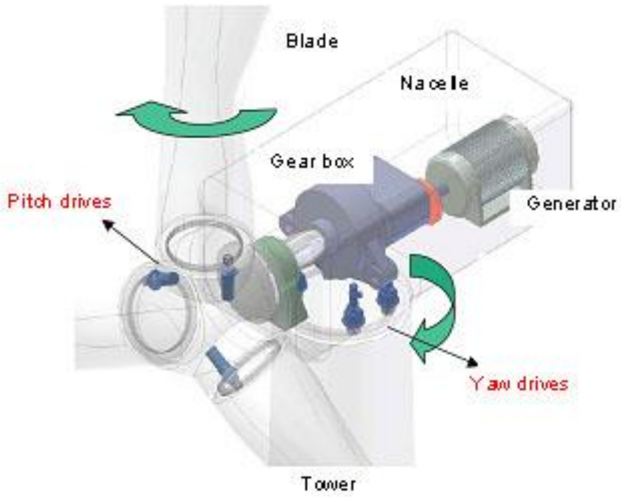

Figure A.16 - Pitch and yaw [51]

The blade element theory is used to calculate the loads on the turbine. This theory assumes a stream tube as shown in Figure A.17. The turbine can be seen as an actuator disk, slowing the flow of air and creating a wake with reduced air flow velocity. The load that the actuator disk exerts on the flow to achieve this is the axial load F_{ax}.

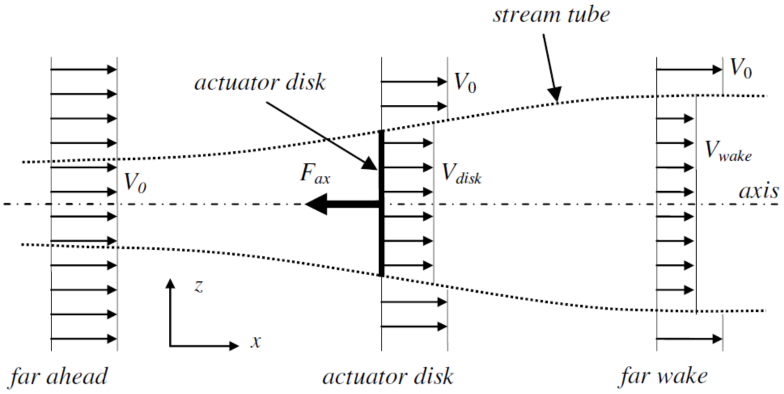

Figure A.17 - Actuator disk with stream tube [14]

The undisturbed wind velocity V_0 is reduced by the rotor to V_{disk} at the turbine and V_{wake} at a certain distance behind the turbine.
Using the Bernoulli theory, the resulting load on actuator disk can be found by:

$$F_{ax} = \frac{1}{2} A_{disk} \rho_{air} V_0^2 \cdot 4a(1-a) \tag{A.1}$$

where:

$$a = \frac{V_0 - V_{disk}}{V_0} \tag{A.2}$$

with:

F_{ax}	axial force	[N]
A_{disk}	area of the rotor disk	[m^2]
ρ_{air}	density of air	[kg/m^3]
V_0	undisturbed wind velocity	[ms/s]
a	induction factor	[-]

In the equation above neither the axial load nor the induction factor is known. Therefore a second theory is used: the blade element theory.

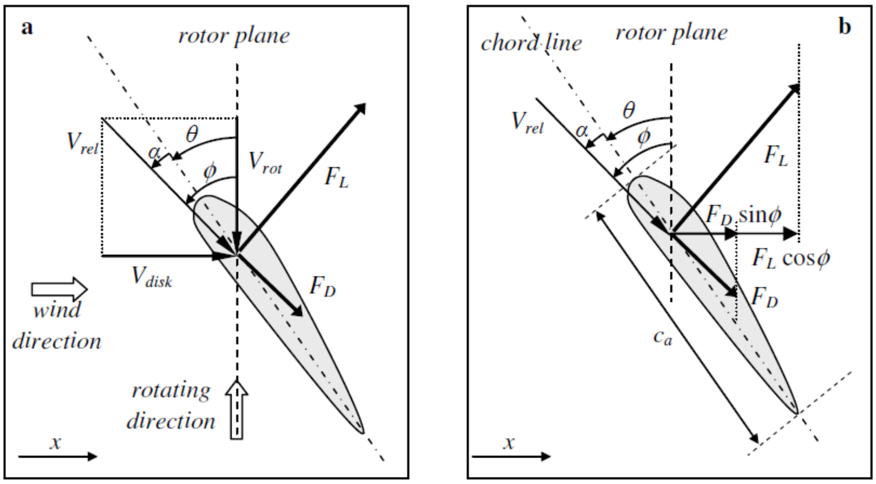

Figure A.18 - a) Lift and drag loads on the blade b) Resulting loads in the x direction [14]

The lift and drag forces on the blade element can be expressed by (Figure A.18a):

$$F_L = \tfrac{1}{2} C_L(\alpha) \rho_{air} V_{rel}^2 c_a \Delta r \qquad F_D = \tfrac{1}{2} C_D(\alpha) \rho_{air} V_{rel}^2 c_a \Delta r \qquad \text{(A.3)}$$

with:

F_L	aerodynamic lift	[N]
F_D	aerodynamic drag	[N]
$C_L(\alpha)$	aerodynamic lift coefficient	[-]
$C_D(\alpha)$	aerodynamic drag coefficient	[-]
ρ_{air}	mass density of air	[kg/m^3]
c_a	airfoil chord length	[m]
Δr	radial length of blade element	[m]
α	angle of attack	[deg]
θ	pitch angle	[deg]
ϕ	angle of inflow	[deg]

These forces are induced by the wind speed and the rotation speed. Combined these two speeds form the relative wind speed over the blade:

$$V_{rel} = \sqrt{V_{disk}^2 + V_{rot}^2} \qquad \text{(A.4)}$$

$$V_{disk} = V_0(1-a) \text{ and } V_{rot} = \Omega r \qquad \text{(A.5)}$$

with:

V_{rot}	linear rotation speed at blade section	[m/s]
Ω	angular rotation speed	[rad/s]
r	distance of blade element to axis of rotation	[m]

The total axial load for N_b blades is (Figure A.18b):

$$F_{ax} = N_b \sum_{r=root}^{r=tip} F_{x,r} \qquad \text{(A.6)}$$

where:

$$F_{x,r} = F_L \cos\phi + F_D sin\phi \qquad \text{(A.7)}$$

When this equation is combined with the equation for F_{ax} resulting from the Bernoulli theory the induction factor a can be found. Now, the power production P (in W) can be calculated according to:

$$P = F_{ax} V_{disk} = 2\rho_{air} A_{disk} V_0^3 a(1-a)^2 \qquad \text{(A.8)}$$

From this above equation it follows that the power production is dependent on the wind velocity to the power three. When the power *P* is divided by the total power in the air flow through the rotor plane, this leads to the following equation for the power coefficient C_p:

$$C_p = \frac{P}{\frac{1}{2}\rho_{air} V_0^3 A_{disk}} = 4a(1-a)^2 \qquad \text{(A.9)}$$

The maximum value for C_p is 0.593 for $a = 1/3$. This means that maximum 59.3% of the total power in the air flow through the rotor plane can be extracted by the actuator disk. This value is known as the Lanchester-Betz limit. This limit has nothing to do with any design, but with the way the air flows around a wind turbine [12].

A.3.2. Wind energy production

The power coefficient C_P is dependent on the ratio between the rotor speed and the wind speed. This ratio can be expressed by the tip-speed ratio λ:

$$\lambda = \frac{V_{tip}}{V_0} = \frac{\Omega R}{V_0} \tag{A.10}$$

with:

V_{tip}	tip speed	[m/s]
R	rotor radius	[m]

The dependence of C_P on the tip-speed ratio is plotted in Figure A.19. To date, no wind turbine has been designed that is capable of exceeding the Lanchester-Betz limit [12], but modern wind turbines reach about 70-80%.

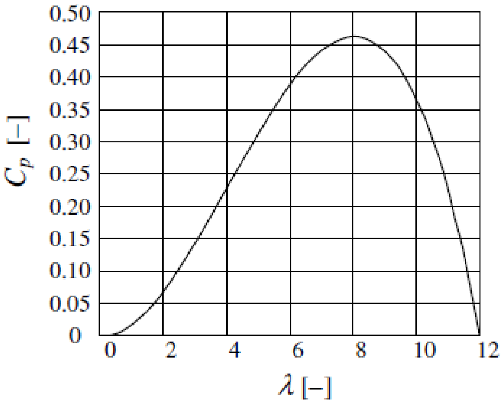

Figure A.19 - Typical C_P-λ curve [14]

The greatest efficiency is achieved when the tip speed is constant as follows from Figure A.19. Two types of turbines exist:

1. Variable speed turbines: the tip speed is kept constant by allowing the rotor to change its rate of rotation as the wind speed changes. As a result the output frequency of the energy also varies. A transformation system is required to export the energy at a constant frequency.
2. Fixed speed turbines: the rotor has to remain at a constant rotational rate. As a result the efficiency decreases.

Some typical terms for a wind turbine are [2]:

- V_{cut-in}: the minimum wind speed to start operation, typically 3 m/s
- V_{rated}: the wind speed at which the generator reaches maximum power
- $V_{cut-out}$: the cut-out wind speed, to prevent damage the turbine is stopped at a certain wind speed, typically 25 m/s

Depending on the wind speed a certain amount of power can be extracted, listed in a power-curve (Figure A.20).

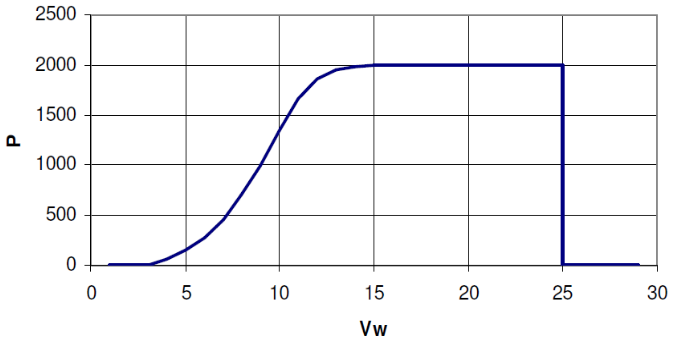

Figure A.20 - Power curve for a Vestas V80 turbine; P = power in kW, Vw = wind speed in m/s [14]

A.4. CHAPTER 3: THEORETICAL BACKGROUND OF LOADS AND DESIGN ASPECTS

A.4.1. Wind load

A.4.1.1. Wind characteristics

The wind velocity measured in the field shows variations in space, time and direction. The wind speed increases with height Figure A.21).

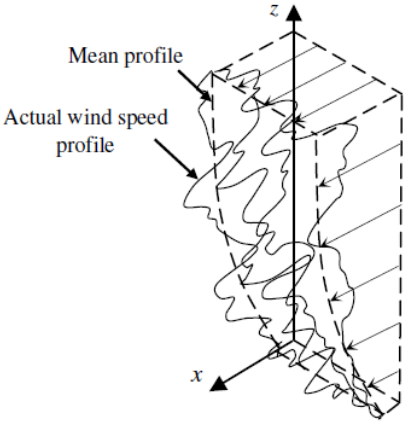

Figure A.21 - Wind speed profile [14]

Wind is often schematized as a mean wind speed with a standard deviation caused by turbulence. Just like for waves standard spectra have been developed for the description of wind signals. A well know spectrum is the Von Karman spectrum (see Figure A.22).

$$S_{Karman}(f) = \frac{\sigma_v^2 4L_v/V_w}{\left(1+70.8\left(\frac{fL_v}{V_w}\right)^2\right)^{\frac{5}{6}}} \tag{A.11}$$

with:

S_{Karman}	Von Karman spectrum	[m^2/s]
σ_v	standard deviation of the average wind speed	[m/s]
L_v	integral length scale (length of turbulence field)	[m]
V_W	mean wind speed	[m/s]
f	frequency	[Hz]

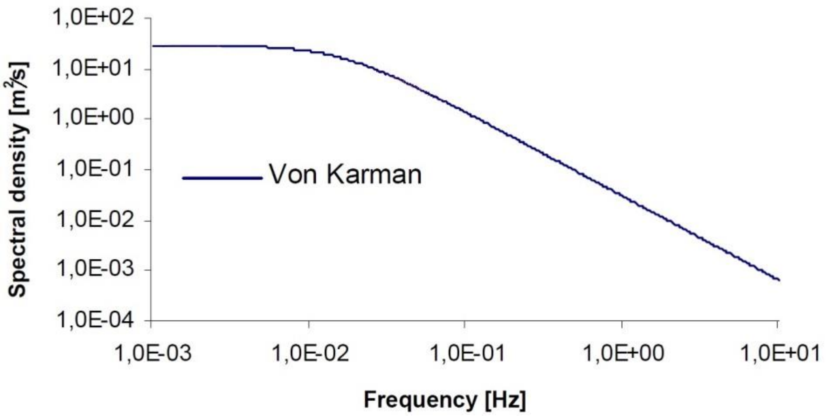

Figure A.22 - Von Karman spectrum for V_w=10 m/s, σ_v=1 m/s and L_v=50 m [14]

For offshore wind turbines two characteristics of the wind are important:

1. the annual average wind speed averaged over many years at hub height (V_{ave})
2. the extreme incident wind-speed within a given short interval (V_{ref})

The International Electrotechnical Commission (IEC) prescribes different classes to be used for a preliminary design, see Table A.6.

Class	I	II	III	IV
V_{ave} (50 y) [m/s]	10	8.5	7.5	6
V_{ref} (10 minutes) [m/s]	50	42.5	37.5	30

Table A.6 - Classifications for offshore turbines according to IEC, wind speeds are at 100 m hub height [2] [41]

For most offshore locations in the northerly half of the North Sea, the average annual wind speed at a height of 100 m is >10 m/s (Figure A.23).

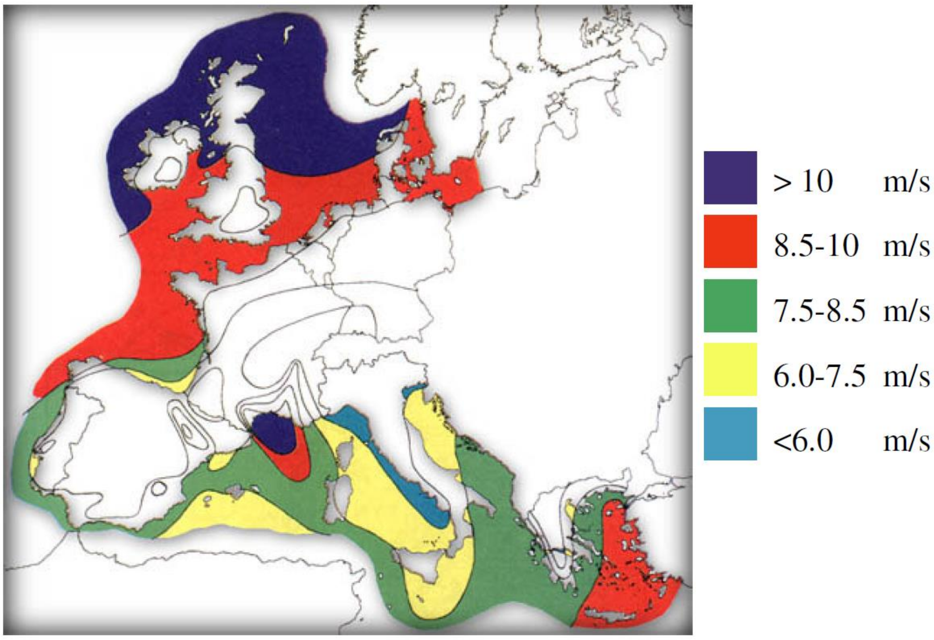

Figure A.23 - Yearly average wind speed V_{ave} at 100 m height for the European Seas [14]

A.4.1.2. General description of wind loads

In general an operational wind turbine leads to the loads given in Table A.7. They can be subdivided by their variation in time:

- Steady: the mean wind speed leads to a horizontal force (section A.4.1.3), in addition the self-weight of the nacelle results in gravity loads. Rotation of the rotor causes a constant bending moment.
- Periodic: tower shadow (a blade passing along the tower where the wind velocity is lower) leads to a periodic load. Gravity forces of rotating blades lead to a bending moment. Due to mass imbalance of the rotor a periodic bending moment will occur. Due to a misalignment between the wind and nacelle direction a torsional moment may occur. Aerodynamic imbalance, of one of the blades for example, leads to a bending moment. All the these effects are included in the response spectrum of the axial wind force, see Figure A.27.

- Random: turbulence is felt by the wind turbine (section A.4.1.4). Due to the randomness of turbulence this a random load. Also this effects is included in the response spectrum of the axial wind force, see Figure A.27.
- Transient: these loads occur due to controlling the wind turbine (breaking, yawing, pitching). In addition a sudden grid loss leads to a transient load peak.
- Wind gusts lead to a sudden increase of the wind speed, which will result in a load peak.

Transient loads can be reduced by a good control system (no sudden breaking/ yawing/ pitching). As follows from the example above processes generating torsional forces can be neglected.

The most important loads in magnitude or with the larges influence on the dynamic behaviour are:

- Mean wind speed, leading to a horizontal static wind load. Gusts are incorporated in the approach described in the next sections
- Turbine gravity loads
- Turbulence, and other rotational effects, leading to 1P and 3P frequencies

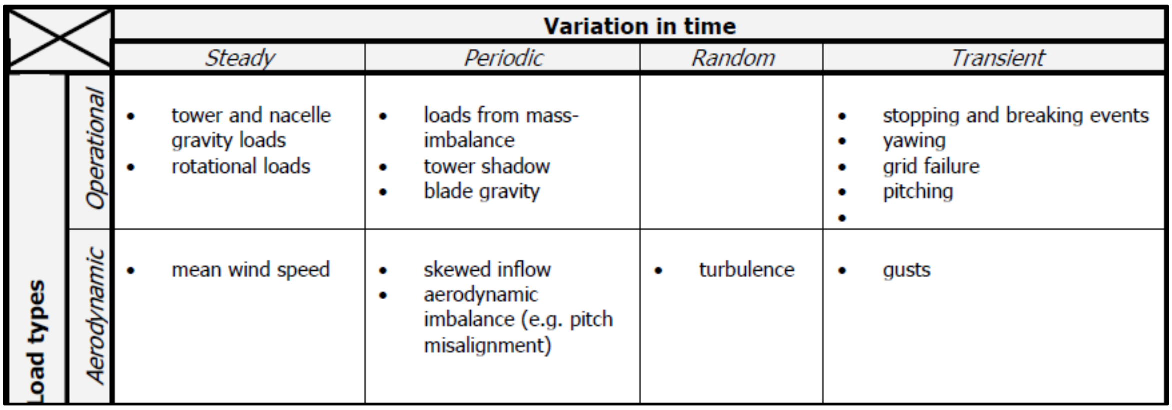

		Variation in time			
		Steady	Periodic	Random	Transient
Load types	Operational	• tower and nacelle gravity loads • rotational loads	• loads from mass-imbalance • tower shadow • blade gravity		• stopping and breaking events • yawing • grid failure • pitching •
	Aerodynamic	• mean wind speed	• skewed inflow • aerodynamic imbalance (e.g. pitch misalignment)	• turbulence	• gusts

Table A.7 - Wind loads [37]

A.4.1.3. Static load

Turbine

In section A.3.1 the relation between het wind speed V_w and the load on the turbine F_{ax} was described.

Shaft

The wind load on an object (caused by drag) can be described with:

$$F_{aero} = \frac{1}{2} C_W \rho_{air} A V_w^2 \tag{A.12}$$

with:

F_{aero}	wind load	[N]
C_W	shape resistance coefficient (= 0.7 for a circular tower [12])	[-]
ρ_{air}	air density	[kg/m^3]
A	area of the object	[m^2]

V_w	wind velocity	[m/s]

>>BAM Van Oord case study – Wind load – [Appendix B]

The wind load consist of two parts:

- Axial rotor load, equation (A.1)
- Shaft load, equation (A.12)

The wind turbine manufacturer prescribes a maximum horizontal force of:

$$F_{hor;max} = F_{ax;max} + F_{shaft;max} \approx 1700\ kN$$

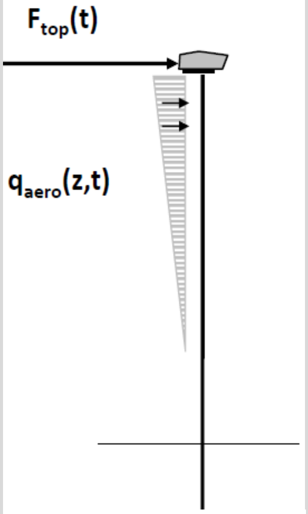

Figure A.24 - Horizontal loads

A.4.1.4. Turbulence

Turbulence effect

Because of turbulence effects (in the shape of eddies) the wind speed at a certain height is never constant. These turbulence fields are 'felt' by the rotating wind turbine (Figure A.25). Often the rotational period is smaller than the time for a turbulence bubble to pass the swept area. So, most of the gusts are seen several times by the blades [21]. This phenomenon is denoted rotational sampling. It transforms the 'stationary' wind spectrum to one seen by a rotating observer.

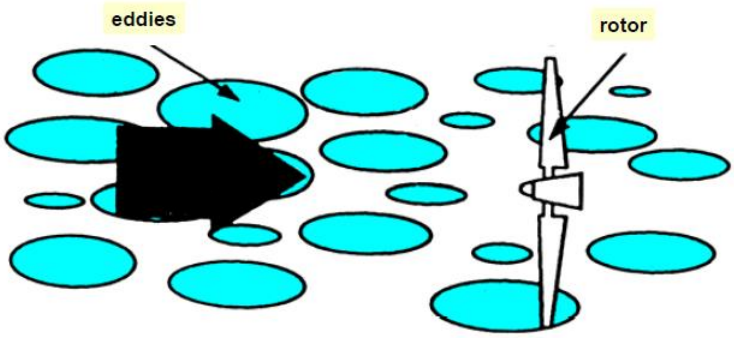

Figure A.25 - Rotational sampling of turbulence [15]

Rotational spectrum

The turbine structure will experience a load peak at the rotation frequency of the rotor, called 1P. This eddy slicing will also create a load peak at the frequency of all the blades passing at 3P (and it's multiples) for a three-bladed turbine [2]. In Figure A.26 the rotation spectrum for a blade for different distances to the nacelle is represented. Also the stationary wind spectrum is made visible. The stationary spectrum is equal to a Von Karman wind spectrum (see section A.4.1.1). The rotational spectrum is defined as:

$$R_n(f) = f \cdot \frac{S_n}{\sigma_v^2} \tag{A.13}$$

with:

R_n	rotational spectrum	[-]
S_n	stationary spectrum	[m^2/s]
f	frequency	[Hz]
σ_v	standard deviation of the wind speed	[m/s]

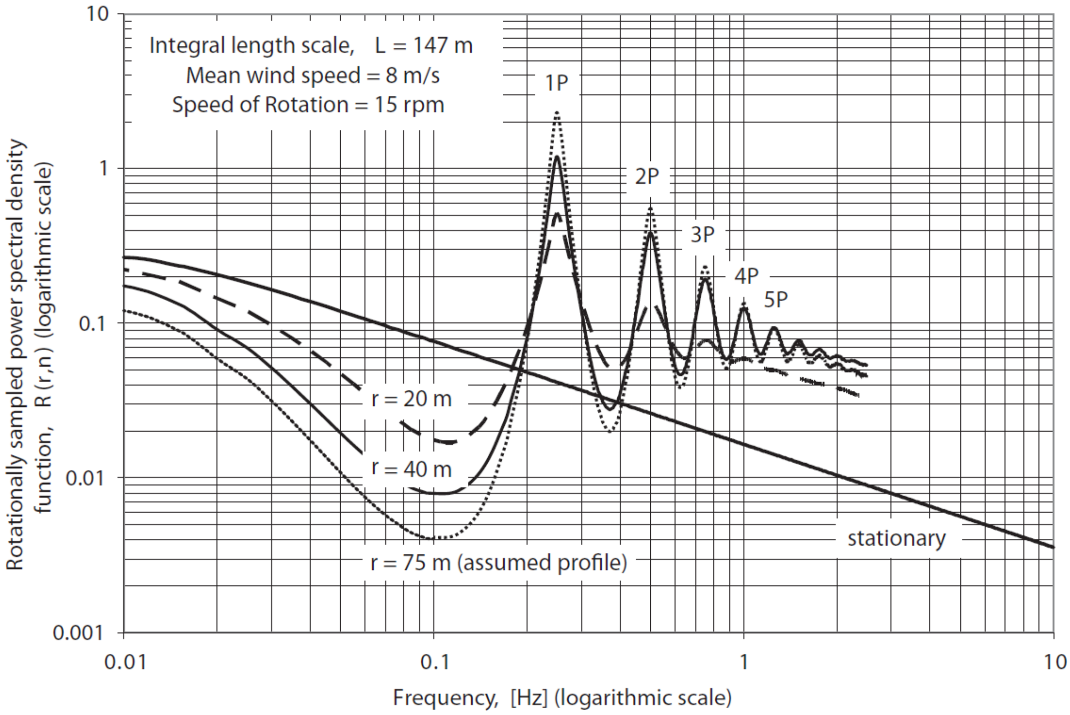

Figure A.26 - Stationary (Von Karman spectrum with V_W=8 m/s and L=147 m) and rotationally sampled power spectrum, r=75m is assumed from r=20 and r=40m, r=distance to nacelle [12]

When the wind spectrum is shoved through the wind turbine the tower top load is found. An example of such a response spectrum can be found in Figure A.27.

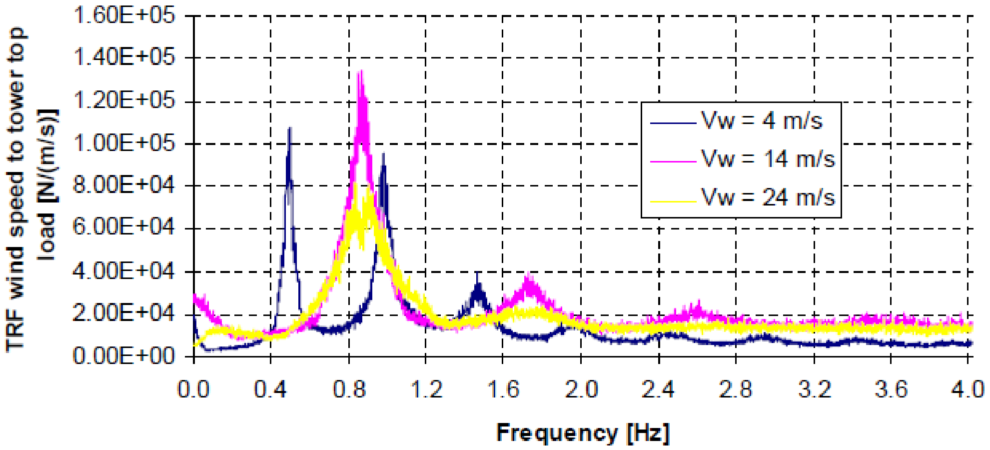

Figure A.27 - Example of a relation between wind speed and tower top load [17]

1P and 3P values

Variable speed turbines (section A.3.2) are gaining market share from fixed speed turbines. Compared to the fixed speed turbine, the frequency interval of a variable speed turbine is wider as it has multiple rotation speeds Figure A.28.

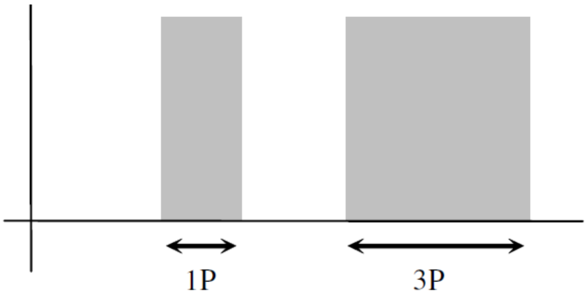

Figure A.28 - Frequency intervals for a variable speed turbine system [14]

Wind turbines have been growing strongly in size since in the past. This trend has consequences on the 1P and 3P frequencies. When the rotor diameter increases this will lead to a smaller value of 1P [2]. Also the natural frequency decreases when the hub height increases.

The 1P and 3P ranges can be calculated with [16]:

$$f_{NP} = N\frac{\lambda V}{2\pi R} \tag{A.14}$$

with:

N	number of blades	[-]
λ	tip speed ratio	[-]
V	wind speed	[m/s]
R	rotor radius	[m]

>>BAM Van Oord case study – 1P and 3P values [Appendix B]

The wind speed is assumed to vary between V_{cut-in} and V_{rated}. Here V_{rated} is the nominal wind speed, leading to maximum power output and the maximum rotational frequency. The tip speed ratio is assumed to be equal to 8 (maximum power output, see Figure A.19). This leads to:
$f_{1P,min} = 0.05\ \ Hz$ and $f_{1P,max} = 0.20\ \ Hz$
$f_{3P,min} = 0.15\ Hz$ and $f_{3P,max} = 0.60\ Hz$

A.4.2. Hydrodynamic loads

A.4.2.1. Waves

Wave spectrum

Waves can be categorised by their frequency (Figure A.29). According to [16] waves containing a lot of energy are located between 2 and 20s (0.5-0.05 Hz), where the extremes have a period between 7 and 13s (0.14-0.076 Hz). For an offshore wind turbine wind- and swell waves will be most important, as their frequency is close to the natural frequency of the structure ($f_{nat} = \sim 0.25\ Hz$, see Appendix B, $f_{swell;wind\ wave} = 0.1 - 1.0\ Hz$).

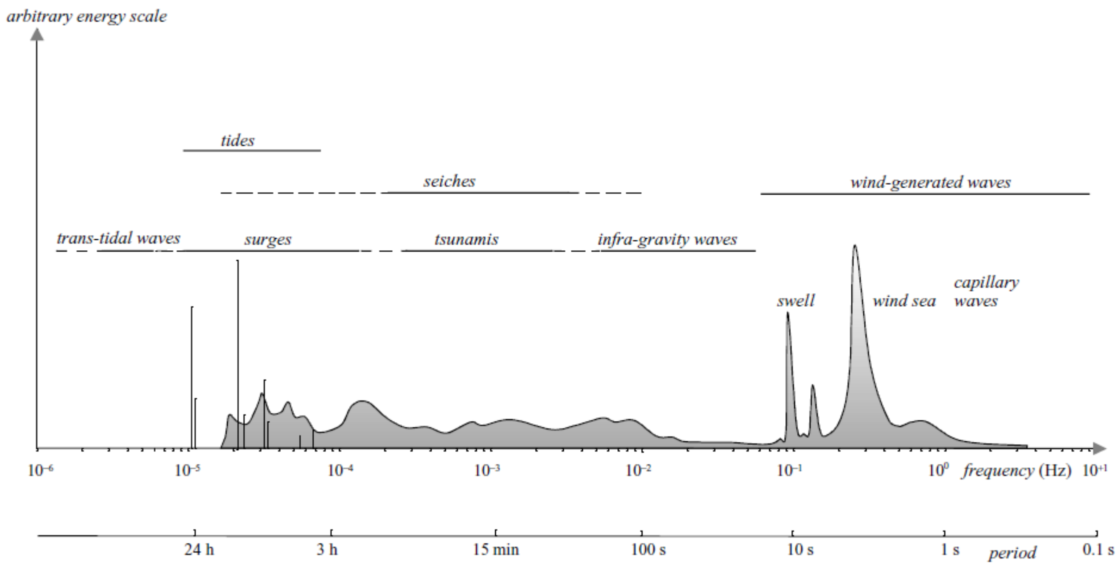

Figure A.29 - Wave energy as a function of the wave period [52]

A fully developed sea with infinite fetch can be described by the Pierson-Moskowitz spectrum:

$$S_{PM}(f) = \frac{5}{16}\frac{H_S^2}{f}\left(\frac{f_p}{f}\right)^4 \exp\left(-\frac{5}{4}\left(\frac{f_p}{f}\right)^4\right) \qquad \text{(A.15)}$$

with:

H_S	significant wave height	[m]
f	wave frequency	[Hz]
f_p	wave frequency corresponding to peak spectral density	[Hz]

In the equation above the significant wave height H_S and the peak period T_P are the only two parameters to describe the spectrum. A long term wave field is described by different environmental classes with each their own H_S and T_P. For each class the probability of occurrence is predicted, based on measurements. Each class can be described by a spectrum with the corresponding values of H_S and T_P.

These parameters follow from long time measurements.

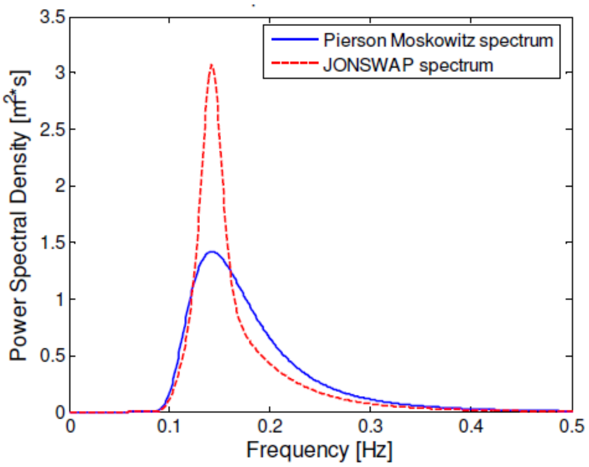

Figure A.30 - JONSWAP and PM spectrum for H_s=1.5m, T_p=7s [14]

Often sea states are not fully developed due to too small storm durations or limited fetch. Then the wave spectrum can best be described by the JONSWAP spectrum. This spectrum is more peaked and is based on the Pierson-Moskowitz spectrum. The PM spectrum is multiplied with a peak-enhancement function $G(f)$. Furthermore a multiplication with a normalising factor F_n has to take place to achieve the same area under the spectrum. The formulation for the JONSWAP spectrum reads [2] [52]:

$$S_{JS}(f) = F_N \cdot S_{PM}(f) \cdot G(f) \tag{A.16}$$

where:

$$F_N = 1 - 0.287\ln\left(\gamma_{JS}\right)$$

$$\gamma_{JS} = \begin{cases} 5 & \text{for} \dfrac{T_p}{H_s^{0.5}} < 3.6 \\ \exp\left(5.75 - \dfrac{1.15T_P}{H_s^{0.5}}\right) & \text{for } 3.6 < \dfrac{T_p}{H_s^{0.5}} < 5 \\ 1 & \text{for} \dfrac{T_p}{H_s^{0.5}} > 5 \end{cases} \tag{A.17}$$

$$G(f) = \gamma_{JS}\,\hat{}\,\exp\left[-\frac{1}{2}\frac{\left(\frac{f}{f_p} - 1\right)^2}{\sigma^2}\right]$$

$$\sigma = \begin{cases} 0.07 \text{ for } f \leq f_p \\ 0.09 \text{ for } f > f_p \end{cases}$$

When $\gamma_{JS} = 1$ the PM spectrum and the JONSWAP spectrum are identical.

It is hard to predict which spectrum gives the highest fatigue load. When all wave frequencies are far below the natural frequency of the structure the PM spectrum will give the highest fatigue load due to the higher tail.

Wave theory

Two types of waves can be distinguished: regular and irregular waves. Regular, or harmonic, waves are waves with a constant period and amplitude (the top three waves of Figure A.26). In order to be (nearly) regular, the wave spectrum should be narrow banded, this is the case for swell waves.
Irregular waves don’t have these characteristics and the wave spectrum is broad banded, meaning that it contains a lot of frequencies. Often storm waves have to be treated as irregular waves. Irregular waves can be composed in harmonic (or regular) waves. This can be seen from Figure A.26 where the irregular wave at the bottom consists of the three regular waves at the top.

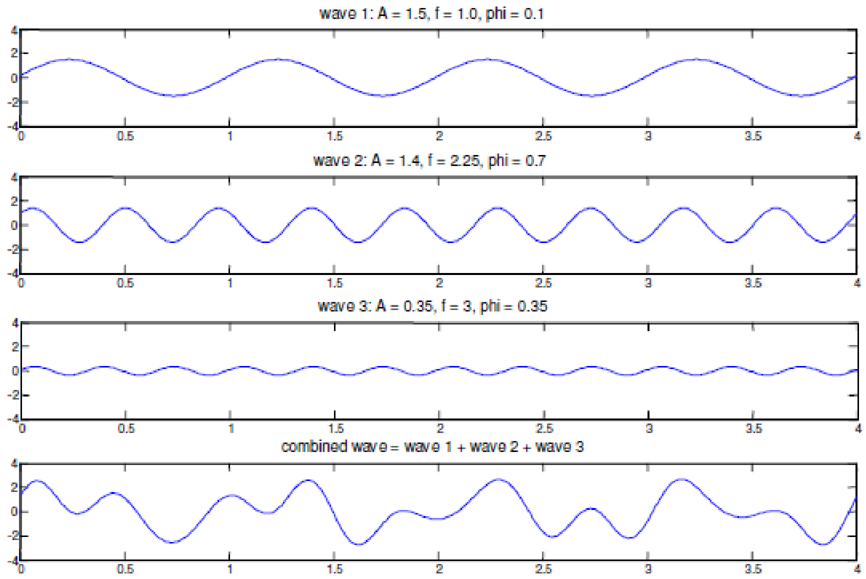

Figure A.31 - 3 regular waves combined to form an irregular wave [14]

For a harmonic wave, the water particle motion can be described by Airy's linear wave theory (Figure A.32). The Airy linear wave theory is only valid up to the 'still water' level [2].

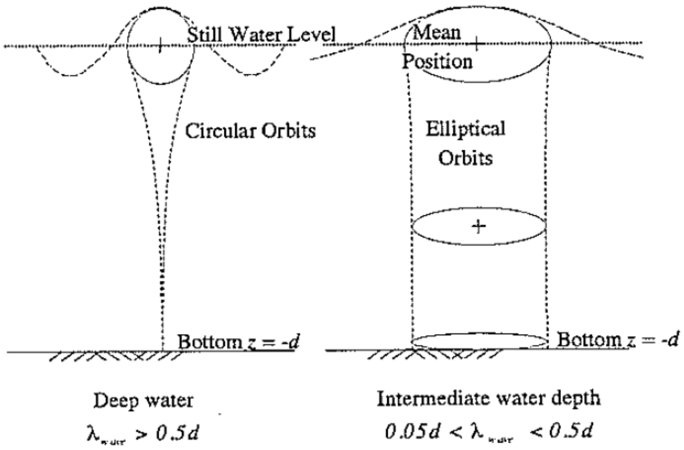

Figure A.32 - Particle orbits according to Airy theory [14]

Furthermore the Airy theory is only valid in deep and intermediate water. The validity also depends on the wave steepness. Extreme waves, with return periods in the order of 50 or 100 years, cannot be described by linear wave theory any more. Other, non-linear wave theories have been developed for these situations. Figure A.33 gives an overview which theory should be used for regular waves [21]. The area of applicable theories is enveloped by the breaking wave limit. Regular waves are assumed to break when H/d>0.78 for shallow water and H/L>0.14 for deep water.

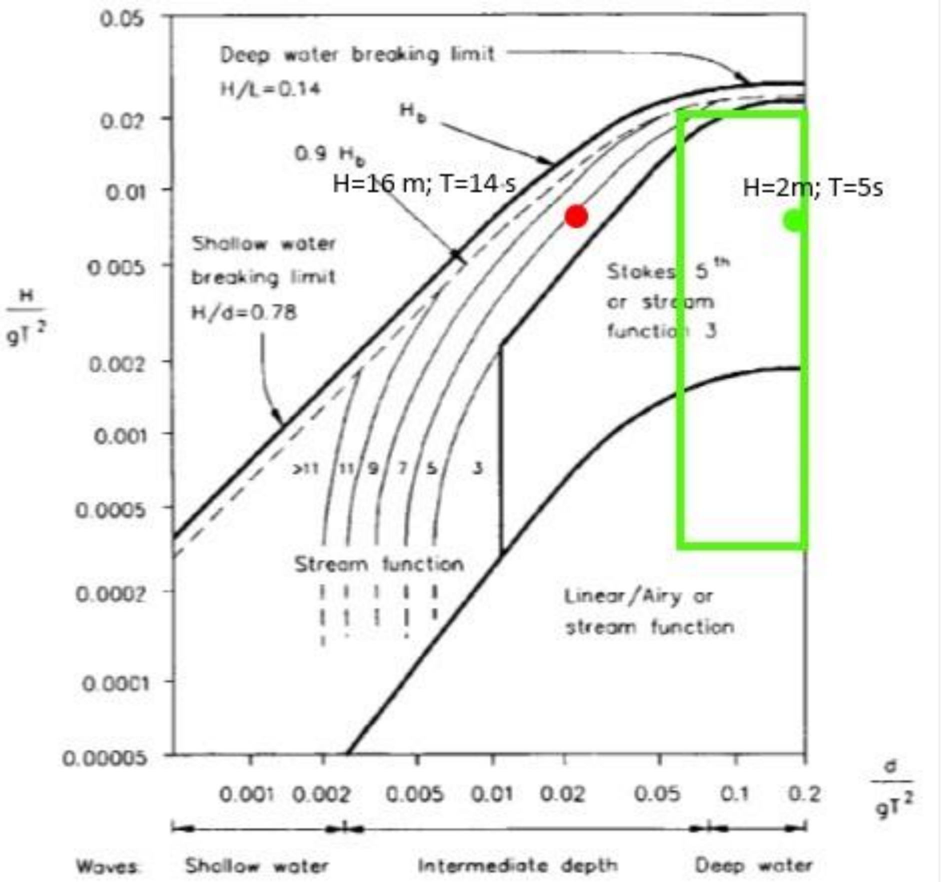

Figure A.33 - Ranges of suitability of regular wave theories (d= water depth, g= gravity acceleration, H = wave height, L = wave length, T = wave period) [21] Green =fatigue waves Red = extreme wave (H=16m; T=14s; d=50m).

Figure A.34 gives an overview of non-linear wave theories and their characteristics. A regular non linear waver theory is Stokes wave theory. This theory is based on adding a wave with the same phase speed as the Airy wave, but with another amplitude. Another approach is Dean's Stream function. In this theory the surface profile is written in terms of a series of harmonics as well. But now the nonlinear basic equations are not solved with the velocity potential function, but with the so called stream function [52]. This stream function is a function of the velocity potential funcion in the Airy wave. The advantage is that the mathematics are a little more easier. For irregular waves other non-linear theories have been developed. The 2nd order irregular wave model developed by Sharma and Dean is often applied and mentioned as an alternative for linear wave theory in the DNV. A more advanced model is the Boussinesq model, but this model is very computationally expensive [53].

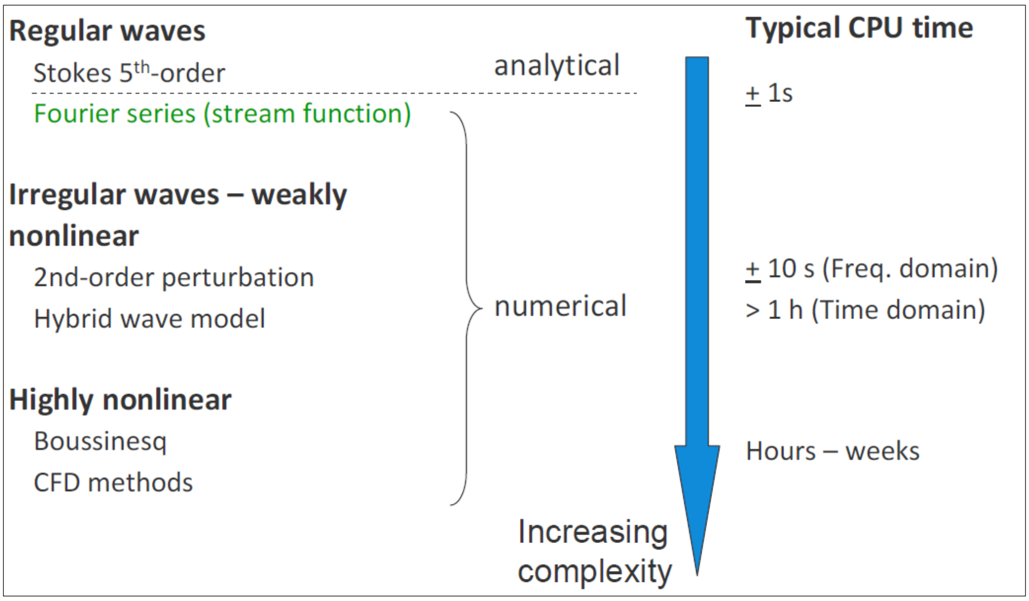

Figure A.34 - Different non-linear wave theories [53]

Non-linear waves cause an increase in the wave loads due to a higher magnitude of particle velocities and accelerations below the waves and a different shape of the waves (sharper crests and flatter troughs).

<u>>>BAM Van Oord case study - Influence of Non-linear waves on wave loads</u>

For a monopile at a location of 25 m water depth (shallow water) the influence of non-linear waves was investigated in [54]. It followed that with respect to irregular linear waves , application of non-linear irregular waves theory led to an increase of the fatigue load of 7.5%. In shallow water non-linear effects are larger compared to intermediate water depth. So, it is expected that this influence will be smaller for the BAM Van Oord case.

<u>Wave loads</u>

When a wave breaks in the vicinity of a pile it will cause a rather large wave breaking load on the structure. Most waves break near the coast or when the bathymetry changes. As the bottom of an offshore wind farm is often nearly horizontal the probability of a breaking wave is low. The wave impact depends on the type of wave breaking. This is expressed by the breaking parameter (slope/wave steepness). For high values a plunging breaker will occur. For low values of the breaking parameter a spilling breaker will be the result. For an almost horizontal bottom the result will be a spilling breaker type. For that case the DNV [11] prescribes the next equation:

$$f = \frac{1}{2}\rho C_S D u^2 \tag{A.18}$$

with:

f	wave impact force per unit length	[N/m]
ρ	water density	[kg/m^3]
C_S	slamming coefficient (range: 1 – 5)	[-]
D	pile diameter	[m]

u	horizontal water particle velocity wave crest	[m/s]

<u>>>BAM Van Oord case study - Wave impact force</u>

For the design wave (ULS) the wave impact force has been calculated. The wave was found to be a spilling type breaker. The breaking wave is assumed to act at the shaft over the full design wave height (z=-8..8 m + SWL). This leads to a force of about 3600 kN.

A non-breaking wave leads to a maximum wave force of about 1500 kN between z=-8..8 m +SWL.

For wave loads a distinction has to be made with regard to the shape of the structure [19]:

- For slender structures (D/L<0.2) the presence of the structure can be ignored when calculating the water particle kinematics. In this case Morison's theory is often used. This theory is also valid for non-linear waves.
- Compact structures on the other hand will influence the movement of the water significantly. For these structures the drag force can be neglected, as inertia dominates (Figure A.35) However, in this case the influence of diffraction has to be taken into account. An adaption (the so called MacCamy-Fuchs correction) of the inertia coefficient in the Morison equation gives acceptable results.

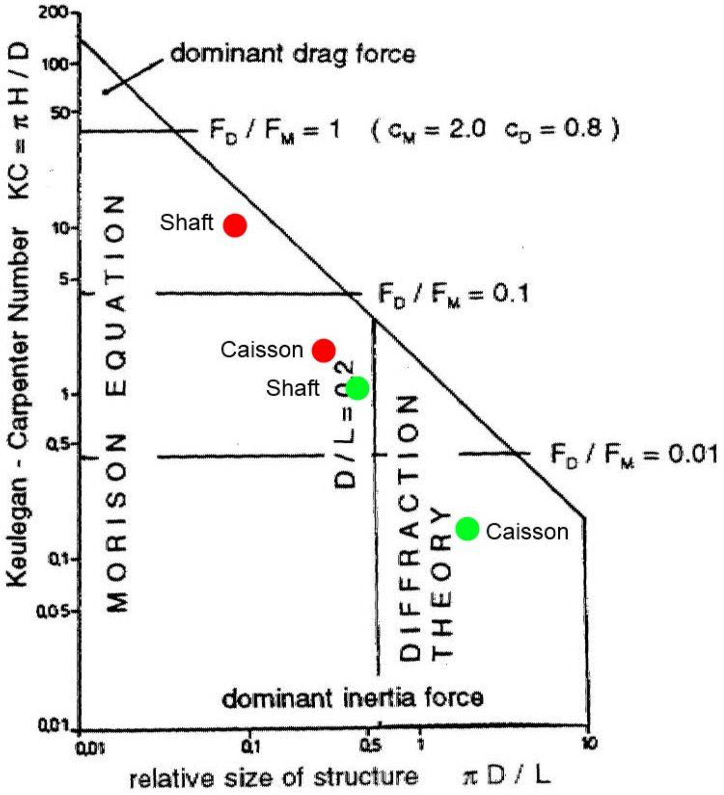

Figure A.35 - Influence of drag, inertia and diffraction per region, green = FLS_{AV}, red = ULS [21]
Green =fatigue waves
Red = extreme wave (H=16m; T=14s; d=50m)

<u>>>BAM Van Oord case study – Wave theory and Morison equation</u> <u>[Appendix B]</u>

With aid of Figure A.33 the validity of Linear wave theory was checked. From the wave scatter diagram it followed that (by plotting H/gT^2 and d/gT^2) in about 90% of the time waves are non-linear. So linear wave theory is not valid here. Therefore one of the non-linear wave theories has to be applied.

To determine whether the Morison is valid and what the influence of the inertia and drag forces is Figure A.35 can be used. It can be concluded that:

- Morison is valid for the ULS
- In 40% of the cases Morison is invalid for the shaft in FLS. However, these are small waves
- Morison is not valid for the caisson in FLS

The Morison formula calculates the total wave force on a slender cylinder and includes an inertia and a drag part [55]:

$$\frac{dF}{dz} = p(t,z) = p_M(t,z) + p_D(t,z) = C_M \rho \frac{\pi D^2}{4} \frac{du}{dt} + C_D \frac{1}{2} \rho D u|u| \qquad \text{(A.19)}$$

with:

$p(t,z)$	pile force per unit of length of the pile at time *t* and in position *z*	[N/m]
$p_M(t,z)$	inertia force (per unit of length of the pile)	[N/m]
$p_D(t,z)$	drag force (per unit of length of the pile)	[N/m]
C_M	inertia coefficient (≈ 2.0)	[-]
C_D	drag coefficient (for low flow velocities $C_D \approx 1.2$)	[-]
ρ	density of the water	[kg/m^3]
D	diameter of the pile	[m]
$u(t)$	horizontal velocity of the water particles (for linear waves): $u(t) = \omega a \frac{\cosh(k(d+z))}{\sinh(kd)} \sin(\omega t)$	[m/s]
$\frac{du}{dt}$	horizontal acceleration of the water: $\frac{du}{dt} = \omega^2 a \frac{\cosh(k(d+z))}{\sinh(kd)} \cos(\omega t)$	[m/s^2]
ω	angular frequency (2π/*T*)	[rad/s]
k	wave number (2π/*L*)	[rad/m]
d	depth	[m]

Because the velocity and the acceleration of the water particles are not in phase, the maximum total force is smaller than the sum of the maximum drag force and the maximum inertia force. The force on the pile over time is found by integration:

$$\begin{aligned} F(t) &= \int_{-d}^{\eta} p(t,z)dz = \int_{-d}^{\eta} p_M(t)dz + \int_{-d}^{\eta} p_D(t)dz \\ &= C_M \rho \frac{\pi D^2}{4} \int_{-d}^{\eta} \frac{du}{dt} dz + C_D \frac{1}{2} \rho D \int_{-d}^{\eta} u|u| dz \end{aligned} \qquad \text{(A.20)}$$

As a simplification of the full Morison equation the maximum drag and inertia forces can be calculated with [56]:

$$\hat{F}_M = \rho g \frac{C_M \pi D^2}{4} \hat{\eta} \cdot \tanh(kd)$$
$$\hat{F}_D = \rho g \frac{C_D D}{2} \hat{\eta}^2 \cdot \left[\frac{1}{2} + \frac{\mathrm{kd}}{\sinh(2kd)}\right] \tag{A.21}$$

with:

$\hat{F}_M$	maximum inertia force	[N]
$\hat{F}_D$	maximum drag force	[N]
$\hat{\eta}$	maximum wave elevation	[m]

The factor C_D depends on the shape of the object and the Reynolds number. The Reynolds number is formulated as:

$$RE = \frac{uD}{\nu} \tag{A.22}$$

with:

RE	Reynolds number	[-]
u	horizontal velocity	[m/s]
D	diameter	[m]
ν	kinematic viscosity	[m^2/s]

Another parameter is the Keulegan-Carpenter number. This number determines the relative contribution of inertia and drag forces and is defined as:

$$KC = \frac{u_a T}{D} \approx \frac{drag}{inertia}$$
$$KC = \frac{\pi H}{D} \text{ (for deep water d>L/2)} \tag{A.23}$$

with:

KC	Keulegan-Carpenter number	[-]
u_a	horizontal flow velocity amplitude	[m/s]
T	wave period	[s]
D	diameter	[m]
H	wave height	[m]
d	water depth	[m]

For high KC numbers the drag force is dominant, while for low values the inertia force is dominant.

The factors C_D and C_M are determined from experiments. In the DNV code they are expressed as a function of KC.
Summarizing (for a relative smooth cylinder):

- C_D varies between 1.2 for small KC numbers (KC<10) till 0.8 for high numbers (KC>30)
- C_M varies between 2.0 for small KC numbers till 0.7 for high numbers (KC>10)

Not only the wave impact in horizontal direction is of importance. According to [19] the buoyancy force on the horizontal surface of a GBS is very significant. The heave force is caused by the vertical particle velocity of the waves.

>>BAM Van Oord case study – Wave forces [Appendix B]

In this case study the wave force with the aid of the Morison equation is calculated. The next aspects form the basis:

- The design wave ($H_S = 16m, T_P = 14s$) is used to determine the maximum wave force. For this ULS wave the Morison equation is valid (see previous example).
- Although not valid, Airy's linear wave theory is chosen as a first approximation to determine the water velocity.
- Wheeler stretching is applied to find the forces up to the crest level.
- Both inertia and drag forces are taken into account.

The wave forces were calculated with aid of the Morison equation. The software package Maple was used for this purpose. The maximum values can be found in the figure below. The maximum bending moment at foundation level is 290 MNm.

The following can be concluded:

- For the FLS the shaft contributes to about 90% of the total force, for the ULS the caisson does.
- Although the force is relatively small, for the ULS the shaft contributes to about 40% of the total bending moment.

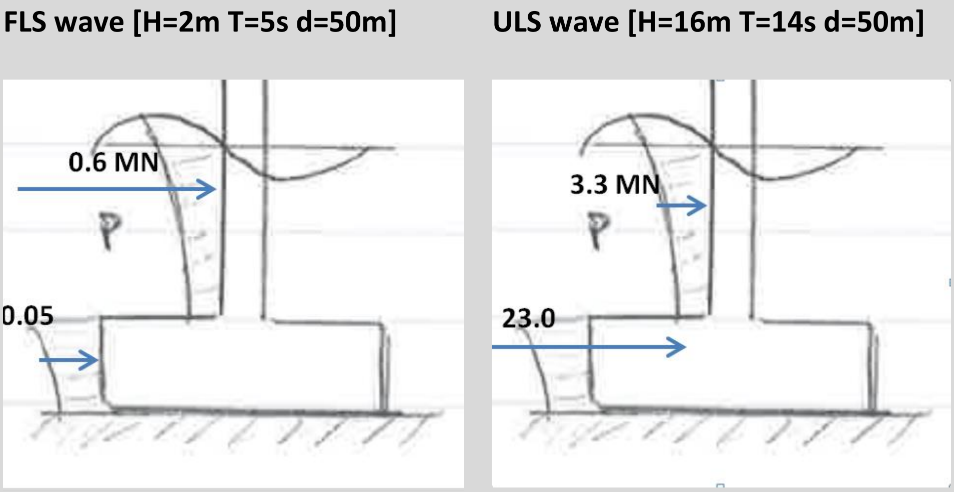

Figure A.36 – Wave forces on shaft and caisson for a) FLS wave B) ULS wave

A.4.2.2. Flow

Sea currents are mostly driven by the tides and ocean circulations. Differences in temperature or salinity and storm surges may cause extra local currents [2].

The flow force on a slender structure consist of a lift force (perpendicular to the flow direction) and a drag force (parallel to the flow direction). Empirical formulas for drag and lift are [55]:

$$F_D = \frac{1}{2}\rho u^2 (C_D + C_D')A \quad \text{and} \quad F_L = \frac{1}{2}\rho u^2 (C_L + C_L')A \tag{A.24}$$

with:

F_D	drag force parallel to the flow direction	[N]
F_L	lift force perpendicular to the flow direction	[N
C_D	drag coefficient (static)	[-]
C_L	lift coefficient (static)	[-]
C'_D	dynamic drag coefficient (time dependent)	[-]
C'_L	dynamic lift coefficient	[-]
A	area facing flow, projected perpendicular to the flow direction	[m^2]

The coefficients C_D and C_L are dependent on the shape of the structure and the flow around the structure.

Depending on the frequency of vortex shedding, it can cause resonance for a structure in a stationary flow. The dynamic drag and lift coefficients are dependent on the frequency of vortex shedding and the natural frequency of the structure.

For the determination of combined flow and wave force the current can be added to the wave particle velocity [2]. Now, three forces can be distinguished:

1. Drag force due to flow and waves (parallel to wave and flow direction)
2. Inertia force due to waves only (parallel to wave direction). No influence of constant flow, due to dependence of acceleration.
3. Lift force due to flow and waves (perpendicular to flow direction)

A.4.2.3. Lift forces

The lift force on a cylinder in oscillatory flow can be calculated with equation (A.24)b. The static lift coefficient C_L is zero for a straight approaching flow [55]. The dynamic lift coefficient C_L' is related to the vortex shedding frequency f_s. This frequency is defined by:

$$f_s = \frac{uS}{D} \tag{A.25}$$

with:

f_s	vortex shedding frequency	[Hz]
u	horizontal particle velocity	[m/s]
S	Strouhal number	[-]
D	cylinder diameter	[m]

When $\frac{f_s}{f_n} = 1$ (with f_n the natural frequency of the system) the value of C_L' increases strongly. For a preliminary design one may assume:

$$C_L' \approx C_D'$$

where:

$C_D' = 0.1 - 0.25C_D$ when $f_s > f_n$
$C_D' = \text{unknown (resonance)}$ when $f_s < f_n$

>>BAM Van Oord case study – Lift force [Appendix B]
For the ULS wave the magnitude of the lift force is estimated by determining the vortex shedding frequency.

A vortex shedding frequency of 0.21 Hz was found, leading to $\frac{f_s}{f_n} = 0.85$. So, there is a possible danger for resonance.

A.4.2.4. Sea level elevations

The main driver of sea level elevations is the tide. The tidal range depends on the location on earth and the local bathymetry. Along the British East coast this range is more than 4 m. Storm surges are another driver. Sea level elevations don't cause direct forces on an offshore structure because of their long period. Indirect they do via sea currents.

A.4.3. Geotechnical aspects

The subsoil must be able to resist all the loads acting on the offshore wind turbine. The next aspects are of importance:

- Vertical bearing capacity & overturning
- Sliding resistance
- Behaviour under cyclic loading
- Relative settlements

A.4.3.1. Bearing capacity and overturning

The vertical bearing capacity can be calculated according to the theory developed by Prandtl, Terzaghi and Brinch Hansen. When the bearing capacity is calculated it is checked whether these limits are exceeded. Two checks have to be performed, one for the vertical bearing capacity and one for overturning.

A.4.3.2. Soil behaviour

Soil behaves in fact as a non-linear material. In addition when soil is loaded it is expected not to return to its original condition, so plastic deformation will occur. This has to do with internal grain displacements. In engineering practise soil is often assumed to be linear-elastic.

The assumption of elastic, instead of plastic, material is only valid when the soil is loaded up to its limit state (stress level of pre-loading). Up to that level the soil behaves much stiffer (up to a factor 10) than above. Even under the limit state small plastic displacements occur. The relation between soil stresses and displacements is in fact non-linear. However, according to the API [57] for small loads with respect to failure loads, the soil behaviour can be estimated to be linear.

A.4.3.3. Sliding resistance

A gravity based structure in water often leads to a large horizontal force due to its large base. The horizontal force has to be transferred to the soil. The underlying principle is friction between the base plate of the GBS and the soil. The allowable horizontal force can be increased by increasing the weight, or the friction factor (soil improvement/roughness base plate). Within the BAM van Oord case the sliding resistance was found to be high enough.

A.4.3.4. Cyclic behaviour

Due to the varying wind and wave loads the soil is cyclically loaded. This leads to several effects [10]:

1. Strength reduction due to excess pore pressure
2. Settlements due to densification/ liquefaction
3. Removal of material due to pumping motion

Ad. 1:
Cyclic loading leads to an excess pore water pressure, reducing the effective stresses (and bearing capacity) and leading to a decrease of the shear strength. Furthermore the excess pore pressures lead to uplift forces on the GBS.

Ad. 2:
Cyclic loads lead to a densification of the soil, this is also called 'cyclic creep'.
Extreme events are the main cause for a significant accumulation of excess pore water pressure depending on the drainage conditions. If the average effective stresses approach null, liquefaction occurs. A spontaneous failure with very large deformations only occurs with very loose soil density and particularly in non-cohesive soils [41].

Ad. 3:
The pumping motion (cyclic tilting) leads to sand removal below the foundation. This effect can be counteracted by applying a scour protection.

Several theories have been developed to describe the effects of cyclic loading, these theories are not described here, more information can be found in Chapter 6 of [41]. For the BAM Van Oord concept the program DCYCLE of Deltares was used to determine the excess pore pressure and settlements during lifetime due to cyclic behaviour. It was found that the subsoil was strong enough.

A.4.3.5. Settlements

Settlements may not only occur due to cyclic behaviour, but also due to static loading of the soil (consolidation). Codes prescribe maximum total and differential settlements. Especially the differential settlements are of importance, because they cause a rotation of the wind turbine. The maximum rotation is prescribed by the turbine manufacturer and is often in the order of 0.25°. The installation tolerances for the GBS concept of BAM Van Oord are 0.68° [10]. However, a shim ring can be applied between the GBS shaft top and the turbine tower after immersing the GBS. By this shim ring a correction of 0.5° can be achieved. So, the maximum rotation due to differential settlements cannot be more than 0.07° (4 cm difference over the base diameter).

A.4.4. Other aspects

A.4.4.1. Corrosion

For design corrosion rates of 0.3 mm/y in the splash zone and 0.1 mm/y below sea water level are prescribed. Corrosion can be dealt with by allowance (and taking into account the corrosion in the design) or by protection (cathodic, coating, corrosion resistant materials).

With respect to the GBS concept the next zones, with each their own solution against corrosion, can be distinguished [10]:

- Atmospheric zone: coating
- Splash zone: coating and allowance (8 mm for a design life of 25 year)
- Submerged zone: cathodic protection

- Inside of the shaft: no corrosion protection due to the low oxygen content (filled with sand)

A.4.4.2. Marine growth

A steel structure in seawater forms a habitat for plant and animals, leading to marine growth. Marine growth may have influence on the hydrodynamic loads, dynamic response (due to added weight) and corrosion rate. The next values are prescribed:

Depth below MWL (m)	Marine growth thickness (mm)
-2 to 40	100
>40	50

Table A.8 - Marine growth for the Central and Northern North Sea, MWL = Mean Water Level [11]

A.4.4.3. Ice load

Ice can lead to the following loads on an offshore wind turbine:

- Ice accumulation as a result of a slight current, this causes a horizontal load.
- Collision by the impact of large ice sheets (horizontal load)
- A vertical load due to ice attachment. The attached ice mass causes an upward load under water and a downward load when the ice mass is above water.

A.4.4.4. Crack width

The reinforced concrete of the caisson is sensitive for the development of cracks. Cracks are caused by concrete effects (like creep, shrinkage and thermal expansion) and by loads. According to [11] the load to be used for crack width calculations is the maximum characteristic load following from the combination of wind and wave loads used for the FLS.

A.4.4.5. Scour

A structure at the bottom of the sea influences the local flow pattern, causing local scour. For a GBS scour is expected to be unacceptable, due to their high reliance on near-surface soil [19]. Scour can be prevented by a scour protection. This protection, together with a gravel bed for the transition from GBS to subsoil, often takes a large part of the costs.

In addition to scour natural sediment displacement may result in in rise or drop of the entire seabed around the structure. The magnitude can be several meters at some North Sea sites. These sites are unsuitable for a GBS. When the magnitude is relative small (~1 m [58]) a solution like at the Thornton Bank (section A.2.3.2) can be applied: the foundation level is chosen at the lowest expected seabed level during the lifetime of the structure.

A.4.5. Dynamic behaviour

A.4.5.1. General overview

The dynamic behaviour of a system can be distinguished in three kinds of responses [2]:

1. Quasi-static: $f_{ex} < f_{nat}$:	displacement of mass follows time varying force almost instantaneously
2. Resonance: $f_{ex} = f_{nat}$:	response is number of times larger than it would be statically
3. Inertia dominated: $f_{ex} > f_{nat}$:	response is small and almost counter-phase

In the above f_{ex} is the excitation frequency of the load, and f_{nat} the first natural frequency of the offshore wind turbine. For linear systems the magnitude of the response can be expressed with the Dynamic Amplification Factor (DAF): the ratio between the dynamic response magnitude and the static response magnitude (Figure 3.6). The phase lag can be related to this factor. The peak in Figure 3.6 corresponds to the system's natural frequency and the height is determined by damping.

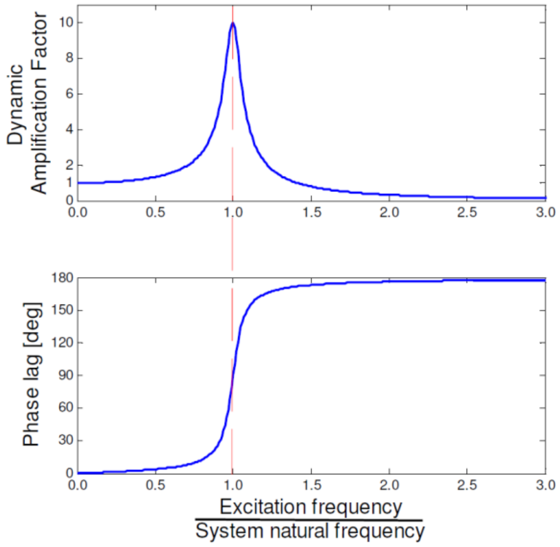

Figure A.37 - Example of a DAF graph [14]

Resonant behaviour can cause severe load damage and even failure, but it is most feared because of possible fatigue damage. Therefore these excitation frequencies should be avoided as much as possible. As such, the structure should be designed so that its first natural frequency (f_0) does not coincide with either 1P (the rotor frequency f_R), or 3P (the blade passing frequency f_B), see section A.4.1.4. This leaves three possible intervals (Table A.9):

Class	Frequency interval
soft-soft	$f_0 < f_R(1P)$
soft-stiff	$f_R(1P) < f_0 < f_B(3P)$
stiff-stiff	$f_B(3P) < f_0$

Table A.9 - Structure classification according to natural frequency [16]

Each type of support structure corresponds with a certain class (Figure A.38).

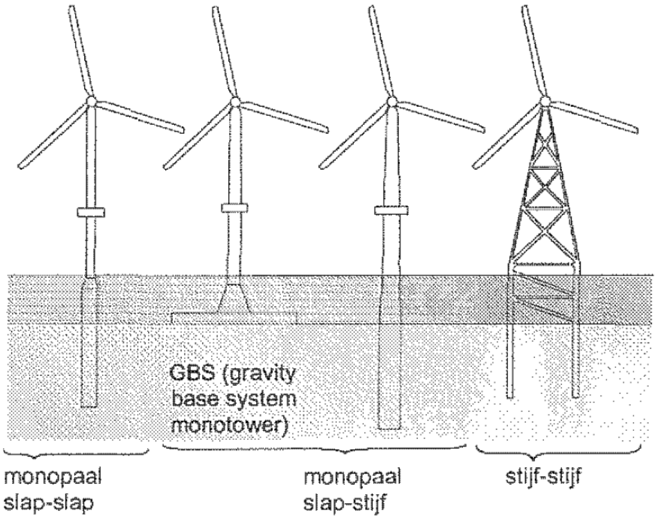

Figure A.38 - Structure classes with corresponding structures [16]

>>BAM Van Oord case study – Frequency intervals

On top of the BAM Van Oord concept a Siemens 6MW turbine is installed. This Siemens SWT 6.0-154 has a rotor diameter of 154 m and a hub height of 105 m above mean sea level. The first natural frequency is prescribed by the turbine manufacturer as 0.25 Hz ± 5% [10].

The waves are described by a PM spectrum with $H_s = 2m$ and $T_p = 5s$ (excitation frequency near natural frequency). The values of 1P and 3P follow from section A.4.1.4. These frequency ranges are plotted in Figure A.39.

In order to prevent coincidence of the natural frequency with the excitation frequencies the natural frequency should be above the waves and 1P nominal frequency range. It follows that the prescribed natural frequency by the turbine manufacturer is just above the 1P rotational frequency.

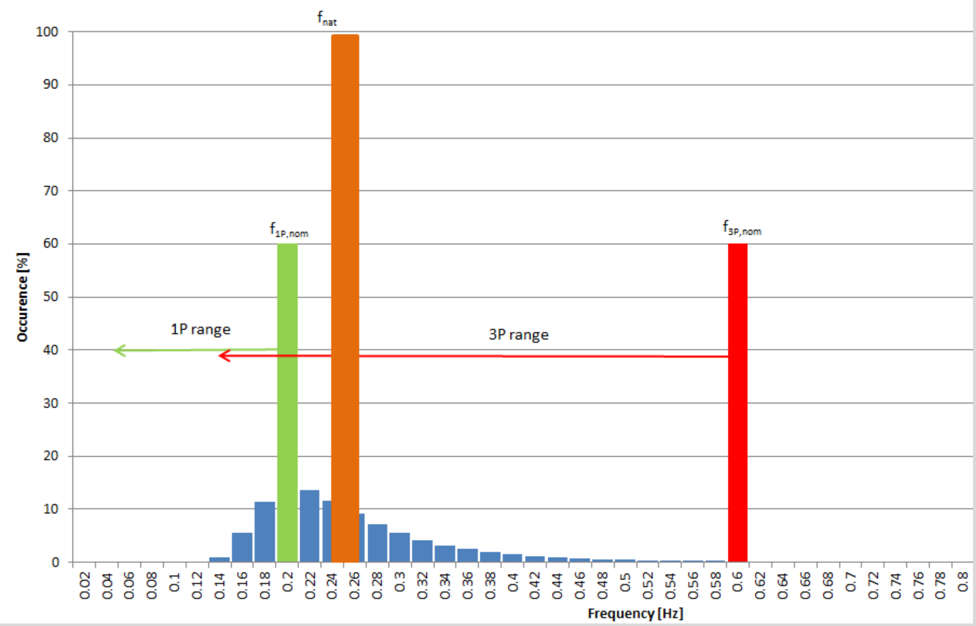

Figure A.39 - Wave, 1P, 3P and prescribed natural frequencies for a variable Siemens SWT 6.0-154 turbine; partly based on [2]

It is not the case that the excitation frequencies should be avoided in all cases. Damping (section A.4.5.3) significantly decreases the DAF peak of Figure A.37 In addition the controller of the rotation speed (for a variable speed turbine) can be tuned to skip the first natural frequency [2]. However, having the natural frequency in the range of the excitation frequency has disadvantages for fatigue, so at least the frequencies with a large occurrence should be avoided.

A.4.5.2. Schematisation

This section treats the schematisation of the structure as a One Degree Of Freedom System (1DOFS). A more sophisticated method is to describe the system as a system with N degrees Freedom (NDOFS). However possible, it is not described here due to its complexity. Often a FEM package is used where this approach is implemented.

1DOFS

The most basic treatment is to schematise the system as a One Degree Of Freedom System (1DOFS). In this case, for example, the offshore wind turbine is regarded as clamped at the bottom. The degree of freedom would then be the deflection at the top of the structure. Another 1DOF model appears when the structure is regarded as a rigid body that can rotate around its foundation. In this case internal deflections of the structure are omitted. Also other degrees of freedom at the foundation are omitted.

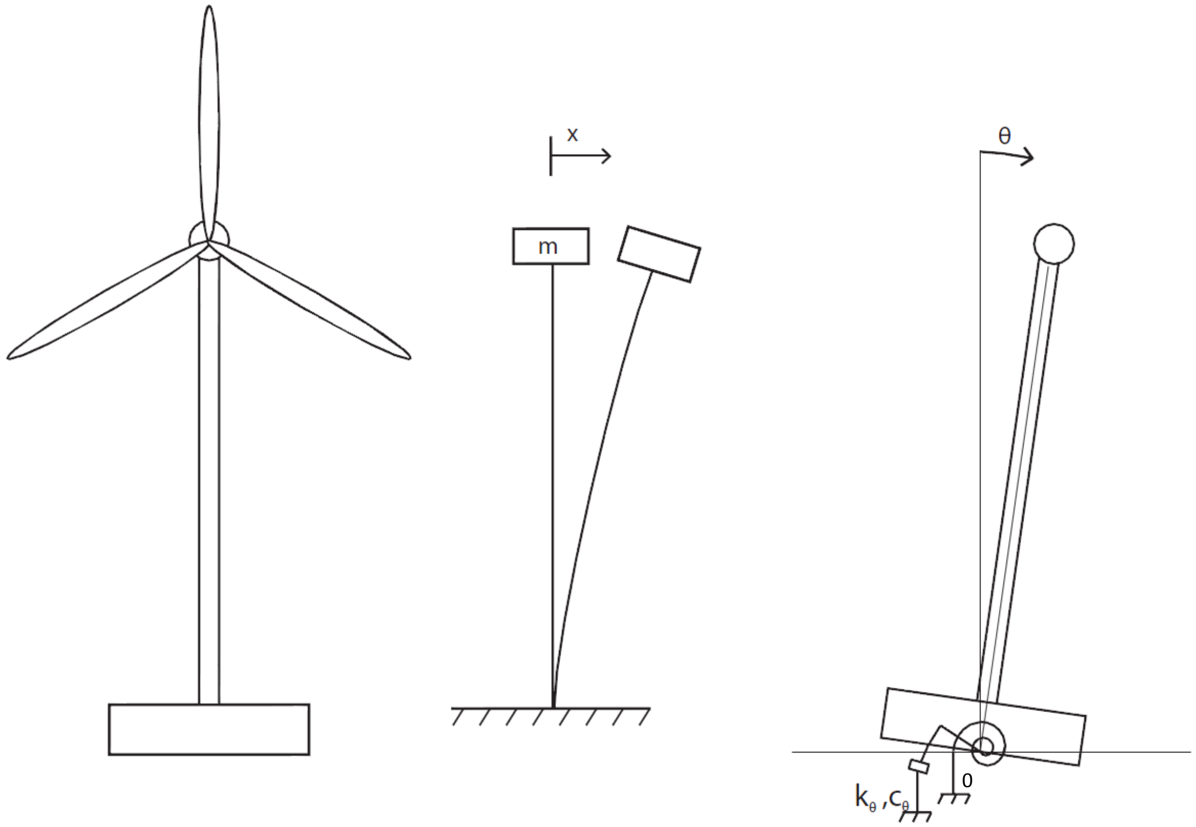

Figure A.40 - 1DOFS schematisation (N.B. the first model is incorrect; the mass can only translate)

The models can be described by Newton's second law: $\Sigma F_x = m\ddot{x}$ where $x = x(t)$ is the displacement, m the mass of the structure and ΣF_x the sum of all the external forces on m. In case of a rotation the equation of motion has the form $\Sigma M_0 = J_0\ddot{\theta}$ where $\theta = \theta(t)$ is the angular rotation of the structure, ΣM_0 the sum of all external moments on the structure and

J_0 the mass moment of inertia with respect to the reference axis perpendicular to the plain of motion and through point 0 [59]. For J_0 applies:

$$J_0 = \int_m r^2 dm \tag{A.26}$$

with:

J_0	mass moment of inertia	[kgm^2]
m	mass of body	[kg]
r	distance from reference axis to mass element dm	[m]

First case (translation)

When the movement in horizontal direction x is the single degree of freedom, the structure can be modelled as the mass-spring-dashpot system of Figure A.41

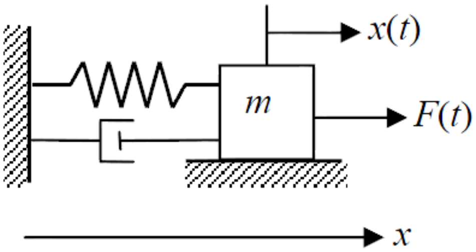

Figure A.41 - Mass-spring-dashpot system [60]

The corresponding equation of motion is:

$$m\ddot{x} + c\dot{x} + kx = F(t) \tag{A.27}$$

with:

x	displacement coordinate	[m]
m	mass	[kg]
c	damping coefficient	[Ns/m]
k	stiffness	[N/m]
$F(t)$	external force	[N]

The spring stiffness can in this case be deduced from simple mechanical laws. For a clamped beam:

$$k = \frac{3EI}{L^3} \tag{A.28}$$

with:

E	elasticity modulus	[N/m^2]
I	area moment of inertia	[m^4]
L	tower length	[m]

Second case (rotation)

When the rotation θ is the only degree of freedom the only difference is the replacement of m for J_0 and x for θ and $F(t)$ for $M(t)$. The equation of motion becomes:

$$J_0\ddot{\theta} + c\dot{\theta} + k\theta = M(t) \tag{A.29}$$

Free, undamped motion

When damping and the external force are absent the equation simplifies to

$$m\ddot{x} + kx = 0 \tag{A.30}$$

This equation describes the free motion of the system. When the structure is given an small displacement amplitude x_0 and is then released the motion can be described by $x = x_0\sin(\omega_n t)$ [59]. Now, the natural frequency of the structure ω_n becomes :

$$\omega_n = \sqrt{\frac{k}{m}} \tag{A.31}$$

with:

ω_n	natural frequency	[rad/s]

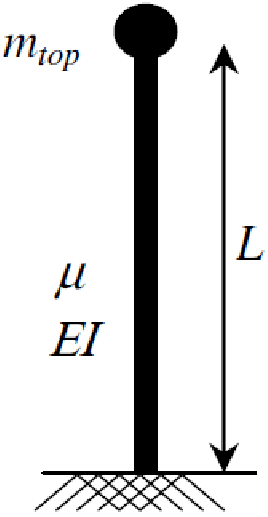

Figure A.42 - Structural model of an offshore wind turbine

By combining equation (A.28) and (A.31) the natural frequency can be expressed as below. For this case the natural frequency can be approximated with:

$$f_{nat}^2 \cong \frac{3.04}{4\pi^2}\frac{EI}{(m_{top} + 0.227\mu L)L^3} \tag{A.32}$$

with:

μ	tower mass per meter	[kg/m]

For flexible structures experience has shown that between 25-40% of the surrounding structural mass has to be lumped in a node [59]. The equation above prescribes 22.7%.

Harmonic response, damped

When loaded with a harmonic load $F(t) = \hat{F}\cos(\omega t)$ the response of the structure becomes $x(t) = \hat{x}\cos(\omega t + \phi)$ where [61]:

$$\hat{x} = \frac{\hat{F}}{k}\frac{1}{\sqrt{\left(1-\left(\frac{\omega}{\omega_n}\right)^2\right)^2+4\zeta^2\left(\frac{\omega}{\omega_n}\right)^2}} = H(\omega)\cdot\hat{F} \quad \text{and}$$

$$\phi(\omega) = \arctan\left(\frac{-c\omega}{k-\omega^2 m}\right) \tag{A.33}$$

where:

$$\zeta = \frac{c}{2\sqrt{km}} \tag{A.34}$$

with:

$\hat{x}$	dynamic displacement amplitude	[m]
$\hat{F}$	load amplitude	[N]
ω	angular frequency	[rad/s]
ζ	damping ratio	[-]
$\phi(\omega)$	phase angle	[rad]
$H(\omega)$	harmonic response function	[-]

The phase angle causes a phase lag $\phi(\omega)$ between the load $F(t)$ and the response $x(t)$. The ratio of $\hat{x}$ over the static deflection $x_{static} = \hat{F}/k$ is defined as the Dynamic Amplification Factor (DAF) [60], see Figure A.43:

$$|H(\omega)| = \text{DAF}=\frac{\hat{x}}{x_{static}} = \frac{1}{\sqrt{\left(1-\left(\frac{\omega}{\omega_n}\right)^2\right)^2+4\zeta^2\left(\frac{\omega}{\omega_n}\right)^2}} \tag{A.35}$$

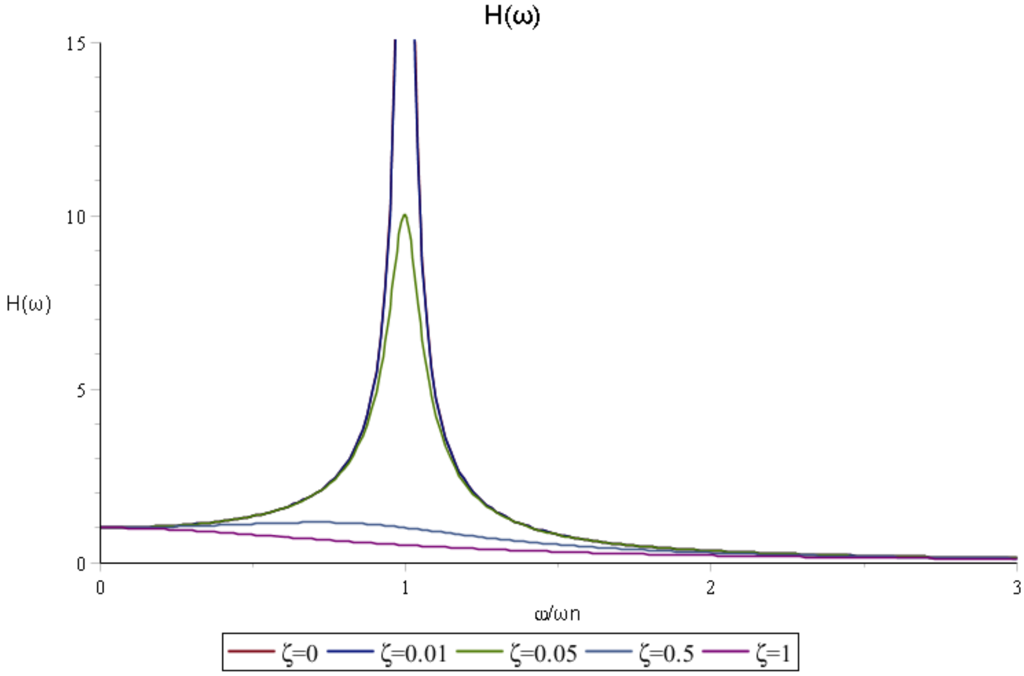

Figure A.43 - DAF for different damping values ζ

Evaluation

A disadvantage of the 1DOFS is the very crude approximation of only one degree of freedom. The model simplifies the real behaviour in the following manner:

- The tower exist of a homogeneous beam instead of a combination of a non-homogeneous steel shaft and a caisson
- All the mass is assumed to be located at the top
- The load can only be applied at the top, which means that only wind load can be taken into account
- The foundation is schematised as clamped to the bottom, instead of a connection allowing for rotation and translations

Although the above simplifications will probably have a large influence on the behaviour, the first model can be used as a first estimation because of its simplicity.

A.4.5.3. Foundation models

In literature different foundation models exist for the schematisation of the foundation of a gravity based structure. In general a distinction can be made between:

- frequency dependent springs and dampers: spring stiffness's and damping values are dependent on the excitation frequency (as in reality). Not very suitable for an analytical approach.
- frequency independent springs and dampers. Suitable for an analytical approach. In [21] it is shown for relative low frequencies up to 5 Hz (as is the case in here) the deviation from the frequency dependent model is small (but leading to non-conservative values).

For gravity platform dynamics the next values are suggested for a disc with radius R [21]

$$\begin{aligned} k_x &= \frac{8G_{dyn}R}{2-\nu} & c_x &= \frac{4.6R^2}{2-\nu}\sqrt{\rho_s G_{dyn}} \\ k_z &= \frac{4G_{dyn}R}{1-\nu} & c_z &= \frac{3.4R^2}{1-\nu}\sqrt{\rho_s G_{dyn}} \\ k_\theta &= \frac{8G_{dyn}R^3}{3(1-\nu)} & c_\theta &= \frac{0.8R^4\sqrt{\rho_s G_{dyn}}}{(1-\nu)\left(1+\frac{3(1-\nu)\Theta_{tilt}^{C.o.G.}}{8\rho_{soil}R^5}\right)} \end{aligned} \qquad \text{(A.36)}$$

Here G_{dyn}, ν, and ρ_s are the dynamic shear modulus, Poisson's ratio, and mass density, respectively, of the soil. The constants k_x and c_x describe the soil stiffness and damping in horizontal direction, k_z and c_z in vertical direction and k_θ and c_θ for rotation.
The parameter $\Theta_{tilt}^{C.o.G.}$ stand for the inertia of the entire structure with respect to the centre of gravity. With respect to the values of the spring stiffness's common agreement exists. The values correspond with the values of the DNV [11] and the API [57]. For the damping different values are found in literature.
The above spring-dashpot model assumes linear behaviour of the soil. In fact, soil behaves non-linear. For fatigue calculations however, most soil reactions remain within the linear range.

A.4.5.4. Damping

Damping will determine the height of the resonance peak. The types of damping to be distinguished are:

1. Structural damping
2. Aerodynamic damping
3. Hydrodynamic damping (viscosity of water)
4. Soil damping

All damping values are expressed as percentages of critical damping ($\zeta = 1$).

Structural damping

Internal material friction leads to structural damping. For a steel shaft in offshore engineering a typical value is 0.2% [12]. In addition the effect of the bolted connection of the transition piece leads to an additional damping effect. The total structural damping is assumed to be 0.5% [12].

Aerodynamic damping

Rotor damping

This type of damping is an important characteristic of a wind turbine. When the turbine moves forward (against the wind), the blades experience an increase in total wind speed. As a result the wind load on the blades increases. This load acts against the tower top motion (Figure A.44), so it introduces a kind of a damping effect. For backward motion, the situation is analogous, now resulting in a reduced tower top load, also reducing the tower top motion. [14]

The amount of aerodynamic is strongly dependent on the type of wind turbine and support structure and the behaviour (rotation speed, pitch angle and so on). For example, the two different wind turbines of Figure A.45 lead to two almost contradicting graphs. Due to the complex behaviour of the turbine the amount of aerodynamic damping cannot easily be determined in a simple manner. In general the next remarks can be made:

- The amount of aerodynamic damping varies between 1% of critical damping for a stiff and heavy tower to above 5% for a soft and light support structure [21].
- The amount of aerodynamic damping is different for every wind class.
- Due to control effects above V_{rated} the aerodynamic damping decreases.

Determining the amount of aerodynamic damping is a difficult process. It is also an important step, because it has significant effect on the fatigue life of the support structure [14]. In [14] some methods are compared, however, a link with practise is missed. One of the conclusions of the report is that more research on this topic is to be done.

As known to the author no simplified methods have been developed yet. The engineering approach in [14] is to take 4% aerodynamic damping into account for all wind speed classes. This value seemed to give most reasonable results for a 2-3MW wind turbine with a first natural frequency around 0.3 Hz or higher. In literature also higher values are found, in [17] a damping value of 10% is mentioned.

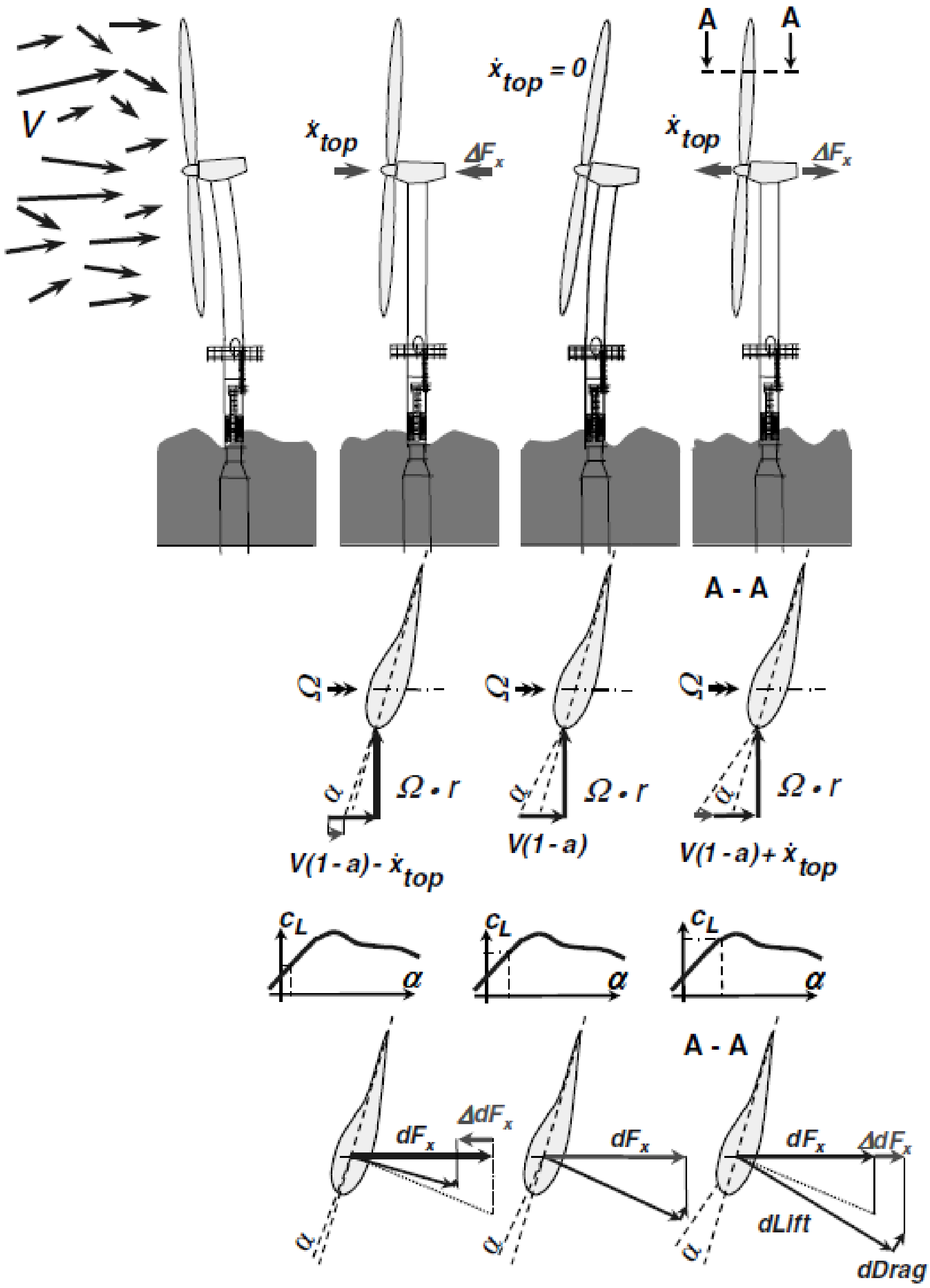

Figure A.44 - Illustration of aerodynamic damping effect [21]

- Fore aft motion $\dot{u}_{top}$ at wind speed V during production
- motion $\dot{u}_{top}$ changes angle of attack a at a blade element
- variation of lift coefficient c_L and drag c_d (not shown)
- variation of thrust ΔF_x opposite to perturbation

The BAM van Oord case has about the same characteristics as the wind turbine of Figure A.45b. The engineering estimate of 4% seems all right (under the assumption that small wind speeds don't contribute very much to the fatigue load).

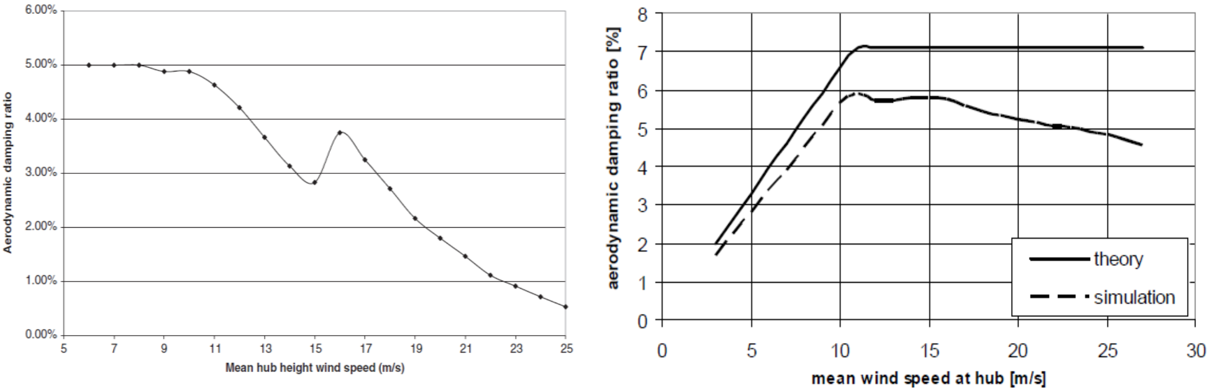

Figure A.45 - Aerodynamic damping as function of wind speed for a) fixed speed pitch regulated 3MW 2 bladed machine [21] b) variable speed pitch regulated 5MW 3 bladed machine [62]. Both wind turbines have a monopile as support structure.

Shaft damping

The movement of the tower shaft through air will, due to the viscosity of air, result in a force opposite to the movement. So, also the shaft will experience aerodynamic damping. Due to the small density of air this effect is very small [63].

Hydrodynamic damping

The viscosity of water leads, via the drag force, to hydrodynamic damping when the support structure moves with respect to the wave. When structural velocities in the submerged part are low (for relative stiff support structures) hydrodynamic damping can be neglected.

If the structural motion is taken into account the Morison equation has to be adapted. The velocity term u is replaced by the relative velocity $u - \dot{x}$ and the acceleration $\dot{u}$ by the relative acceleration $\dot{u} - \ddot{x}$. The resulting equation is called the relative Morison equation [37]:

$$q = \frac{dF}{dz} = C_M \rho \frac{\pi D^2}{4} \dot{u} - C_A \rho \frac{\pi D^2}{4} \ddot{x} + C_D \frac{1}{2} \rho D |u - \dot{x}|(u - \dot{x}) \qquad \text{(A.37)}$$

with:

$\dot{x}$	velocity of the structure	[m/s]
$\ddot{x}$	acceleration of the structure	[m/s^2]
C_A	added water mass coefficient (=$C_M - 1$)	[-]

1. The first term is the inertia contribution, which is equal to equation (A.19)
2. The 2nd term represents the so called water added mass force. When the structure moves the ‘attached’ water causes a force. When the water velocity is equal to zero the added water mass is equal to the weight of the displaced volume:

$$m' = \frac{1}{4} \pi D^2 \cdot \rho \qquad \text{(A.38)}$$

with:

m'	added water mass (circular structure)	[kg/m]

In that case C_M is equal to 1. When the body moves in water with a certain velocity the amount of added water mass increases, because C_M is larger than 1 for $u > 0$ m/s.

3. The third term is the (nonlinear) drag term. This force causes hydrodynamic damping, because it contains terms proportional to $\dot{x}$, see equation (A.37).

When inserted in the equation of motion, see equation (A.27), the next appears:

$$m\ddot{x} + c\dot{x} + kx = \int_{-d}^{\eta} q dz = F(t) \tag{A.39}$$

When structural motions are small, the non-linear drag term can be linearized, this leads to [59]:

$$q = \frac{dF}{dz} = C_M \rho \frac{\pi D^2}{4} \dot{u} - C_A \rho \frac{\pi D^2}{4} \ddot{x} + C'_D \rho (D/2)(u - \dot{x}) \tag{A.40}$$

where:

$$C'_D = C_D |u - \dot{x}| \tag{A.41}$$

with:

C'_D	dynamic drag coefficient (≈0.1-0.25 C_D [55])	[-]

By combining equations (A.42), (A.43) and (A.44), the resulting hydrodynamic drag term is found to be [59]:

$$c_{hd} = C'_D \frac{\rho D}{2} l \tag{A.45}$$

with:

l	length of submerged part of the structure	[m]

Also [25] prescribes an analytical expression for the hydrodynamic damping.
In [63] a critical damping value of 1% is found for a monopile structure.

Soil damping

This type of damping is introduced by internal soil friction and radiation of vibration energy, where the latter influence is most important for a GBS. For a GBS soil damping is in the order of 1% of critical damping for bending [21].

Cumulative damping values

Taking all the individual damping values into account a conservative damping estimate (as a percentage of the critical damping) is:

- Non-operating: 0.5% (structural) + 0.1% (hydrodynamic) + 1% (soil) = 1.6%
- Operating: 1.6% + 4% (aerodynamic) = 5.6%

>>BAM Van Oord case study – Damping influence [Appendix B]

The influence of the damping is calculated with aid of the DAF graph. When 4% aerodynamic damping is taken into account the damping value ζ is assumed to increase from 0.01 to 0.05.

Due to the increase in damping the structural response (bending moment) will reduce. The magnitude depends on ratio between the forcing frequency and the natural frequency.

For example (see Figure B.5):

- For a wave of T = 2s ($\omega > \omega_n$) aerodynamic damping leads to a reduction in bending stress response of 0% (leading to a reduction in fatigue load of 1%)
- For a wave of T = 4s ($\omega = \omega_n$) on the other hand aerodynamic damping leads to a reduction in bending stress response of about 30% (leading to a reduction of fatigue load of 100%)

For the FLS a full fatigue calculation has to be performed in order to predict the influence of aerodynamic damping. This has to with the fact that the distribution of the fatigue load per wave category plays an important role.

For the ULS the wind turbine will probably be turned off, so no aerodynamic damping is available.

Appendix B CASE STUDY CORRESPONDING TO CHAPTER 3

N.b. This case study is only used as support for the examples of Appendix A.4.

B.1. PARAMETERS

A schematisation of the offshore wind turbine is given in Figure B.1.

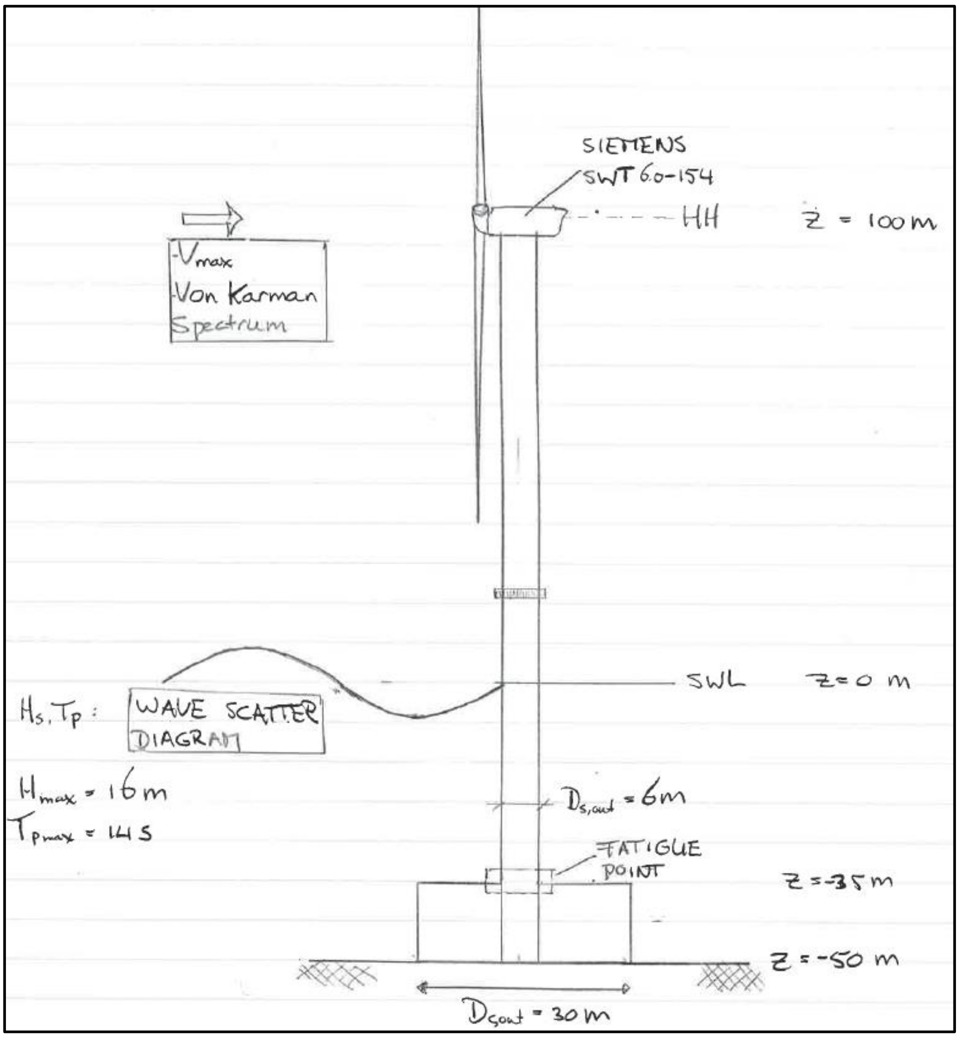

Figure B.1 – Schematisation of the offshore wind turbine for the case study in this section.

Below the parameters of the offshore wind turbine are listed.

Structural parameters							
Caisson				**Turbine**			
outer diameter	$D_{c,out}$	30	m	type		SWT-6.0-154	
wall height	H_{wall}	15	m	rotor diameter	D_{rotor}	154	m
				disk area	A_{disk}	18627	m^2
				hub height	H_h	100	m
Shaft				cut-in velocity	V_{cut-in}	3	m/s
outer diameter	$D_{s,out}$	6	m	rated velocity	V_{rated}	12	m/s
wall thickness	t_s	0.07	m	cut-out velocity	$V_{cut-out}$	25	m/s
inner diameter	$D_{s,in}$	5.86	m	no of blades	N	3	-
cross sectional area	A	1.30	m^2				
area moment of inertia	I_y	5.73	m^4	$I_y=(\pi/64)*(D_{s.out}^4-D_{s.in}^4)$			
section modulus	W_y	1.91	m^3	$W_y=I_y/(D_{s;out}/2)$			
				$V_{tot}=m_{b;s}/\rho'_{s;ballast}$			
Masses							
mass turbine	m_t	350	t				
mass shaft tower	$m_{s;tower}$	1017	t	mass ballast;sand	$m_{b;s}$	8050	t
mass shaft GBS	$m_{s;GBS}$	509	t	filled volume	V_{tot}	8944	m^3
mass caisson (empty)	m_{ce}	5750	t	mass water	$m_{b;w}$	8944	t
Total structural weight		7626	t	Total ballast		16994	t

Additonal parameters							
gravitational accelerleration	g	9.81	m/s^2	steel quality		S355	
mass density steel	ρ_s	7800	kg/m^3	yield strength	f_{yd}	355	N/mm^2
mass density seawater	ρ_{ws}	1025	kg/m^3		f_{yd}	355	Mpa
mass density air	ρ_a	1.225	kg/m^3				
mass density sand (saturate	ρ_{sand}	2400	kg/m^3				
mass density ballast sand (s	$\rho_{s;ballast}$	1900	kg/m^3				
elasticity of steel	E	210000	N/mm^2				
elasticity of steel	E	210	GPa				

B.2. BOUNDARY CONDITIONS

With respect to the boundary conditions the parameters are as below. For the waves a wave-scatter diagram is used. This wave scatter diagram is deduced for the Beatrice offshore wind farm. It is assumed that it can be used for a water depth of 50 m. The results are achieved by measurements.

The case study is performed for the ULS and the FLS_{AV} ('average' FLS condition). Safety factors are not taken into account.

Boundary conditions							
Soil				**Waves**			
water depth	d	50	m	significant wave height	H_s	2	m
				peak period	T_p	5	s
Wind				extreme wave height $_{(1/50y)}$	H_{max}	16	m
max wind speed 10m	$V_{10m,3s,50}$	45	m/s	peak period	$T_{p;max}$	14	s
max wind speed 100m	$V_{100m,3s,5}$	53	m/s				

Load cases

	FLS_{AV}	ULS	
H	2	16	m
T	5	14	s
V_{100m}	12	53	m/s

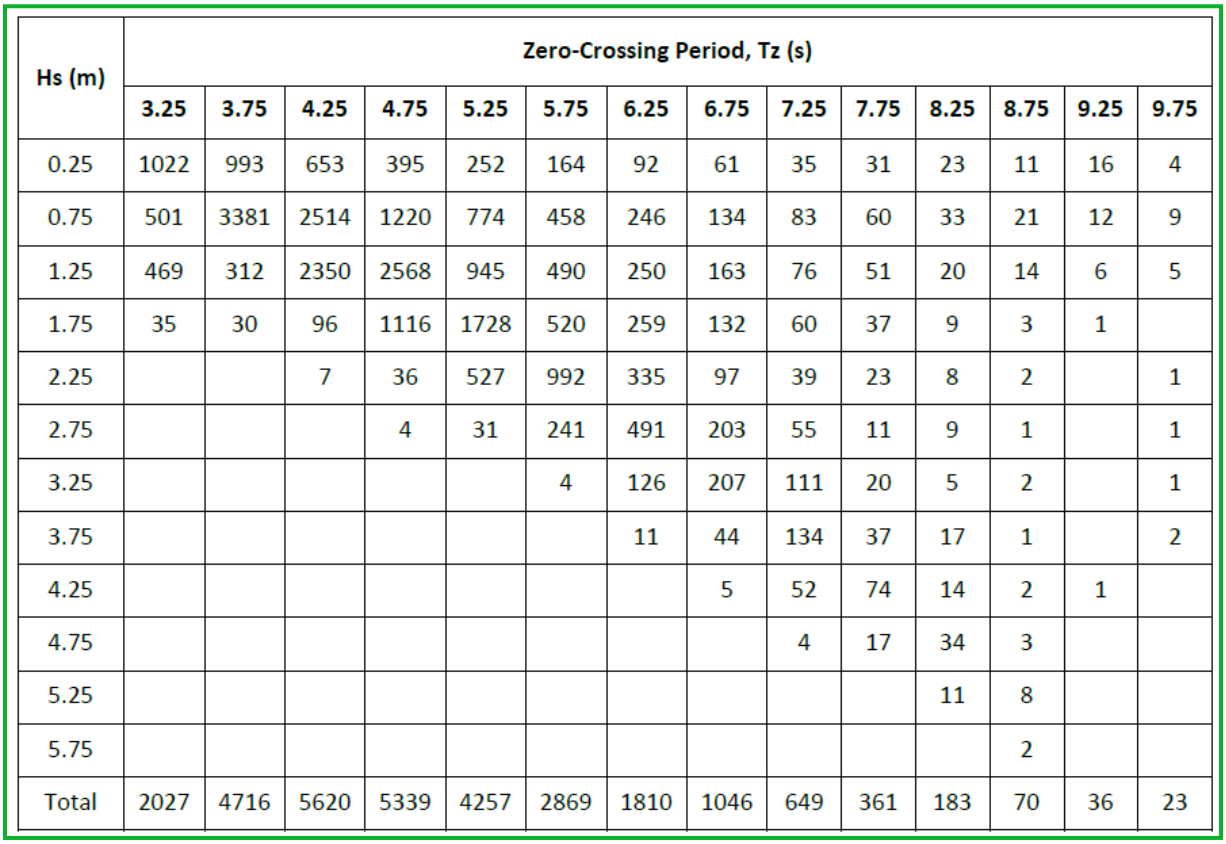

Hs (m)	Zero-Crossing Period, Tz (s)													
	3.25	3.75	4.25	4.75	5.25	5.75	6.25	6.75	7.25	7.75	8.25	8.75	9.25	9.75
0.25	1022	993	653	395	252	164	92	61	35	31	23	11	16	4
0.75	501	3381	2514	1220	774	458	246	134	83	60	33	21	12	9
1.25	469	312	2350	2568	945	490	250	163	76	51	20	14	6	5
1.75	35	30	96	1116	1728	520	259	132	60	37	9	3	1	
2.25			7	36	527	992	335	97	39	23	8	2		1
2.75				4	31	241	491	203	55	11	9	1		1
3.25						4	126	207	111	20	5	2		1
3.75							11	44	134	37	17	1		2
4.25								5	52	74	14	2	1	
4.75									4	17	34	3		
5.25											11	8		
5.75												2		
Total	2027	4716	5620	5339	4257	2869	1810	1046	649	361	183	70	36	23

Figure B.2 – Wave-scatter diagram for the Beatrice wind farm [10]

B.3. WIND LOADS

With aid of some given wind turbine characteristics and basic theory of wind turbines (see Appendix A.3) the total axial force could be calculated. However, the behaviour of a wind turbine is rather complex and such a model could only be used as a first approximation. The axial force found was about 850 kN. In addition a shaft load of about 50 kN was found.

In comparison: the maximum horizontal force at 90 m below hub height, provided by the wind turbine manufacturer, is equal to 2300 kN [10]. This is including a partial safety factor of 1.35, so the actual value is 1700 kN. This is twice as much, but is should be noted that the force provided by the manufacturer is the resulting dynamic force (taking into account the movement of the top mass). For further applications the resulting forces provided by the wind turbine manufacturer are used.

Wind load					
Loading frequencies			$f_{Np}=N\lambda V/2\pi R$		
Tip speed ratio			λ	8	-
V	V	f_{1p}	f_{3p}		
-	[m/s]	[Hz]	[Hz]		
Vcut-in	3	0.05	0.15		
Vrated	12	0.20	0.60		

B.4. WAVE LOADS

B.4.1. Wave parameters

The wave length can be determined with the next equation:

$$L = \frac{gT^2}{2\pi}\tanh(kd) \tag{B.1}$$

with:

L	wave length	[m]
T	wave period	[s]
k	wave number (=$2\pi/L$)	[1/m]
d	water depth	[m]

Due to the fact that the parameter L is as well left as right from the = sign, the wave length has to be solved iteratively. The table below gives the results for two types of waves.

Wave length Tool				
	H	2	16	m
amplitude	a	1	8	m
	T	5	14	s
wave length	L	39	257	m
	L/d	0.78	5.14	-
angular frequency	ω	1.257	0.449	1/s
wave number	k	0.161	0.024	1/m
	k*d	8.055	1.222	-
	n	0.500	0.714	-
	Type	deep	intermediate	

B.4.2. (Non)linear waves

With respect to fatigue loads (FLS) due to waves there is a whole range of wave heights and periods to be taken into account. For the ULS only the extreme wave is taken into account.

The validity of a certain wave theory is checked with

Wave theory FLS				
	FLS		FLS_{AV}	ULS
	min	max		
d/gT^2	0.054	0.483	0.204	0.026
H/gT^2	0.0003	0.017	0.008	0.008

For the FLS waves have to be treated with Stokes' 5th order wave theory or stream function 3. The extreme wave (ULS) has to be treated with a 5th order stream function.

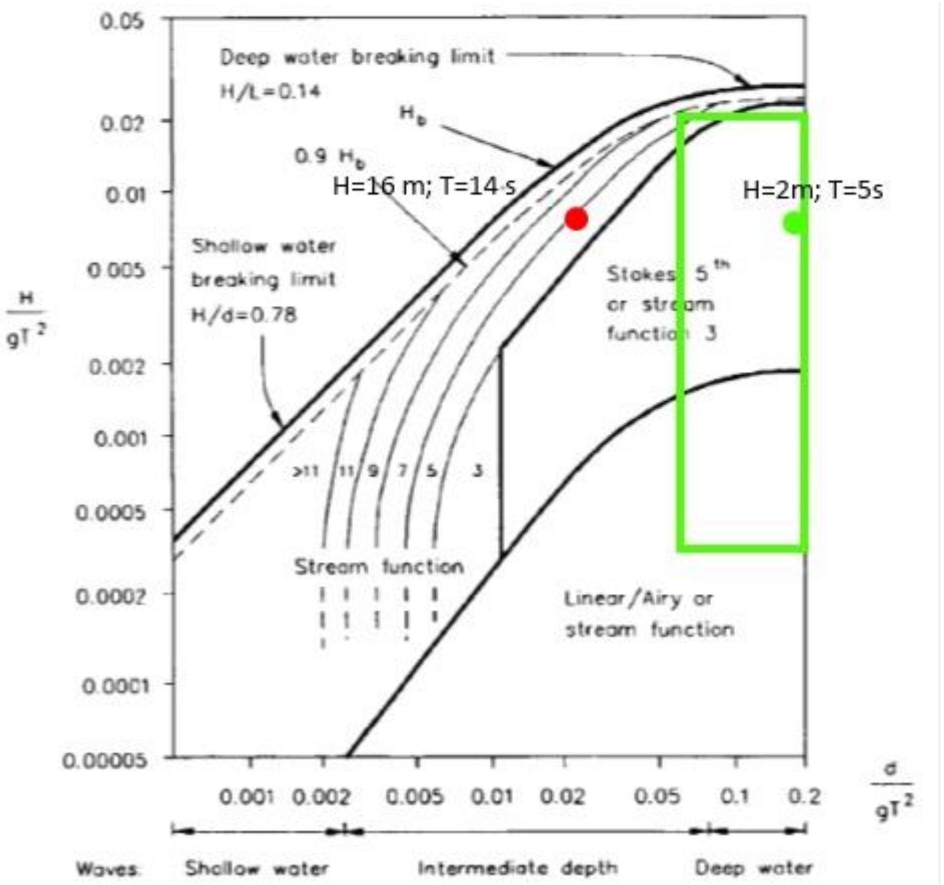

Wave theory FLS				
	FLS		FLS_{AV}	ULS
	min	max		
d/gT^2	0.054	0.483	0.204	0.026
H/gT^2	0.0003	0.017	0.008	0.008

Figure B.3 – Ranges of suitability of regular wave theories (d= water depth, g= gravity acceleration, H = wave height, L = wave length, T = wave period), green = lifetime, red = extreme [21]

Below in the wave scatter diagram the values for H/gT^2 are calculated. By calculating d/gT^2 for each column and the maximum value for H/gT^2 from the cases where waves are non-linear can be determined. The red cells correspond with the non-linear cases.

Wave theory FLS				
	FLS		FLS_{AV}	ULS
	min	max		
d/gT^2	0.054	0.483	0.204	0.026
H/gT^2	0.0003	0.017	0.008	0.008

If follows that in about 90% of the time waves are non-linear. Only some small waves with a high period can be treated with linear wave theory. So it can be stated that the linear wave theory is not valid.

H/gT^2	Zero Crossing period Tz (s)													
Hs (m)	**3.25**	**3.75**	**4.25**	**4.75**	**5.25**	**5.75**	**6.25**	**6.75**	**7.25**	**7.75**	**8.25**	**8.75**	**9.25**	**9.75**
0.25	0.0024	0.0018	0.0014	0.0011	0.0009	0.0008	0.0007	0.0006	0.0005	0.0004	0.0004	0.0003	0.0003	0.0003
0.75	0.0072	0.0054	0.0042	0.0034	0.0028	0.0023	0.0020	0.0017	0.0015	0.0013	0.0011	0.0010	0.0009	0.0008
1.25	0.0121	0.0091	0.0071	0.0056	0.0046	0.0039	0.0033	0.0028	0.0024	0.0021	0.0019	0.0017	0.0015	0.0013
1.75	0.0169	0.0127	0.0099	0.0079	0.0065	0.0054	0.0046	0.0039	0.0034	0.0030	0.0026	0.0023	0.0021	
2.25			0.0127	0.0102	0.0083	0.0069	0.0059	0.0050	0.0044	0.0038	0.0034	0.0030		0.0024
2.75				0.0124	0.0102	0.0085	0.0072	0.0062	0.0053	0.0047	0.0041	0.0037		0.0029
3.25						0.0100	0.0085	0.0073	0.0063	0.0055	0.0049	0.0043		0.0035
3.75							0.0098	0.0084	0.0073	0.0064	0.0056	0.0050		0.0040
4.25								0.0095	0.0082	0.0072	0.0064	0.0057	0.0051	
4.75									0.0092	0.0081	0.0071	0.0063		
5.25											0.0079	0.0070		
5.75												0.0077		

B.4.3. Validity Morison equation

The Keulegan-Carpenter number, see equation (5.3), determines the relative contribution of inertia and drag forces.

For high KC numbers the drag force is dominant, while for low values the inertia force is dominant.

The parameter $\pi D/L$ stands for the relative size of the structure. The next applies:

$$\frac{D}{L} < 0.2 \text{ slender structure: Morison equation}$$

$$\frac{D}{L} > 0.2 \text{ compact structure: Diffraction theory}$$

In Figure B.4 both parameters are plot for the ULS and FLS wave. For the ULS case the KC number can be calculated with the simplified expression for deep water. For the FLS case the maximum horizontal particle velocity is used.

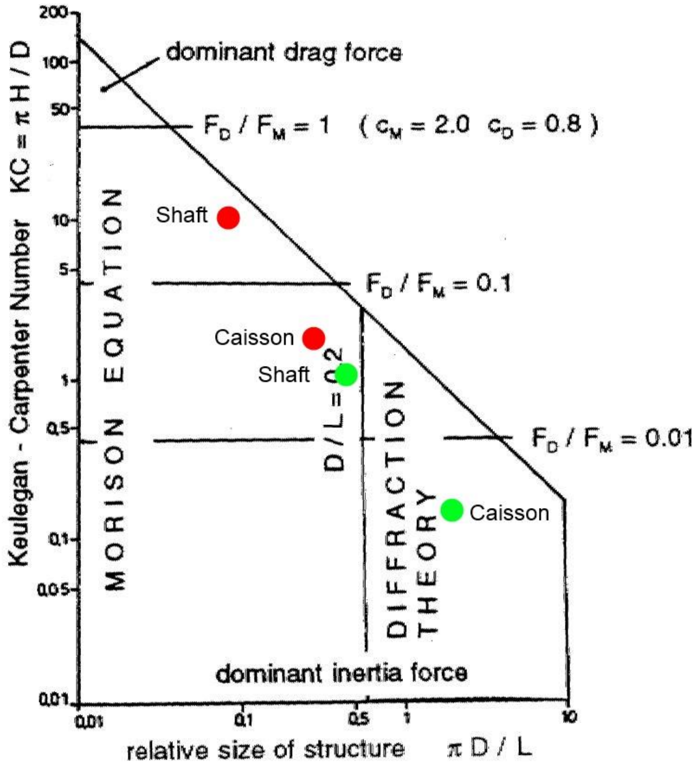

Figure B.4 – Influence of drag, inertia and diffraction per region, green = FLS$_{AV}$, red = ULS [21]

Validity Morison Equation

	Lifetime		Extreme	
	Shaft	Caisson	Shaft	Caiss
KC = πH/D	1.0	0.2	10.0	2.0
Rel size	0.5	2.4	0.1	0.4

deep water [T<√(d/0.08g)]	T<	8.01	s	occurence (from wave	p	0.99	-
Mor. shaft deep [T>√(D/0.312	T>	4.39	s	occurence scatter diagram)	p	0.57	-
Mor. caissoin deep	T>	9.81	s	occurence	p	0.00	-
drag >5% shaft [H>1D/π]	H>	1.91	m	occurence	p	0.14	-
drag >10% shaft [H>5D/π]	H>	9.55	m	occurence	p	0.00	-

B.4.3.1. Validity of the Morison equation

- From the figure it can be concluded that the Morison equation is valid for the ULS.
- For the FLS the significant wave height just fits in the region where Morison is valid. But waves with a smaller wave length cannot always be treated with Morison any more.

  For a water depth of 50 m waves can be seen as deep water waves for T<8 sec ($d/gT^2=0.08$). This situation occurs 99% of the time (from wave scatter diagram). The corresponding wave length can be calculated with $L=1.56T^2$.
  - Shaft: when given that Morison is only valid for D/L<0.2 this corresponds to T>4.4 s for the shaft. This occurs in about 60% of the cases, so in about 40% of the cases the Morison equation is not valid and diffraction should be taken into account for the shaft. It should be noted that Morison is only invalid for smaller

waves (T<4.4 s) with a corresponding low wave height. It should be checked whether these waves give a large contribution to the fatigue load.

  - Caisson: for the caisson Morison is valid for T>9.8 s, this situation has a probability of occurrence of 0%. So, for the caisson the Morison equation is invalid and diffraction theory has to be applied.

B.4.3.2. Influence of drag

The influence of drag becomes significant for KC>1 (from thereon the influence of drag is >5%). So, for H>1D/π the influence of drag should be taken into account.

- For the shaft (FLS) this situation has a probability of occurrence of 0.15. A drag influence >10% (H>5D/π) has a probability of occurrence of nearly 0. So, it can be stated that the drag influence can be left out of the Morison equation for the FLS.
- For the shaft in ULS the drag force is about ½ the inertia force (see Figure B.4). This cannot be neglected, although the maximum force is, due to the phase lag, fully determined by the inertia force.

B.4.4. Wave forces (GBS, z=-50 m till water level)

In this example the full Morison equation is applied to the simplified GBS structure (instead of a steel shaft only). Basics for the calculation are:

- The wave force for the caisson (-50 till -35 m) and the wave force for the shaft (-35 till η m) are calculated separately.
- The velocity profile remains the same. So, it is expected that the increasing diameter will cause an increase is.
- Wheeler stretching is applied to find the forces up to the crest level.
- Both inertia and drag forces are taken into account.

The drag and inertia coefficients are assumed to be:

Coefficients Morison equation

		shaft	caisson
KC_{max}		10.0	2.0
drag coefficient	C_D	1.2	1.2
inertia coefficient	C_M	1.7	2.0

The resulting forces and bending moments are:

Wave forces (GBS, from bottom to water level)

Case: shaft + caisson, z=η..-50 m

	FLS; z=-50 m					ULS; z=-50 m				
	Force [kN]	% -	Moment [kNm]	% -	Arm [m]	Force [kN]	% -	Moment [kNm]	% -	Arm [m]
Shaft;$_{z=H\ till\ -35m}$	566	92.0%	2.2E+04	98%	39	3286	12.5%	1.2E+05	40%	35
Caisson;$_{z=-35\ till\ -50m}$	49	8.0%	4.8E+02	2%	9.8	22983	87.5%	1.7E+05	60%	7.6
Total	6.2E+02		2.2E+04			2.6E+04		2.9E+05		

It follows that the maximum horizontal wave force is 26 MN. It can clearly be seen that the largest part of the force acts on the caisson (~90%). The inertia force also here plays a dominant role. The bending moment is also calculated. Although the force on the shaft is relative small the influence on the bending moment is significant.

B.4.5. Lifting frequency

The natural frequency (f_{nat}) is assumed to be about 0.25 Hz.

Lifting force				
Strouhal number	S	0.3	-	f_s=uS/D
Horizontal particle velocity	u	4.27	m/s	
Vortex shedding frequency	f_s	0.21	Hz	
Ratio	f_s/f_n	0.85	-	

B.4.6. Wave breaking

The impact force due to wave breaking depends on the breaking type. Under the assumption that the bottom is almost flat a spilling breaker will occur.

For such a breaker the impact force can be calculated with the equation below. The slamming coefficient can roughly vary between 1 and 5, here a value of 4 is chosen. The particle velocity is assumed to be equal to the horizontal particle velocity of a wave at SWL. The impact force is assumed to act at a height H_{max} (z=-8..8 m +SWL).

Wave breaking				$\xi_{br}=\tan(\alpha)/\sqrt{(H\infty/L\infty)}$	$f=0.5\rho C_s D u^2$		
Deep water wave height	$H\infty$	16	m	Slamming coefficient	C_s	4	-
Deep water wave length	$L\infty$	306	m	Particle velocity	u	4.27	m/s
Slope	$\tan(\alpha)$	1.0E-02	-	Impact force	f	225	kN/m
Breaking parameter	ξ_{br}	0.04	-	Force wave impact	F	3592	kN
Breaking type		spilling	-	Force non-breaking	F	1500	kN

In addition the wave force resulting from a non-breaking wave is calculated to compare the magnitude. It follows that a breaking wave doubles the wave impact at this section.

B.5. (AERODYNAMIC) DAMPING INFLUENCE

The influence of the aerodynamic damping on the fatigue load depends on the forcing frequency. When 4% aerodynamic damping is taken into account the damping value ζ is assumed to increase from 0.01 to 0.05.

With the aid of section A.4.5.2 the DAF is calculated for the two different damping values. For different forcing frequencies (waves with T=2..14 s) the reduction in the DAF is calculated (Figure B.5).

Influence of damping

S-N slope m 5 -

$\Delta\sigma \sim \Delta H(\omega)$

$D_{fat} \sim \Delta\sigma^m$

						H(ω)				
						ζ	ζ	$\Delta\sigma$	D_{fat}	ΔD_{fat}
				f [Hz]	ω/ω_n	0.01	0.05	% of origin	% of origin	reduction
wave	T=	14	s	0.07	0.28	**1.087**	**1.087**	100%	100%	0%
	T=	13	s	0.08	0.30	**1.102**	**1.102**	100%	100%	0%
	T=	12	s	0.08	0.33	**1.122**	**1.122**	100%	100%	0%
	T=	11	s	0.09	0.36	**1.149**	**1.148**	100%	100%	0%
	T=	10	s	0.10	0.40	**1.186**	**1.185**	100%	99%	1%
	T=	9	s	0.11	0.44	**1.241**	**1.239**	100%	99%	1%
	T=	8	s	0.13	0.50	**1.325**	**1.323**	100%	99%	1%
	T=	7	s	0.14	0.57	**1.472**	**1.467**	100%	98%	2%
	T=	6	s	0.17	0.66	**1.774**	**1.763**	99%	97%	3%
	T=	5	s	0.20	0.79	**2.690**	**2.633**	98%	90%	10%
	T=	4	s	0.25	0.99	**37.524**	**9.931**	26%	0%	100%
	T=	3	s	0.33	1.32	**1.339**	**1.320**	99%	93%	7%
	T=	2	s	0.50	1.98	**0.341**	**0.341**	100%	99%	1%

Due to the shape of the S-N curve, a small reduction of the stresses gives a larger reduction in the fatigue load ($D_{fat} \sim \Delta\sigma^m$, where m is the slope of the S-N curve).

It follows that the reduction in stresses $\Delta\sigma$ due to the increase in damping is in general small, except from the forcing frequencies near the natural frequency.

The reduction of the total fatigue load will strongly depend on the distribution of the fatigue load per wave category. If the categories with 4<T<6 contribute a lot to the fatigue damage (and especially around T=4 s), a large reduction can be gained.
A full fatigue analysis should be performed in order to predict the influence of aerodynamic damping on the total fatigue load.

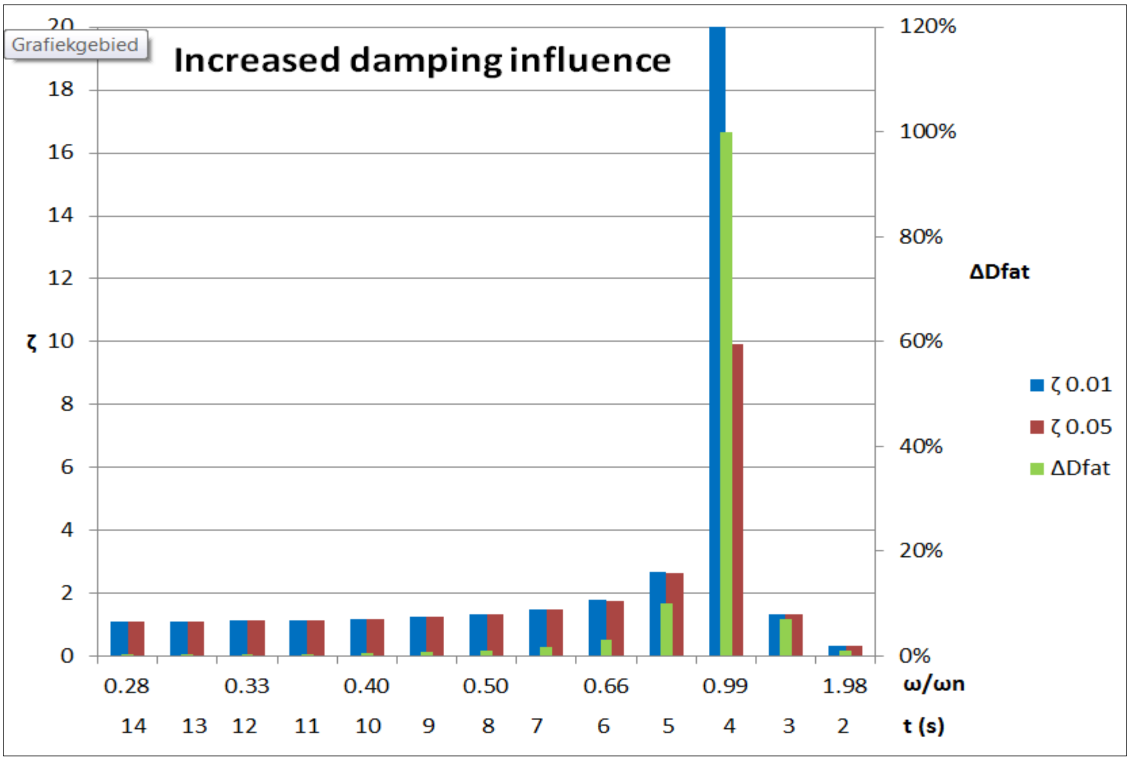

Figure B.5 – DAF graph for different damping values

Appendix C **FINLAB**

C.1. **PHYSICAL PROCESSES**

C.1.1. Flow around a cylinder

When water streams around a cylinder two regions can be distinguished:

- The boundary layer (thickness small with respect to diameter D)
- The wake region (length comparable with D)

The Re number is best to describe the flow around a cylinder. In general:
For very small Re numbers (Re<5) no separation occurs and the flow is completely laminar.
For higher number(Re>40) vortex shedding occurs, first leading to a laminar wake and boundary layer (see Figure C.1). For higher Re numbers the wake becomes turbulent. The flow changes from subcritical to supercritical when the boundary layer becomes turbulent instead of laminar.
Very high Re numbers (Re>4e6, so called trans-critical flow) lead to a completely turbulent boundary layer and wake.

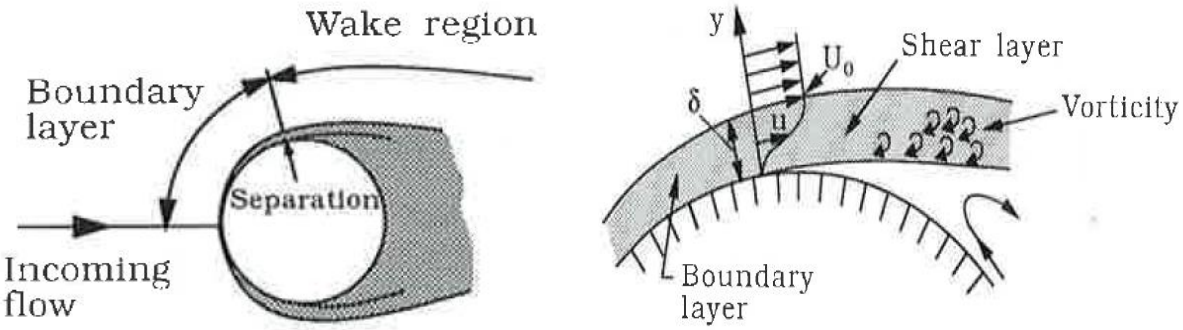

Figure C.1 – Flow around a cylinder [25]

Separation occurs due to the divergent geometry of the flow at the rear side of the cylinder. The difference in water velocity between the boundary layer and the velocity in at the rear of the cylinder leads to vorticities. At both sides of the cylinder vortices will develop. One vortex grows larger than the other, leading to the so called effect of vortex shedding. This effect lead to the lift force perpendicular to the flow direction.

In this thesis for all the flows around the shaft the Re number is > 3e6 (u_max_min~0.3 m/s; D=6m) . So in almost every case the flow is trans-critical.

C.1.2. Forces due to flow

Flow around a cylinder leads to two force contributions:

- Pressure force (caused by a pressure difference between the front and rear of the cylinder). The pressure force is related to the separation angle [25]:
    - Subcritical flow: large negative pressure area
    - Supercritical flow: small negative pressure area
    - Transcritical flow: medium negative pressure area
- Friction force (cause by wall friction)

Both forces lead to the so called drag force:

$$F_D = \frac{1}{2}\rho C_D D u|u|$$

For Re>1e4 the friction drag is small with respect to the total drag (< 2-3%).

C.1.3. Oscillatory flow around a cylinder

For oscillatory flows the Keulegan-Carpenter number (KC number) describes the way the flow behaves. For very small KC numbers (hardly any motion), separation behind the cylinder may not even occur (leading to the same flow pattern as Re<5). For an increase in KC number about the same happens as for an increase in Re number for steady current:

- For about KC>1.5 vortices develop
- For about KC >7 vortex shedding starts to occur

For different ranges (7<KC<15, 15<KC<24 etc) one can distinguish different vortex shedding regimes.
Very high KC numbers on the other hand resemble the flow experienced in steady current for each half period.

C.1.4. Forces due to oscillatory flow

For oscillatory flow in addition to the drag force the next forces occur:

- Hydrodynamic mass force (resistance against movement, inertia)
- Froude-Krylov force (pressure gradient due to accelerated motion of the fluid in the outer-flow region)

Both forces form the so called 'inertia force':

$$F_M = \quad \rho C_m A\dot{u} \quad + \quad \rho A\dot{u}$$

Hydro-dynamic mass

Froude-Krylov force

C.1.5. The Morison equation

By defining a new coefficient, C_M, by

$$C_M = C_m + 1$$

With: C_m=added mass coefficient
The so called Morison equation arises:

$$F = F_D + F_M = \frac{1}{2}\rho C_D D u|u| + \rho C_M A\dot{u}$$

From potential flow theory follows that C_M=2 for a circular cylinder for low KC number. This means that an imaginary volume of twice the water volume of the cylinder is accelerated during movement.

The values for C_D and C_M were found experimentally. Both coefficients are dependent of:

- Re number
- KC number

- k/D (roughness)

Further the next influences play a role:

- Influence of current
- Angle of attack (for a sloping cylinder)
- Orbital motion

C.1.6. Validity of the Morison equation

C.1.6.1. Validity according to literature

In literature different statements can be found for the applicability of the Morison equation:

Coastal Engineering Manual [26]:
"The effect of the pile on the wave-induced flow is assumed negligible."(p. VI-249)
"It is apparent that the influence of the pile on the flow field a short distance away from the pile has been neglected." (p. VI-5-251)
"When the size of the solid structure/object is large enough to modify the incident wave field by wave diffraction and/or wave scattering (..)" (p. VI-5-170)

Offshore Hydrodymechanics [27]:
"The ambient water motions in the immediate vicinity of the cylinder are all about the same at any instant in time. This is assumed to be true both horizontally and vertically; the spatial variation in the undisturbed flow near a unit length of cylinder is simply neglected." (p. 12-1)

Comparison of monopile, tripod, suction bucket and gravity base
design for a 6 MW turbine [19]:
"For slender structures the presence of the structure can be ignored when calculating the water particle kinematics."

All the statements above are consequences of the diffraction effect as described in the following section.

C.1.6.2. Basic principle of the Morison equation

The Morison equation is nothing but a coupling between the wave kinematics at a distance far away from a cylinder and the forces on that cylinder, see Figure C.2.
When a wave 'hits' a structure, always some reflection will occur. For slender structures this effect can be neglected. For these cases the Morison equation is valid.
However, for compact structures the effects of reflection cannot be neglected anymore. The diffracted wave of Figure C.2 will interact with the 'original' wave near the cylinder.
When these effects start to play a role the force cannot be predicted with the aid of the Morison equation anymore, but diffraction theory should be applied.

In literature the following ranges for the validity of the Morison equation are given:

- $D/L<0.1\text{-}0.2$ (slender structures)
- $D/h<<1$ (Diameter/waterdepth)

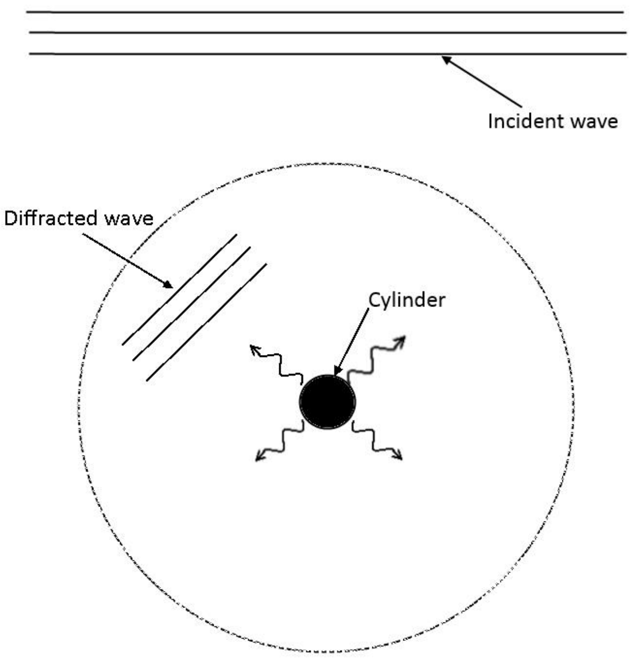

Figure C.2 – Basic principle of the Morison equation and the presence of a diffracted wave.

C.1.7. Determining Coefficients

As said, the values for C_D and C_M were found experimentally. Different methods (like oscilating flows in a U-tube or placing a vertical cylinder in regular waves) exist. Within such an experiment the force on the cylinder is measured. Due to the (often strong) variation of u over the depth, the force for a certain section of the cylinder is measured. Within that section the change in u over such a short distance can be neglected. Data processing gives the link between the wave kinematics and the force. A lot of test were performed by Sarpkaya for $10^4 < Re < 10^6,\ 0 < KC < 100$ and varying roughness (see Fig 1 and 2).

Design codes like Det Norske Veritas (DNV) and the American Petroleum Institute (API) prescribe certain values for design, see Figure C.3 - Figure C.5. Comparison of the coefficients show that there is little agreement on exact values. Differences up to 40% can be found for a specific flow situation [27]. This difference is caused by experimental inaccuracy, like different model set-ups methods of data-processing. However, for extreme wave conditions the difference are generally less. For these conditions the Re number is often very high (>1e6). From the experiments it appears that the data tends to converge for these high Re numbers.

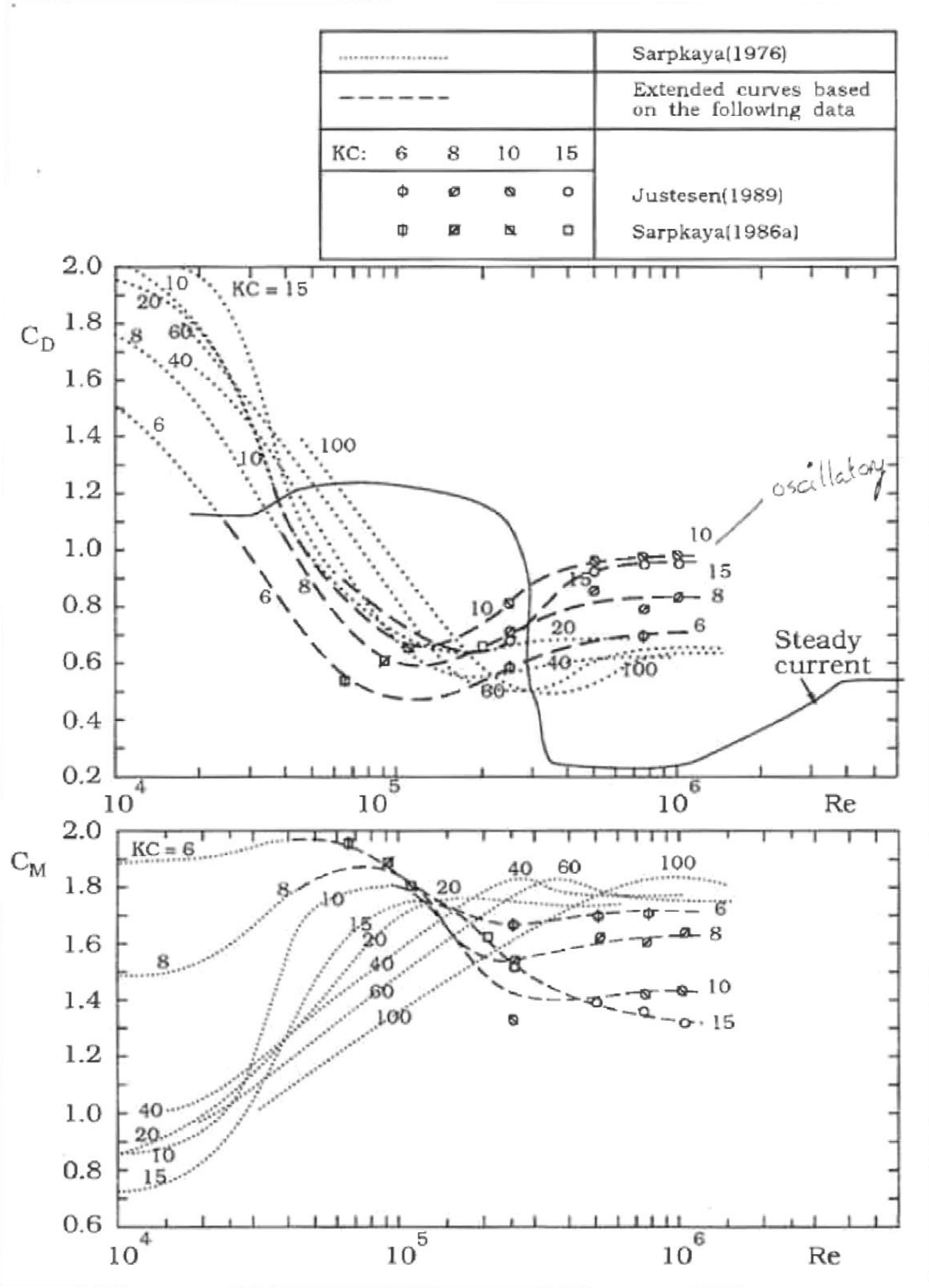

Figure C.3 - Variation of coefficients for a smooth cylinder as function of Re and KC number, based on Sarpkaya [25].

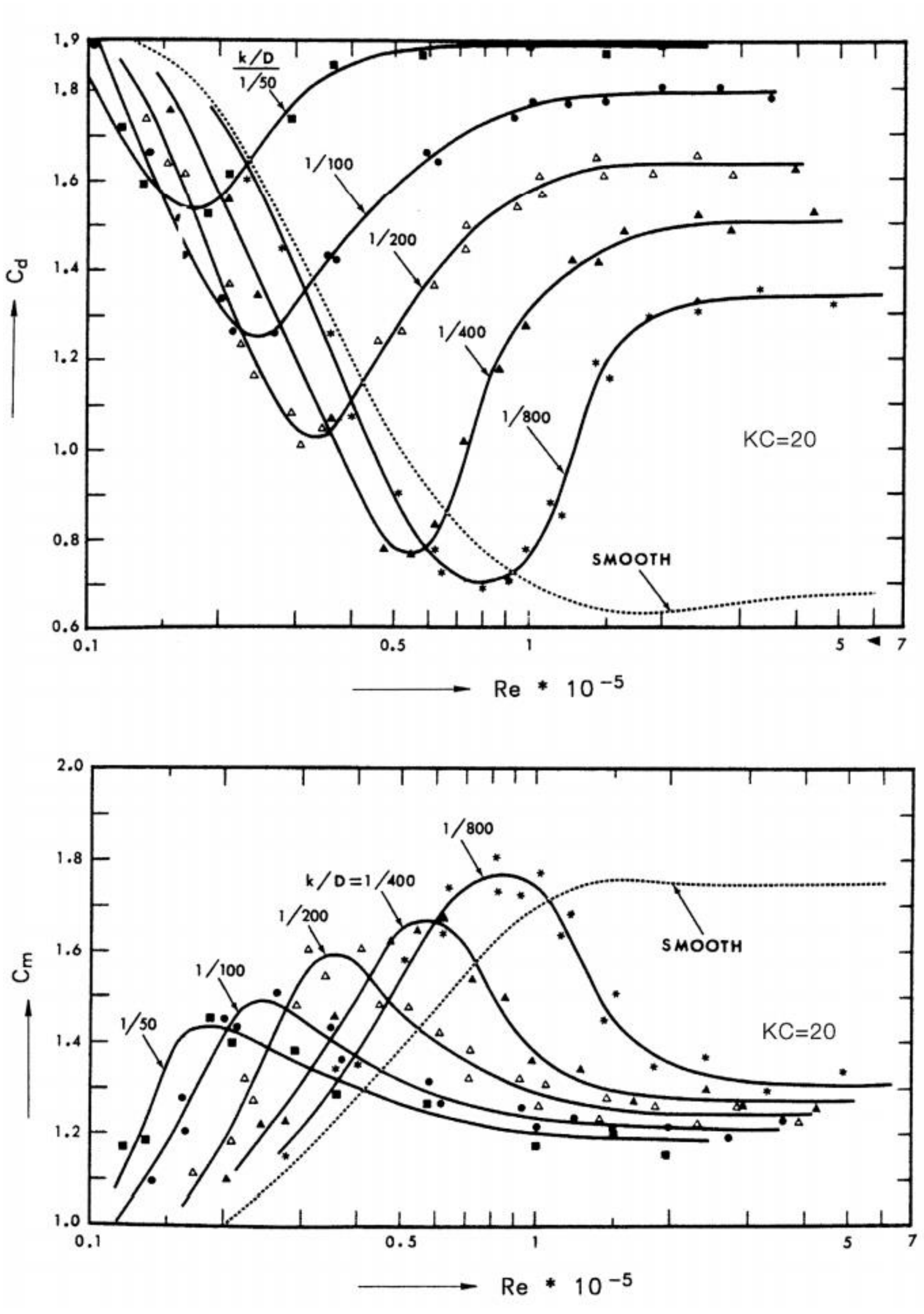

Figure C.4 - Variation of coefficients for a smooth cylinder as function of Re and roughness, based on Sarpkaya [64].

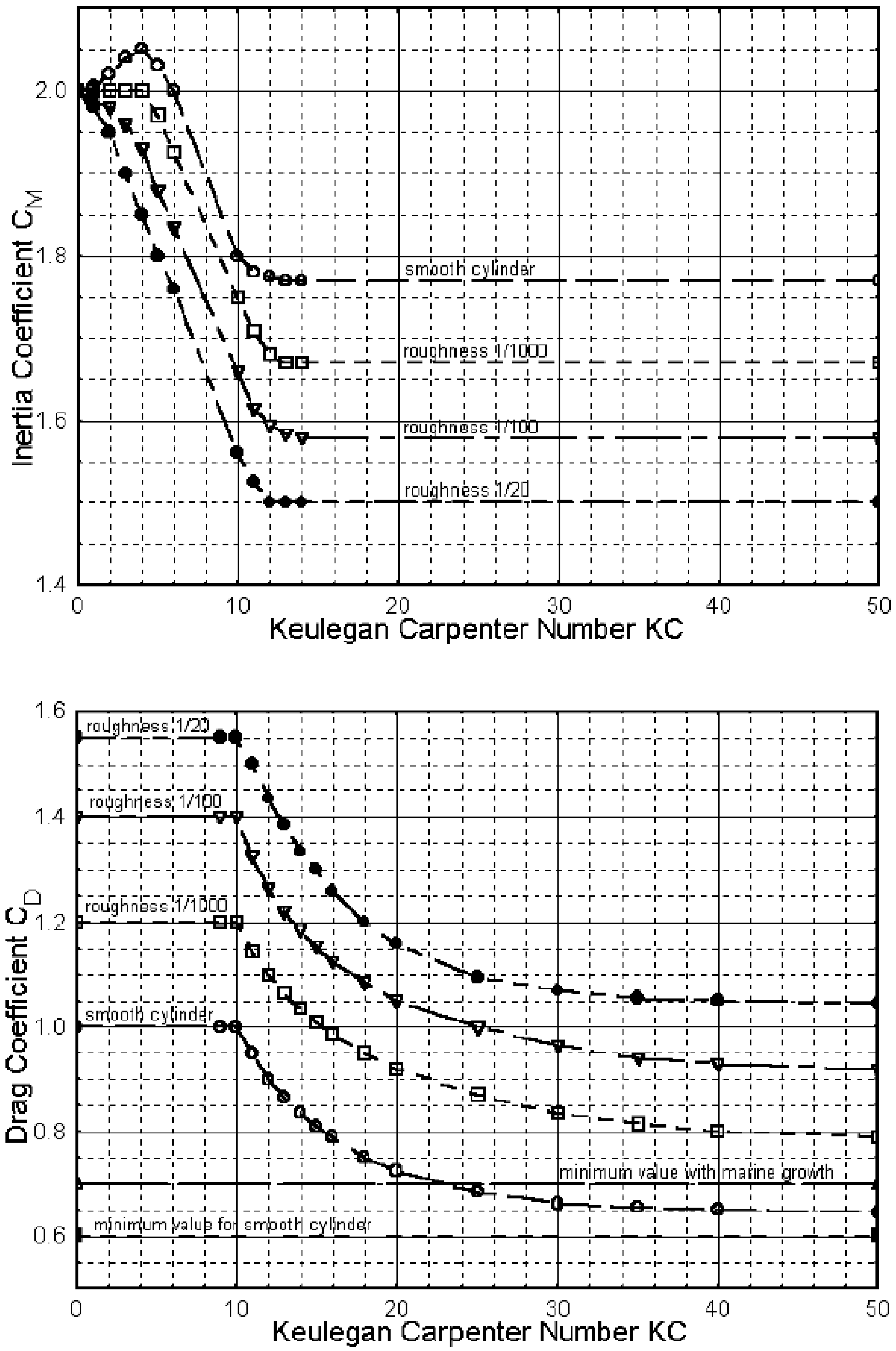

Figure C.5 - Prescribed values for a cylinder as function of Re and roughness [27].

C.2. FINLAB INPUT

C.2.1. Grid

C.2.1.1. Grid description

The 3D grid was created by stacking multiple 2D layers on top of each other with a vertical layer distance in the order of 2m.

For every case the 2D grid (Figure C.6) has the following characteristics:

- 48 cells around the circumference of the cylinder
- An unscaled radius of R=3000m (see Figure C.8)
- A maximum cell size dS_{max} (see Figure C.7)

Note that original grid is scaled (with a factor R/r) in order to obtain a grid with a smaller radius r (in the order of 100 m).

Resolution demands require about 40 cell sizes per wave length. Based on the following indications a combination of dS_{max} and grid radius r is chosen:

- The maximum cell size dS_{max} shall be smaller than 1/40 of the wave length
- The perimeter of the structure shall contain at least 40 grid cells
- The radius of the grid (r) is > ½ L
- The radius of the grid (r) is preferably > $10 \cdot D_{shaft}$

For example: for case 1 the wave length is 217m. This requires:

- r>½ L and > $10 \cdot D_{shaft}$ = 109 m. Chosen radius r=120 m
- dS_{max}<L/40=5.4 m. Chosen: 4m
- With a scale factor R/r=25, the maximum cell size of the unscaled grid is ds_{max}=100 m.

C.2.1.2. SEPRAN file

The input file for SEPRAN is:

```
MESH2D
COARSE(UNIT=1)
POINTS
  P1 = (0,0,10)
  P2 = (76.5,0,10)
  P3 = (0,76.5,10)
  P4 = (-76.5,0,10)
  P5 = (0,-76.5,10)

  P6 = (300,0,25)
  P7 = (0,300,25)
  P8 = (-300,0,25)
  P9 =(0,-300,25)

  P10= (600,0,40)
  P11= (0,600,40)
  P12= (-600,0,40)
```

```
  P13=(0,-600,40)

  P14= (1500,0,80)
  P15= (0,1500,80)
  P16= (-1500,0,80)
  P17=(0,-1500,80)

  P18= (3000,0,100)
  P19= (0,3000,100)
  P20= (-3000,0,100)
  P21=(0,-3000,100)


CURVES
  C1  = CARC1(P2,P3,P1)
  C2  = CARC1(P3,P4,P1)
  C3  = CARC1(P4,P5,P1)
  C4  = CARC1(P5,P2,P1)
  C5  = CURVES(-C4,-C3,-C2,-C1)

  C6 = CLINE1(P2,P6)
  C7 = CLINE1(P3,P7)
  C8 = CLINE1(P4,P8)
  C9 = CLINE1(P5,P9)
  C10 = CARC1(P6,P7,P1)
  C11 = CARC1(P7,P8,P1)
  C12 = CARC1(P8,P9,P1)
  C13 = CARC1(P9,P6,P1)

  C14 = CLINE1(P6,P10)
  C15 = CLINE1(P7,P11)
  C16 = CLINE1(P8,P12)
  C17 = CLINE1(P9,P13)
  C18 = CARC1(P10,P11,P1)
  C19 = CARC1(P11,P12,P1)
  C20 = CARC1(P12,P13,P1)
  C21 = CARC1(P13,P10,P1)

  C22 = CLINE1(P10,P14)
  C23 = CLINE1(P11,P15)
  C24 = CLINE1(P12,P16)
  C25 = CLINE1(P13,P17)
  C26 = CARC1(P14,P15,P1)
  C27 = CARC1(P15,P16,P1)
  C28 = CARC1(P16,P17,P1)
  C29 = CARC1(P17,P14,P1)
```

```
  C30 = CLINE1(P14,P18)
  C31 = CLINE1(P15,P19)
  C32 = CLINE1(P16,P20)
  C33 = CLINE1(P17,P21)
  C34 = CARC1(P18,P19,P1)
  C35 = CARC1(P19,P20,P1)
  C36 = CARC1(P20,P21,P1)
  C37 = CARC1(P21,P18,P1)

SURFACES
  S1 = QUADRILATERAL3(c6,c10,-c7,-c1)
  S2 = QUADRILATERAL3(c7,c11,-c8,-c2)
  S3 = QUADRILATERAL3(c8,c12,-c9,-c3)
  S4 = QUADRILATERAL3(c9,c13,-c6,-c4)

  S5 = QUADRILATERAL3(C14,C18,-C15,-C10)
  S6 = QUADRILATERAL3(C15,C19,-C16,-C11)
  S7 = QUADRILATERAL3(C16,C20,-C17,-C12)
  S8 = QUADRILATERAL3(C17,C21,-C14,-C13)

  S9 = QUADRILATERAL3(C22,C26,-C23,-C18)
  S10= QUADRILATERAL3(C23,C27,-C24,-C19)
  S11= QUADRILATERAL3(C24,C28,-C25,-C20)
  S12= QUADRILATERAL3(C25,C29,-C22,-C21)

  S13= QUADRILATERAL3(C30,C34,-C31,-C26)
  S14= QUADRILATERAL3(C31,C35,-C32,-C27)
  S15= QUADRILATERAL3(C32,C36,-C33,-C28)
  S16= QUADRILATERAL3(C33,C37,-C30,-C29)

MESHLINE
  LELM1 = (SHAPE=1,C5)
  LELM2 = (SHAPE=1,C34)
  LELM3 = (SHAPE=1,C35)
  LELM4 = (SHAPE=1,C36)
  LELM5 = (SHAPE=1,C37)

MESHSURF
  SELM6 = (S1,S16)

NORENUMB
END
```

C.2.1.3. Visual output

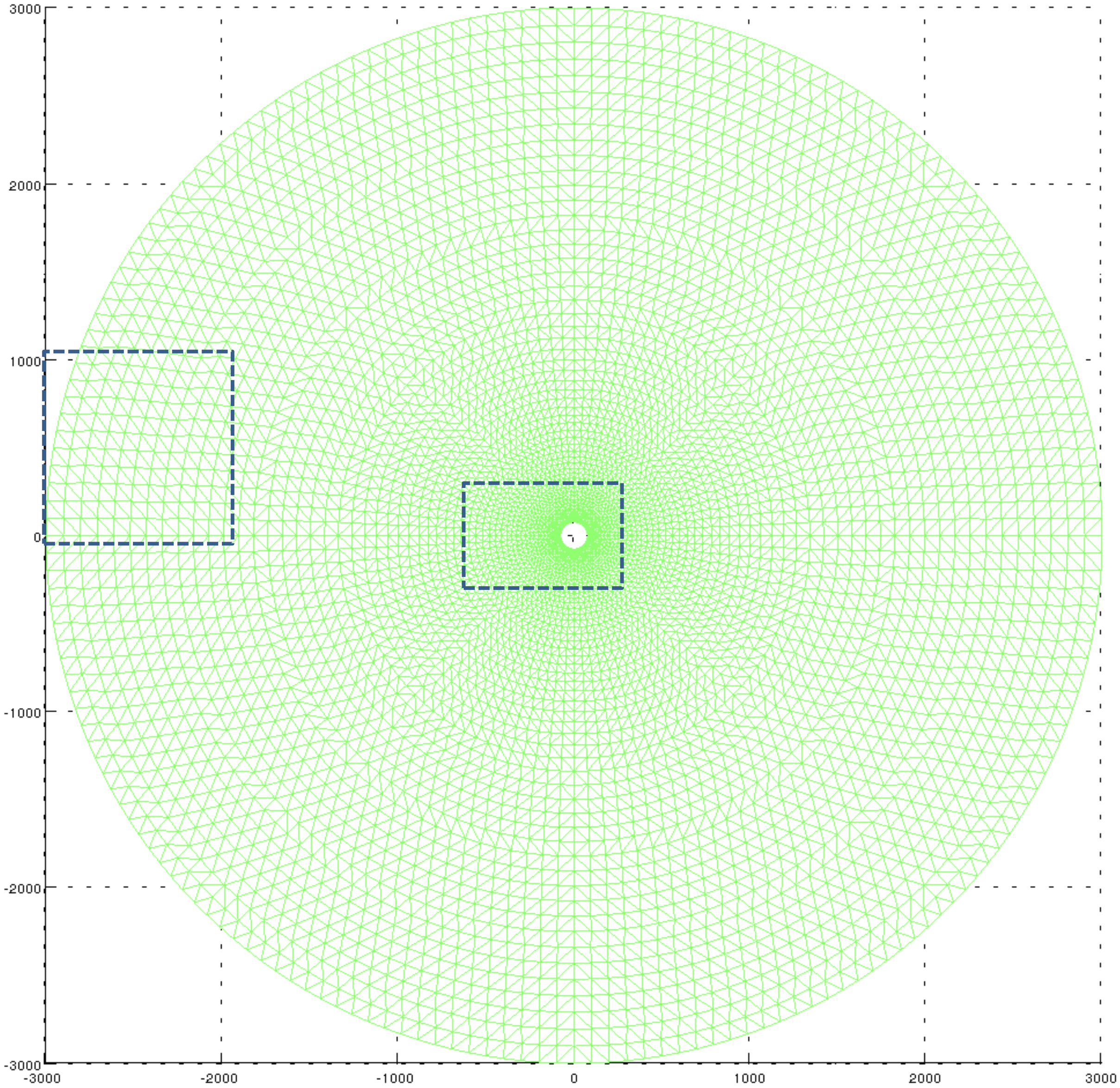

Figure C.6 – Unscaled 2D grid corresponding to case 1 [H=16.9m T=12.7s d=34m L=217m, scale factor =25] (dotted sections are shown on next page)

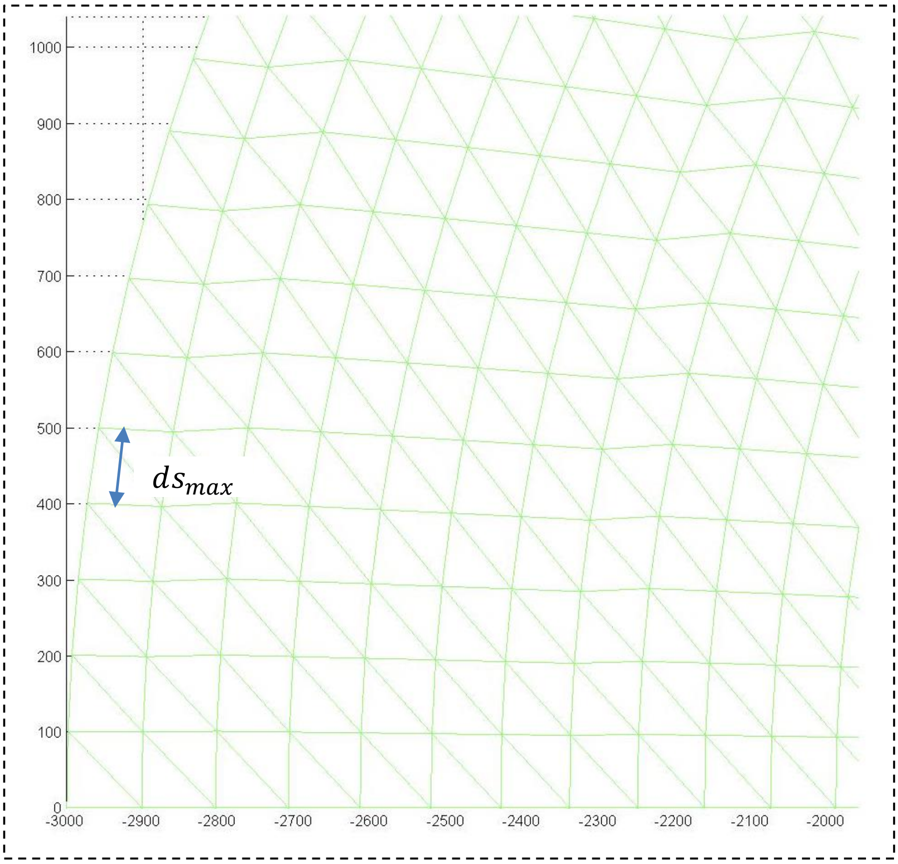

Figure C.7 – Zoom 1. Case 1 [H=16.9m T=12.7s d=34m L=217m, scale factor =25]

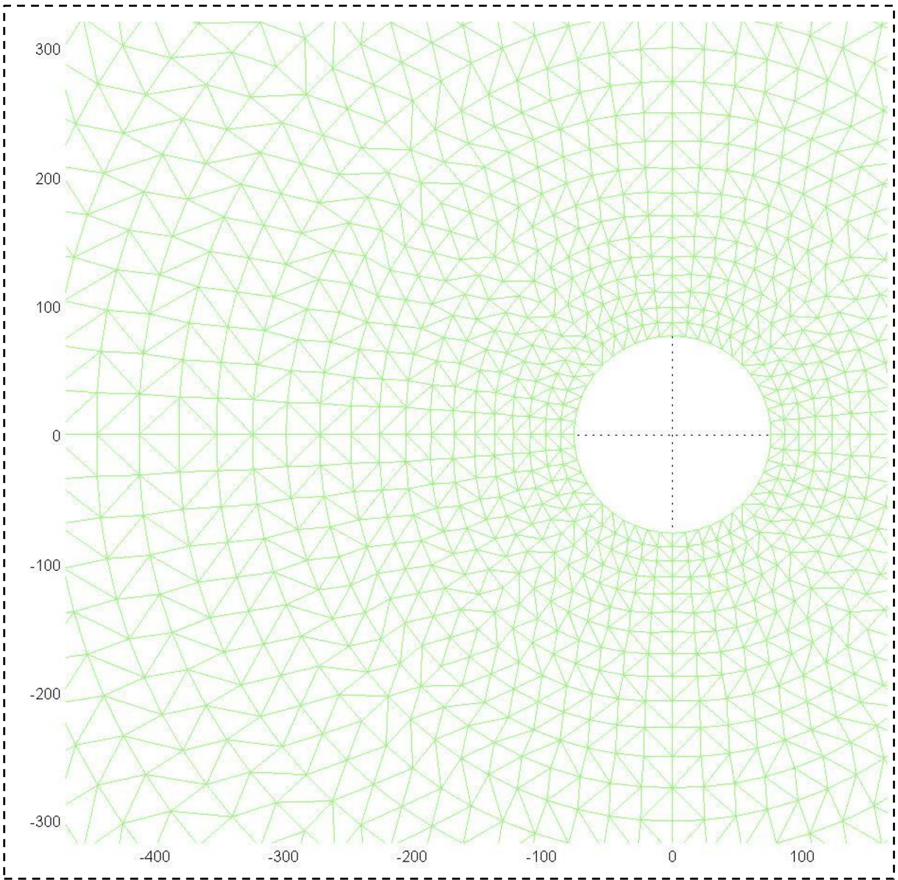

Figure C.8 - Zoom 2. Case 1 [H=16.9m T=12.7s d=34m L=217m, scale factor =25]

C.2.2. Input file FinLab

All input parameters corresponding to case 1, as defined in file mainPC.f. Structure: upper part of monopile.

```
Wave boundary conditions
Hm=16.9             ! (mean) wave height                      [m]
Tp=12.7             ! peak period                             [s]
d0=34               ! water depth                             [m]
d_shaft=-16         ! bottom level shaft                      [m]
fi0=0               ! wave direction                          [degrees]
Ux0=0               ! velocity x-component                    [m/s]
Uy0=0               ! velocity y-component                    [m/s]

Grid parameters
meshfile='./grid_FLS_LIN_v1.1.out'
nz=17 !17 - 8*(SQRT(SUM(x*x,2))-R1)/(R2-R1)
Rt=3.125
RR=(Rt*(1-R2/RR) - 80*(1-R1/RR))/(R2-R1)

Physical constants
grav=9.81           ! gravitational acceleration              [m/s2]
U0=1                ! velocity scale                          [m/s]
L0=1                ! length scale                            [m]
R0=0                ! relative density transport variable     [-]

Time stepping parameters
dt=Tp/90            ! time step                               [s]
theta=1             ! implicitness momentum equation          [-]
zeta=0.5            ! implicitness continuity equation        [-]
method=3            ! time discretization: 1=Crank-N 2=Fract.
Stepmove=1          ! move surface (1) or rigid lid (0)       [-]
Tdamp=Tp            ! damping time                            [s]
Tstart=0            ! initial time                            [s]

In-/output settings
neind=3600          ! number of time steps
nwrit=3             ! write result each nwrit timesteps
mwrit=30            ! maximum output steps before rewind

Turbulence modelling
turb=2              ! turbulence model: 0=const 1=Lmix 2=k-eps 3=LES
visc0=1.E-5         ! (minimum) kinematic viscosity           [m2/s]
Lmix=0              ! (turbulent) mixing length               [m]
kN0=2.E-2           ! default Nikuradse wall roughness        [m]
cf0=0               ! default wall friction factor            [-]
Cs=.145             ! Smagorinsky constant                    [-]
fluc=0              ! relative random velocity fluctuation    [-]
```

```
Advection-diffusion scheme
gamma=.5            ! advective flux switch [0;1]  advective-conservative
upw=1               ! upwind parameter advection [0;1]            [-]
eta=-1              ! diffusive flux switch [-1;1] skew symmetric-symmetric
limu=1              ! polynomial order advection scheme: 0, 1, 9=adaptive
limc=1              ! polynomial order transport scheme: 0, 1, 9=adaptive

Flooding and drying
dmin=2.D-2          ! minimum water depth                         [m]
amin=2.D-2          ! depth clipping parameter                    [m]

Transport parameters
nconc=0             ! number of concentration species
mu=0                ! leap-frog factor density [0;1]
nsource=0           ! number of source terms (max 10)
sigma=1             ! Prandtl-Schmidt number                      [-]

Sediment transport
Wsed=2.E-3          ! settling (+) rising (-) velocity            [m/s]
D50=200.E-6         ! median grain size                           [m]
Dr=1.65             ! relative submerged density                  [-]
Shields=.05         ! Shields parameter                           [-]
chi=1.6E-3          ! transport factor                            [-]
psi=1.0             ! stress exponent transport                   [-]
por=.3              ! porosity                                    [-]
morf=0              ! morphological factor                        [-]

Boundary coding
1=wall 2=surface 3=level 4=velocity 5=Riemann 6=wave 9=symm 0=internal
group(1)%code=1
group(2)%code=2
group(3)%code=1
group(4:7)%code=5
group(8)%code=0
```

C.3. VALIDATION FOR A MONOPILE

C.3.1. Overview

Validation has taken place for the next cases:

- H=2.5m T=10.0s d=34m
- H=16.9m T=12.7s d=34m (velocities only)

All structures are full monopiles, see Figure C.9.

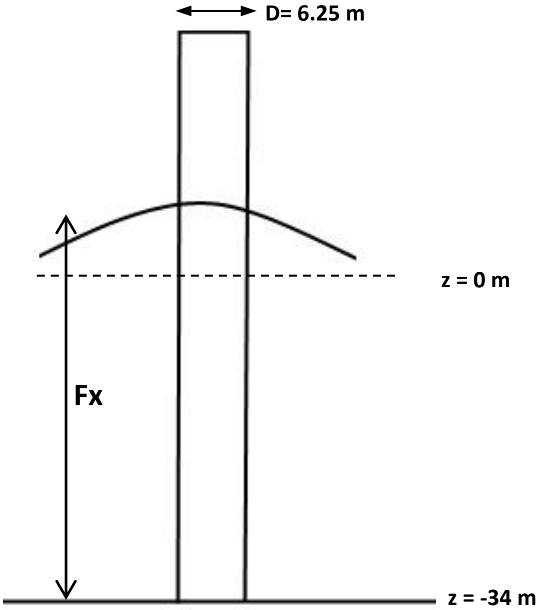

Figure C.9 – Monopile structure used for the validation

The following comparisons are made:

1. The undisturbed velocity profile from FinLab is compared with non-linear wave theory (Stream function 18).
2. The force on the monopile calculated by FinLab is compared with the Morison equation.

Ad. 1:
The undisturbed velocity in FinLab is found by extracting the horizontal velocity profile over depth. This is done at a location far 'upstream' of the structure, so at a location near the boundary ($x \approx -60$). At this location the wave field is not influenced by the structure yet. This velocity profile is compared with the velocity profile according to (non-)linear wave theory. Stream function 18 was used for all cases. Wave kinematics were found with the software package WaveLab.

Ad. 2:
For the forces resulting from the Morison equation the next procedure has been used:

- Determine the wave kinematics based on the non-linear wave theory (Stream function 18).
- Determine the maximum KC number.
- Determine the inertia and drag coefficients, based on design curves from the DNV [11]. With kN0=0.02 m the relative roughness k/D = 0.02/6.25≈0.003≈1/300. For $u_{min} = 0.3\ m/s$ Re=$0.3 \cdot 6.25/1 \cdot 10^{-6}$≈$2 \cdot 10^{6}$, so the for almost all cases the flow is trans-

critical (the coefficients are only dependent on the KC number and k/D value, due to converging values for high Re numbers). Here u_{min} is the lowest value of the horizontal velocity in this thesis, occurring at the bottom for a wave [H=5.5m T=7.4s d=34m]. See the main report for the corresponding KC and Re numbers.

- Calculate the resulting distributed force on the structure. Integration gives the total force.
- The forces are compared with results from design graphs of the Coastal Engineering Manual.

Per case a table with the next calculation parameters is added:

H	wave height	[m]
T	wave period	[s]
d	water depth	[m]
dT	time step (>1/80T)	[s]
per	no of calculated periods	[-]
theta	time integration scheme (0.5 = no damping, 1.0 = significant damping)	[-]
section	part of the structure where the total force is calculated for	[-]
r	outer radius grid	[m]

C.3.2. Results for H=2.5 m T=10.0s

H [m]	2.5	dT [s]	1/90T	section	z=-34..WL
T [s]	10.0	per [-]	15	r [m]	60
d [m]	34	theta [-]	1.0		

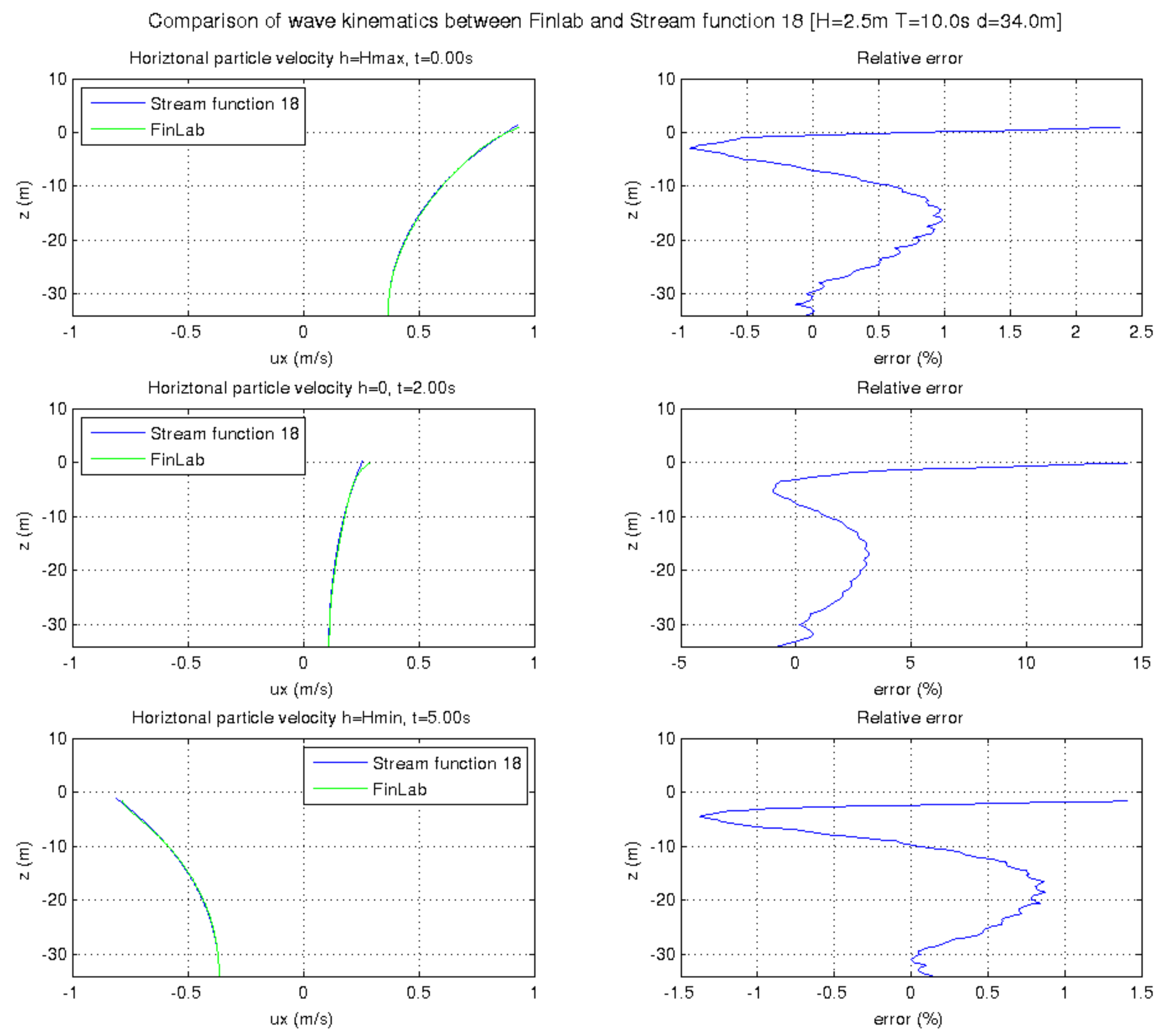

a	1.25	m
T	10	s
$L_{nonlinear}$	142	m
k	0.044	1/m
ω	0.628	1/s

Airy's linear wave theory		
z	u_{max}	u_{min}
0	0.867	-0.867
-2	0.801	-0.801
-6	0.687	-0.687
-10	0.594	-0.594
-14	0.520	-0.520
-18	0.463	-0.463
-22	0.420	-0.420
-26	0.390	-0.390
-30	0.373	-0.373
-34	0.367	-0.367

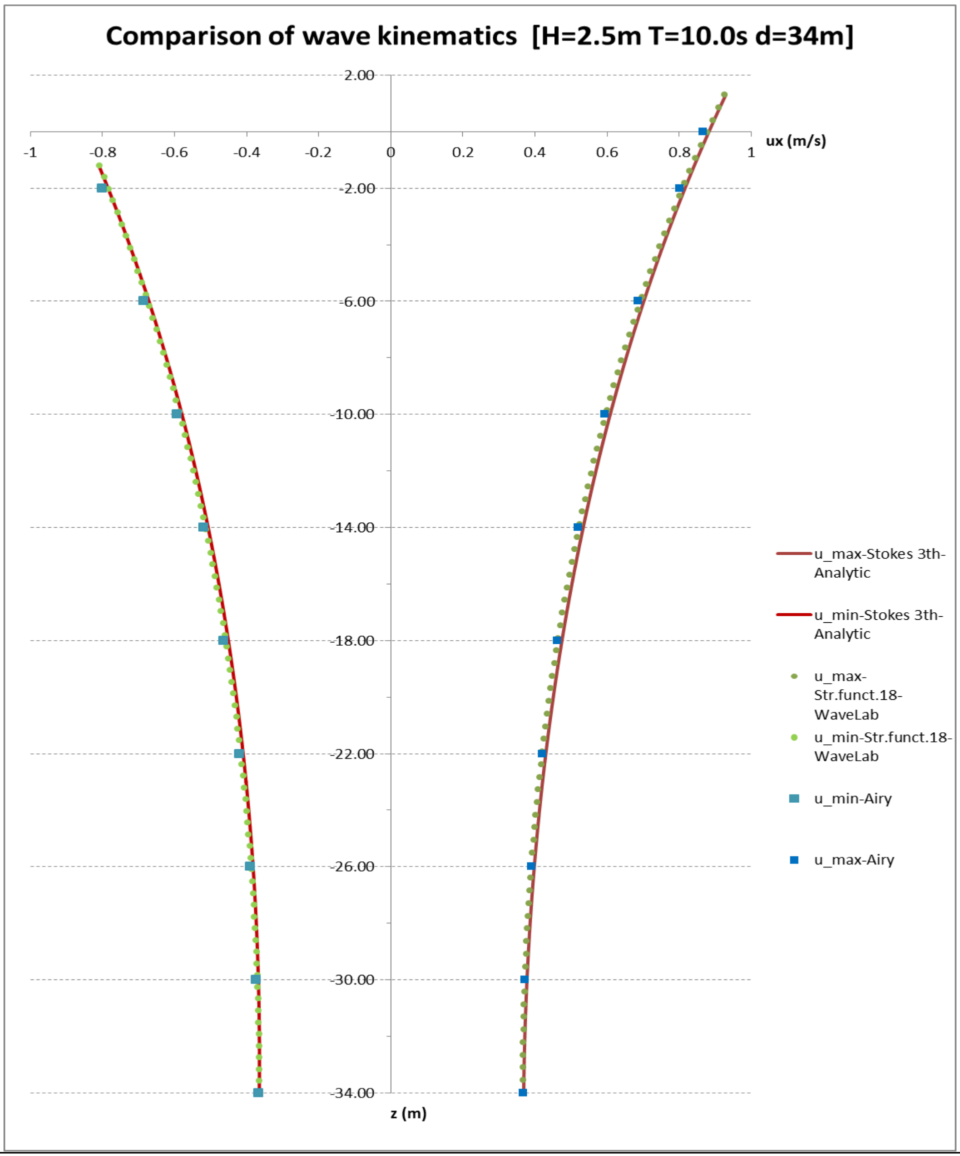

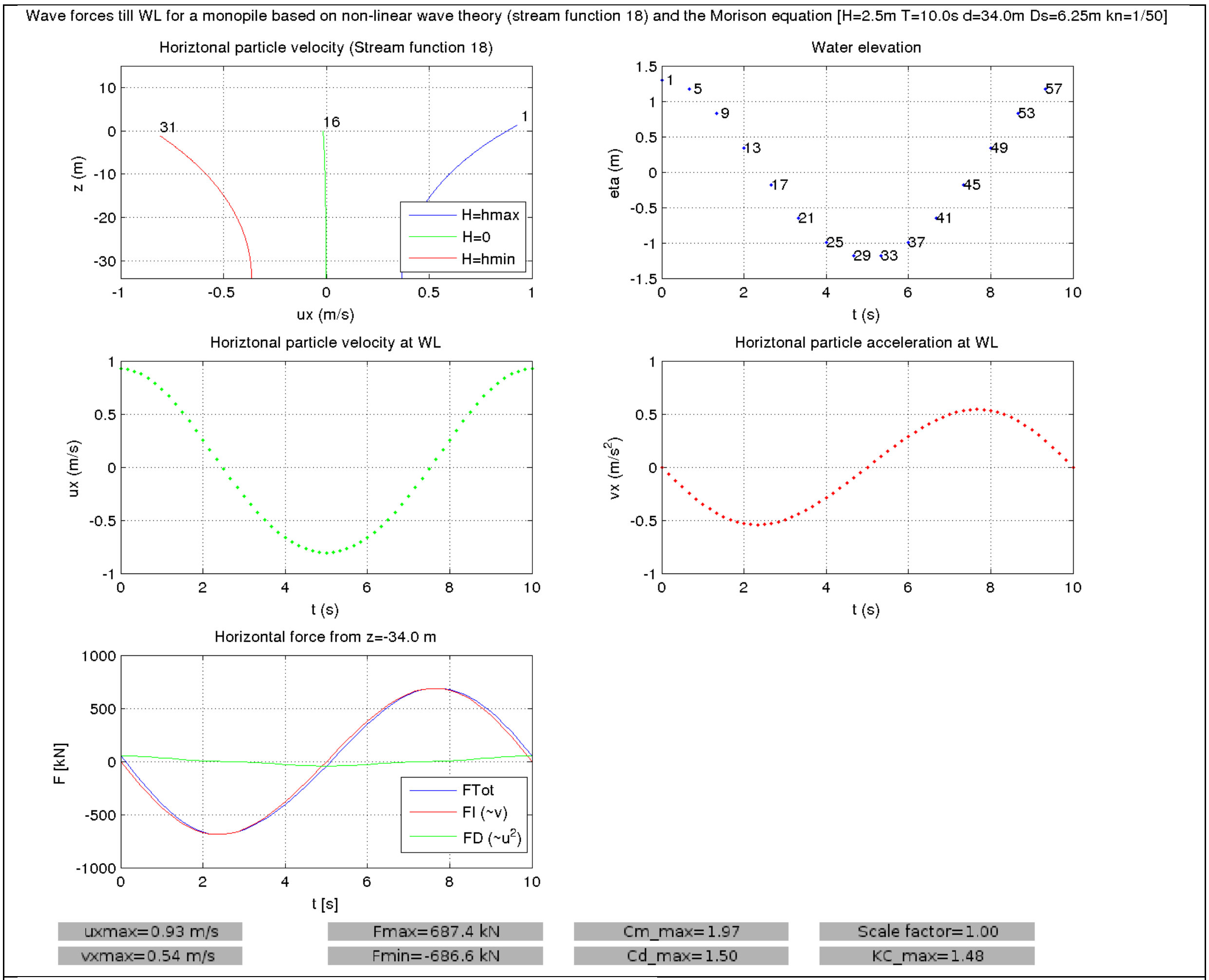
Wave forces till WL for a monopile based on non-linear wave theory (stream function 18) and the Morison equation [H=2.5m T=10.0s d=34.0m Ds=6.25m kn=1/50]
Horiztonal particle velocity (Stream function 18)
z (m)
ux (m/s)
31
16
1
H=hmax
H=0
H=hmin
Water elevation
eta (m)
t (s)
1
5
9
13
17
21
25
29
33
37
41
45
49
53
57
Horiztonal particle velocity at WL
ux (m/s)
t (s)
Horiztonal particle acceleration at WL
vx (m/s^2)
t (s)
Horizontal force from z=-34.0 m
F [kN]
t [s]
FTot
FI (~v)
FD (~u^2)
uxmax=0.93 m/s
vxmax=0.54 m/s
Fmax=687.4 kN
Fmin=-686.6 kN
Cm_max=1.97
Cd_max=1.50
Scale factor=1.00
KC_max=1.48

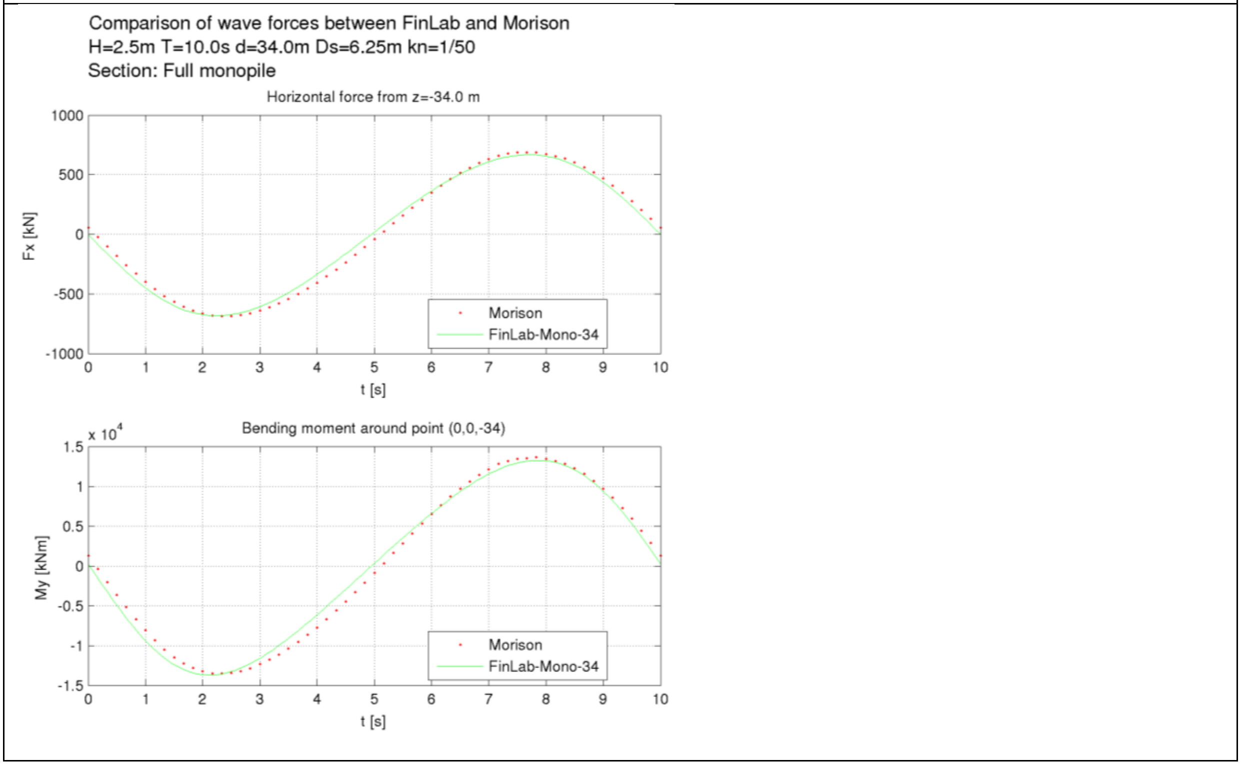
Comparison of wave forces between FinLab and Morison
H=2.5m T=10.0s d=34.0m Ds=6.25m kn=1/50
Section: Full monopile
Horizontal force from z=-34.0 m
Fx [kN]
t [s]
Morison
FinLab-Mono-34
Bending moment around point (0,0,-34)
x 10^4
My [kNm]
t [s]
Morison
FinLab-Mono-34

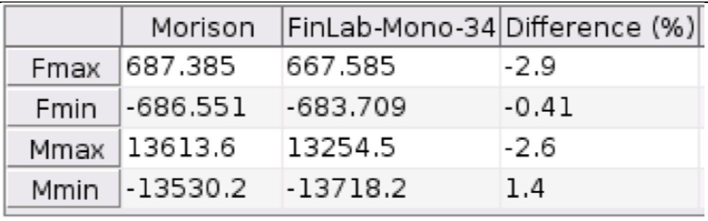

	Morison	FinLab-Mono-34	Difference (%)
Fmax	687.385	667.585	-2.9
Fmin	-686.551	-683.709	-0.41
Mmax	13613.6	13254.5	-2.6
Mmin	-13530.2	-13718.2	1.4

Interpretation

- Velocities: the undisturbed velocity profile resulting from FinLab matches very well with non-linear theory. Differences are in the order of 2% at the extremes.

  Also the comparison between WaveLab (Stream function 18) and the analytic 3th order Stokes and Airy's linear wave theory is very well. In order to find the 3th order stokes profile a Matlab script as described by [65] has been used.

- Force dominance: The force is strongly inertia-dominated.
- Force comparison: The forces and bending moments resulting from FinLab match very well with the Morison equation. Differences are in the order of 3%.

N.b.: the same simulation was performed with theta =0.5. This resulted in about the same differences, only due to the lower damping the force magnitudes became higher instead of lower. In general all extremes increased with 5%:

H [m]	2.5	dT [s]	1/90T	section	z=-34..WL
T [s]	10.0	per [-]	10	r [m]	60
d [m]	34	**theta [-]**	**0.5**		

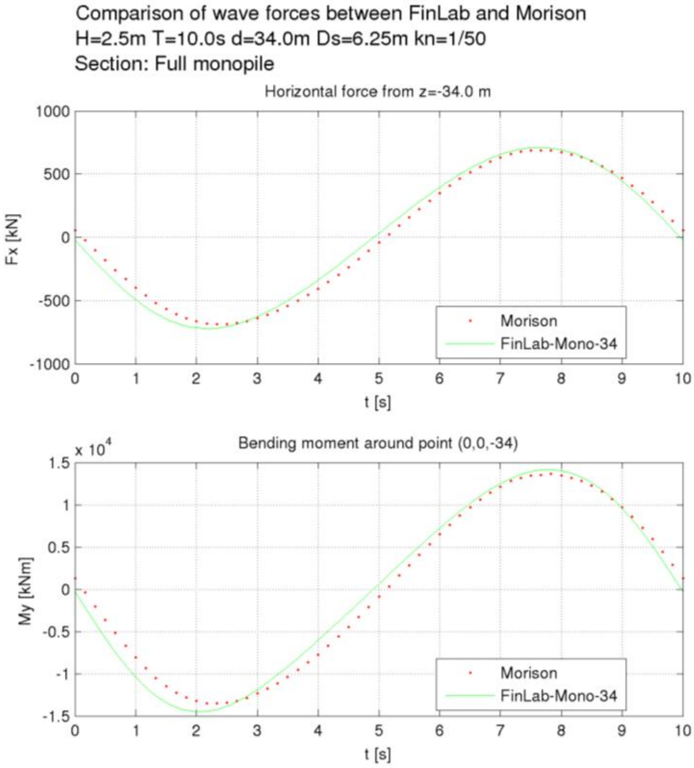

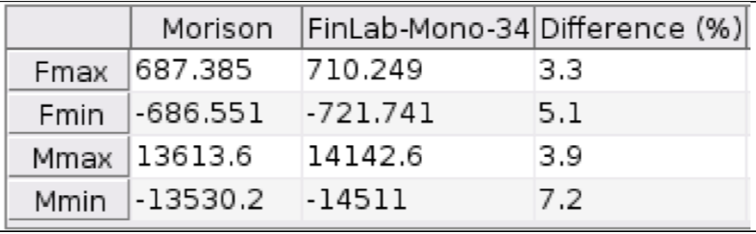

	Morison	FinLab-Mono-34	Difference (%)
Fmax	687.385	710.249	3.3
Fmin	-686.551	-721.741	5.1
Mmax	13613.6	14142.6	3.9
Mmin	-13530.2	-14511	7.2

C.3.3. Results for H=16.9 m T=12.7s

H [m]	16.9	dT [s]	1/90T	section	-34..WL
T [s]	12.7	per [-]	40	r [m]	80
d [m]	34	theta [-]	1.0		

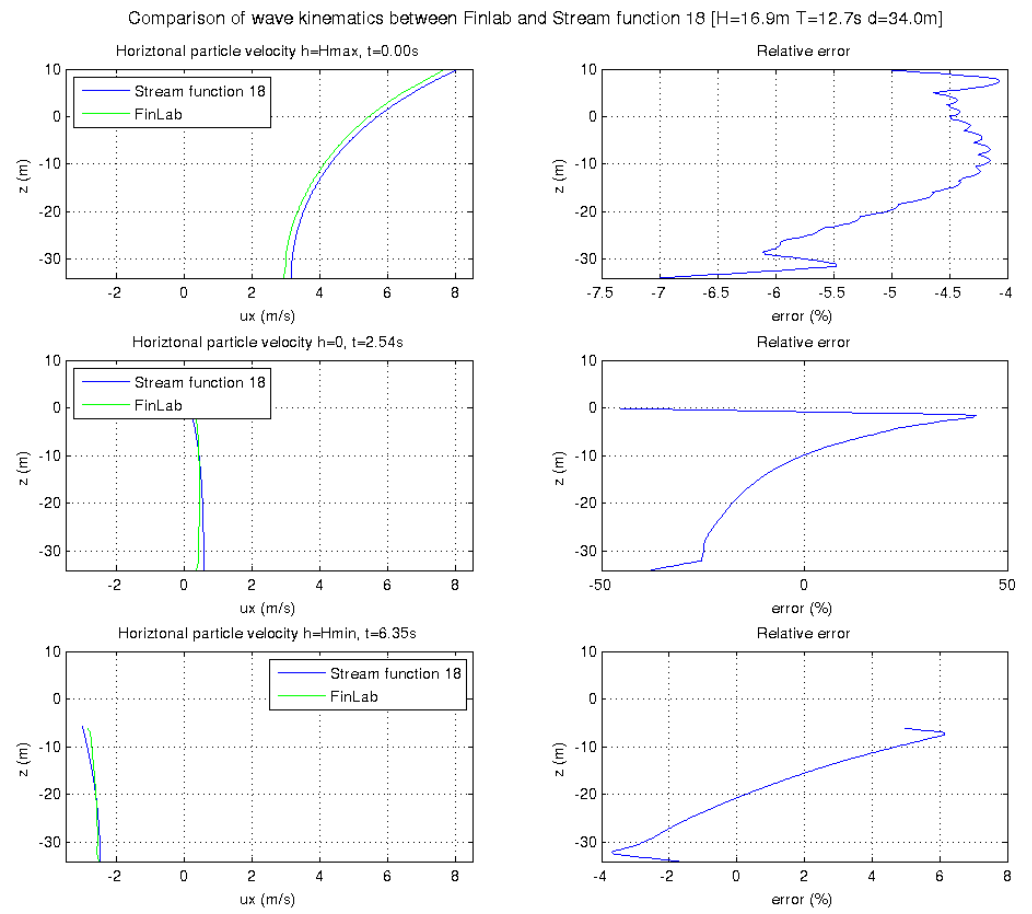

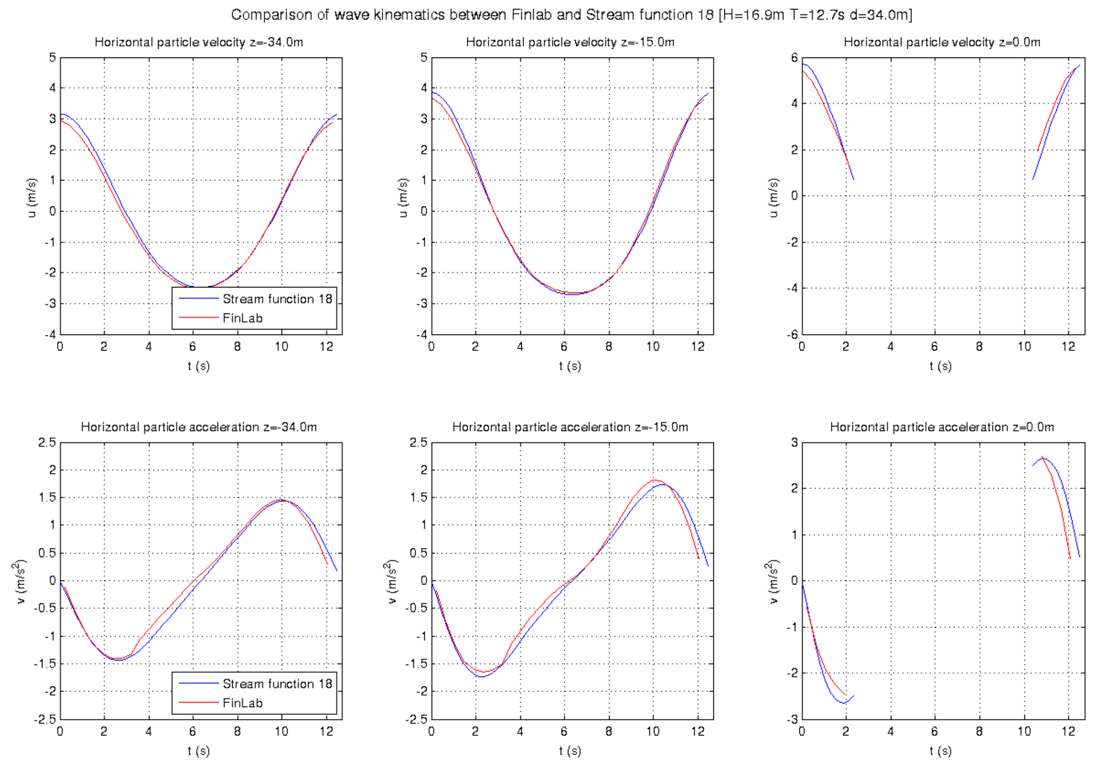

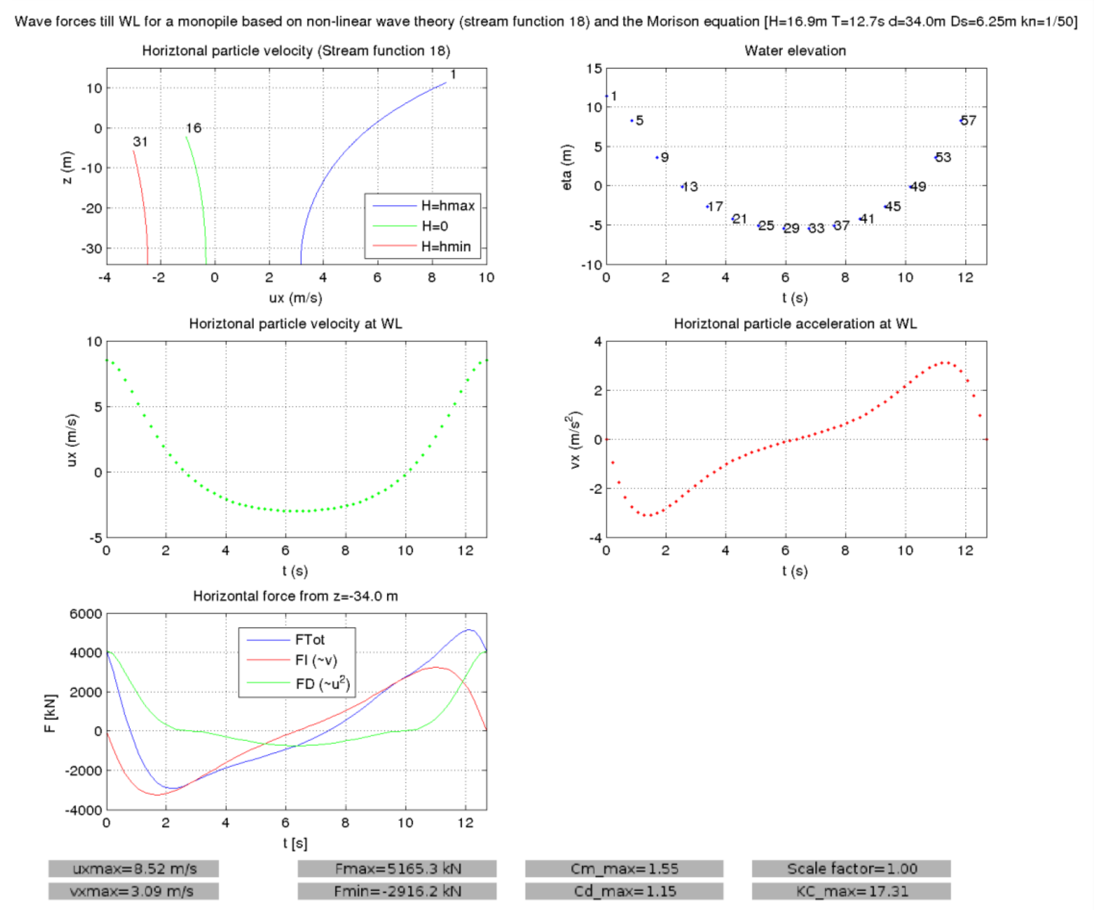

Wave forces till WL for a monopile based on non-linear wave theory (stream function 18) and the Morison equation [H=16.9m T=12.7s d=34.0m Ds=6.25m kn=1/50]

uxmax=8.52 m/s
vxmax=3.09 m/s
Fmax=5165.3 kN
Fmin=-2916.2 kN
Cm_max=1.55
Cd_max=1.15
Scale factor=1.00
KC_max=17.31

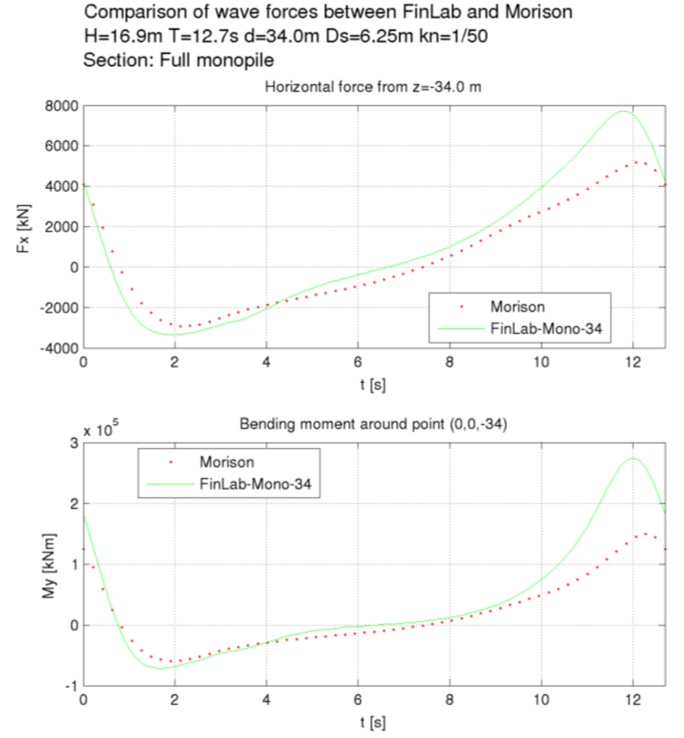

Comparison of wave forces between FinLab and Morison
H=16.9m T=12.7s d=34.0m Ds=6.25m kn=1/50
Section: Full monopile

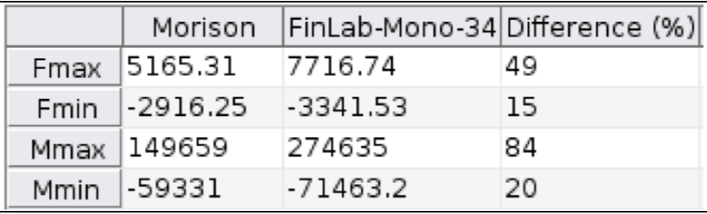

	Morison	FinLab-Mono-34	Difference (%)
Fmax	5165.31	7716.74	49
Fmin	-2916.25	-3341.53	15
Mmax	149659	274635	84
Mmin	-59331	-71463.2	20

Interpretation

- Velocities: the undisturbed velocity profile resulting from FinLab is not completely equal to non-linear theory. But due to the high velocities relative differences are still quite small, maximum in the order of 5%. At h=0 the relative error is much larger due to the small velocities, but the pattern still has about the same shape.
  Under interest is the difference in velocities at the time where the force has its maximum value ($t \approx 11.8s$). Here the velocity is almost maximal and FinLab results in 5% lower values.
- Accelerations: for this extreme wave the accelerations also have been compared. The accelerations are deviated from the velocities. But due to the relative low resolution (30 points per wave period), errors may have appeared. Especially where the slope of the velocity profile changes (around zero acceleration). The accelerations show about the same pattern, but deviate about 5% at the maxima.

- Force dominance: The force is both inertia- and drag-dominated.
- Force comparison: Although the shape is about the same, the maximum and minimum forces and bending moments resulting from FinLab differ from the Morison equation. The maximum force is about 50% higher. The maximum bending moment about 85%, indicating that in FinLab the force is not only higher in magnitude, but is also acting at a higher level. See Appendix C.8 for a discussion on these higher forces found by FinLab.

- Influence of different wave kinematics: The influence of the little differences in wave kinematics on the force is argued to be small: at the time of maximum force ($t \approx 11.8s$) the velocities simulated by FinLab may be 5% lower than theory. The accelerations were calculated from the velocities where the velocity profile exists of 60 points only. Therefore, escpecially around zero acceleration, they are poorly usable. The visible phase shift around t$\approx 11.8s$ is attributed to this effect. But suppose FinLab would calculate 10% lower accelerations. This would, together with the lower velocities, lead to a lower drag, inertia and total force around $t \approx 11.8s$ by FinLab.
  So, the slightly different wave kinematics found by FinLab cannot be the cause of the difference in total force by FinLab and the Morison equation.

C.3.4. Forces based on design graphs

Based on design graphs of the Coastal Engineering Manual [26] the maximum force can be estimated. Design curves are based on non-linear wave theory if necessary. When the inertia and drag force are out of phase a different method has to be applied.

C.3.4.1. Maximum inertia and drag forces

The maximum inertia and drag force are calculated with:

$$F_M = C_M \rho g \cdot \frac{\pi D^2}{4} \cdot H K_M \tag{C.1}$$

$$F_D = C_D \frac{1}{2} \rho g D H^2 K_D \tag{C.2}$$

with:

F_M	maximum inertia force	[N]
F_D	maximum drag force	[N]
C_M	inertia coefficient	[-]
C_D	drag coefficient	[-]
H	wave height	[m]
D	pile diameter	[m]
K_M	correction for extent of inertia force	[-]
K_D	correction for extent of drag force	[-]

For both waves the *K* coefficients were deduced based on the design graphs. Therefore the dimensionless water depth (d/gT^2) and wave steepness (H/gT^2) were calculated. Based on these values the breaking wave height could be determined from Figure C.10. The resulting coefficients can be found in Table C.1.

H [m]	T [s]	d [m]	d/gT^2 [-]	H/gT^2 [-]	H/H_b	K_M [-]	K_D [-]
2.5	10.0	34	0.035	0.0025	0.11	0.45	0.18
16.9	12.7	34	0.021	0.011	0.68	0.42	0.38

Table C.1 – Correction coefficients following from design graphs VI-5-126 and VI-5-127 of the CEM. Inertia and drag coefficients from design graphs of the DNV, see Figure C.5.

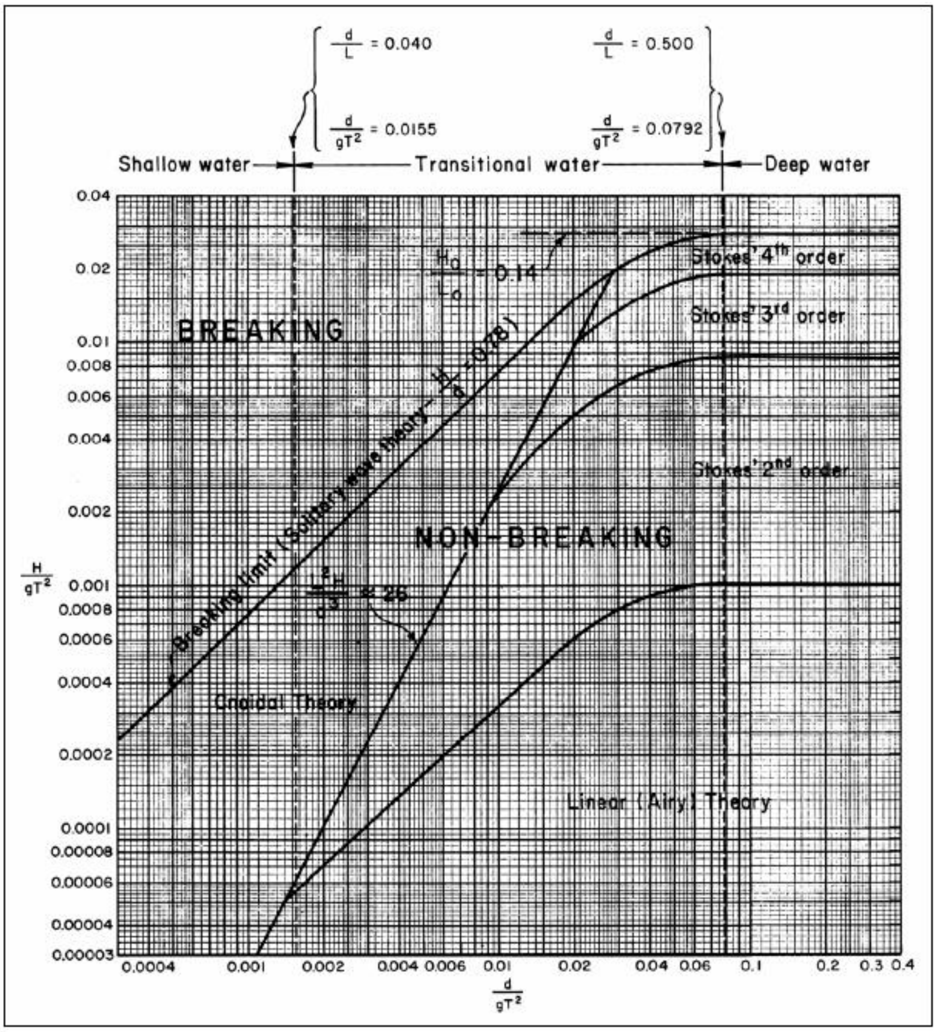

Figure C.10 - Breaking wave height and validity of wave theories

Based on Table C.1 and equation (C.1) and (C.2) the forces following from the design graphs were determined, see Table C.2. The results match very well with the maximum values found by the non-linear wave kinematics + Morison equation.

			Design graphs		Morison equation			
H [m]	T [s]	d [m]	F_M [MN]	F_D [MN]	F_M [MN]	F_D [MN]	Diff F_M [%]	Diff F_D [%]
2.5	10.0	34	0.68	0.05	0.69	0.05	1.5	0
16.9	12.7	34	3.28	3.90	3.24	4.08	-1.2	4.6

Table C.2 – Maximum wave forces resulting from design graphs

C.3.4.2. Maximum total forces

The first case (H=2.5m) is strongly inertia dominated. The maximum drag force is very small, so the maximum force peak is equal to 0.68 MN. This corresponds very well (diff 0%) with the value found by the application of the Morison equation (see Appendix C.3.2).

The second case (H=16.9m) is both drag and inertia dominated. Now a different approach has to be followed in order to determine the maximum force from the design graphs of the CEM:

$$F_{tot} = \phi_m C_D \rho g H^2 D \tag{C.3}$$

with:

F_{tot}	maximum total force	[N]
ϕ_m	force parameter for phase difference	[-]
C_D	drag coefficient	[-]
H	wave height	[m]
D	pile diameter	[m]

The parameter ϕ_m can be determined based on design graphs VI-5-131 – VI-5-134 of the CEM, based on the parameter:

$$W = \frac{C_M D}{C_D H}$$

For $W = 0.48$ this leads to $\phi_m = 0.26$. Now $F_{tot} = 5.37$ MN. This corresponds very well (diff 3.2%) with the value found by the application of the Morison equation (see Appendix C.3.3).

C.3.5. Conclusions for validation

Based on this evaluation for a full monopile the following conclusions can be drawn:

- For a near-linear wave (H=2.5s T=10.0s) the results from FinLab (both velocity and force) match very well with theory. These observations gives confidence in the output of FinLab.
- For a high non-linear wave the differences in velocity profiles increase, but are still relative small at the maxima (maximum in the order of 5%).
  The accelerations lead to about the same maxima as follows from theory, only the distribution as function of time is a bit different. This may lead to relative large differences at time of the maximum wave force (~40%). However, FinLab gives smaller velocities and accelerations, so it was argued that this would lead to a lower wave force found by FinLab instead of a higher.
- The theoretical values from the Morison equation were checked with design graphs form the Coastal Engineering Manual. Both approaches gave the same output (differences in the order of maximum 3% only).

C.4. ERRORS FOR RELATIVE SHORT WAVES

For relative short waves FinLab seemed to give strange flow patterns.
A wave with the following characteristics resulted in the flow pattern of Figure C.11a:
-H=2.5m; T=5.4s; L=47m (d/L=0.7 → short wave/deep water)

In Figure C.11b the flow pattern for case 4 (d/L=0.4 → relative long wave, intermediate water depth) is inserted as a comparison. The flow pattern for the shortest wave is not as it should be: the wave crest are not uniform. Also the wave crests vary in height when the wave propagates through the domain. The occurring effect is a common problem in numerical wave models. It may have to do with reflection of the boundaries.

When the force comparison with theory is performed the resulting forces are lower than expected. But please note that $\Theta = 1.0$ has been used here. This is too much damping for such a small wave height. When $\Theta = 0.5$ is used a better fit is expected (less damping, higher forces).

For all the cases with d/L<0.4 the flow patterns looked as expected.

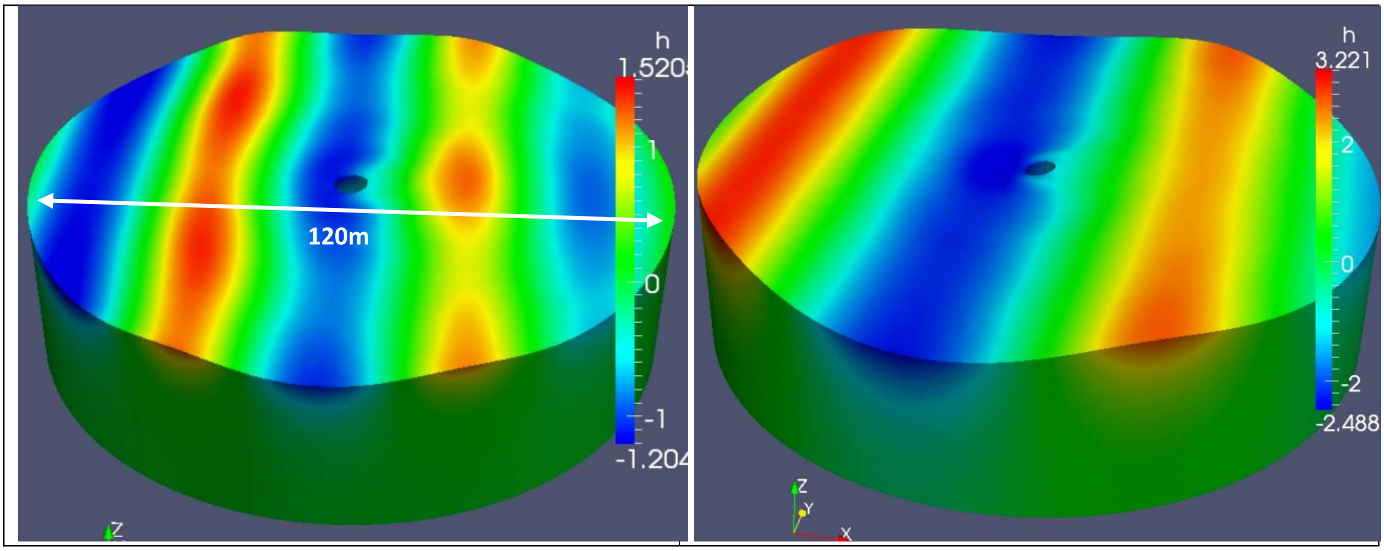

Figure C.11 – Resulting flow patterns for a) H=2.5m and T=5.4s and b) H=5.5m and T=7.4s (case 4)

H [m]	2.5	dT [s]	1/90T	section	-34..WL
T [s]	5.4	per [-]	20	r [m]	60
d [m]	34	theta [-]	1.0*		

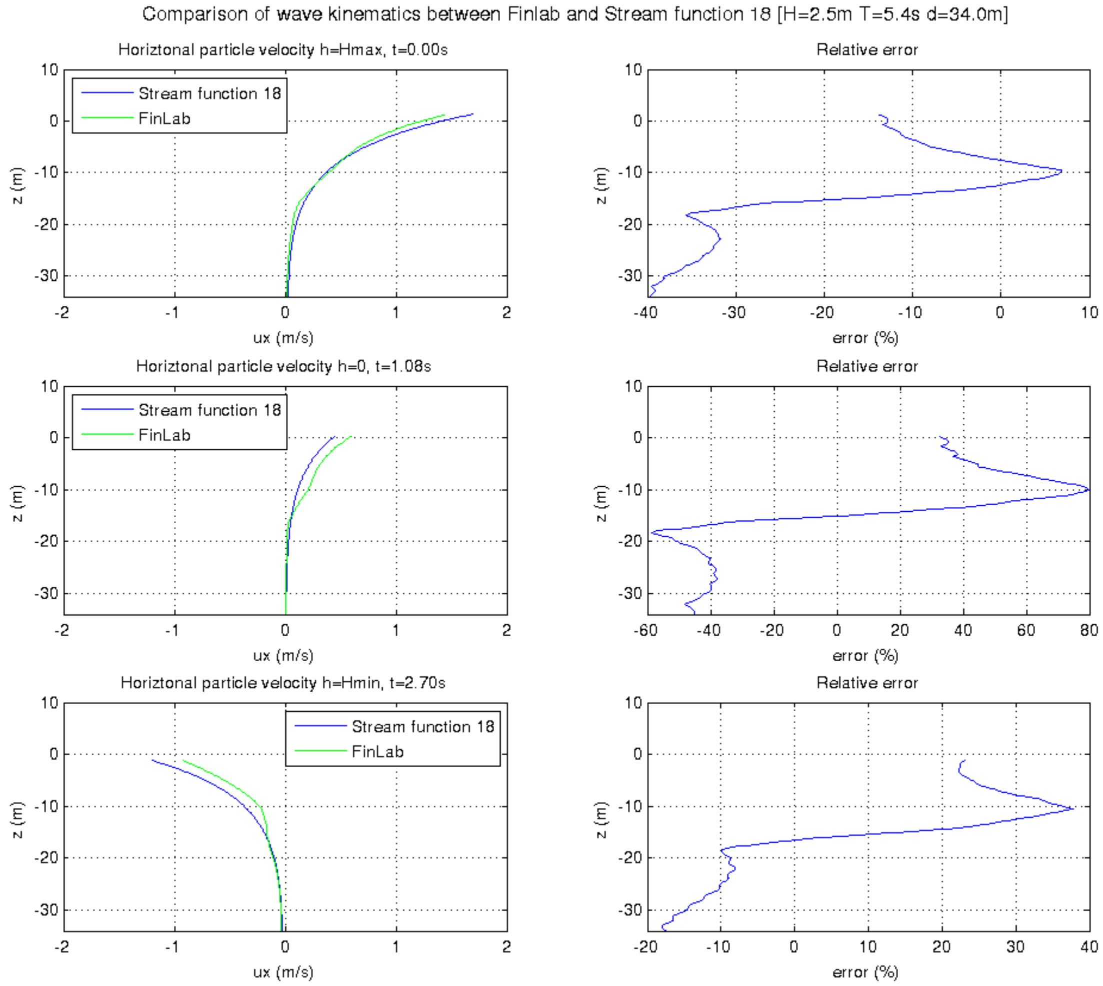

*Too high value for this relative low wave.

Wave forces till WL for a monopile based on non-linear wave theory (stream function 18) and the Morison equation [H=2.5m T=5.4s d=34.0m Ds=6.25m kn=1/50]

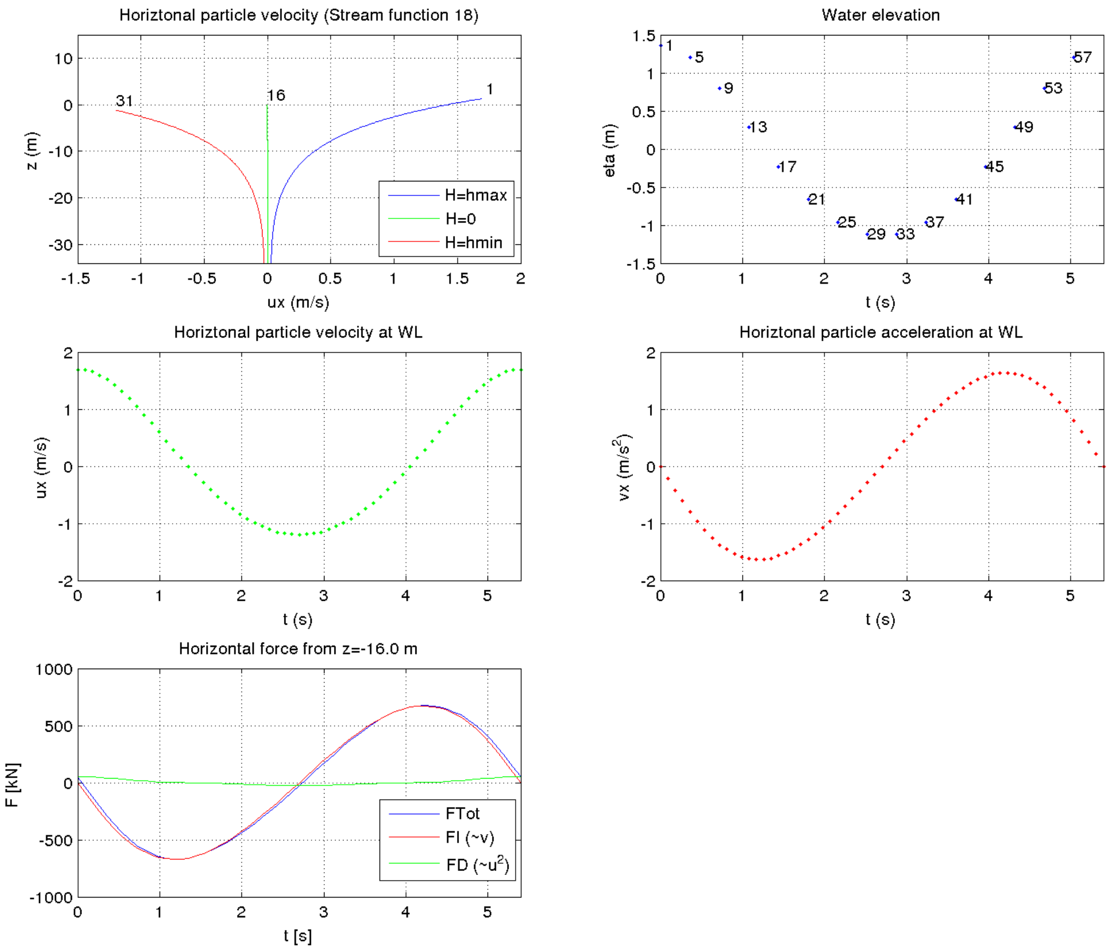

uxmax=1.69 m/s	Fmax=674.4 kN	Cm_max=1.97	Scale factor=1.00
vxmax=1.64 m/s	Fmin=-672.6 kN	Cd_max=1.50	KC_max=1.46

Comparison of wave forces between FinLab and Morison
H=2.5m T=5.4s d=34.0m Ds=6.25m kn=1/50
Section: Shaft (from z=-16)

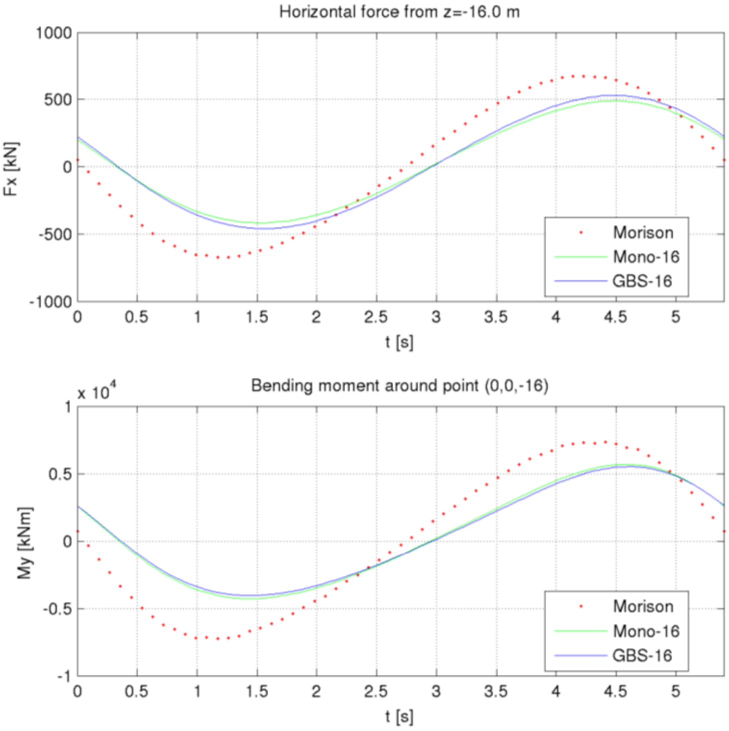

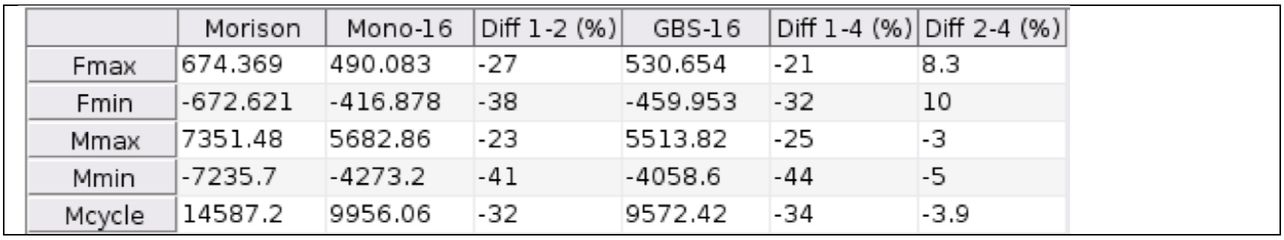

	Morison	Mono-16	Diff 1-2 (%)	GBS-16	Diff 1-4 (%)	Diff 2-4 (%)
Fmax	674.369	490.083	-27	530.654	-21	8.3
Fmin	-672.621	-416.878	-38	-459.953	-32	10
Mmax	7351.48	5682.86	-23	5513.82	-25	-3
Mmin	-7235.7	-4273.2	-41	-4058.6	-44	-5
Mcycle	14587.2	9956.06	-32	9572.42	-34	-3.9

C.5. STREAM PATTERNS AROUND THE SHAFT OF THE GBS

C.5.1. Velocity profile around support structure

The vertical wall and sloped cone of the caisson would theoretically lead to an increase in stream velocities around the structure. In this section the velocities next to the shaft of the monopile and the GBS are compared. By doing so the influence of the caisson becomes clear.

C.5.2. Stream patterns for the ULS wave [H=16.9m T=12.7s d=34m]

Velocities

For the next locations the horizontal particle velocities are plotted:

- At [0;7;z] (about 4 m from the shaft)
- At [0;14;z] (about 11 m from the shaft)
- At [0;20;z] (5.5 m from the caisson)
- At [0;50;z] (5.5 m from the caisson)

The used coordinate system is [x;y;z]. So [-7;0;z] means a vertical line at point (-7;0) (about 4 m in cross-flow direction of the shaft)

For each point the following results are given:

- Horizontal particle velocity at wave crest
- Horizontal particle velocity at wave through

Where the wave elevation is equal to still water level, the difference are much smaller see Figure C.12.

Observations

- From the result clearly follows the increase in the absolute value of the horizontal particle velocity. At [0;4;z] and [0;7;z] this is about 40% just above the cone.
- The increase is most strong just above the cone, and decreases with lower water depths.
- At [0;14;z] the increase is less than for [0;7;z] indicating that the increase is most strong around the shaft.
- At [0;20;z] the increase is also visible, this is probably due to the water flowing around the caisson (diffraction).
- At [0;50;z] there are no differences, indicating that the caisson has no influence at such a large distance.

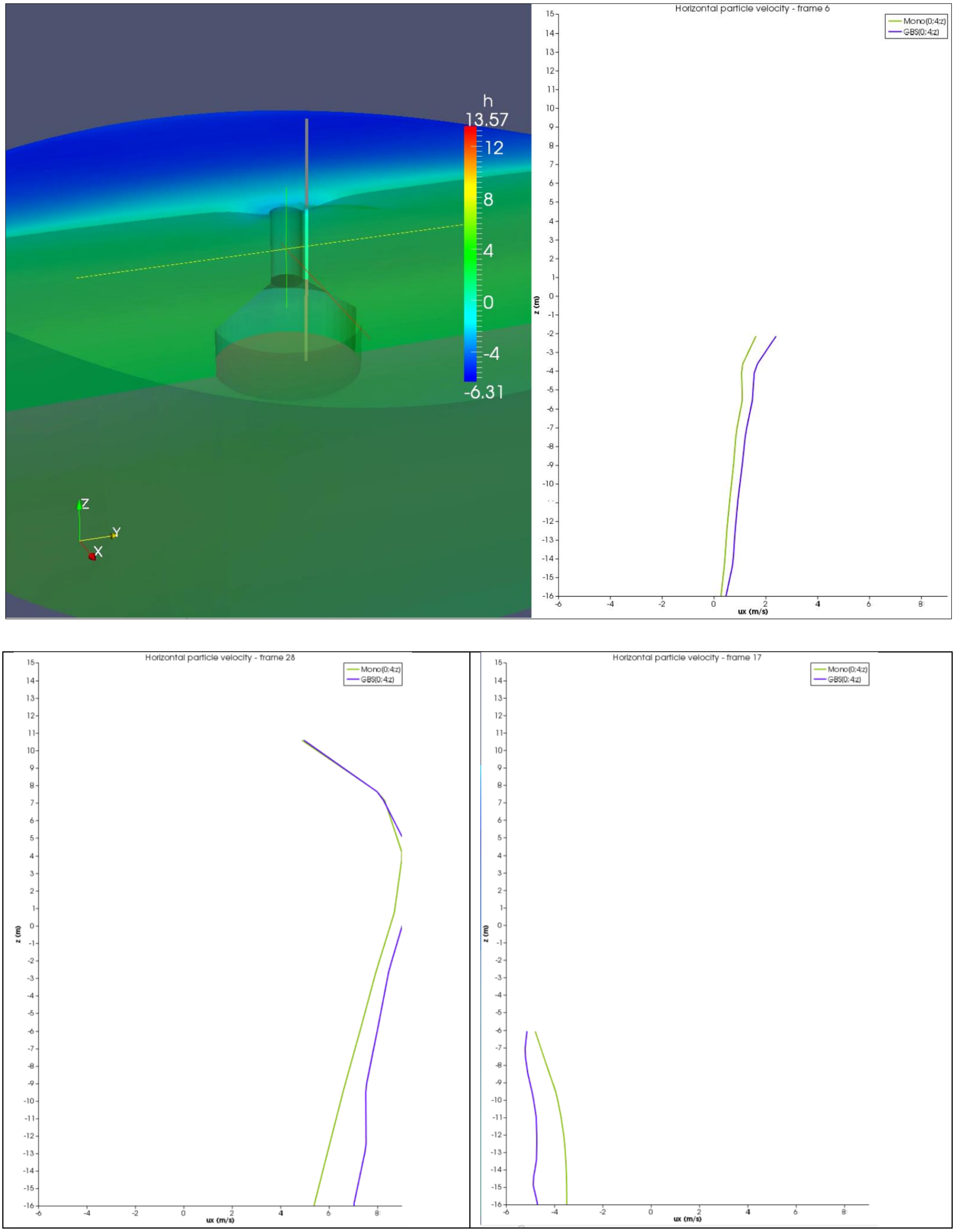

Figure C.12 - Comparison of ux for GBS and Monopile at zero crossing, wave crest and trough at [0;4;z]. N.b.: a part of the left plot is missing.

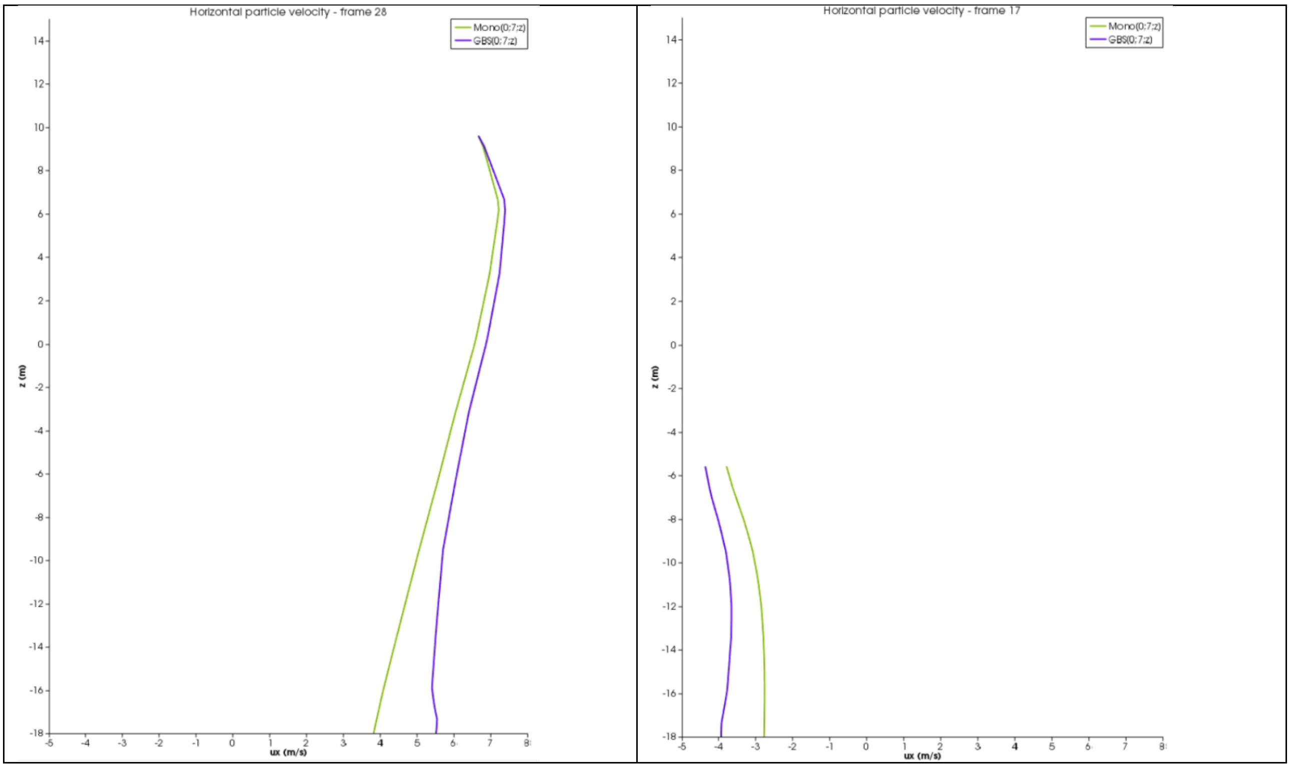

Figure C.13 - Comparison of ux for GBS and Monopile at wave crest and trough at [0;7;z]

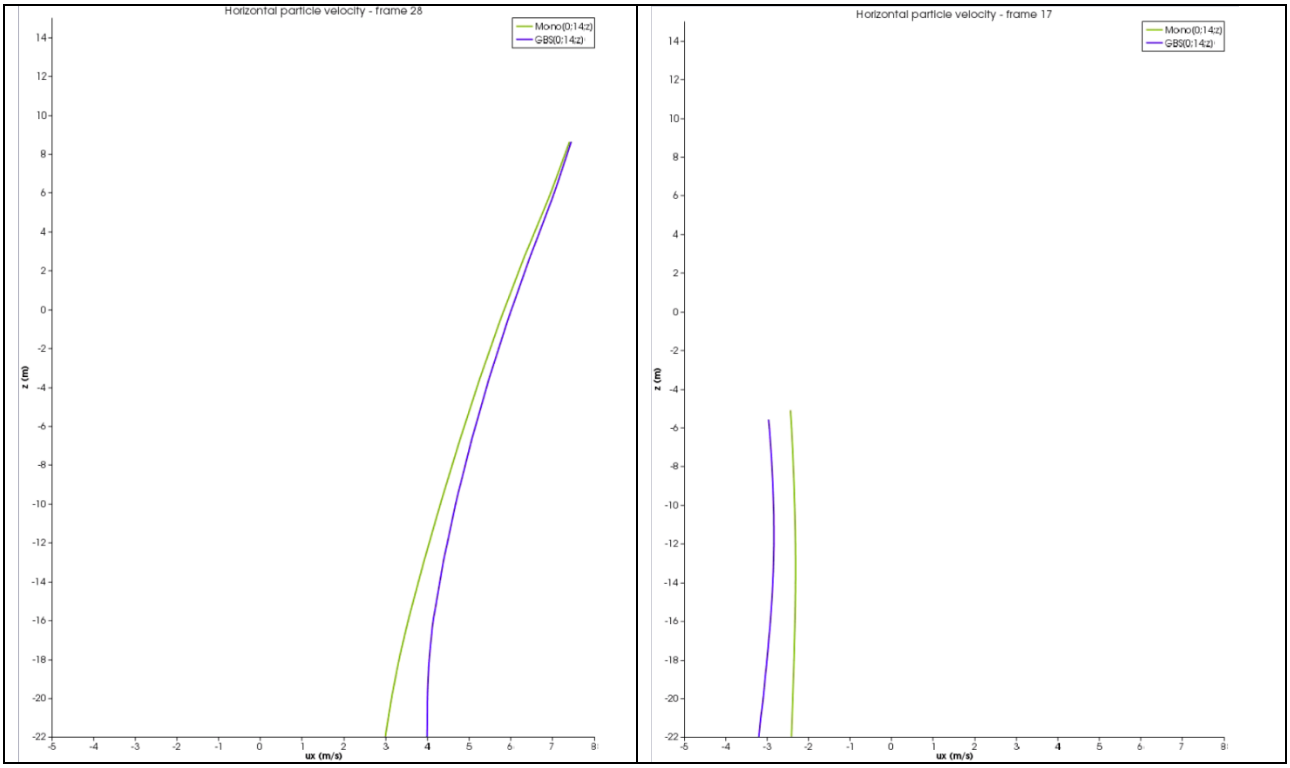

Figure C.14 - Comparison of ux for GBS and Monopile at wave crest and trough at [0;14;z]

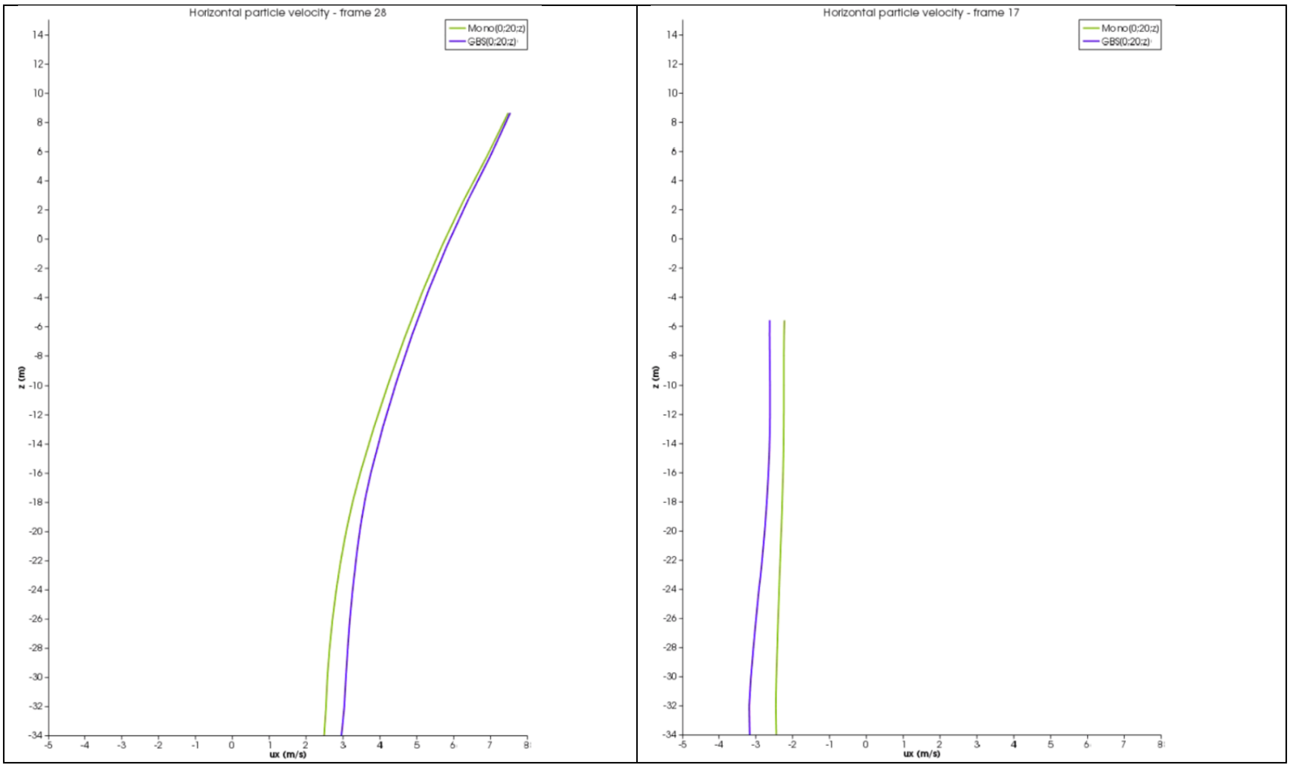

Figure C.15 - Comparison of ux for GBS and Monopile at wave crest and through at [0;20;z]

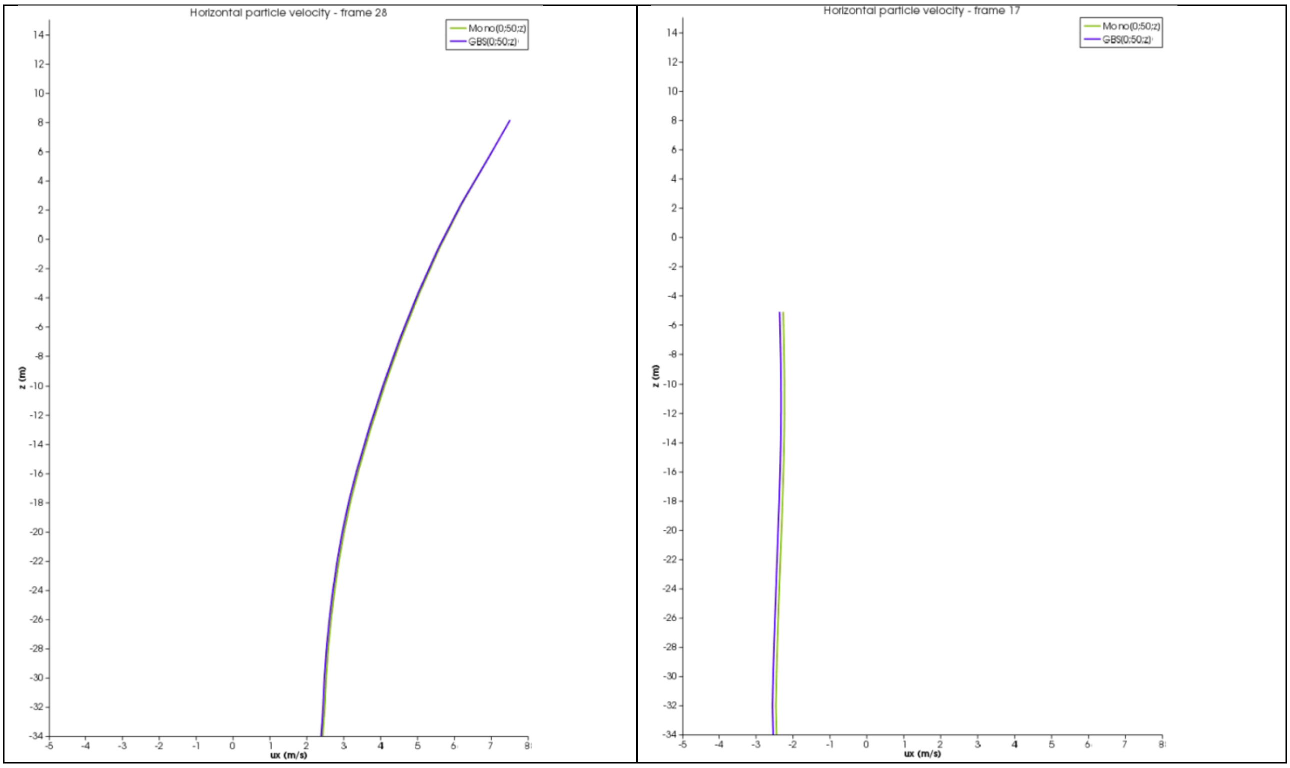

Figure C.16 - Comparison of ux for GBS and Monopile at wave crest and trough at [0;50;z]

Piezometric level

In addition at different points along the circumference the piezometric level is given:

- At [-3.125;0;z]
- At [3.125;0;z]

Obervations

- For the case of the GBS, at the front side of the cylinder, the piezometric level increases with about 5% just above the cone. The increase decays for lower water depth.
- At the rear of the cylinder no significant differences in piezometric level are visible.

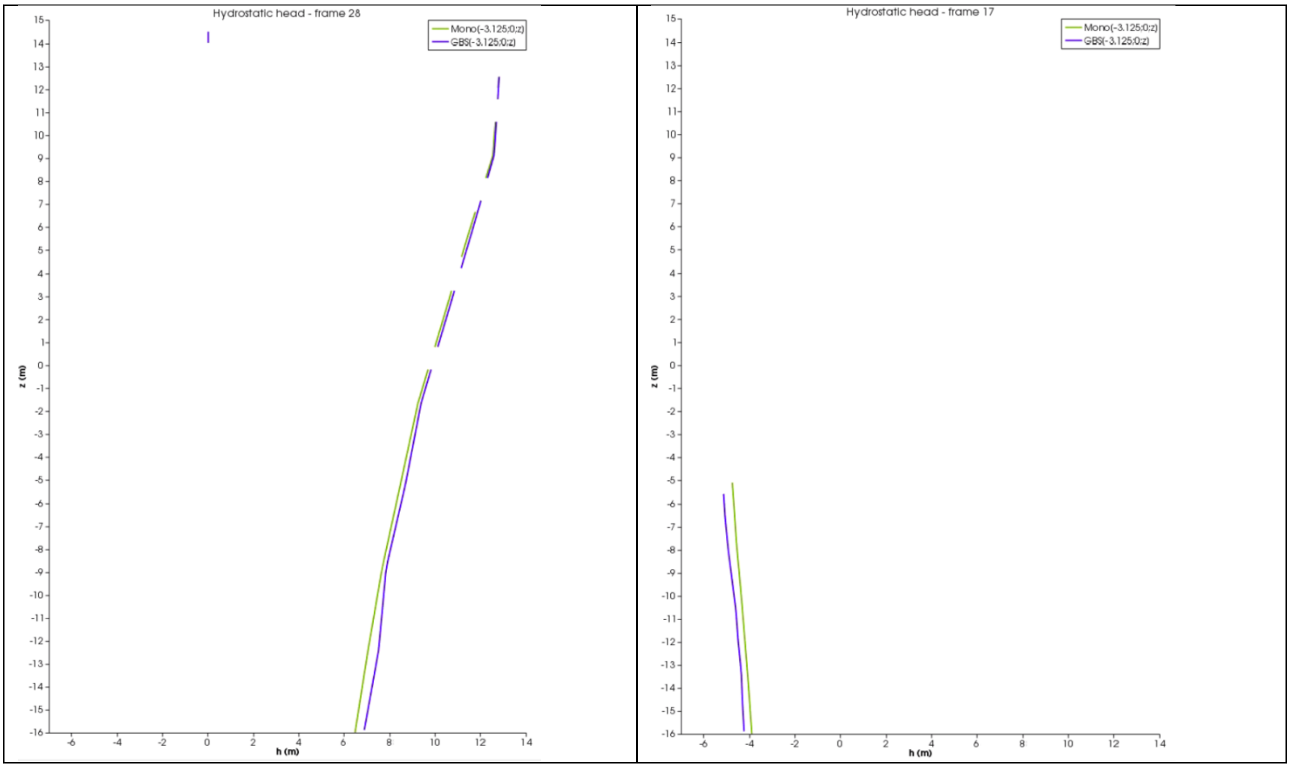

Figure C.17 - Comparison of h for GBS and Monopile at wave crest and trough at [-3.125;0;z]. N.b.: parts of the left plot are missing.

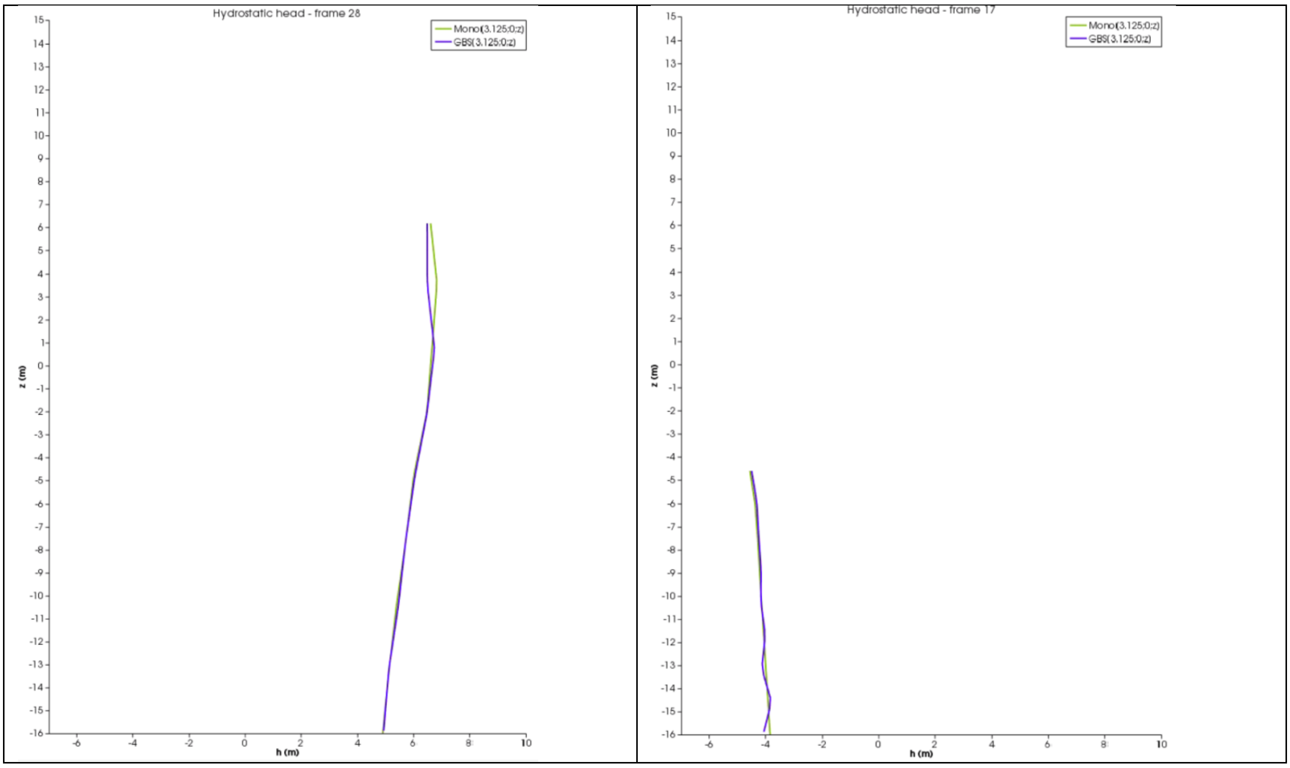

Figure C.18 - Comparison of h for GBS and Monopile at wave crest and trough at [3.125;0;z]

C.5.2.1. FLS wave [H=5.5m T=7.4s d=34m]

For the next location the horizontal particle velocities are plotted:

- At [0;4;z] (about 1 m from the shaft)

Observations

- Also for this wave from the result clearly follows the increase in the absolute value of the horizontal particle velocity.
- The increase is most strong just above the cone, and decreases with lower water depths.
- With respect to the ULS wave the difference only seems to occur just above the cone instead of over the full water depth (for the situation with the wave crest only).

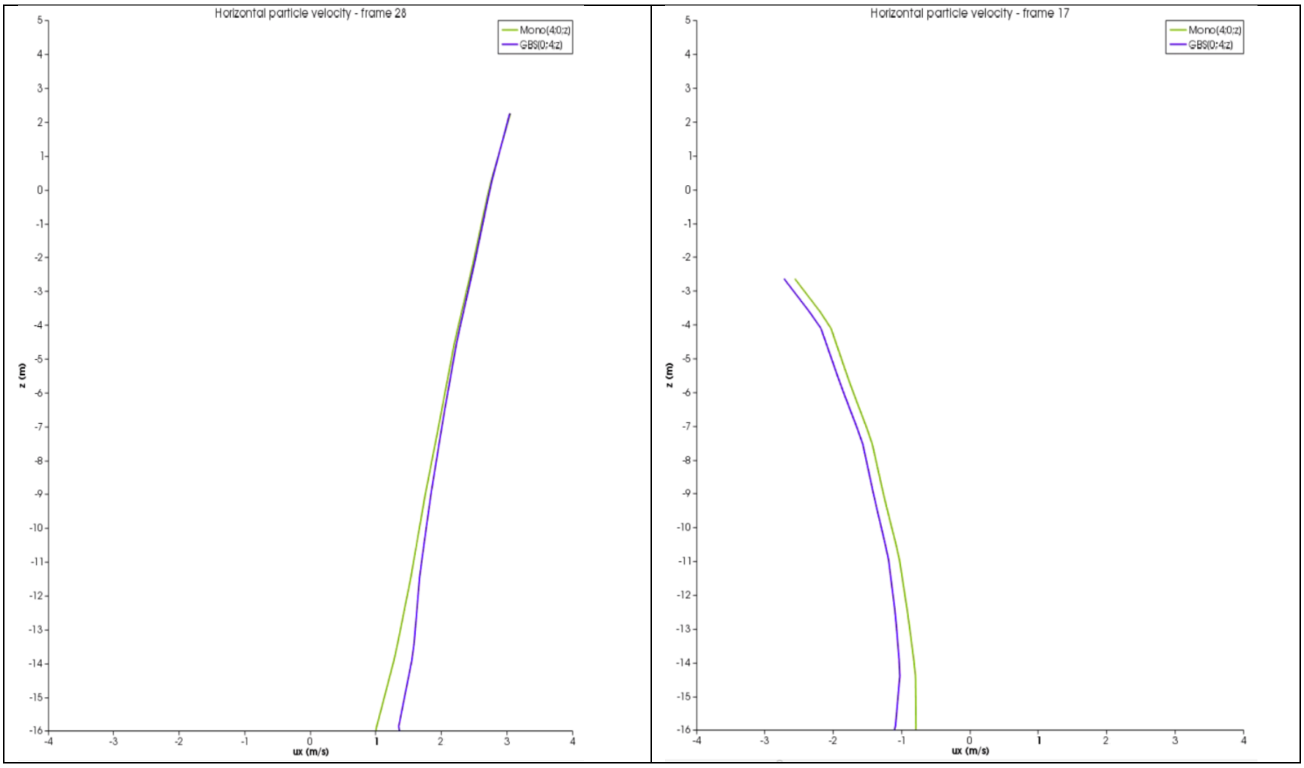

Figure C.19 - Comparison of ux for GBS and Monopile at wave crest and trough at [0;4;z]

Piezometric level

Also here the piezometric level is given for:

- [-3.125;0;z]
- [3.125;0;z]

Observation

- Near the caisson at the rear an increase in the piezometric level is visible. At the front no significant differences occur due to the presence of the caisson.

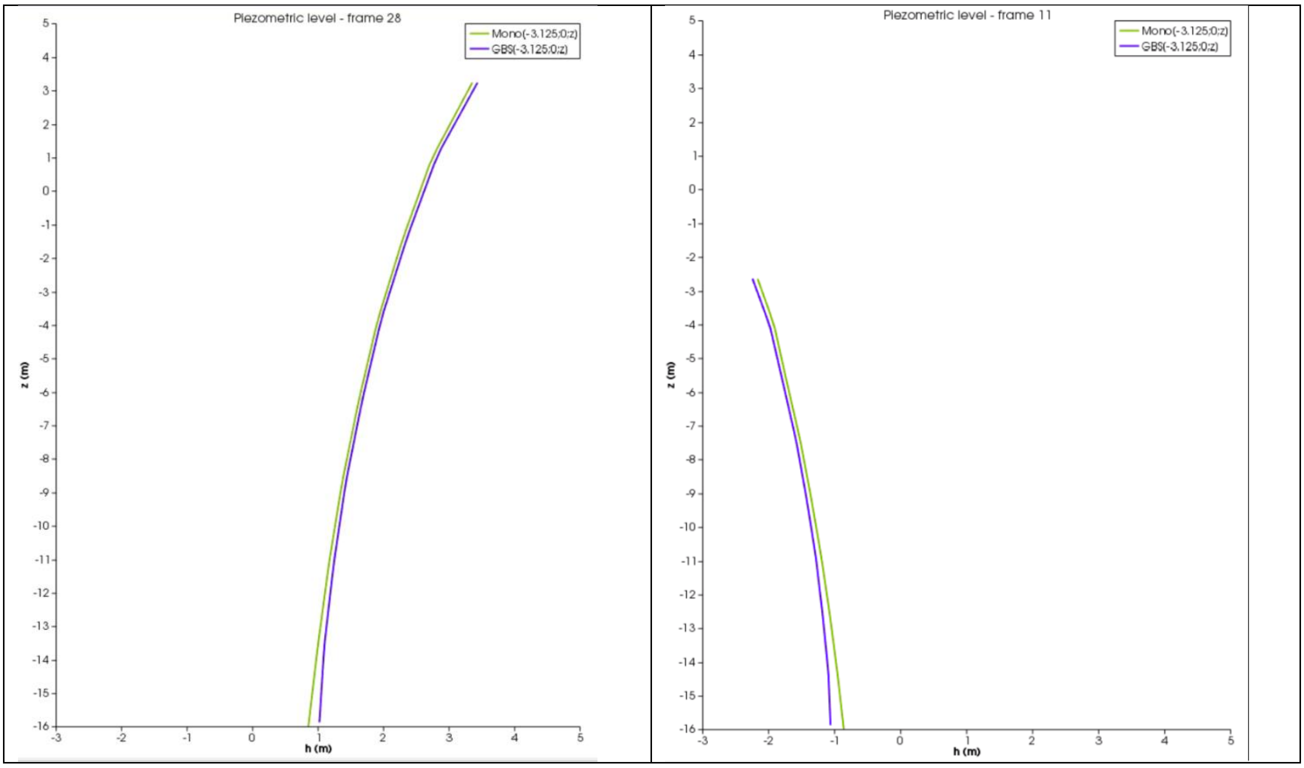

Figure C.20 - Comparison of h for GBS and Monopile at wave crest and trough at [-3.125;0;z]

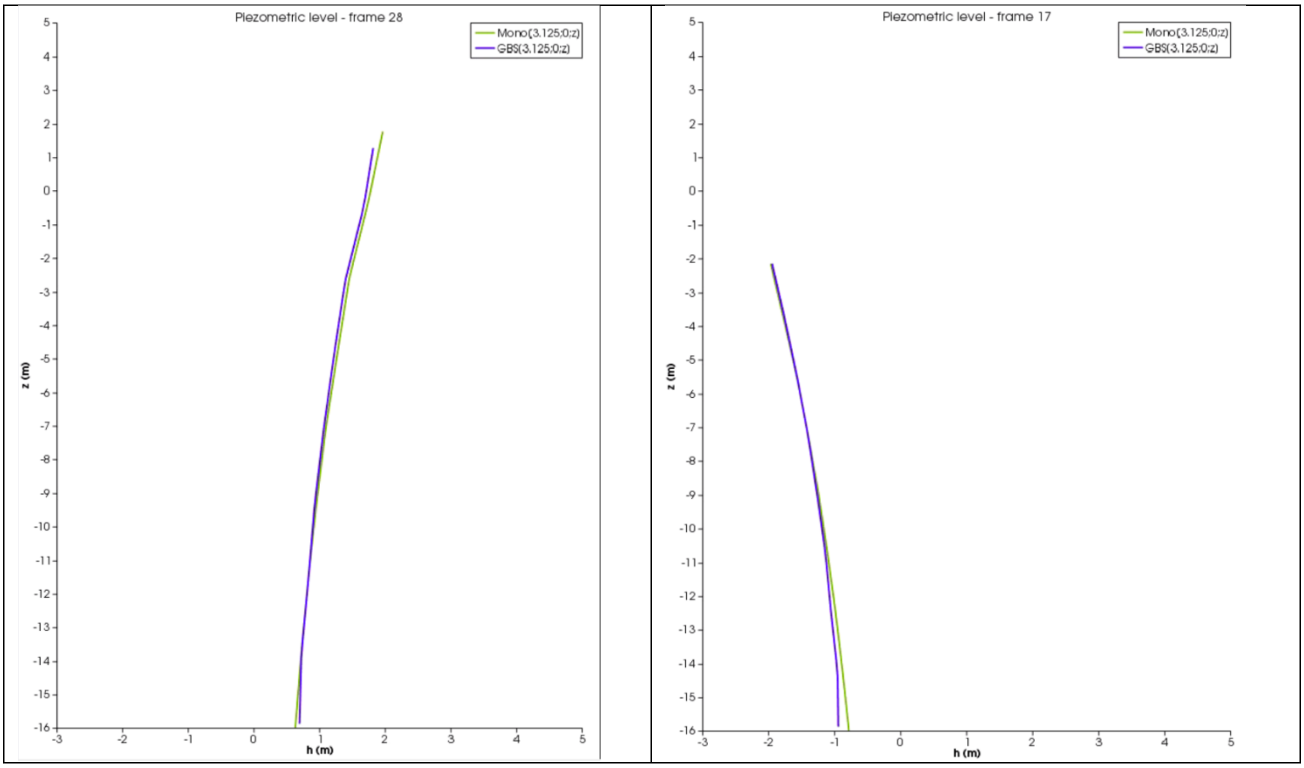

Figure C.21 - Comparison of h for GBS and Monopile at wave crest and trough at [3.125;0;z]

C.5.3. Wave shapes

When a wave moves along the cylinder this may result in a local distortion of the original wave shape. For the following waves different figures of this distortion effect are given:

- H=2.5m, T=10.0s, d=34m, D=6.25m (validated wave)
- H=16.9m, T=12.7s, d=35m, D=6.25m (case 1)
- H=16.9m, T=12.7s, d=34m, D=1.0m (case 1 with smaller diameter)

C.5.3.1. Validated wave

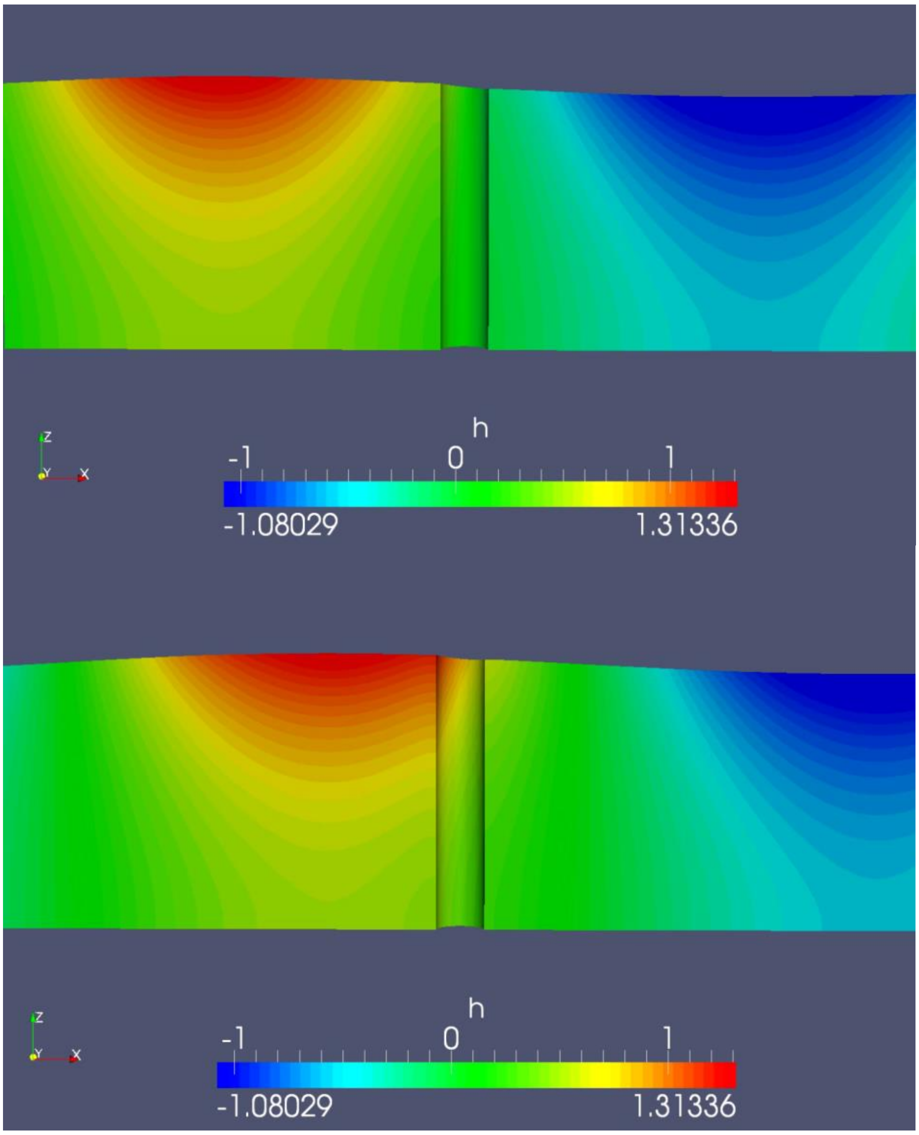

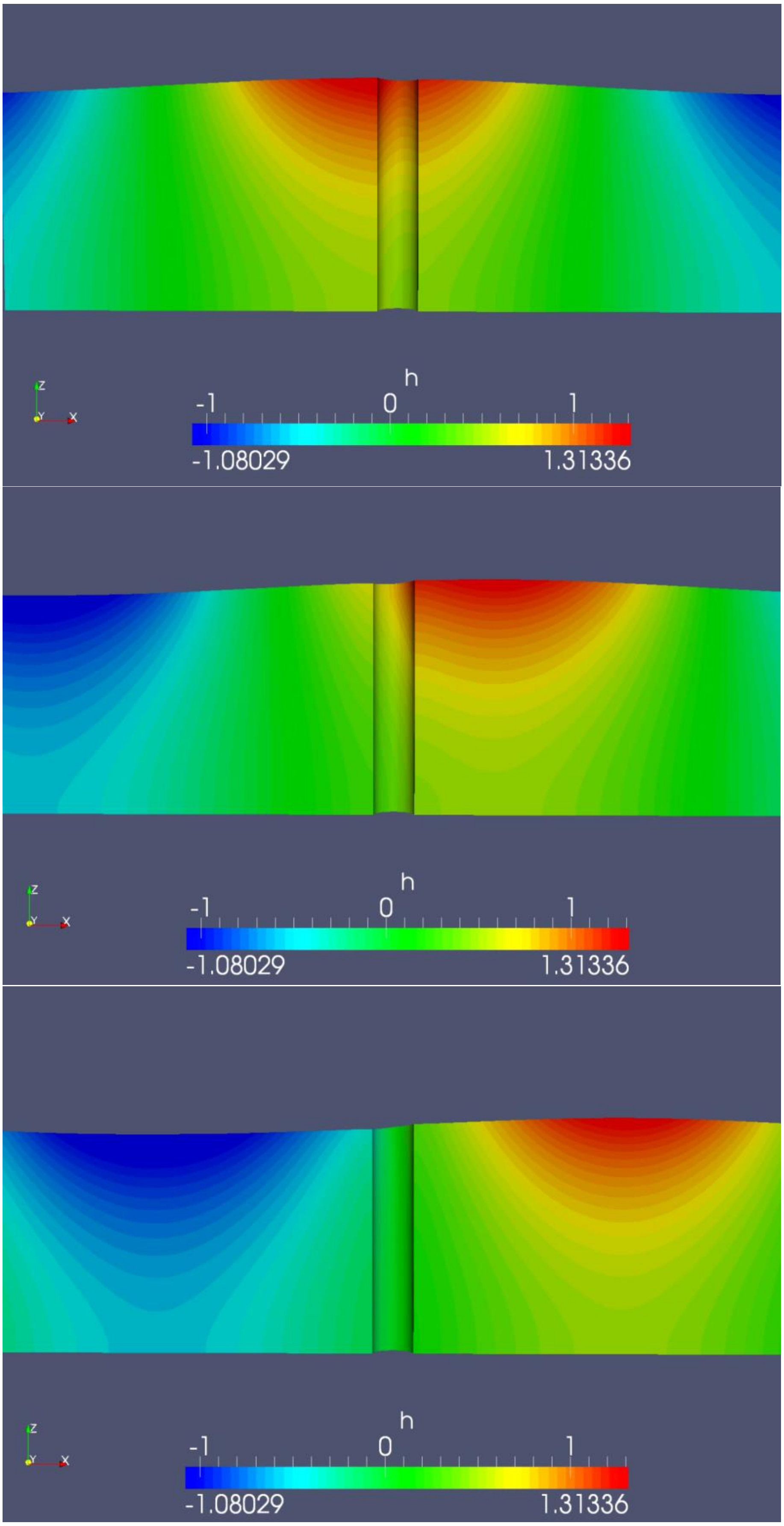

Figure C.22 – Wave shape near the cylinder for different wave phases. Case 1 [H=2.5m, T=10.0, d=34m, D=6.25m]

C.5.3.2. Case 1, D=6.25m

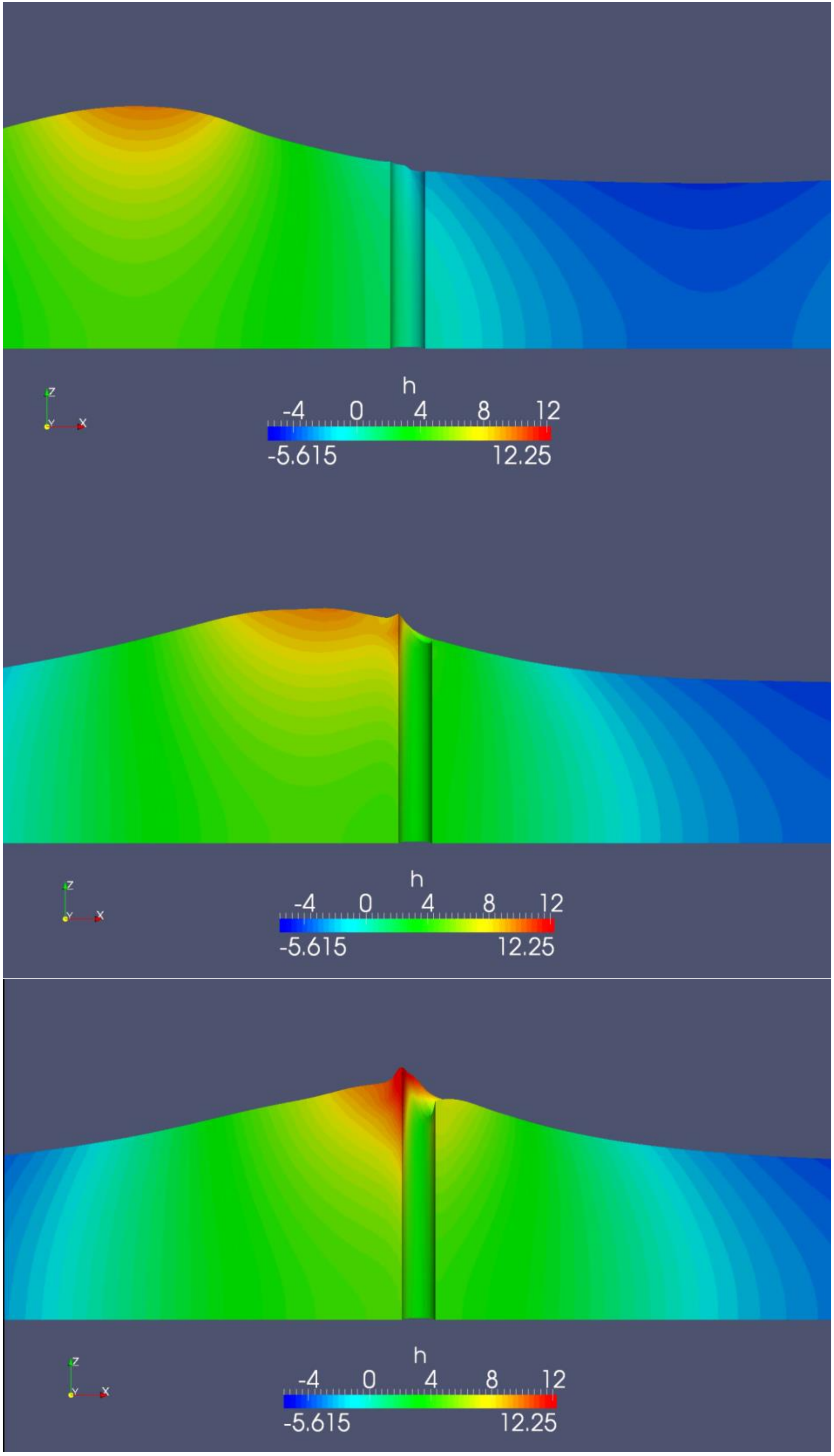

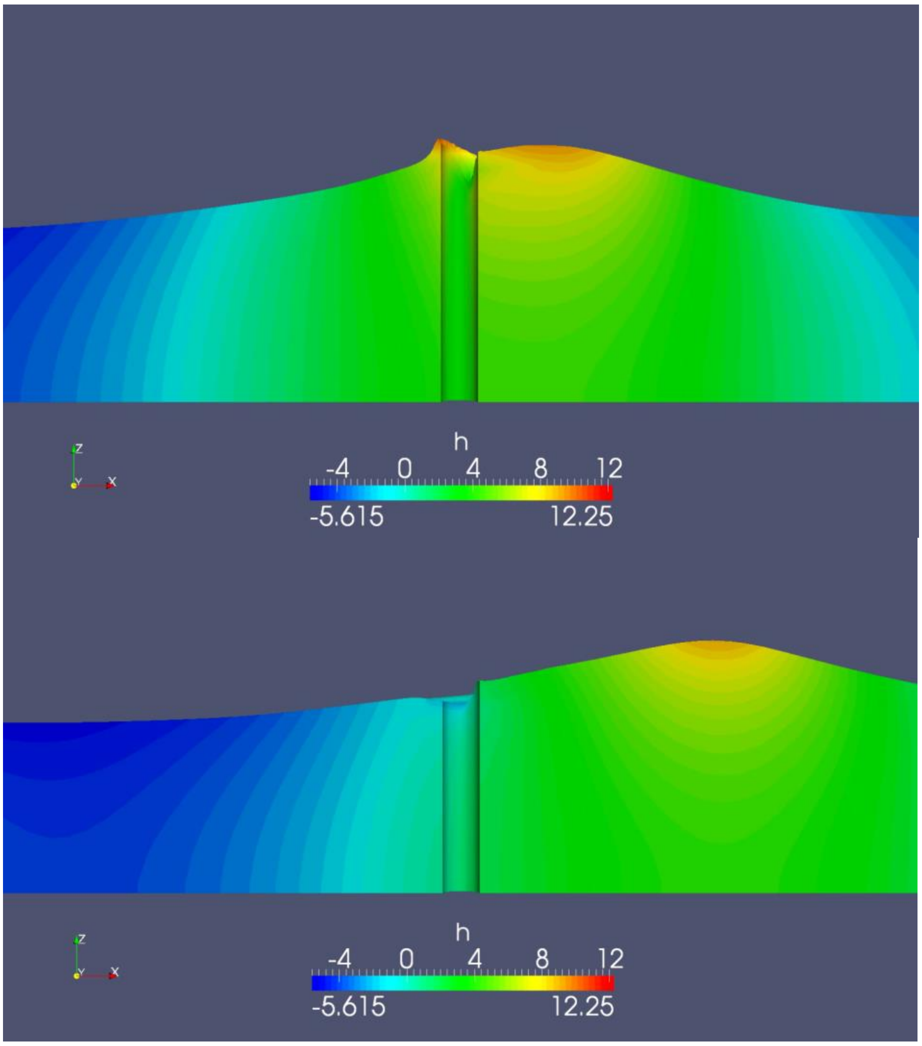

Figure C.23 – Wave shape near the cylinder for different wave phases. Case 1 [H=16.9m, T=12.7s, d=34m, D=6.25m]

C.5.3.3. Case 1, D=1.0m

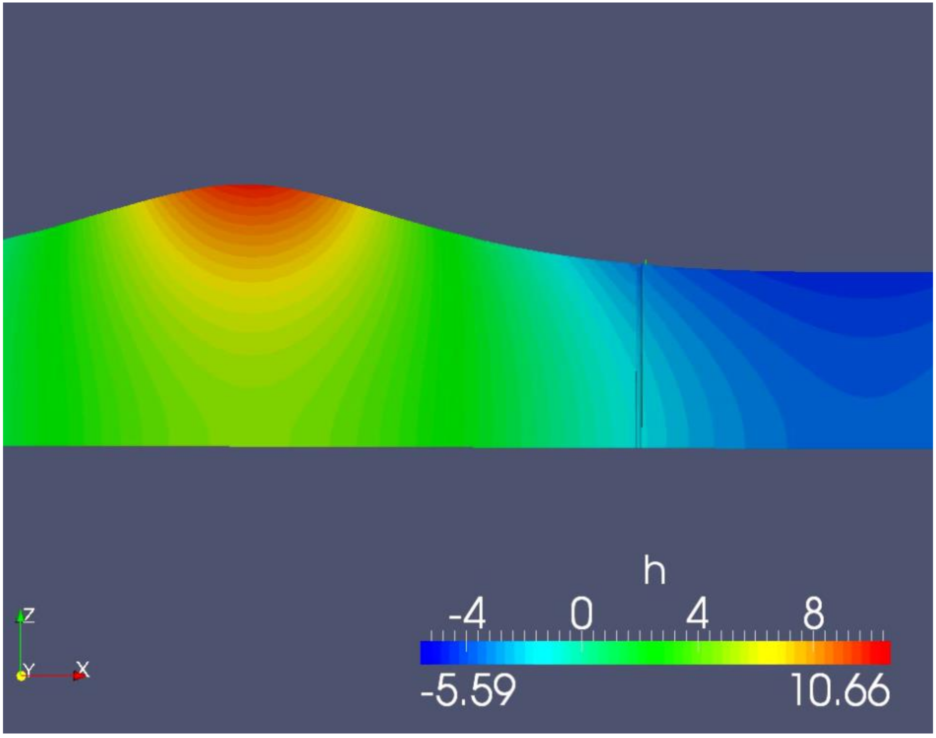

[frame 2: not available (video didn't cover the whole wave period)]

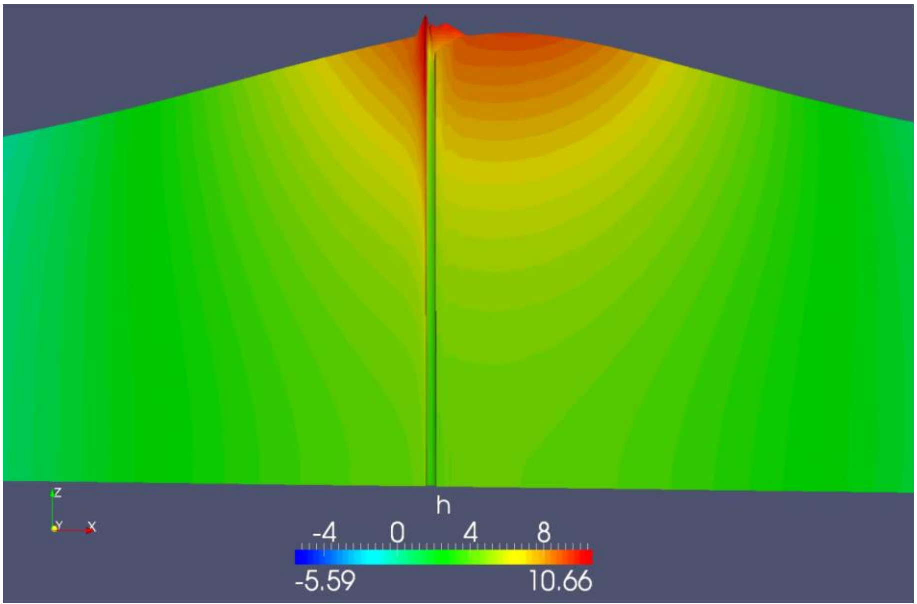

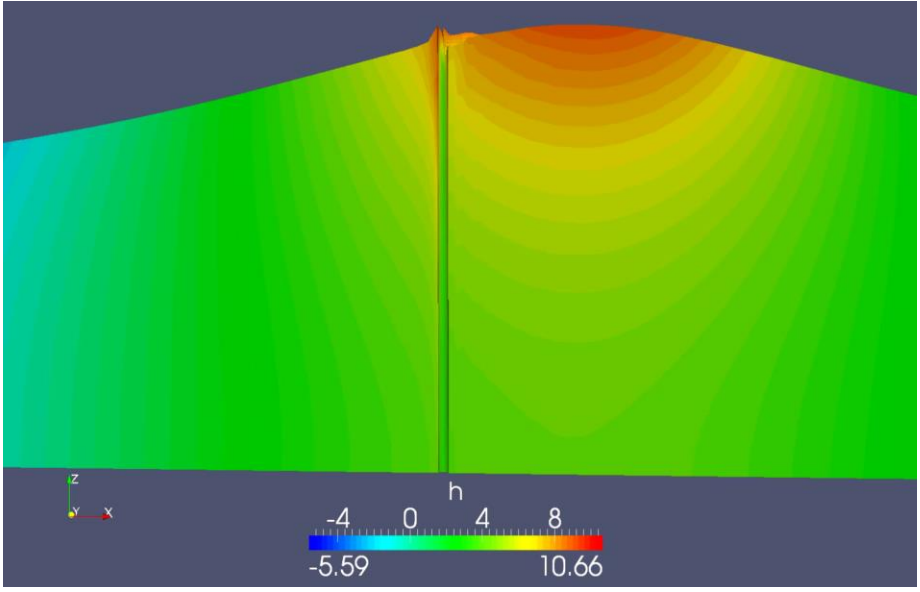

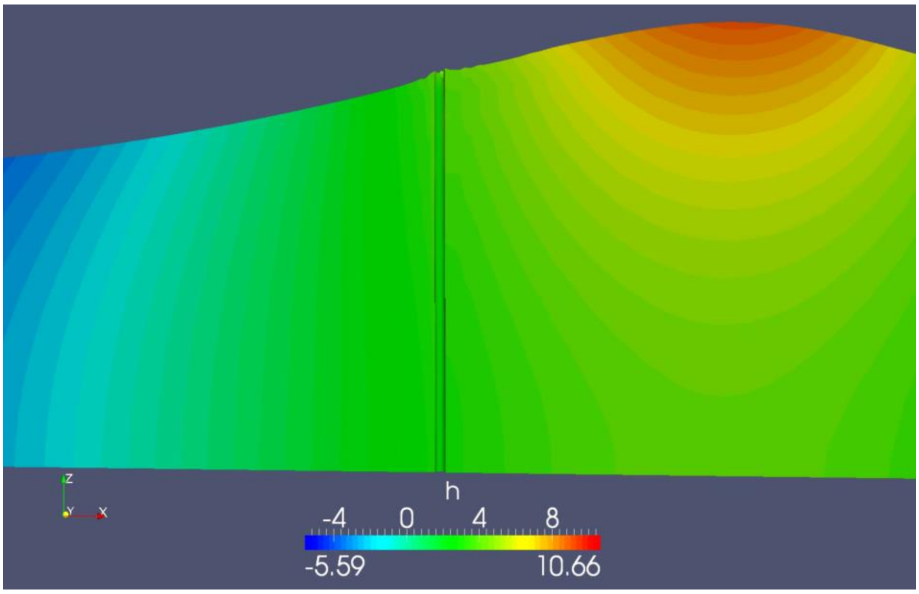

Figure C.24 – Wave shape near the cylinder for different wave phases. Case 1 [H=16.9m, T=12.7s, d=34m, D=1.0m]

C.6. RESULTING FORCES ON THE SHAFT OF THE GBS

C.6.1. Overview

In this section the resulting forces from FinLab on the shaft are listed.
A comparison is made between the force on the shaft of the GBS and the monopile, see Figure C.25.

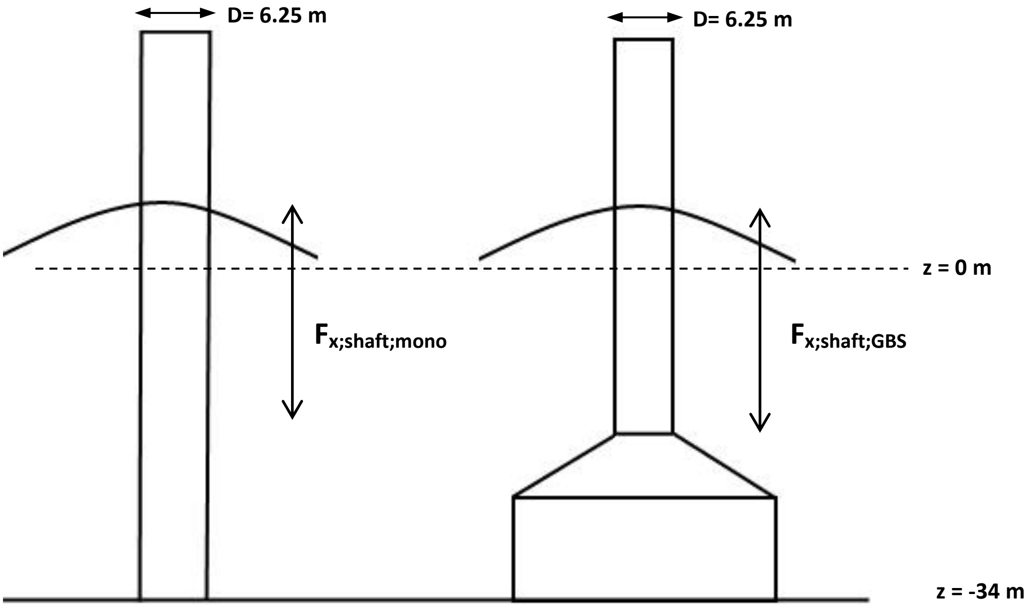

Figure C.25– Structures used to investigate the influence of the caisson

This was done for the following cases:

- Case 1: H=16.9m T=12.7s d=34m (ULS wave)
- Case 2: H=16.9m T=12.7s d=50m
- Case 3: H=10.0m T=9.7s d=34m
- Case 4: H=5.5m T=7.4s d=34m

Per case the next results are given:

- (A comparison of the undisturbed velocity in FinLab with non-linear wave theory)
- A comparison between the forces following from FinLab and the Morison equation.
- The force on the upper part of the shaft for a monopile and a GBS

See Chapter 5.6.1 in the main report and Appendix C.3.1 for a description on how the analytical results from the Morison equation, as represented below, were obtained.

The background of the wave cases can be found in Chapter 5.7 of the main report.

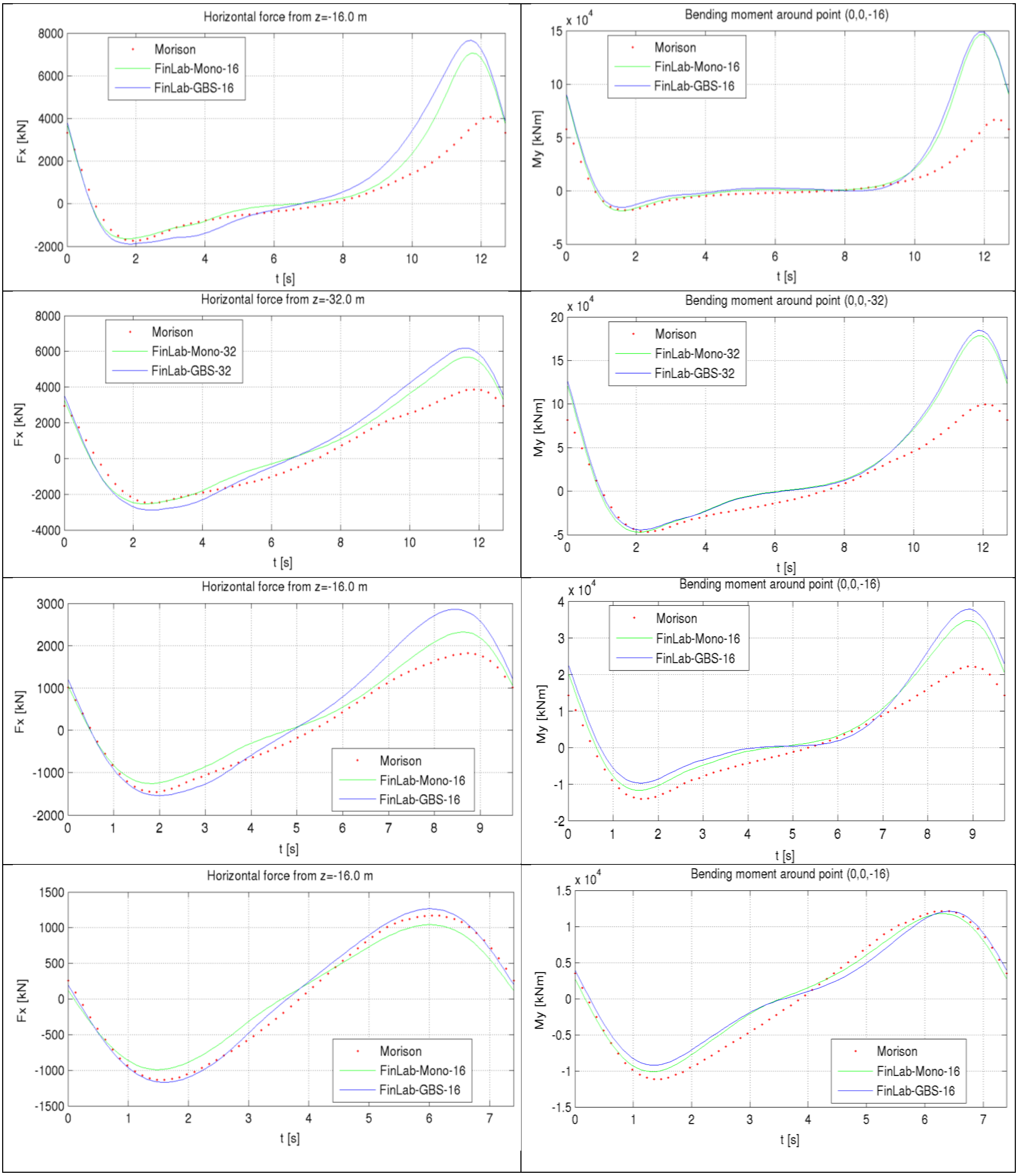

Figure C.26 – Overview of the results, left: Horizontal force. Right: Bending moment. Cases 1-4

C.6.2. Results

H [m]	16.9	dT [s]	1/90T	section	-16..WL
T [s]	12.7	per [-]	40	r [m]	80*
d [m]	34	theta [-]	1.0		case 1

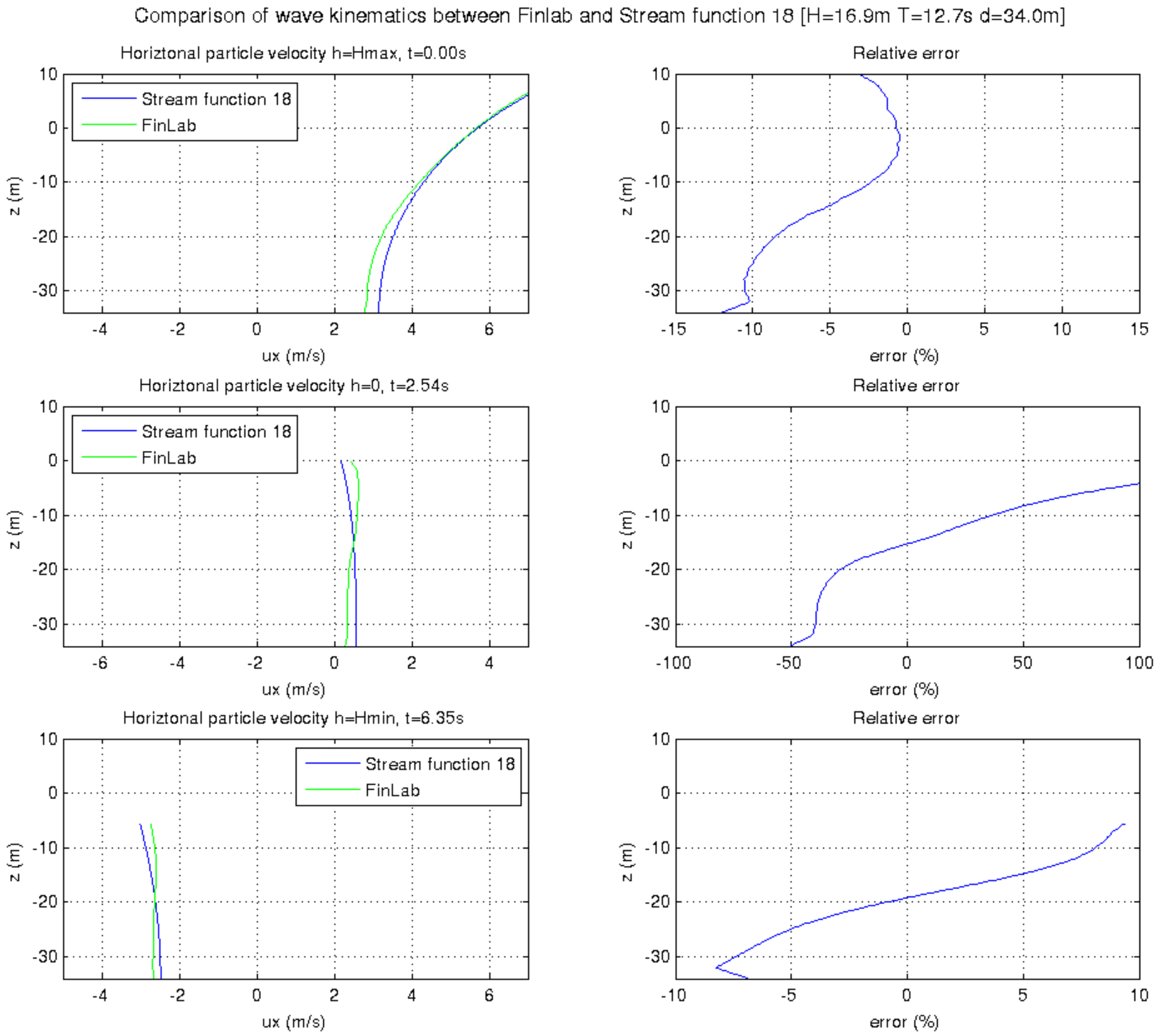

*Note that the radius is actually too small (<1/2L). The influence was investigated by means of the sensitivity check in Appendix C.7 and found to be small.

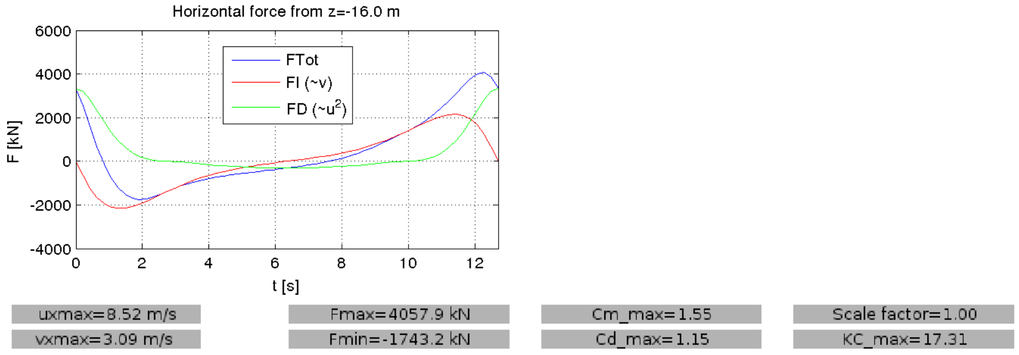

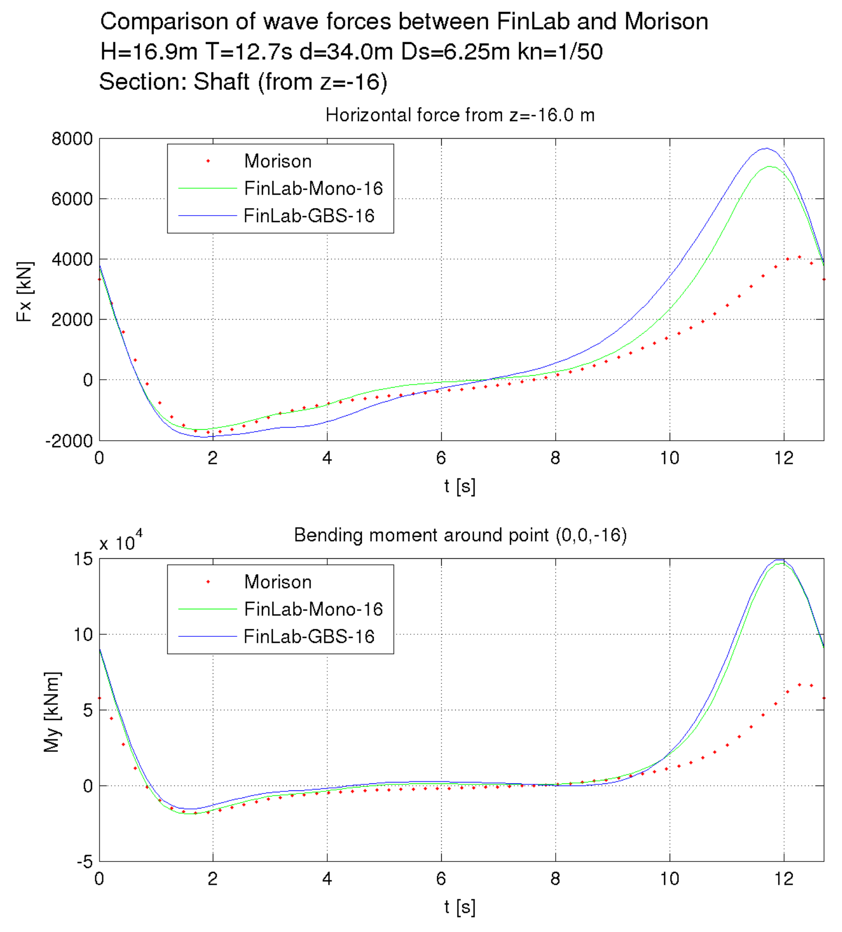

	Morison	FinLab-Mono-16	Diff 1-2 (%)	FinLab-GBS-16	Diff 1-4 (%)	Diff 2-4 (%)
Fmax	4057.87	7068.35	74	7663.37	89	8.4
Fmin	-1743.19	-1645.97	-5.6	-1890.08	8.4	15
Mmax	66503.8	146569	1.2e+02	148946	1.2e+02	1.6
Mmin	-18259.7	-18789.9	2.9	-15721.2	-14	-16
Mcycle	84763.6	165359	95	164667	94	-0.42

Interpretation

- Velocities and force dominance: The undisturbed velocity pattern resulting from FinLab does not correspond very well with theory here. This probably has to do with fixing the grid in order to calculate the force on the upper part of the shaft, because compared to the case with the full monopile (see Appendix C.3.3) the situation has worsened. Although the profiles don't have exactly the same shape, relative differences at the extremes are still quite small (~10%).
- Force dominance: the force is both drag-and inertia dominated

- Force comparison between FinLab and Morison: the green line (FinLab) represents the same case as the red line (Morison). The maximum horizontal force increases with 89%. The maximum bending moment even with 120%, indicating that, compared to Morison, the force is not only increasing, but also acting at a higher level. The bending moment cycle also increases.
  See the discussion of Appendix C.8 for this difference between FinLab and Morison.

- Force influence of the caisson: with respect to a single monopile the caisson leads to:
    - An increase in the magnitude of the force peaks (8% for the maximum horizontal force and 15% for the minimum).
    - On the other hand the maximum bending moment is not influenced, indicating that the increase in force is mainly at the bottom of the shaft.
    - The minimum bending moment decreases, while the force increases in magnitude, indicating that it acts at a lower level.
    - With respect to the overall bending moment cycle no differences occur due to the presence of the caisson.

H [m]	16.9	dT [s]	1/90T	section	-32..WL
T [s]	12.7	per [-]	40	r [m]	120
d [m]	**50 m**	theta [-]	1.0		case 2

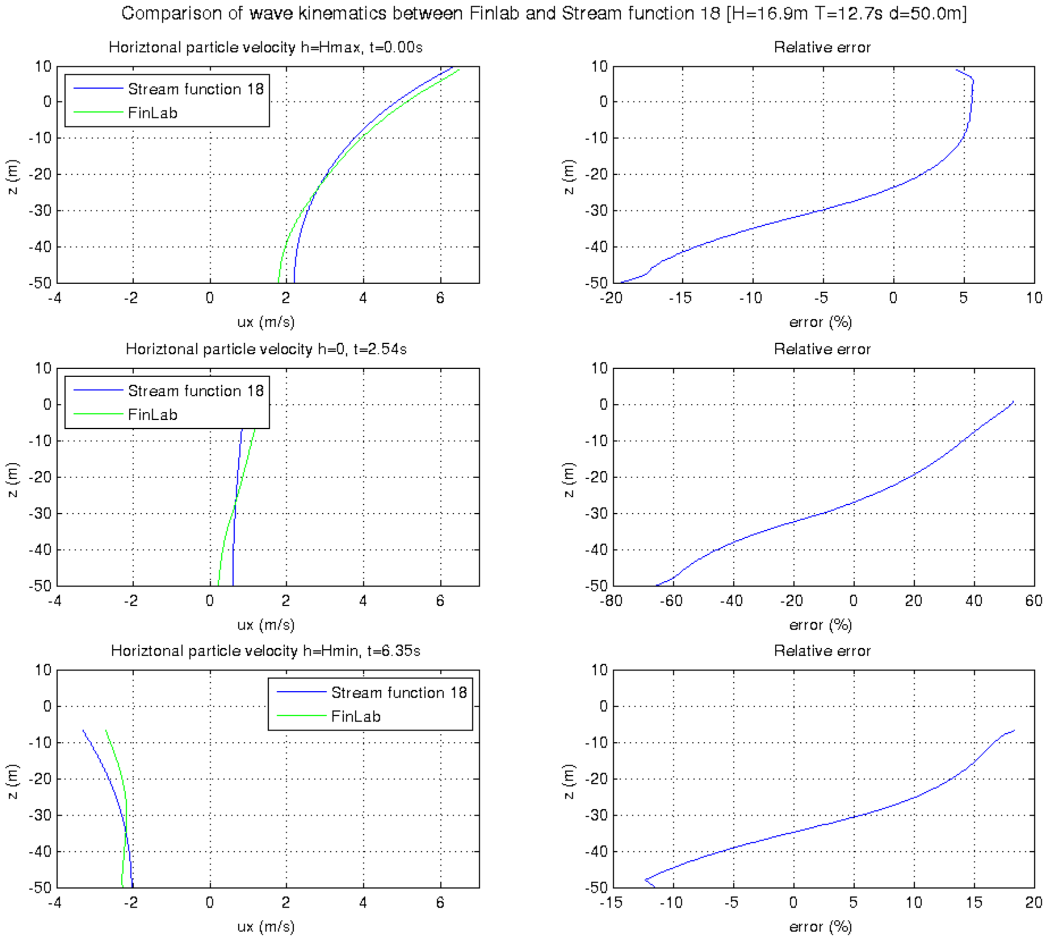

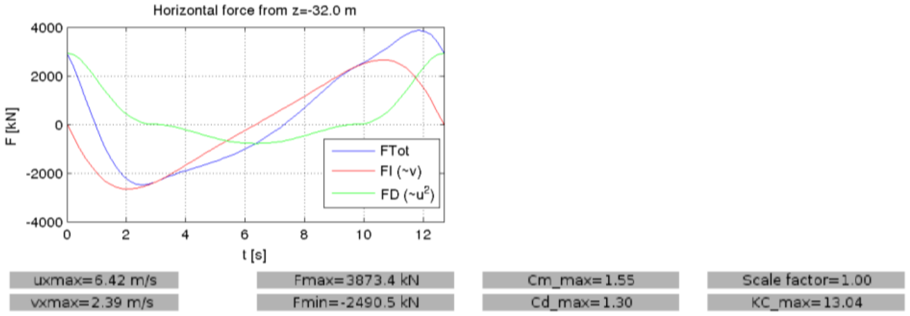

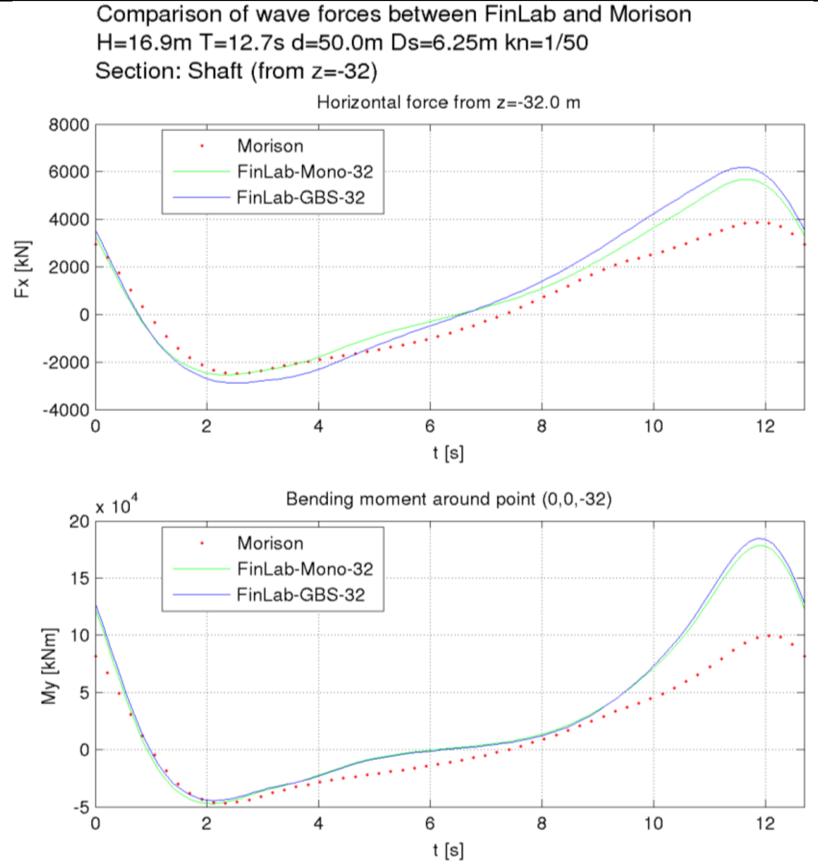

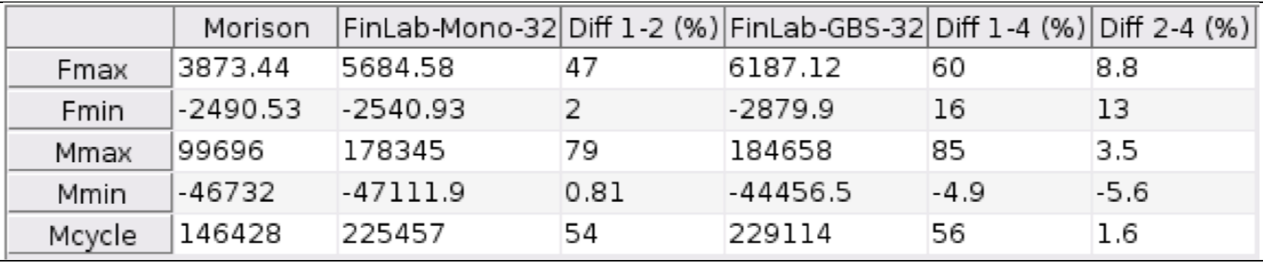

	Morison	FinLab-Mono-32	Diff 1-2 (%)	FinLab-GBS-32	Diff 1-4 (%)	Diff 2-4 (%)
Fmax	3873.44	5684.58	47	6187.12	60	8.8
Fmin	-2490.53	-2540.93	2	-2879.9	16	13
Mmax	99696	178345	79	184658	85	3.5
Mmin	-46732	-47111.9	0.81	-44456.5	-4.9	-5.6
Mcycle	146428	225457	54	229114	56	1.6

Interpretation

- Velocities, force dominance and force comparison: the same remarks as for the case with d=34m are valid here.

- Force influence of the caisson: with respect to a single monopile the caisson leads to:
  - An increase in the magnitude of the force peaks (9% for the maximum horizontal force and 13% for the minimum).
  - On the other hand the maximum bending moment is hardly influenced, indicating that the increase in force is mainly at the bottom of the shaft.
  - The minimum bending moment decreases a bit, while the force increases in magnitude, indicating that it acts at a lower level.
  - With respect to the overall bending moment cycle no differences occur due to the presence of the caisson.

  So, compared to the water depth of 34 m the effects are the same.

H [m]	10.0	dT [s]	1/90T	section	-16..WL
T [s]	9.7	per [-]	30	r [m]	80
d [m]	34	theta [-]	1.0		case 3

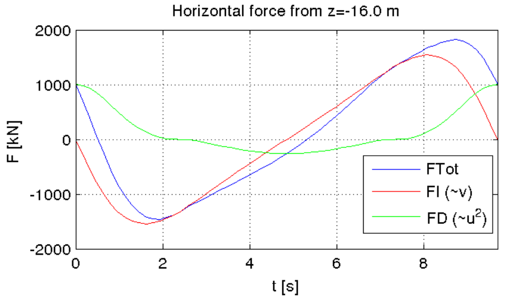

uxmax=4.63 m/s
vxmax=2.27 m/s

Fmax=1822.7 kN
Fmin=-1461.3 kN

Cm_max=1.75
Cd_max=1.50

Scale factor=1.00
KC_max=7.18

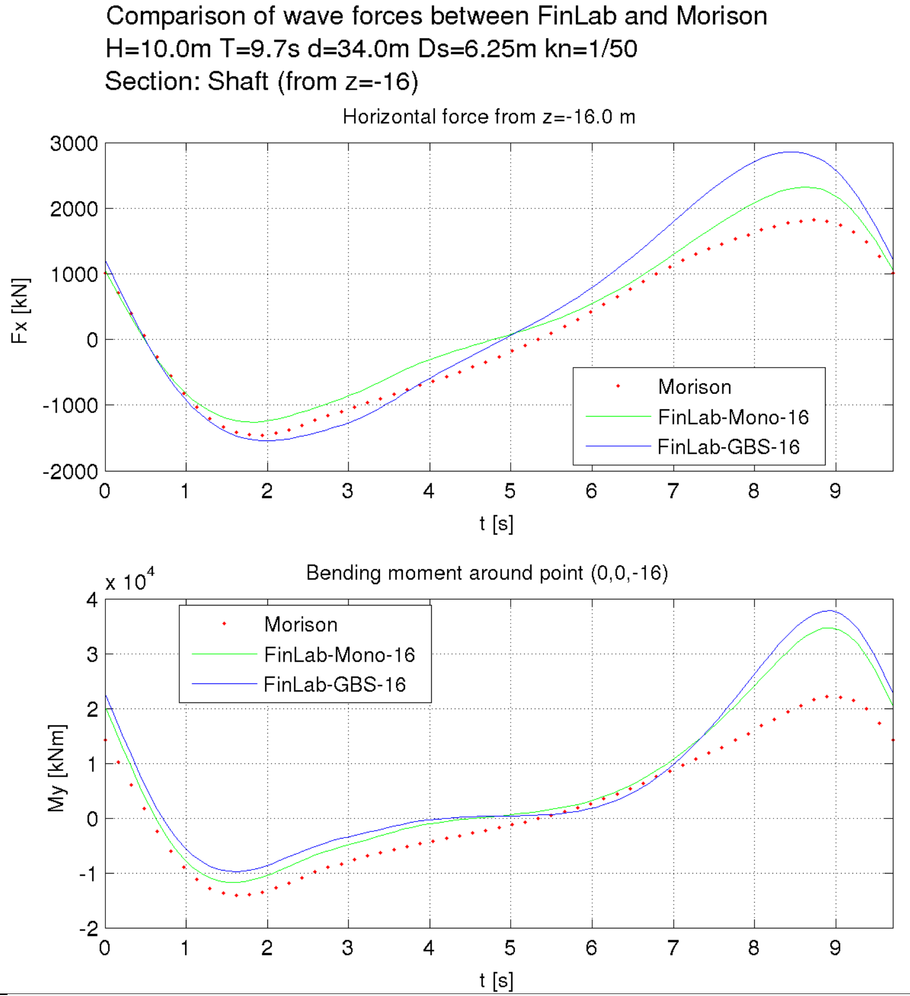

	Morison	FinLab-Mono-16	Diff 1-2 (%)	FinLab-GBS-16	Diff 1-4 (%)	Diff 2-4 (%)
Fmax	1822.69	2325.03	28	2856.02	57	23
Fmin	-1461.26	-1257.58	-14	-1543.11	5.6	23
Mmax	22153.4	34716.6	57	37782.6	71	8.8
Mmin	-14159.9	-11758.3	-17	-9756.27	-31	-17
Mcycle	36313.4	46474.9	28	47538.9	31	2.3

Interpretation

- Force dominance: the force is mainly inertia dominated.
- Force comparison between FinLab and Morison: The same effect as for case 1 and 2 occurs. The maximum horizontal force increases with 28%. The maximum bending moment with 57%. The bending moment cycle also increases with 28%.

- Force influence of the caisson: with respect to a single monopile the caisson leads to:
    - Also here an increase in the magnitude of the force peaks (23% for the maximum and minimum horizontal force, which is higher than the previous case).
    - Here the maximum bending moment is influenced a bit, but not as much as the maximum force, indicating that the increase in force is mainly at the bottom of the shaft.
    - Also here the minimum bending moment decreases, while the force increases in magnitude, indicating that it acts at a lower level.
    - Also here with respect to the overall bending moment cycle hardly any differences (2%) occur due to the presence of the caisson.

H [m]	5.5	dT [s]	1/90T	section	-16..WL
T [s]	7.4	per [-]	20	r [m]	70
d [m]	34	theta [-]	1.0		case 4

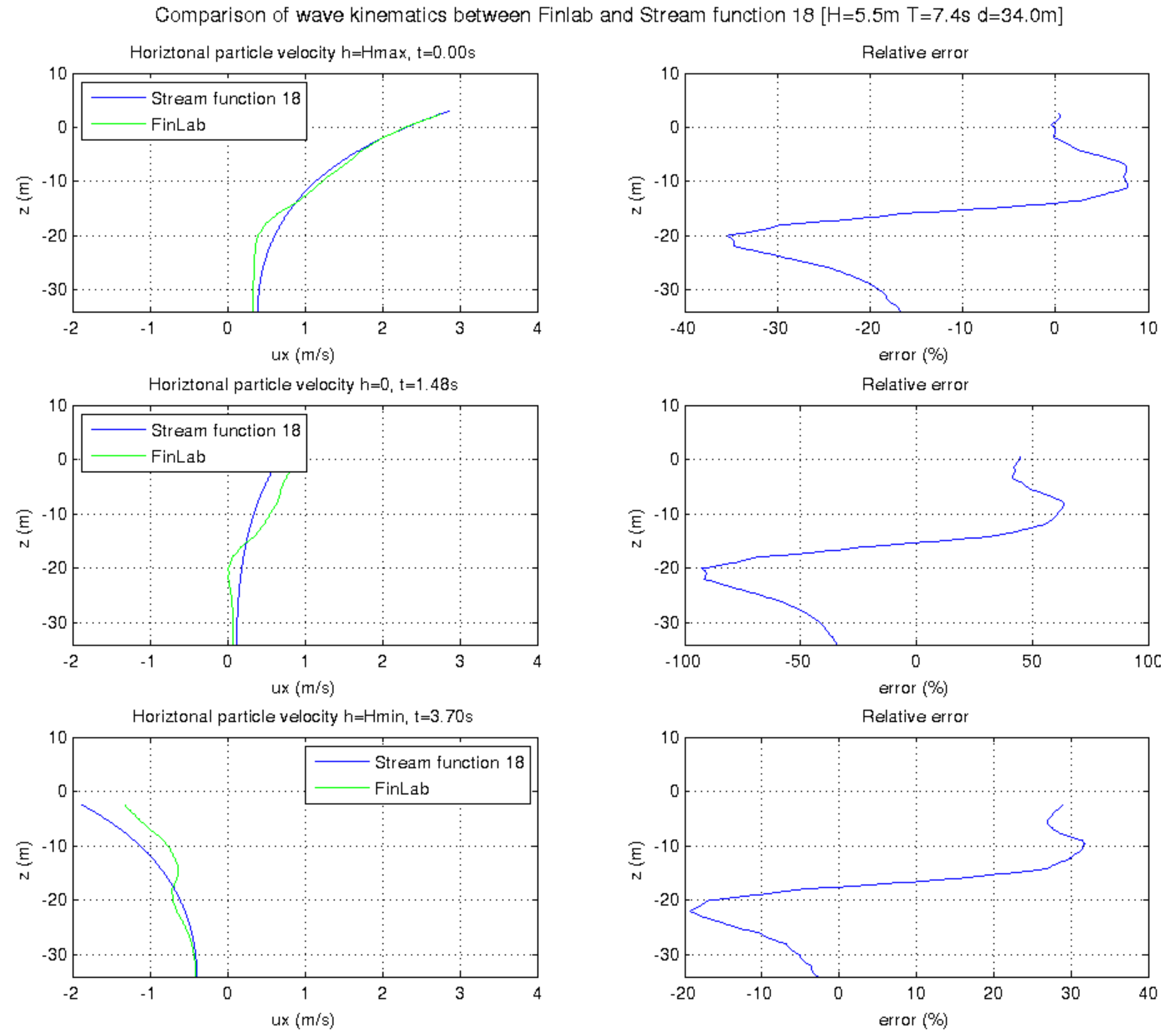

*see discussion below for distortion of velocity profile

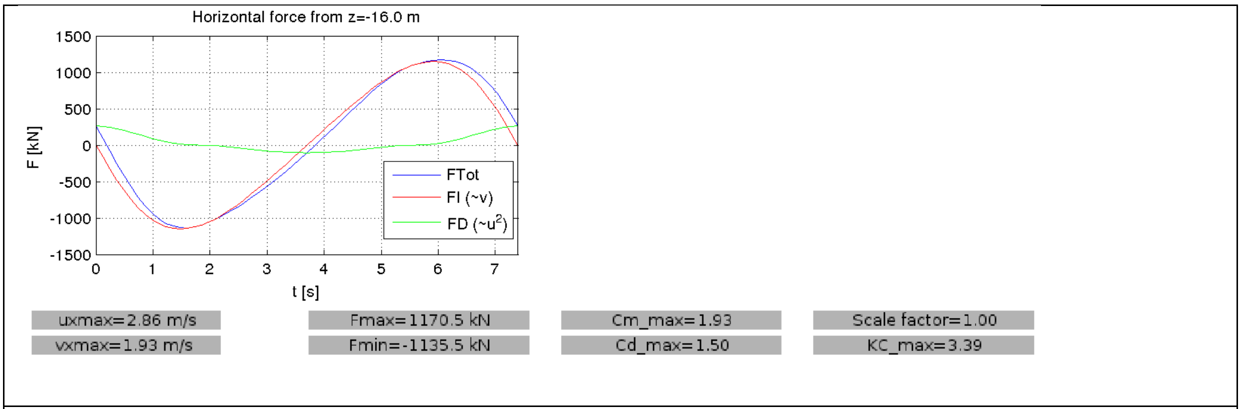

uxmax=2.86 m/s
vxmax=1.93 m/s
Fmax=1170.5 kN
Fmin=-1135.5 kN
Cm_max=1.93
Cd_max=1.50
Scale factor=1.00
KC_max=3.39

Comparison of wave forces between FinLab and Morison
H=5.5m T=7.4s d=34.0m Ds=6.25m kn=1/50
Section: Shaft (from z=-16)

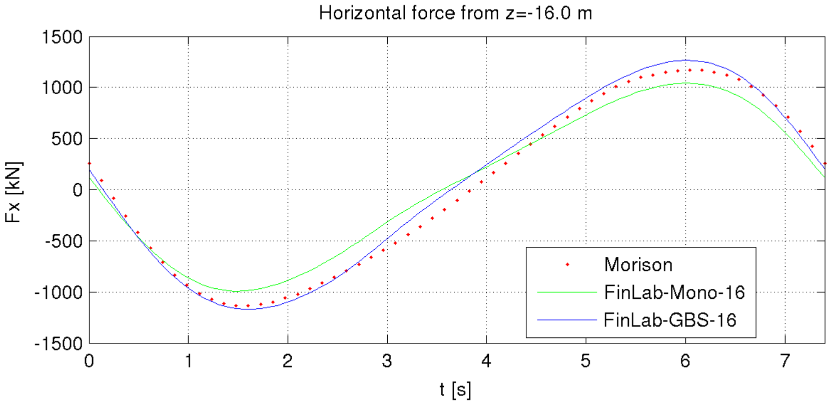

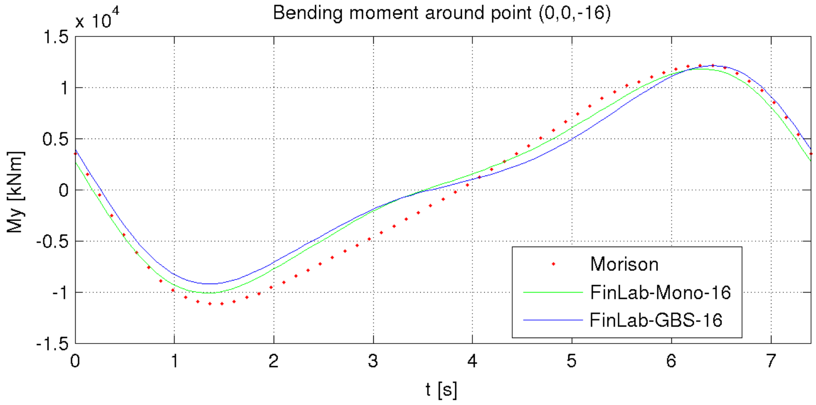

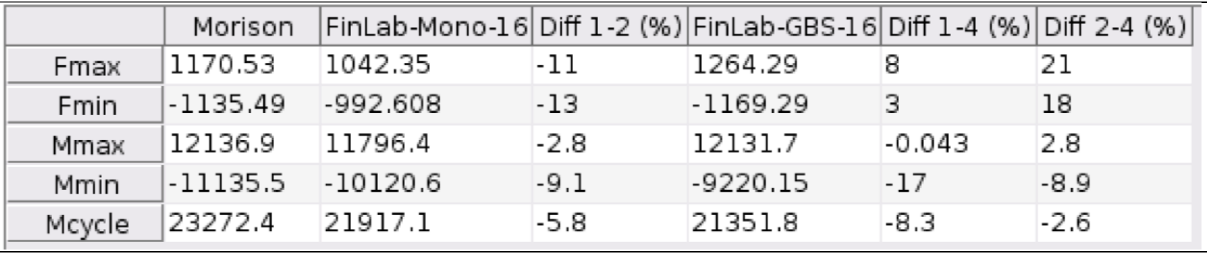

	Morison	FinLab-Mono-16	Diff 1-2 (%)	FinLab-GBS-16	Diff 1-4 (%)	Diff 2-4 (%)
Fmax	1170.53	1042.35	-11	1264.29	8	21
Fmin	-1135.49	-992.608	-13	-1169.29	3	18
Mmax	12136.9	11796.4	-2.8	12131.7	-0.043	2.8
Mmin	-11135.5	-10120.6	-9.1	-9220.15	-17	-8.9
Mcycle	23272.4	21917.1	-5.8	21351.8	-8.3	-2.6

Interpretation

- Velocities: the undisturbed velocity pattern resulting from FinLab does not correspond very well with theory here. The situation is even worse as for H=16.9m (case 1). Here the velocity profile clearly looks distorted around the level of the top of the cone (-16m).
  By performing the sensitivity check (see Appendix C.7) it was found that for 2.5 as much periods the differences became smaller, and the profiles didn't contain a bump any more. Apparently for this number periods the velocity pattern under the wave hasn't built up completely yet. The influence on the force is however small, because for the situation with 50 periods the difference is in the order of 5%.
  Later it was also found that by having the values of theta and zeta equal to each other the bump also disappeared.

- Force dominance: the total force is highly inertia dominated.
- Force comparison between FinLab and Morison: compared to case 1-3 another effect occurs here. Instead of higher peaks, FinLab now gives lower force peaks (~-10%). The maximum bending moment is about the same, but the minimum bending moment is 10% lower, resulting in a 6% lower bending moment cycle.

- Force influence of the caisson: The velocity profile doesn't match very well with theory here. So one could say little about the forces. But in the sensitivity check of Appendix C.7 it was found that for a better fit of the wave kinematics the force didn't change significantly. So, therefore the following conclusions can be drawn with the note that the errors in the velocities are still quite high for the wave through, and that the magnitude of the differences may change when also for the GBS a calculation with 50 periods is performed. With respect to a single monopile the caisson leads to:
  - Also here an increase in the magnitude of the force peaks (21% for the maximum and 18% for the minimum horizontal force, being about equal to the previous case).
  - The maximum bending moment is hardly influenced, indicating that the increase in force is mainly at the bottom of the shaft.
  - Also here the minimum bending moment decreases, while the force increases in magnitude, indicating that it acts at a lower level.
  - Also here with respect to the overall bending moment cycle hardly any differences occur due to the presence of the caisson.

C.7. SENSITIVITY CHECK

C.7.1. Overview

The following sensitivity checks (of model parameters) have been performed:

- Increasing the radius of the grid [case 1: H=16.9m T=12.7s d=34 m]
- Densification of the grid (2x as dense) [case 1: H=16.9m T=12.7s d=34 m]
- Decrease damping value [case 1: H=16.9m T=12.7s d=34 m]
- Decrease time step with a factor 2 [case 3: H=10.0m T=9.7s d=34m]
- Increasing the number of periods calculated [case 1: H=16.9m T=12.7s d=34m]
- Increasing the number of periods calculated [case 4: H=5.5m T=7.4s d=34m]

In addition for the ULS wave (case 1) the following sensitivity check (of geometry) has been performed:

- Decreasing the diameter of the shaft: D=1.0m

This check was performed in order to investigate whether FinLab also gave higher forces than the Morison equation for this smaller diameter. (D/L ratio is smaller than for D=6.25m, so the Morison equation is expected to be even more valid).

C.7.2. Sensitivity of model parameters

H [m]	16.9	dT [s]	1/90T	section	-16..WL
T [s]	12.7	per [-]	40	r [m]	80 / 120
d [m]	34	theta [-]	1.0	sensitivity:	**lager radius**

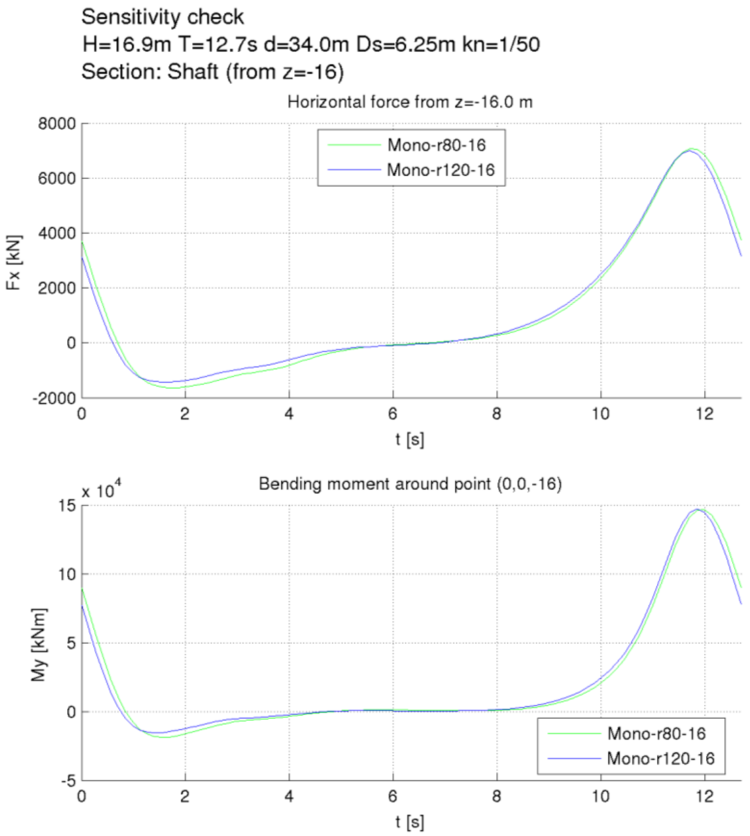

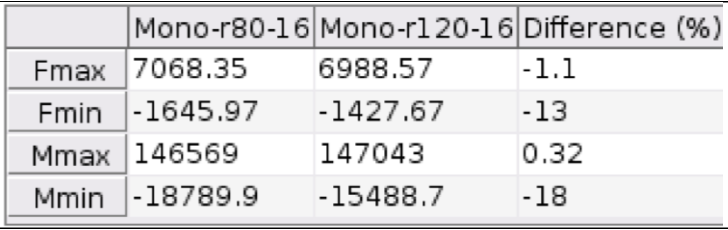

	Mono-r80-16	Mono-r120-16	Difference (%)
Fmax	7068.35	6988.57	-1.1
Fmin	-1645.97	-1427.67	-13
Mmax	146569	147043	0.32
Mmin	-18789.9	-15488.7	-18

Interpretation:

- The difference in maximum forces and bending moments is almost negligible. The minimum forces and bending moments seem to be influenced (a larger radius leads to a lower magnitude of the minimum force and bending moment).

H [m]	16.9	dT [s]	1/90T	section	-16..WL
T [s]	12.7	per [-]	40	r [m]	80*
d [m]	34	theta [-]	1.0	sensitivity:	**grid 2x dense**

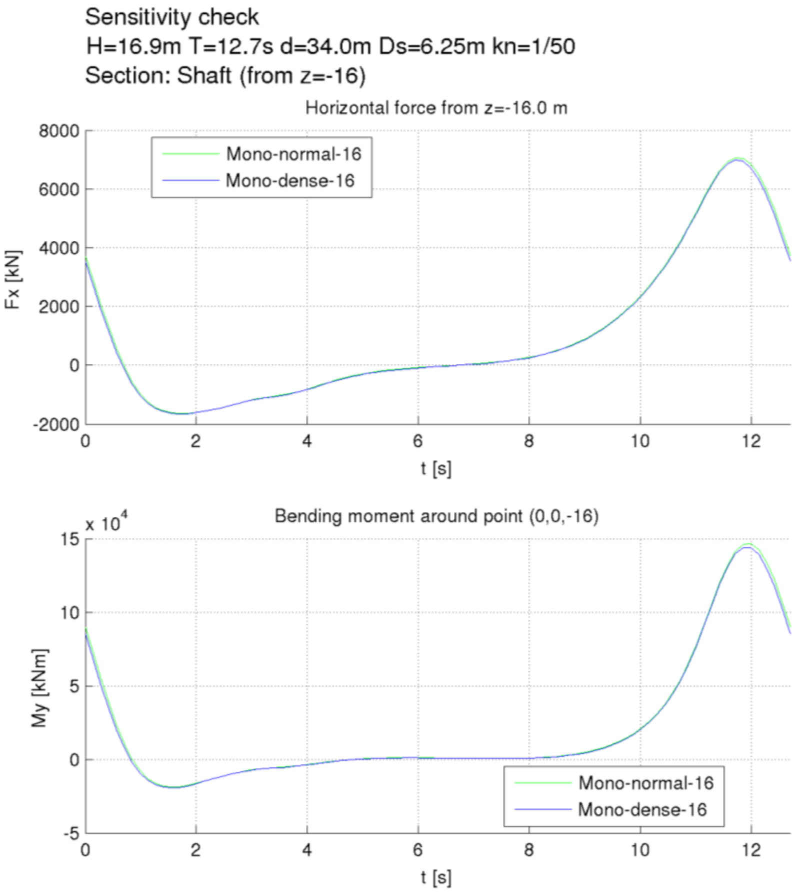

*Note that the radius is actually too small (<1/2L). The influence was investigated by means of the sensitivity check in Appendix C.7 and found to be small.

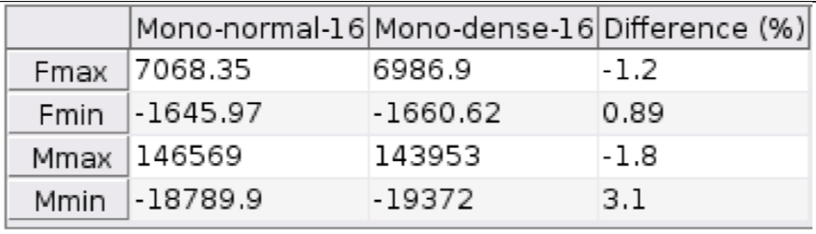

	Mono-normal-16	Mono-dense-16	Difference (%)
Fmax	7068.35	6986.9	-1.2
Fmin	-1645.97	-1660.62	0.89
Mmax	146569	143953	-1.8
Mmin	-18789.9	-19372	3.1

Interpretation

- The difference in forces and bending moments is almost negligible. So it can be concluded that a densification of the grid with a factor 2 has no impact on the outcome.

H [m]	16.9	dT [s]	1/90T	section	-34..WL
T [s]	12.7	per [-]	30	r [m]	80*
d [m]	34	**theta [-]**	**0.5 & 1.0**	sensitivity:	**theta**

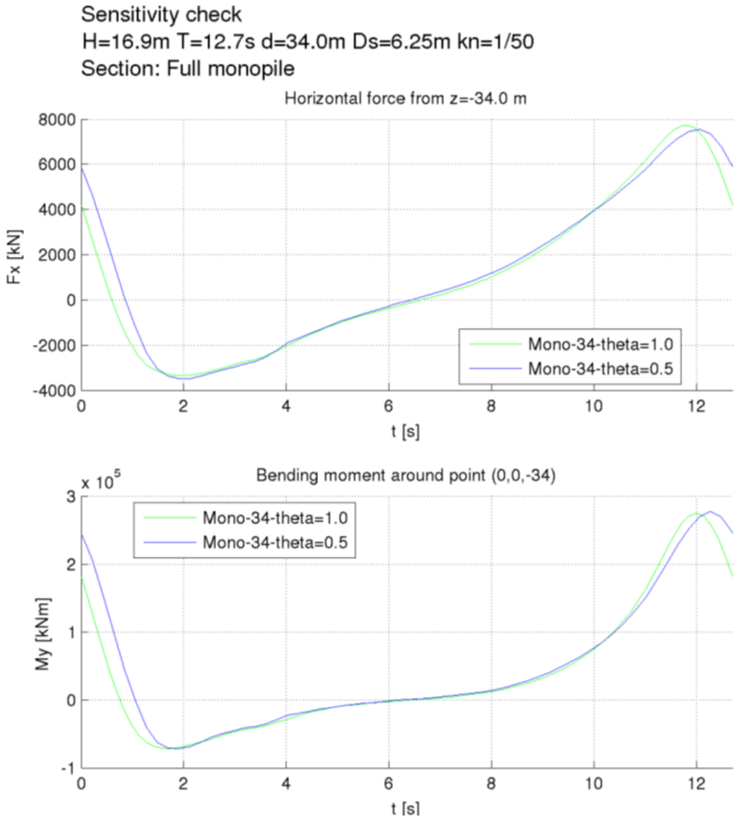

*Note that the radius is actually too small (<1/2L). The influence was investigated by means of the sensitivity check in Appendix C.7 and found to be small.

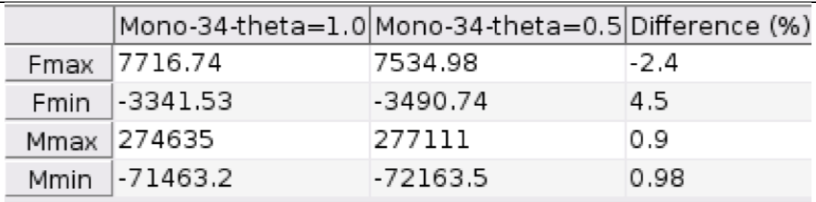

	Mono-34-theta=1.0	Mono-34-theta=0.5	Difference (%)
Fmax	7716.74	7534.98	-2.4
Fmin	-3341.53	-3490.74	4.5
Mmax	274635	277111	0.9
Mmin	-71463.2	-72163.5	0.98

Interpretation:

- The influence of the higher damping value (theta =1.0) on the forces is negligible. The highest damping value results even in the highest horizontal force. This may be due to the fact that the time step or the grid size was a bit different, because these parameters also influence the amount of damping. But differences are small, so no strong influences are expected and it can safely be concluded that the amount of damping doesn't influence the force peaks (for the validated wave the same was concluded, see Appendix C.3).

H [m]	10.0	dT [s]	1/90T & 1/180T	section	-34..WL
T [s]	9.7	per [-]	30	r [m]	80
d [m]	34	theta [-]	1.0	sensitivity:	**dt**

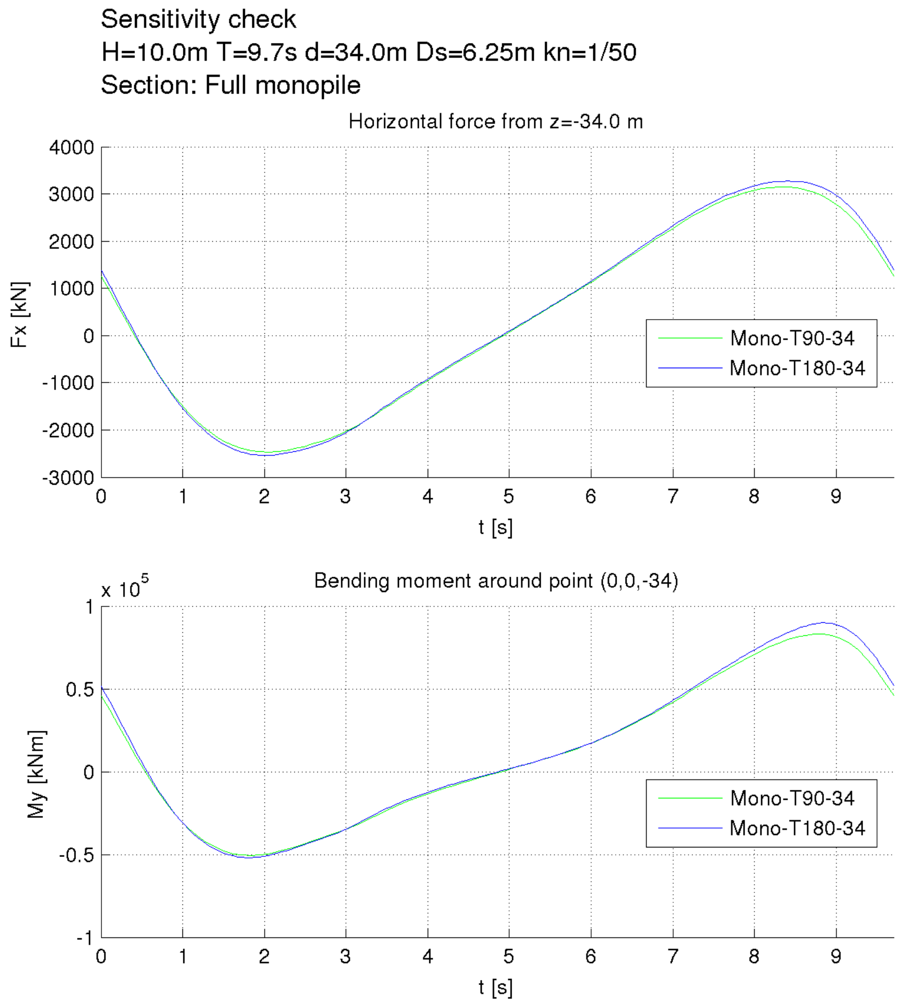
Sensitivity check
H=10.0m T=9.7s d=34.0m Ds=6.25m kn=1/50
Section: Full monopile

Horizontal force from z=-34.0 m

Bending moment around point (0,0,-34)

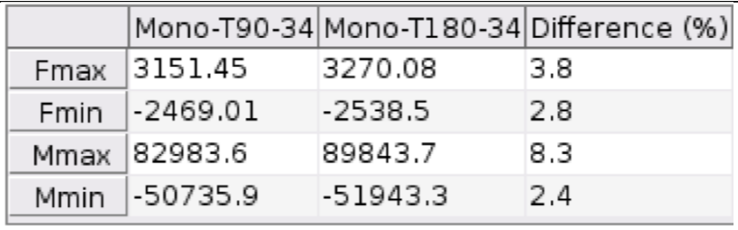

	Mono-T90-34	Mono-T180-34	Difference (%)
Fmax	3151.45	3270.08	3.8
Fmin	-2469.01	-2538.5	2.8
Mmax	82983.6	89843.7	8.3
Mmin	-50735.9	-51943.3	2.4

Interpretation:

- Forces: Due to the smaller timestep the magnitude of the maximum and minimum forces and bending moments increases with about 5%.

H [m]	16.9	dT [s]	1/90T	section	-16..WL
T [s]	12.7	per [-]	40 & 60	r [m]	80*
d [m]	34	theta [-]	1.0	sensitivity:	**long run case 1**

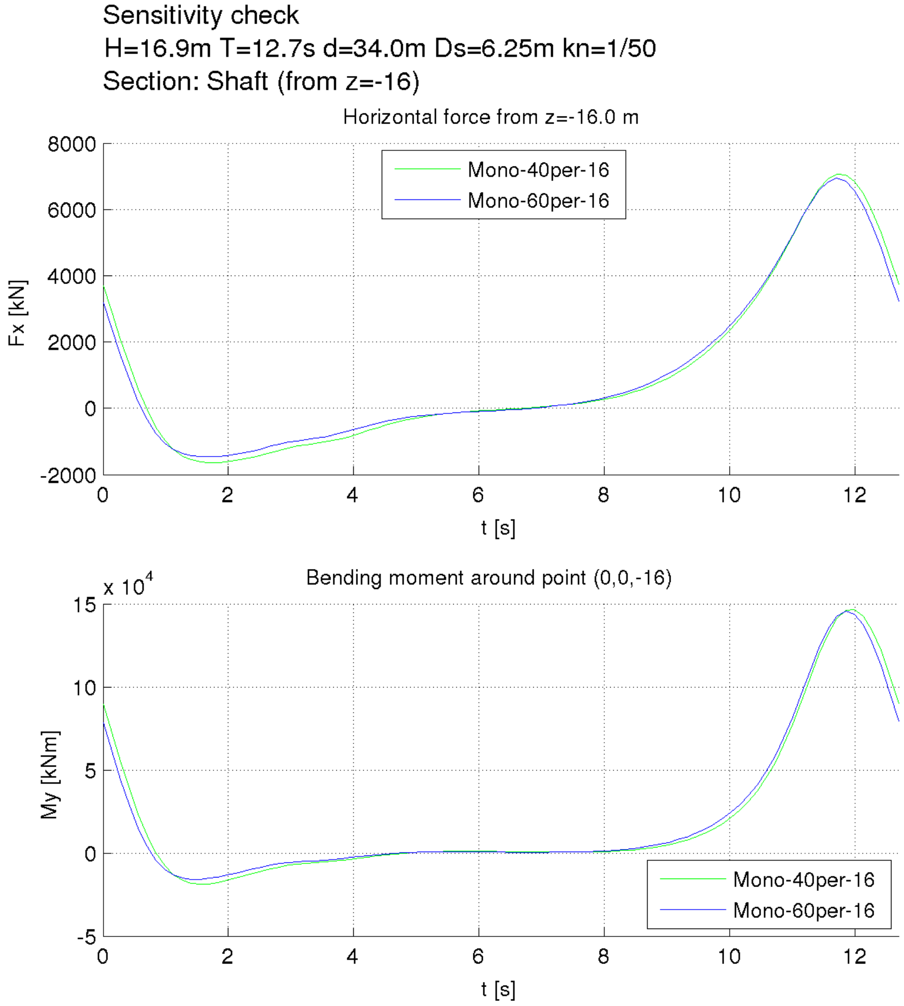

*Note that the radius is actually too small (<1/2L). The influence was investigated by means of the sensitivity check in Appendix C.7 and found to be small.

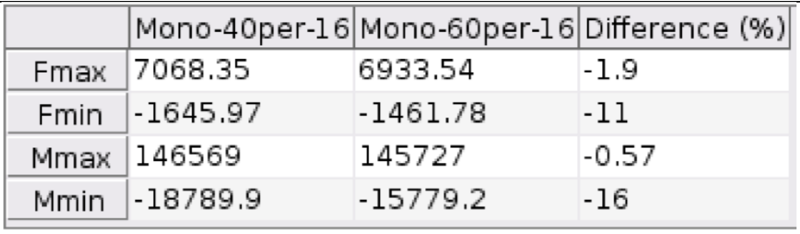

	Mono-40per-16	Mono-60per-16	Difference (%)
Fmax	7068.35	6933.54	-1.9
Fmin	-1645.97	-1461.78	-11
Mmax	146569	145727	-0.57
Mmin	-18789.9	-15779.2	-16

Interpretation:

- Also here the difference in maximum forces and bending moments is almost negligible. The minimum forces and bending moments seem to be influenced (a longer run leads to a lower magnitude of the minimum force and bending moment).

H [m]	5.5	dT [s]	1/90T	section	-16..WL
T [s]	7.4	per [-]	20 & 50	r [m]	70
d [m]	34	theta [-]	1.0	sensitivity:	**long run case 4**

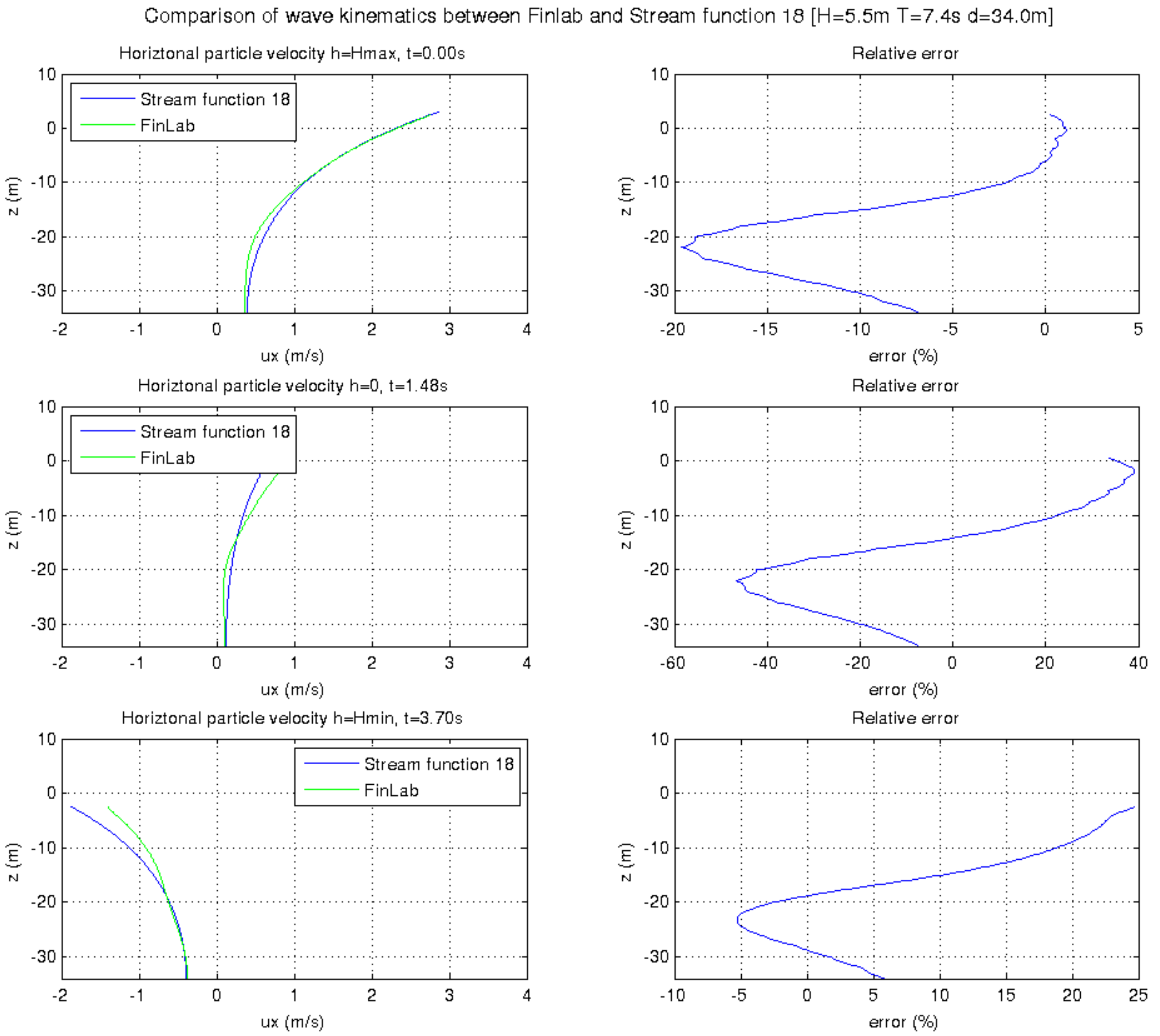

*figure based on run with 50 periods

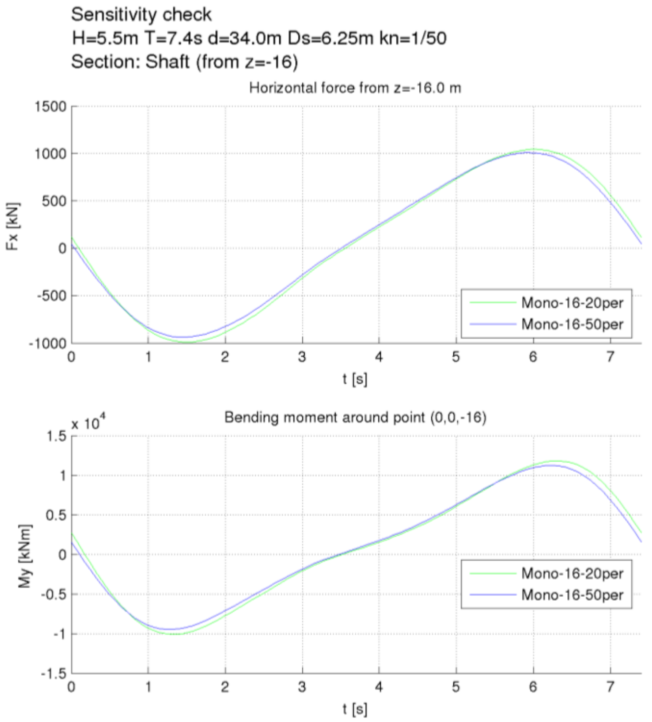

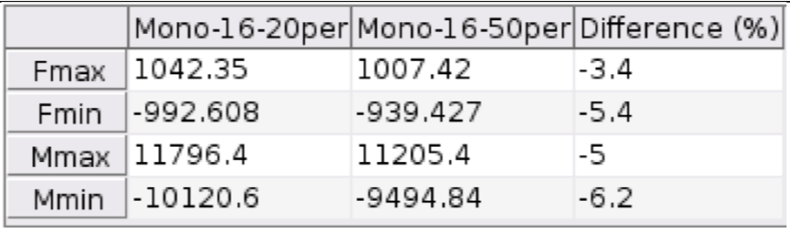

	Mono-16-20per	Mono-16-50per	Difference (%)
Fmax	1042.35	1007.42	-3.4
Fmin	-992.608	-939.427	-5.4
Mmax	11796.4	11205.4	-5
Mmin	-10120.6	-9494.84	-6.2

Interpretation:

- Velocities: with respect to the shorter run the velocity patterns look more like expected from theory. At wave crest the match is quite good, but at wave trough errors are still quite high (~20%). ‘Luckily’ the maximum force occurs at wave crest.
- Forces: Due to the longer run the magnitude of the maximum and minimum forces and bending moments decrease with about 5%.

C.7.3. Conclusions for sensitivity of model parameters

- Variation of the different model parameters leads to differences in the order of -2% in maximum bending moment and forces, and ~-10% for minimum force and bending moment.
  When the distinctive effects are combined the effect on the maximum force and bending moment is relative small (~-5%).
  The effect on the minimum force and bending moment is higher (~-25%)
- Especially the longer run and larger radius have significant impact on the magnitude of the minimum force and bending moment (leading to lower values).

C.7.4. Sensitivity of geometry

H [m]	16.9	dT [s]	1/90T	section	-34..WL
T [s]	12.7	per [-]	50	r [m]	120
d [m]	34 m	theta [-]	1.0	sensitivity:	**smaller D (1.0m)**

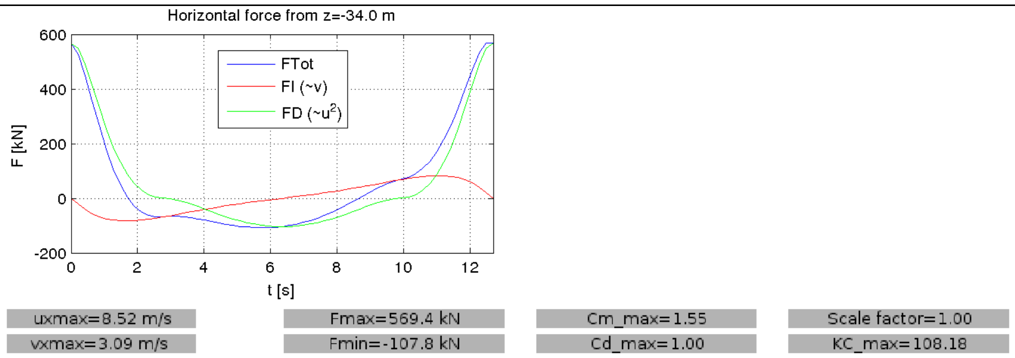

Comparison of wave forces between FinLab and Morison
H=16.9m T=12.7s d=34.0m Ds=1.00m kn=1/50
Section: Full monopile

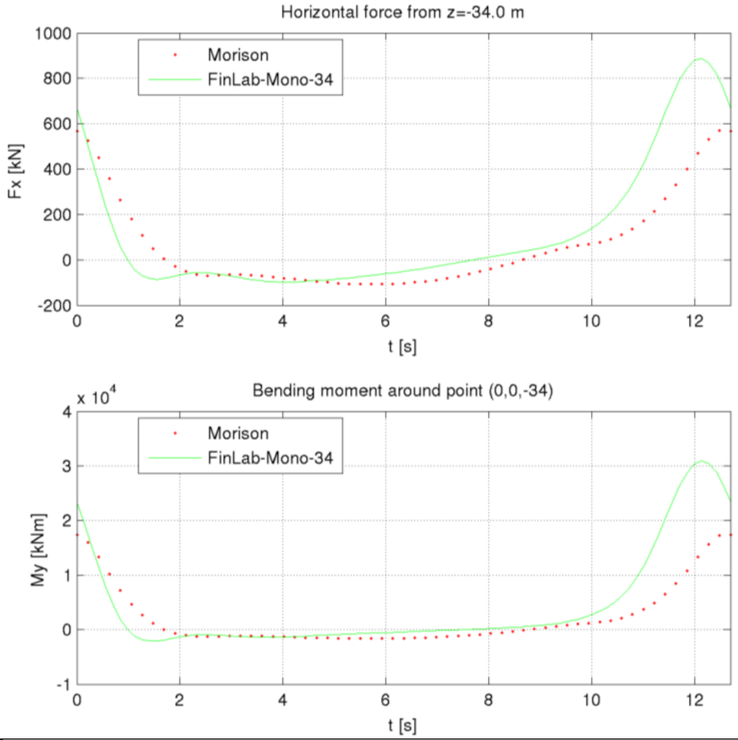

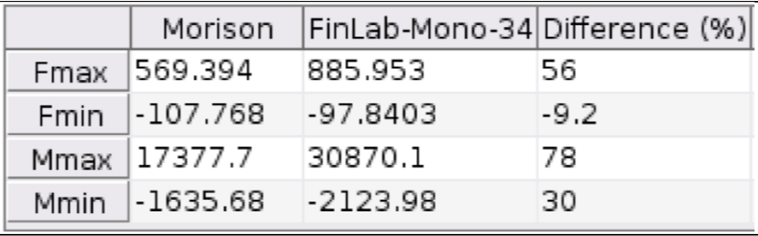

	Morison	FinLab-Mono-34	Difference (%)
Fmax	569.394	885.953	56
Fmin	-107.768	-97.8403	-9.2
Mmax	17377.7	30870.1	78
Mmin	-1635.68	-2123.98	30

Interpretation

- Force dominance: The force is almost fully drag-dominated.
- Force comparison between FinLab and Morison: Compared to the larger diameter (D=6.25) the same effect occurs. The maximum force given by FinLab also is about 50% higher. The bending moment about 80%.

C.8. ANALYSIS OF THE RESULTS

C.8.1. Observed results

The degree of non-linearity can be expressed by the so called Ursell number:

$$U_r = \frac{HL_0^2}{d^3} \tag{C.4}$$

with:

U_r	Ursell number	[-]
H	wave height	[m]
L_0	deep water wave length	[m]
d	water depth	[m]

For low Ursell numbers ($U_r \ll 1$) linear wave theory is valid. High numbers ($U_r > \sim 20$) correspond to higly non-linear waves. The wave profiles of wave cases 1,3 and 4 are listed in Figure C.27. The corresponding Ursell numbers can be found in Table C.3. From the wave profiles is clearly seen that the ULS wave (case 1) is highly non-linear, due to the high peak and relative flat through. Case 4 looks more like a liner wave, although it isn't.

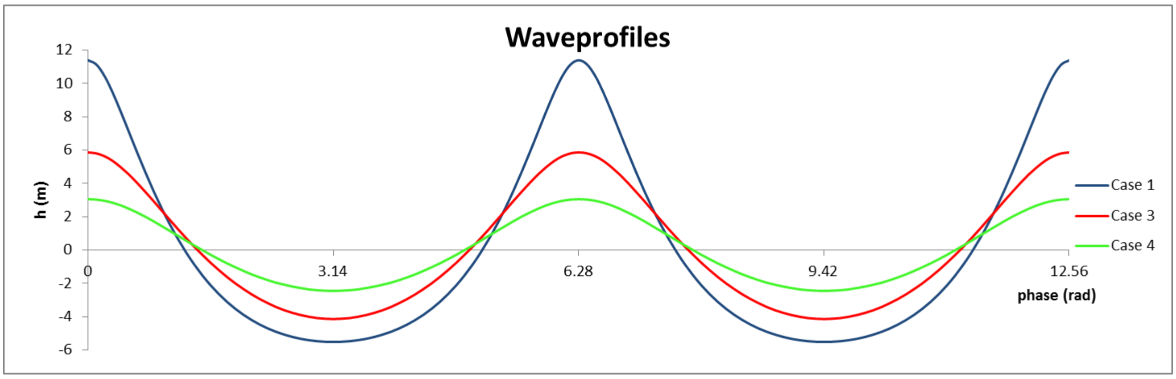

Figure C.27 - Water elevation for wave cases 1,3 and 4

Case	H [m]	T [s]	d [m]	L [m]	L0 [m]	U_r [-]	H/d [-]
1	16.9	12.7	34	217	252	27.2	0.50
2	16.9	12.7	50	236	252	8.6	0.34
3	10	9.7	34	142	147	5.5	0.29
4	5.5	7.4	34	88	85	1.0	0.16

Table C.3 - Ursell numbers and H/d ratio

C.8.2. Difference between FinLab and the Morison equation

It is not uncommon that a numerical package gives other outcomes than theory/experimental data. This often has to do with limitations of the methods used:

- The Morison equation is nothing but a model to describe the force, where the total force can be composed in a drag and inertia force. All physical processes are incorporated in the C_M and C_D values. It is however unclear what the exact test conditions have been (except from a given Re and KC number and roughness).
- FinLab on the other hand simulates the real flow around a structure and incorporates almost all the physical processes. The force is only based on pressure differences over the structure and a force due to wall friction. But it also is a source of differences, due

to assumptions (for example with respect to the turbulence) and it is sensible to numerical ‘error-sources’ like grid resolution or damping values.

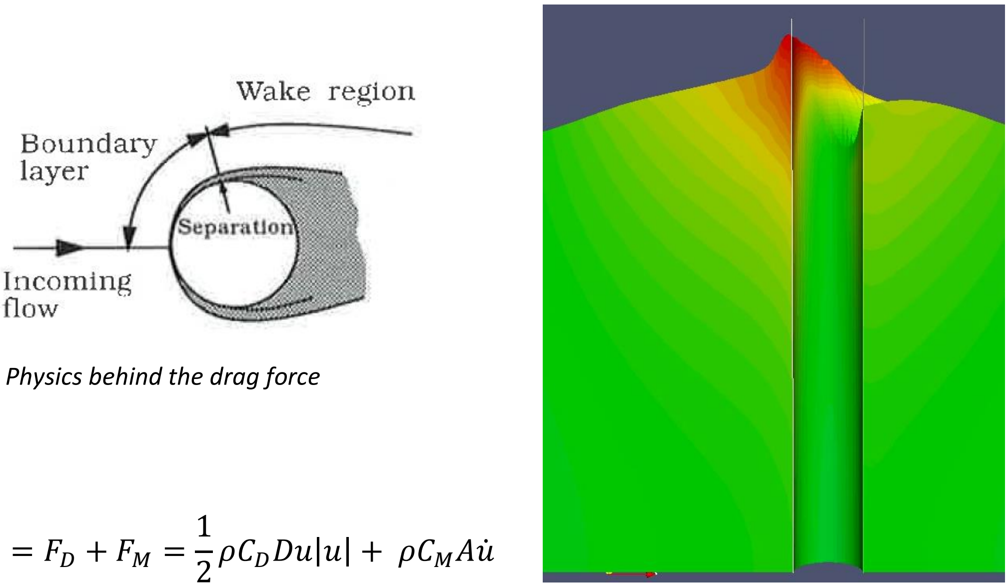

Physics behind the drag force

$$F = F_D + F_M = \frac{1}{2}\rho C_D D u|u| + \rho C_M A \dot{u}$$

Figure C.28 – Basis of a) the Morison equation and b) FinLab

C.8.2.1. Influence of inertia and drag coefficients

In order to determine the influence of the coefficients they were varied until a best fit appeared. In order to coincide with the peak at t=11.8 sec, both the C_M and C_D coefficient had to increase. Experimental limits for a rough cylinder like this one (k/D=0.003) in trans-critical flow (Re>4e6) are: $C_M \leq 2.0$ and $C_D \leq 1.50$ (see Appendix C.1.6).
With these parameters the maximum force comes closer to the force peak of FinLab (5.3 MN instead of 4.1 MN, so +30%), but now the minimum force starts to deviate (see Figure C.29).

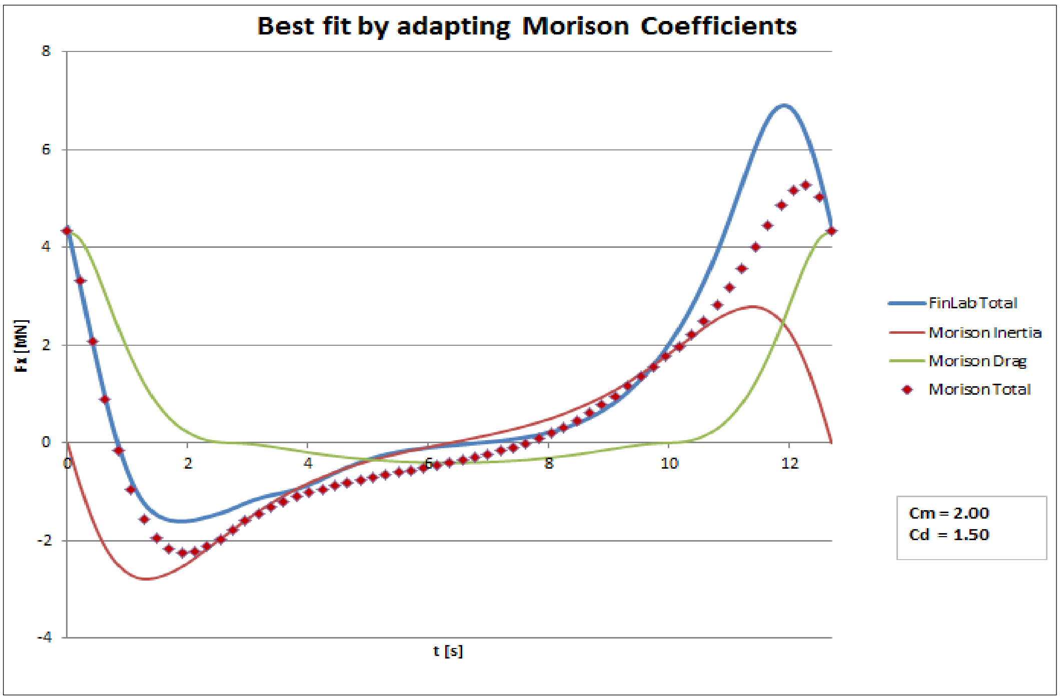

Figure C.29 – Globally adapting the Morison coefficient in order to obtain a ‘best fit’

Concluding it can be stated that, within the limits given by literature, there seems to be some scatter within the maximum force of the Morison equation (+30%). But it seems unrealistic that by adapting the coefficients the whole gap between Morison and FinLab (75%) is covered.

C.8.2.2. Influence of variable coefficients as function of depth

In the Morison equation used in this thesis only one set of C_M and C_D coefficients was used for the whole height. This simplification is theoretically not correct. Below a comparison is made with the results from a spreadsheet available at BAM. This spreadsheets divides the structure in sections. For every small section the KC number and corresponding C_M and C_D values are determined.

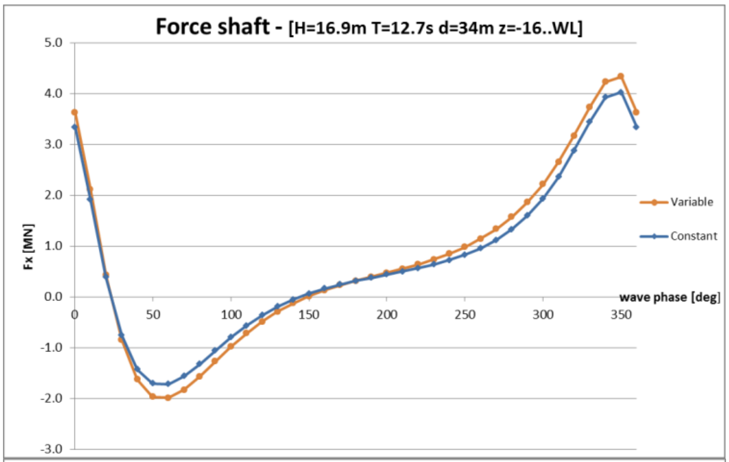

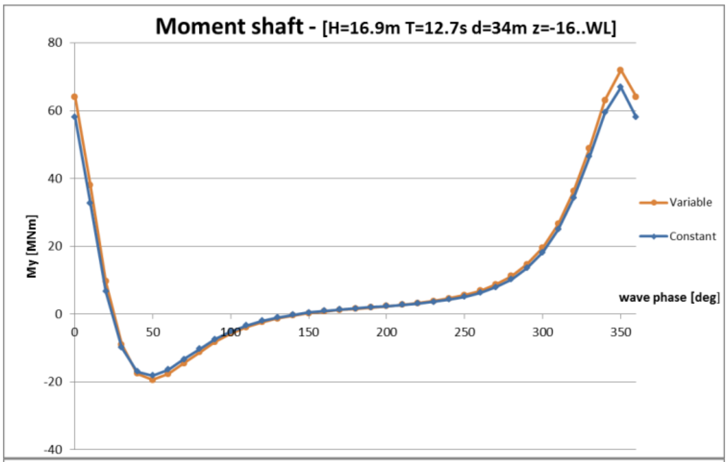

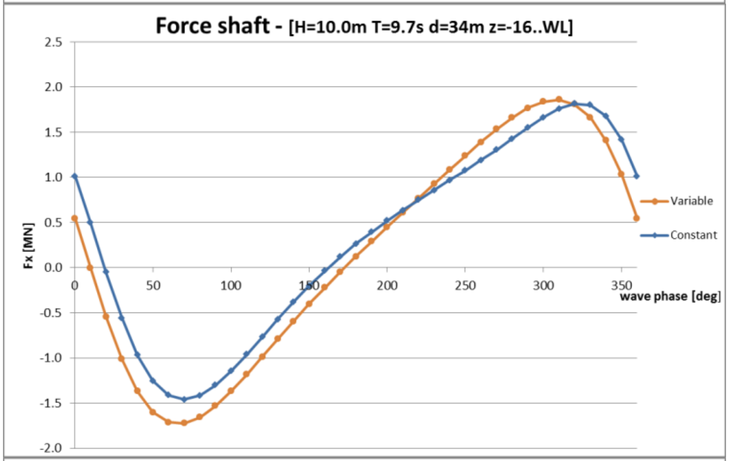

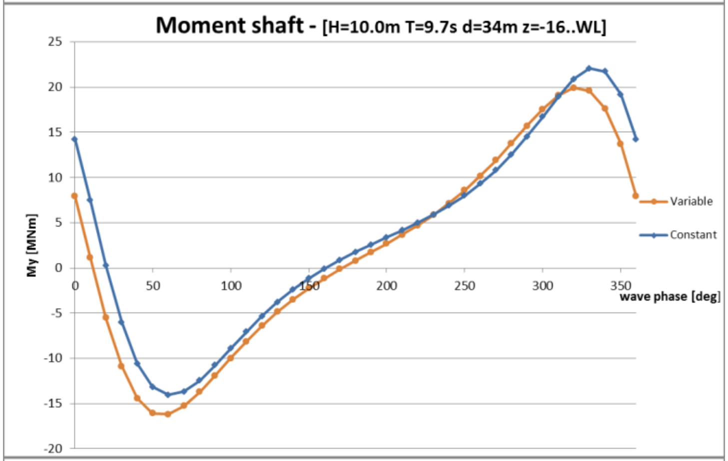

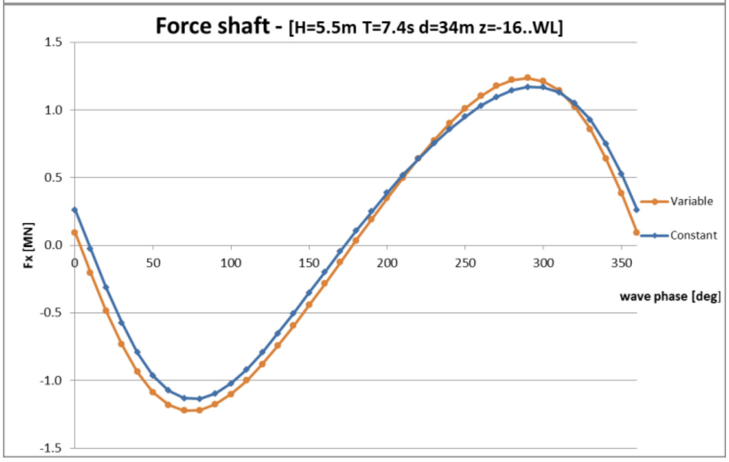

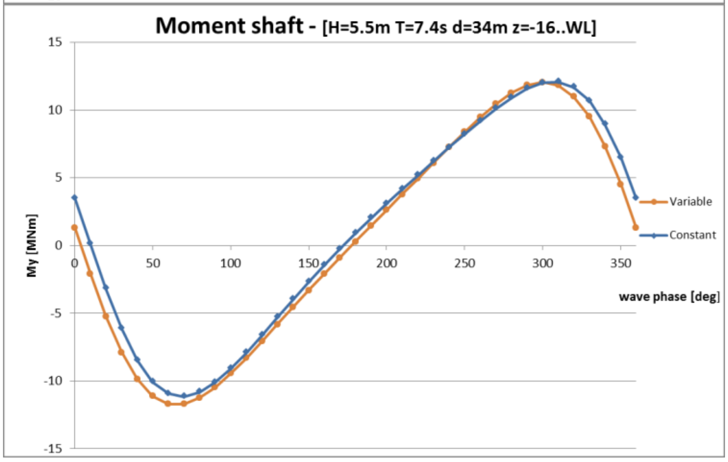

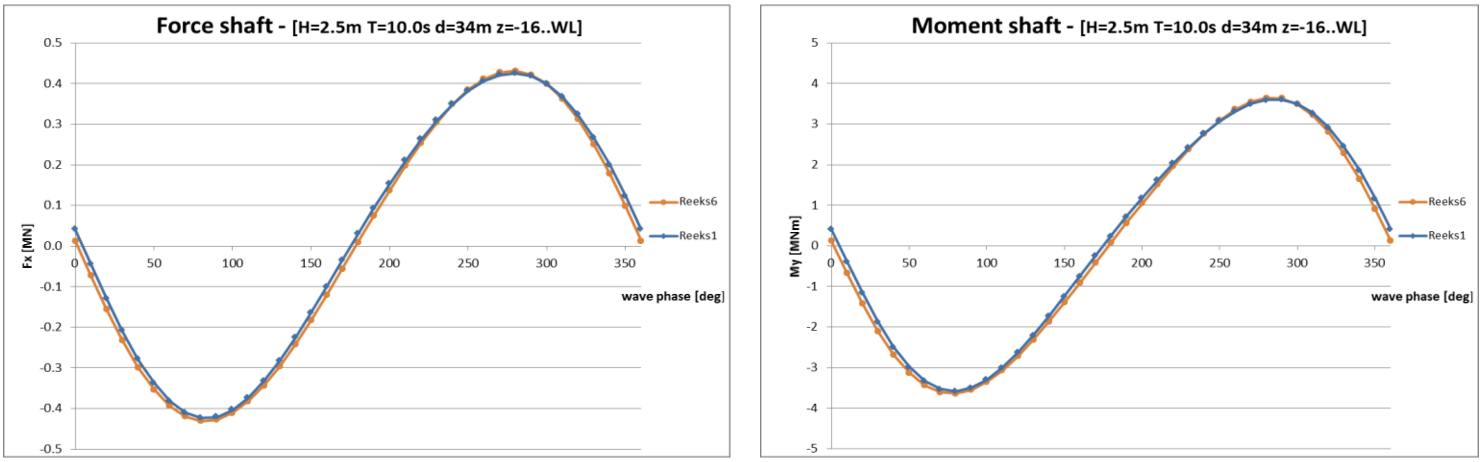

Figure C.30 - Influence of variable C_M and C_D coefficients as a function of height

The influences are:

- H=16.9m T=12.7s d=34m: the variable C_M and C_D approach leads to slightly higher force peaks.
- H=10.0m T=9.7s d=34m: the variable approach leads to a lower minimum.
- H=5.5m T=7.4s d=34m: the variable approach leads to slightly higher force peaks.
- H=2.5m T=10.0s d=34m: the variable approach has no noticeable influences.

C.8.2.3. Free surface effect

From field measurements the free surface effect can be estimated.
Based on model tests Frigaard [34] shows that the measured force in the surface zone is higher than calculated with the Morison equation, see Figure C.31.
On the other hand, according to [35], field measurements during a hurricane lead to a lower force than calculated with the Morison equation, see Figure C.32.

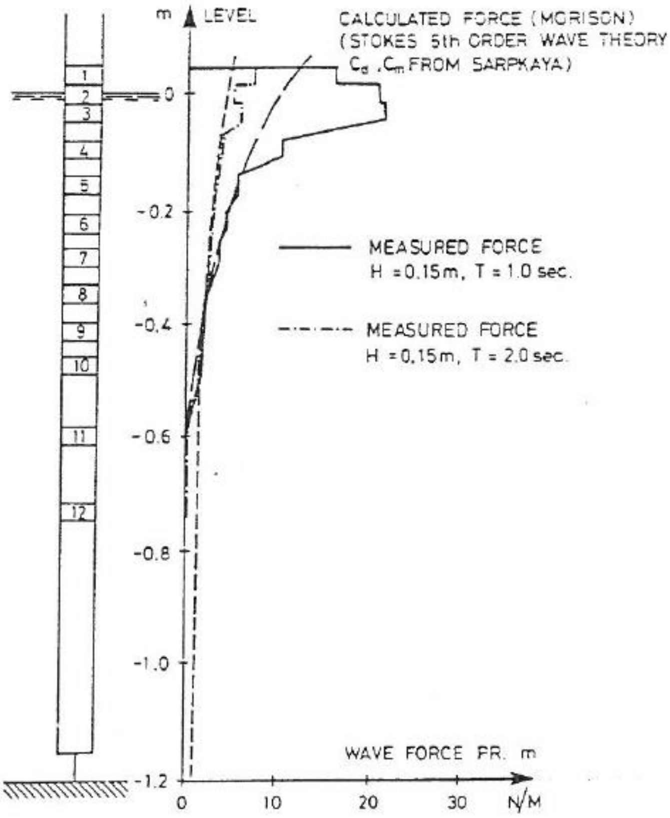

Figure C.31 - Comparison between measured and computed distributed force. Note that the measured force (discontinuous profile) is higher than the computed force (continuous profile) [34]

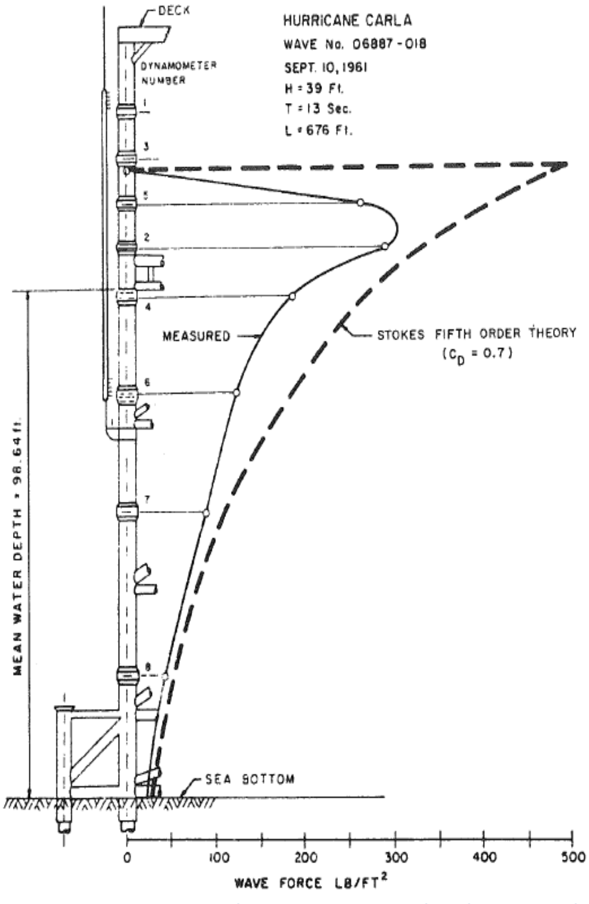

Figure C.32 – Comparison between measured and computed distributed force. Note that the measured force is lower than the computed force. [35]

Tϕrum recommended the use of modified force coefficients, see Figure C.33.

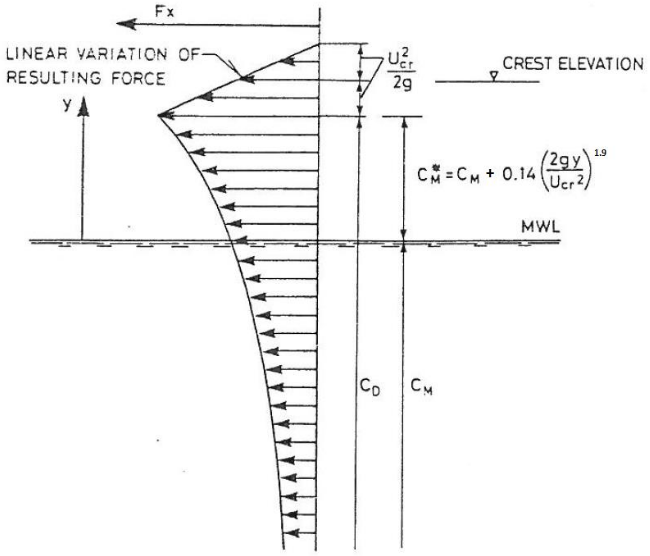

Figure C.33 - Recommended force coefficients in the free surface zone [34]

In order to investigate the influence, this was applied to case 1 (H=16.9m T=12.7s d=34m). The force is maximal for t=12.0 s (see Figure C.34). The corresponding force distribution can be found in Figure C.35 (red line).

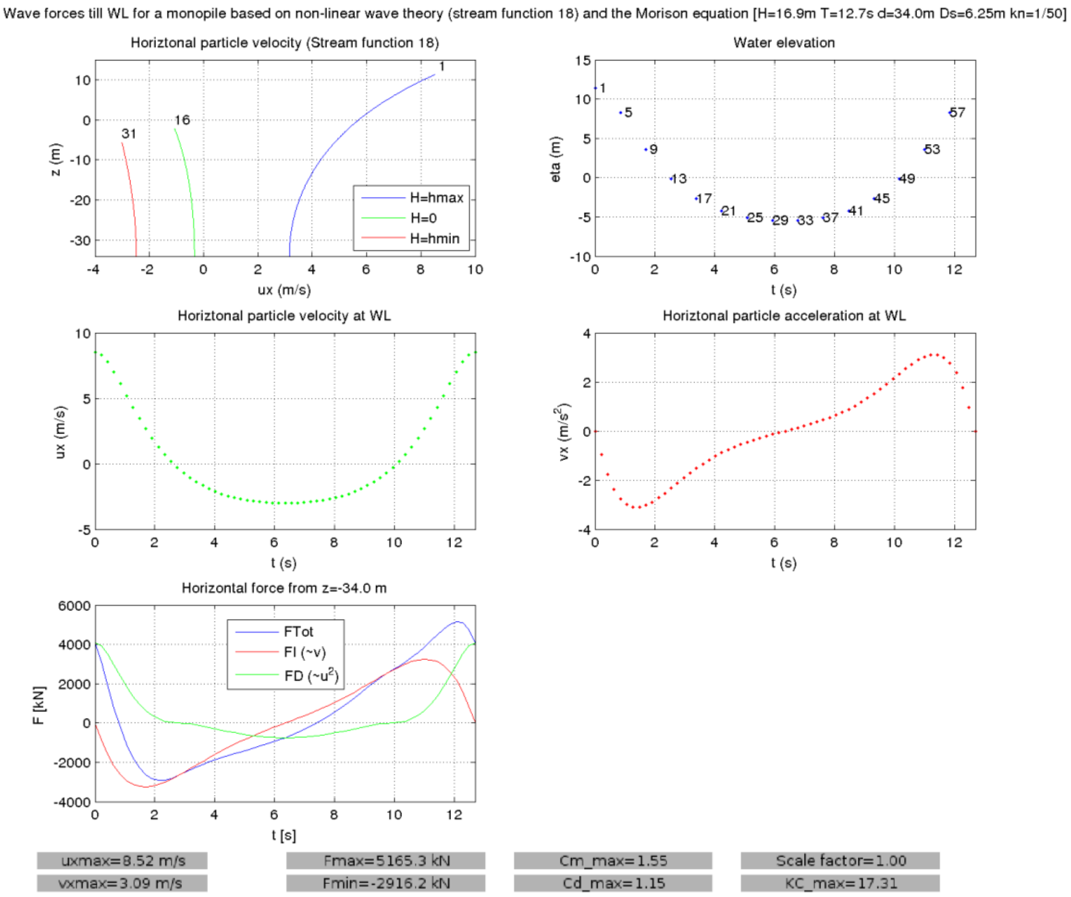

Figure C.34 – Forces based on the 'original Morison equation' (constant coefficients as function of depth, and excluding the free surface effect). Same figure can be found in Appendix C.6.

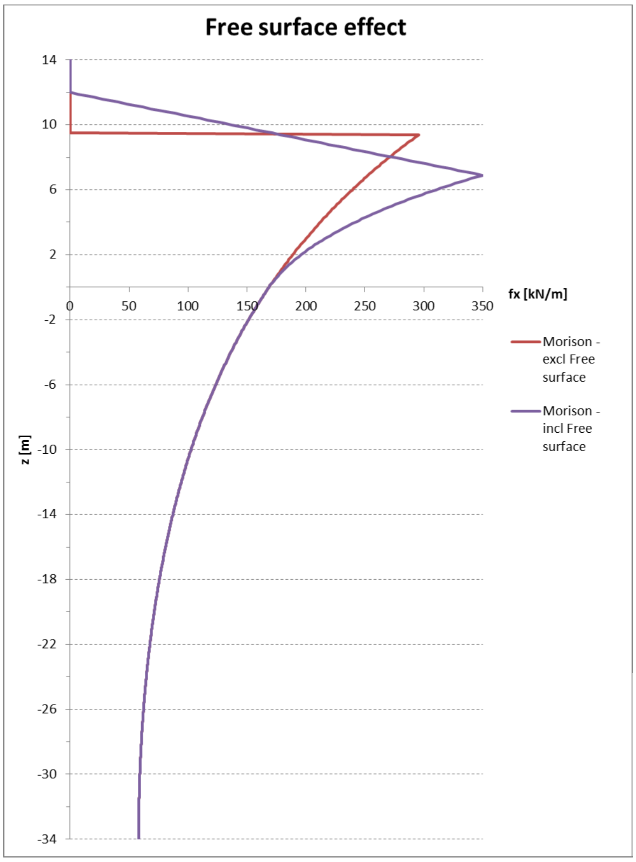

	-34<z<WL	-16<z<WL
Mor_excl	5111	3911
Mor_incl	5515	4315
	108%	110%

Figure C.35 – Force distribution as calculated with the original Morison equation and due to inclusion of the free surface effect. Forces calculated for case 1 (H=16.9m, T=12.7s, d=34m) at time of maximum force.

At t=12.0s, the velocity at the wave crest $U_{cr} = 7.0$ m/s, leading to $U_{cr}^2/2g$=2.50 m. The water elevation is $\eta(t12) = 9.45$ m.

Now the effect of the free surface is investigated, by (according to Figure C.33):

- Increasing the inertia coefficient between z=0 and z=6.95m.
- Linear variation of the force between z=6.95 and z=11.95m.
- Integration of the force distributions leads to the total forces. Two cases were investigated: from z=-34m till Water Level (WL) and from z=-16m till WL. For both cases the total force increased with about 10% due to inclusion of the free surface effect.

Appendix D **DESIGN OF THE STEEL SHAFT**

D.1. SCHEMATISATION

A schematisation of the offshore wind turbine is given in Figure D.1.

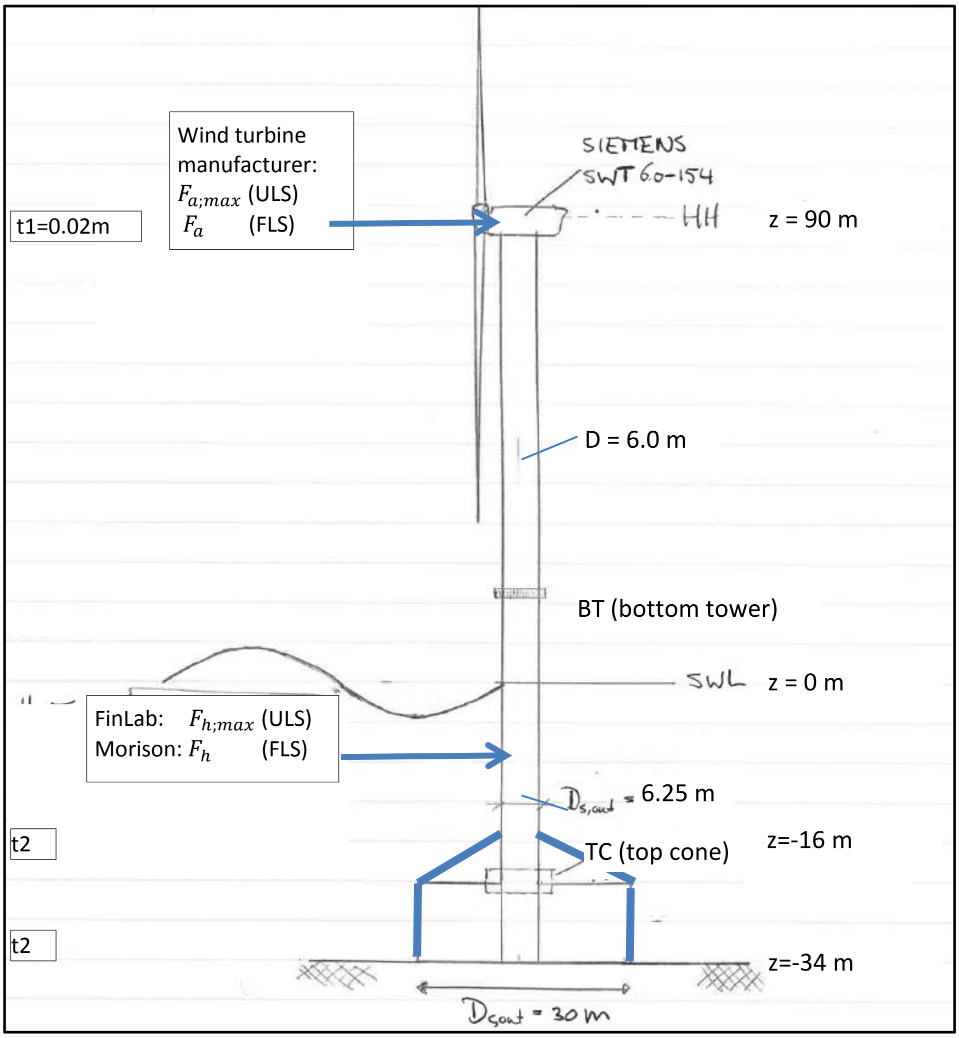

Figure D.1 – Schematisation of the offshore wind turbine for the case study in this section.
*** linear varying wall thickness**

Below the parameters of the offshore wind turbine for this section are listed.

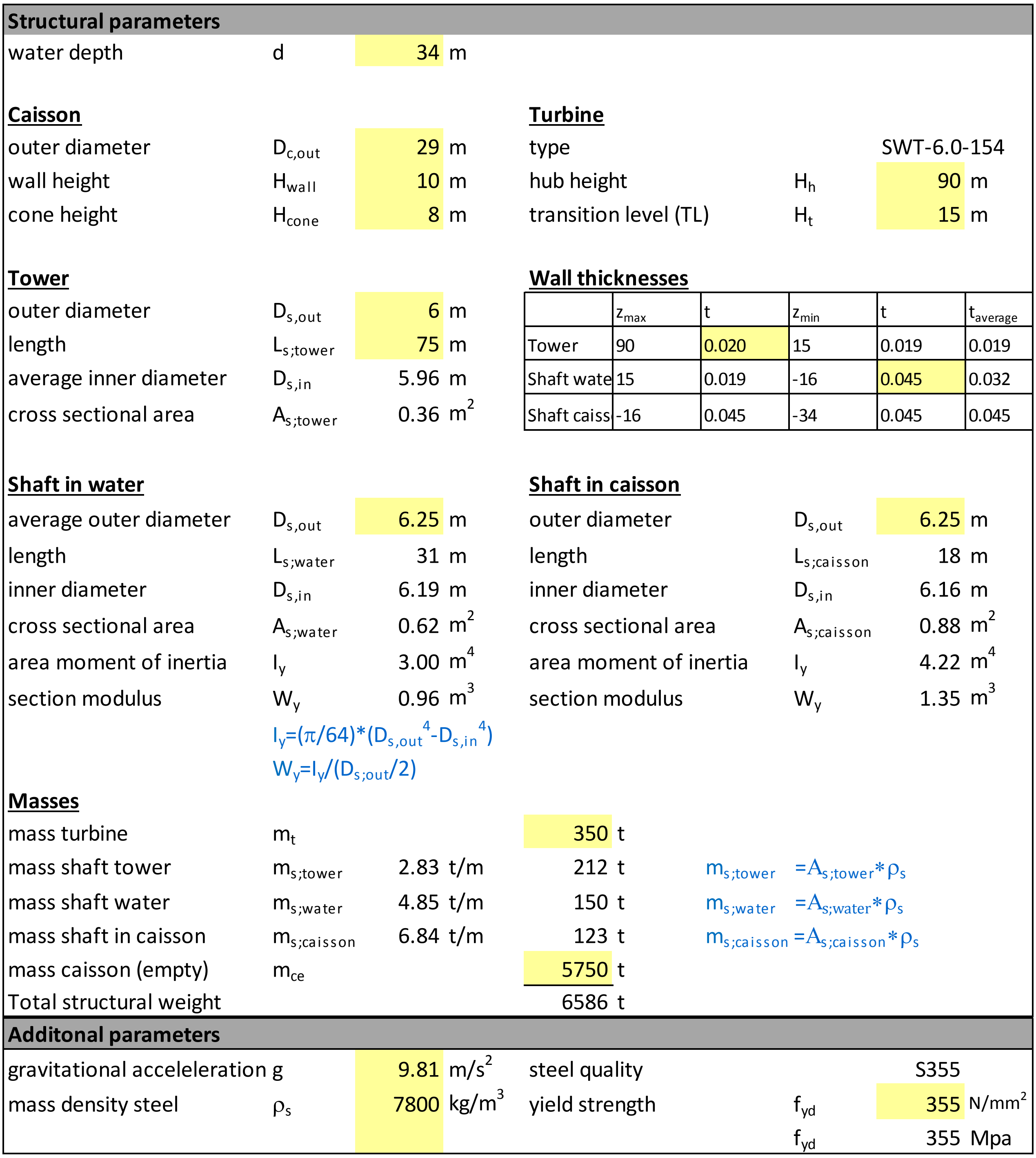

Structural parameters							
water depth	d	34	m				
Caisson				**Turbine**			
outer diameter	$D_{c,out}$	29	m	type		SWT-6.0-154	
wall height	H_{wall}	10	m	hub height	H_h	90	m
cone height	H_{cone}	8	m	transition level (TL)	H_t	15	m
Tower							
outer diameter	$D_{s,out}$	6	m				
length	$L_{s;tower}$	75	m				
average inner diameter	$D_{s,in}$	5.96	m				
cross sectional area	$A_{s;tower}$	0.36	m^2				

Wall thicknesses

	z_{max}	t	z_{min}	t	$t_{average}$
Tower	90	0.020	15	0.019	0.019
Shaft wate	15	0.019	-16	0.045	0.032
Shaft caiss	-16	0.045	-34	0.045	0.045

Shaft in water				**Shaft in caisson**			
average outer diameter	$D_{s,out}$	6.25	m	outer diameter	$D_{s,out}$	6.25	m
length	$L_{s;water}$	31	m	length	$L_{s;caisson}$	18	m
inner diameter	$D_{s,in}$	6.19	m	inner diameter	$D_{s,in}$	6.16	m
cross sectional area	$A_{s;water}$	0.62	m^2	cross sectional area	$A_{s;caisson}$	0.88	m^2
area moment of inertia	I_y	3.00	m^4	area moment of inertia	I_y	4.22	m^4
section modulus	W_y	0.96	m^3	section modulus	W_y	1.35	m^3

$I_y=(\pi/64)*(D_{s,out}{}^4-D_{s,in}{}^4)$

$W_y=I_y/(D_{s;out}/2)$

Masses						
mass turbine	m_t			350	t	
mass shaft tower	$m_{s;tower}$	2.83	t/m	212	t	$m_{s;tower} = A_{s;tower}*\rho_s$
mass shaft water	$m_{s;water}$	4.85	t/m	150	t	$m_{s;water} = A_{s;water}*\rho_s$
mass shaft in caisson	$m_{s;caisson}$	6.84	t/m	123	t	$m_{s;caisson} = A_{s;caisson}*\rho_s$
mass caisson (empty)	m_{ce}			5750	t	
Total structural weight				6586	t	

Additonal parameters							
gravitational acceleleration	g	9.81	m/s^2	steel quality		S355	
mass density steel	ρ_s	7800	kg/m^3	yield strength	f_{yd}	355	N/mm^2
					f_{yd}	355	Mpa

D.2. ULS DESIGN

For the ULS the next two loads are taken into account:

- Wind load: A thrust force of 1700 kN. Together with aerodynamic shaft loading and extreme loads from turbine operations (inertia effects) the wind turbine manufacturer prescribes an extreme load of: $M_{TL} = 30 + 1.8 * L_{tower}$ MN. This is including a safety factor of 1.35.
- Wave load: Wave loads on the steel shaft follow from the hydrodynamic analysis with FinLab Three cases are compared:
  - Forces on the shaft calculated by the Morison equation (theory)

- Forces on the shaft resulting from the Monopile calculation

For the first approach a safety factor of 1.25 is applied according to [11]. Due to the more sophisticated method applied within FinLab and the more conservative results obtained a safety factor of 1.1 is chosen for this evaluation.

Below the wind and wave loads are calculated. All bending moments are calculated with respect to the top of the cone (highest bending moment).

ULS shaft loading - d=34 m

Wave load	section: z=BT..WL		**Wind load**		
	$M_{y\|BT}$				
S1. Morison equation	6.65E+04	kNm	Bend. Moment TL $M_{y\|BT}$	1.22E+05	kNm
S2. FinLab monopile	1.47E+05	kNm	Bend. Moment TC $M_{y\|TC}$	1.64E+05	kNm
S3. FinLab GBS shaft	1.49E+05	kNm			

	Wave loads				Wind loads					
	M	γ	M_d	%	M	γ	M_d	%	$M_{d;tot}$	Increase
Morison equation	6.65E+04	1.25	8.3E+04	27%	1.64E+05	1.35	2.21E+05	73%	3.0E+05	
FinLab monopile	1.47E+05	1.10	1.6E+05	42%	1.64E+05	1.35	2.21E+05	58%	3.8E+05	26%

D.3. FLS DESIGN

D.3.1. Environmental data

For the FLS calculation the next steps have been taken:

- A wave scatter diagram based on 27 years of data and $1.86 \cdot 10^8$ wave cycles forms the input for the calculation.
- The wave scatter diagram is transformed to a lumped wave scatter diagram with 18 combinations of H_s and T_s for each one of the 8 wave directions, leading to 144 cases (Table D.1).

Lumped wave scatter diagram				Annual Wave Conditions: Sea & Swell							
Class	Sign. wave height		Period	Wave direction (coming from) [deg]							
	Range	Average	T02	N	NE	E	SE	S	SW	W	NW
(-)	[m]	[m]	(s)	0	45	90	135	180	225	270	315
1	0 - 1	0.5	3.8	117249	1224952	449588	222917	307944	366480	384716	200702
2	0 - 1	0.5	5.1	84457	365254	241443	111423	164237	564644	357057	178436
3	0 - 1	0.5	7	2100	4677	5693	774	6784	34799	22097	10127
4	1-2	1.5	4.8	38972	215350	125899	60129	78761	102070	123895	65399
5	1-2	1.5	5.9	29411	58180	62718	25954	16525	26960	42608	16119
6	1-2	1.5	7	7348	17158	20796	2799	6219	27737	21741	8985
7	2-3	2.5	5.4	16314	41336	37595	16084	12894	19304	28055	11828
8	2-3	2.5	7.2	2039	4854	5871	801	692	2326	2810	972
9	3-4	3.5	5.9	2176	3713	4457	1810	979	1711	2864	1004
10	3-4	3.5	7.2	2674	6410	7731	1192	603	1518	2739	847
11	4-5	4.5	5.9	375	640	768	312	169	295	494	173
12	4-5	4.5	7.3	777	1709	2052	457	230	485	862	280
13	5-6	5.5	7.4	229	840	1023	76	15	78	205	63
14	6-7	6.5	7.5	48	219	272	12		13	46	13
15	7-8	7.5	7.9	5	57	77				7	
16	8-9	8.5	7.9		14	24					
17	9-10	9.5	8.5			6					
18	10-11	10.5	8.5			1					
		Total		304173	1945362	966014	444739	596052	1148419	990194	494949

Table D.1 - Lumped wave scatter diagram (one year)

D.3.2. Fatigue calculation d=34 m

D.3.2.1. Wave forces

- For each of the 18 combinations the resulting wave force on the structure is determined (Table D.2). For the coupling between sea state and wave force the Morison equation can be used, as concluded in chapter 5.11. A spreadsheet available at BAM was used for this purpose. (velocities based on non-linear wave theory, inertia and drag coefficients based on the design code of DNV.
For classes 14-18 a scale factor for the total bending moment cycle is applied, based on Figure 5.19.
- It should be noted that for the first wave category Morison is not valid any more, due to the fact that D/L>0.2. But the difference is small, so it assumed that this has no influence.
- For the highest waves (H>5.5 m) results from FinLab show higher wave forces. The influence is investigated at the end of this section.
- In order to find the resulting bending stresses at the top of the cone the dynamic wave load is calculated. This load is determined by multiplying the static wave load

with the DAF. Per wave class the DAF is calculated with the aid of equation (A.35), under the assumptions:

  - Natural frequency $f_n = 0.25\ Hz$ (Appendix A.4.5.1)
  - Critical damping value $\zeta = 5.0$ (Appendix A.4.5.4)

The assumption of the critical damping value means that aerodynamic damping is always present. In reality this is not the case due to parked and fault conditions or misalignment of wind and waves (section 3.3.2). So this assumption is non-conservative.

- Per sea state, both the minimum and maximum bending stresses are calculated, leading to stress cycles.

Class	Sign. wave height		Period				Analytic	Factor	DAF		
	Range	Average	T02	L	Ursell no.		$M_{cycle;static}$	linearity		$M_{cycle;dynam}$	σ_s
(-)	[m]	[m]	(s)	(m)	(-)	ω/ω_n	(kNm)	[-]	[-]	(kNm)	(N/mm^2)
1	0 - 1	0.5	3.8	23	0.01	1.05	3,839	1.0	6.63	25,448	18.8
2	0 - 1	0.5	5.1	41	0.02	0.78	3,102	1.0	2.55	7,898	5.8
3	0 - 1	0.5	7	76	0.07	0.57	2,203	1.0	1.48	3,259	2.4
4	1-2	1.5	4.8	37	0.05	0.83	9,827	1.0	3.16	31,026	23.0
5	1-2	1.5	5.9	55	0.11	0.68	8,075	1.0	1.84	14,827	11.0
6	1-2	1.5	7	76	0.22	0.57	6,634	1.0	1.48	9,815	7.3
7	2-3	2.5	5.4	47	0.13	0.74	14,748	1.0	2.19	32,246	23.9
8	2-3	2.5	7.2	81	0.42	0.56	10,741	1.0	1.44	15,487	11.5
9	3-4	3.5	5.9	56	0.26	0.68	19,018	1.0	1.84	34,920	25.8
10	3-4	3.5	7.2	82	0.58	0.56	15,196	1.0	1.44	21,909	16.2
11	4-5	4.5	5.9	58	0.34	0.68	24,620	1.0	1.84	45,209	33.5
12	4-5	4.5	7.3	85	0.79	0.55	19,438	1.0	1.42	27,693	20.5
13	5-6	5.5	7.4	88	1.02	0.54	23,757	1.0	1.41	33,467	24.8
14	6-7	6.5	7.5	91	1.27	0.53	28,246	1.0	1.39	39,365	29.1
15	7-8	7.5	7.9	100	1.81	0.51	31,528	1.1	1.34	46,530	34.4
16	8-9	8.5	7.9	102	2.05	0.51	36,234	1.1	1.34	53,475	39.6
17	9-10	9.5	8.5	116	3.07	0.47	38,594	1.2	1.28	59,378	43.9
18	10-11	10.5	8.5	117	3.39	0.47	44,152	1.2	1.28	67,929	50.3

Table D.2 - Minimum and maximum bending moments due to waves, based on the Morison equation; d=34m. DAF based on a 1DOFS, Non-linearity scale factor based on Figure 5.19.

D.3.2.2. SN curve

- Now for each wave category the fatigue load is calculated. The direction of the waves is therefore taken into account, by taking the normal stress in North-West direction (most occurring wave direction).
- Next the stress cycles are compared with an S-N curve (Figure D.2), described by the following formula:

$$log N = log a - m \cdot log\left(\Delta\sigma\left(\frac{\mathrm{t}}{\mathrm{t_{ref}}}\right)^{k}\right) \qquad \text{(D.1)}$$

with:

N	number of stress cycles to failure at stress range $\Delta\sigma$	[-]
$\Delta\sigma$	stress range	[N/mm^2]
m	slope of S-N curve (3-5)	[-]
$\log a$	intercept of log *N* axis (a = value of N where $\Delta\sigma$ is zero)	[-]
t_{ref}	reference thickness, 32 mm for tubular joints	[mm]

t	thickness through which the potential fatigue crack will grow ($t \geq t_{ref}$)	[mm]
k	thickness exponent (0.20 – 0.25)	[-]

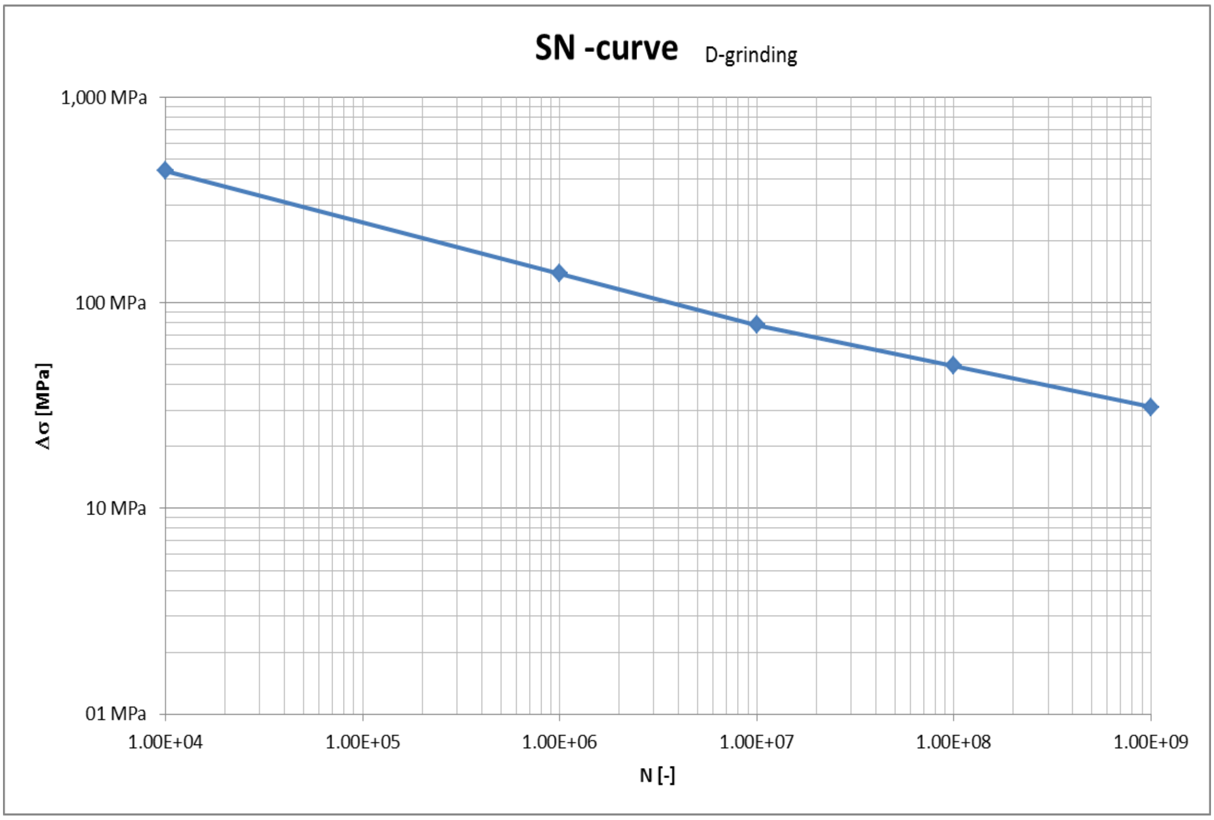

Figure D.2 – SN curve used $[\mathrm{m1} = 4; \log(\mathrm{a1}) = 14.574][m2 = 5; log(a2) = 16.468]$

- It is assumed that $t = t_{ref}$.

D.3.2.3. Fatigue load due to waves

- Now per stress cycle Δσ the number N is calculated based on the SN curve.
- For each stress cycle the influence on the total allowable fatigue is calculated (n_i/N_i), where n_i follows from Table D.1, but then for the whole lifetime. These influences are summed up according to the Miner Rule leading to a fatigue load due to waves of $D_{fat} = 0.0069$.
- In order to add the fatigue load of the waves to the wind the same amount of cycles has to be regarded. Therefore the fatigue load is transformed to a damage equivalent stress for $N_R = 1 \cdot 10^7$ cycles.

  The following formula for the damage equivalent stress is used:

$$\Delta\sigma_{eq} = \Delta\sigma\left(\frac{N_R}{D_{fat}}\right) \tag{0.1}$$

  Where $\Delta\sigma$ is a function of (N_R/D_{fat}). So, it is the corresponding $\Delta\sigma$ for a number of cycles $1 \cdot 10^7/D_{fat}$. This leads to: $\Delta\sigma_{eq,h} = 29.0\ N/mm^2$

D.3.2.4. Fatigue load due to wind

- The stress range from wind loads are provided by the wind turbine manufacturer, who has performed a TD analysis of the fatigue loads. For a lifetime of 25 years 19 combinations of horizontal force, overturning moment and torsional moment accompanied by a certain number of cycles is prescribed. With the aid of a structural model these forces are converted to stress cycles. The result is a list of stress cycles accompanied by their number of occurrence. The wind turbine manufacturer also gives a damage equivalent load for $N_R = 1 \cdot 10^7$ cycles. This combination leads, with aid of a structural model, to a damage equivalent stress for wind $\Delta\sigma_{eq,a} = 55.2\ N/mm^2$ $(D_{fat} = 0.1748)$.

D.3.2.5. Superposition of wind and wave loads

- Next, the quadratic superposition method (section 4.3) is used to combine the wind and wave stress cycles, leading to $\Delta\sigma_{eq,ah} = 62.4\ N/mm^2$.
- This value is be compared with the maximum allowable damage equivalent stress $\Delta\sigma_{eq,max}$ which follows from the S-N curve for $N_R = 1 \cdot 10^7$and $D_{fat} = 1$. In [11] a safety factor DFF (the so-called Design Fatigue Factor) of 3 is prescribed for seawater environments. This means that $\Delta\sigma_{eq,max}$ has to be determined from the S-N curve for $N_R = 3 \cdot 10^7$and $D_{fat} = 1$, resulting in $\Delta\sigma_{eq,max} = 62.8\ N/mm^2$
- Now a unity check is performed by:
- $UC = \Delta\sigma_{eq,ah} / \Delta\sigma_{eq,max}$

N.b. The quadratic superposition method is rather easy to apply. The disadvantage is that it gives little insight in the behaviour of the system. Also the magnitude of the error is uncertain, especially when the offshore wind turbine and boundary conditions with respect to the investigation of [21] are changed.

wave category	direction α	n		Δσ	Δσ∗cos(α)	(t/tref)^k	Δσ x ks	m	Log (No;1)	N	n/N	n/N cumulative
1	0	33073704	NE	18.8	**18.8**	1	18.8	5	16.46800	1.24E+10	0.00266945	0.00266945
2	0	9861858		5.8	**5.8**	1	5.8	5	16.46800	4.30E+12	0.00000229	0.00267174
3	0	126279		2.4	**2.4**	1	2.4	5	16.46800	3.59E+14	0.00000000	0.00267174
4	0	5814450		23.0	**23.0**	1	23.0	5	16.46800	4.60E+09	0.00126417	0.00393591
5	0	1570860		11.0	**11.0**	1	11.0	5	16.46800	1.85E+11	0.00000851	0.00394442
6	0	463266		7.3	**7.3**	1	7.3	5	16.46800	1.45E+12	0.00000032	0.00394474
7	0	1116072		23.9	**23.9**	1	23.9	5	16.46800	3.79E+09	0.00029427	0.00423900
8	0	131058		11.5	**11.5**	1	11.5	5	16.46800	1.48E+11	0.00000088	0.00423989
9	0	100251		25.8	**25.8**	1	25.8	5	16.46800	2.55E+09	0.00003937	0.00427925
10	0	173070		16.2	**16.2**	1	16.2	5	16.46800	2.62E+10	0.00000661	0.00428586
11	0	17280		33.5	**33.5**	1	33.5	5	16.46800	7.00E+08	0.00002468	0.00431054
12	0	46143		20.5	**20.5**	1	20.5	5	16.46800	8.12E+09	0.00000568	0.00431622
13	0	22680		24.8	**24.8**	1	24.8	5	16.46800	3.15E+09	0.00000720	0.00432342
14	0	5913		29.1	**29.1**	1	29.1	5	16.46800	1.40E+09	0.00000423	0.00432765
15	0	1539		34.4	**34.4**	1	34.4	5	16.46800	6.06E+08	0.00000254	0.00433019
16	0	378		39.6	**39.6**	1	39.6	5	16.46800	3.02E+08	0.00000125	0.00433144
17	0	0		43.9	**43.9**	1	43.9	5	16.46800	1.79E+08	0.00000000	0.00433144
18	0	0		50.3	**50.3**	1	50.3	5	16.46800	9.14E+07	0.00000000	0.00433144
1	45	12138876	E	18.8	**13.3**	1	13.3	5	16.46800	7.01E+10	0.00017320	0.00450463
2	45	6518961		5.8	**4.1**	1	4.1	5	16.46800	2.43E+13	0.00000027	0.00450490
3	45	153711		2.4	**1.7**	1	1.7	5	16.46800	2.03E+15	0.00000000	0.00450490
4	45	3399273		23.0	**16.2**	1	16.2	5	16.46800	2.60E+10	0.00013065	0.00463555
5	45	1693386		11.0	**7.8**	1	7.8	5	16.46800	1.04E+12	0.00000162	0.00463717
6	45	561492		7.3	**5.1**	1	5.1	5	16.46800	8.21E+12	0.00000007	0.00463724
7	45	1015065		23.9	**16.9**	1	16.9	5	16.46800	2.15E+10	0.00004731	0.00468455
8	45	158517		11.5	**8.1**	1	8.1	5	16.46800	8.40E+11	0.00000019	0.00468474
9	45	120339		25.8	**18.3**	1	18.3	5	16.46800	1.44E+10	0.00000835	0.00469310
10	45	208737		16.2	**11.5**	1	11.5	5	16.46800	1.48E+11	0.00000141	0.00469450
11	45	20736		33.5	**23.7**	1	23.7	5	16.46800	3.96E+09	0.00000523	0.00469974
12	45	55404		20.5	**14.5**	1	14.5	5	16.46800	4.59E+10	0.00000121	0.00470095
13	45	27621		24.8	**17.5**	1	17.5	5	16.46800	1.78E+10	0.00000155	0.00470250
14	45	7344		29.1	**20.6**	1	20.6	5	16.46800	7.91E+09	0.00000093	0.00470342
15	45	2079		34.4	**24.4**	1	24.4	5	16.46800	3.43E+09	0.00000061	0.00470403
16	45	648		39.6	**28.0**	1	28.0	5	16.46800	1.71E+09	0.00000038	0.00470441
17	45	162		43.9	**31.1**	1	31.1	5	16.46800	1.01E+09	0.00000016	0.00470457
18	45	27		50.3	**35.6**	1	35.6	5	16.46800	5.17E+08	0.00000005	0.00470462

Table D.3 - Part of the fatigue calculation

Unity check Fatigue

	D_{fat}	%	$\Delta\sigma_{eq}$ [N/mm^2]
Wind	0.1748	96.2	55.2
Waves	0.0069	3.8	29.0
Total	0.1818	100	

Damage equivalent stress	$\Delta\sigma_{eq;ah}$	62.4	N/mm^2
Allowable damage equivalent stress	$\Delta\sigma_{eq;max}$	62.8	N/mm^2
Unity Check fatigue	U.C. Fatigue	0.99	-

Table D.4 – Combination of wind and wave loads and unity check

D.3.2.6. Sensitivity wave loads

The influence of the higher wave forces for the categories 14-18 was found to be negligible. When the scale factors for these classes were set to 1.0 this resulted in the same fatigue load. This mainly has to do with the low probability of occurrence of these classes.

D.4. WALL THICKNESS REQUIRED

Now, per wave load case (Morison equation as a lower bound and results from FinLab as an upper bound) the strength check for the steel shaft is performed. This is done by:

- ULS: Calculating the bending stress at the TC level
- ULS: Performing a unity check for yielding and local buckling (assumed to be 20% lower than yielding).
- FLS: Determining the unity check for fatigue.

- To determine the amount of material necessary the wall thickness is reduced until one of the unity checks becomes ≥1 (wall diameter remains the same).
- Now the amount of material is calculated.

Strength check for the steel shaft - d=34

$M_{d\|TC}$	3.8E+05	kNm	
$\sigma_{s;d}$	283	N/mm^2	$\sigma_{s;d}=M_{d;max}/W_y$
unity check yielding	0.80	-	$f_{y;d}/\sigma_s$
unity check local buckling	0.96	-	20% lower than yielding moment
unity check fatigue	0.99	-	strength/resistance

Type d=34 m	$M_{d\|TC}$	$t_{required}$	U.C. Buc	U.C. Fat	$m_{s;water}$	$m_{s;caisson}$		Incr
S1. Morison equation	3.04E+05	0.045	0.76	0.99	195	123	318	
S2. FinLab monopile	3.82E+05	0.045	0.96	0.99	195	123	318	0%

Based on this analysis the following can be concluded:

- For the ULS wave the increase in bending moment of 120% leads to an increase of the total bending moment of 26% only.
- The increase of bending moment cycles for classes 14-18 does not result in a higher fatigue load. This has to do with the low probability of occurrence.
- The fatigue load due to waves is only a small percentage of the total fatigue load.

- When the design of the shaft would be based on the Morison equation only, this would result in the same shaft dimensions as when FinLab would be used (at least: for this water depth). This has to do with the fact that FinLab doesn't give significant higher bending moment cycles (FLS), while it does give a higher maximum bending moment (ULS). Due to this effect only the unity check of the ULS has a higher value for the second case. Due to the capacity still being present the wall thickness doesn't have to be increased.
- So, for this case with a water depth of 34m, the detailed hydrodynamic loading analysis doesn't result in larger dimensions of the shaft.
  For the largest water depth (~60m) the situation may however be different.